FUNSHO OLAITAN KOLAWOLE

Mechanical and Temperature-Dependent Tribological Behavior of CrN/DLC and Multilayer DLC-W Coatings for Automobile Engine Applications

versão corrigida

São Paulo

2022

FUNSHO OLAITAN KOLAWOLE

Mechanical and Temperature-Dependent Tribological Behavior of CrN/DLC and Multilayer DLC-W Coatings for Automobile Engine Applications

Thesis submitted to the Escola Politécnica of the University of São Paulo for a Doctoral Degree in Science.

Supervisor: Prof. Dr. Andre Paulo Tschiptschin

São Paulo

2022

FUNSHO OLAITAN KOLAWOLE

Mechanical and Temperature-Dependent Tribological Behavior of CrN/DLC and Multilayer DLC-W Coatings for Automobile Engine Applications

Thesis submitted to the Escola Politécnica of the University of São Paulo for a Doctoral Degree in Science.

Area of Concentration
Engenharia Metalúrgica e de Materiais

Supervisor: Prof. Dr. Andre Paulo Tschiptschin

São Paulo

2022

Este exemplar foi revisado e corrigido em relação à versão original, sob responsabilidade única do autor e com a anuência de seu orientador.

São Paulo, 03 de November de 2022

Assinatura do autor: _____

Assinatura do orientador: _____

Catalogação-na-publicação

Kolawole, Funsho Olaitan
Mechanical and Temperature-Dependent Tribological Behavior of CrN/DLC and Multilayer DLC-W Coatings for Automobile Engine Applications / F. O. Kolawole -- versão corr. -- São Paulo, 2022.
171 p.

Tese (Doutorado) - Escola Politécnica da Universidade de São Paulo. Departamento de Engenharia Metalúrgica e de Materiais.

1.Nitreto de cromo, carbono em forma de diamante e tungstênio 2.Filme fino 3.Mecânico e Tribológico 4.Deposição fiscia de vapor 5.Deposição química de vapor assistida por plasma. I.Universidade de São Paulo. Escola Politécnica. Departamento de Engenharia Metalúrgica e de Materiais II.t.

Dedication

I dedicate this PhD thesis to God Almighty the giver of life and inspiration.

ACKNOWLEDGEMENT

First of all, I thank God Almighty, who gave me the opportunity and grace to start and complete this program.

Secondly, my sincere appreciation to my supervisor Prof. Andre Paulo Tschiptschin for his mentorship, kindness, guidance and fatherly care towards me throughout my program.

I am very grateful to my wife, Ibiwumi Damaris Kolawole, who stood by me throughout the program to support and encourage me. My Sons, Daniel Oluwatiresimi Kolawole and Gabriel Motirireoluwa Kolawole for their patience and understanding.

Special thanks to my father, Prof. Victor Are Kolawole and my mother, Mrs. Rachael Bola Kolawole, my brothers, Dr. Shola Kolade Kolawole, Dipo David Kolawole and sister, Bukola Abigail Sanni-Manuel for their moral support and encouragement.

I would like to acknowledge my father-in-law, Hon. Joseph Segun Ayeni, mother-in-law, Mrs Felicia Taiwo Ayeni and brother-in-law, Tomiwa Pudens Ayeni for their support during this program. Thanks to my brother-in-law, Engr. Victor Sanni-Manuel and sisters-in-law, Abisola Kolawole and Grace Kolawole for the encouragement.

Special thanks to my friends Patience Shamaki who has been so wonderful to my family and has always been there by us. Thanks to my PTDF friends and family, Michael, Bashiru, Amir, Dickson, Adukwu, Abba and Ahmad. Thanks to the Makinde family who have been so kind to my family. I would also like to sincerely acknowledge my friends Luis, Andre, Wilmar, Newton, Luiz, Andrei, Anderson, Dany, Daniel, Livio, Rafael,

Mateus, Pedro, Rafael Maia, Mohammed Masoumi, Marcos Dantas, Arnaldo, and Andre, who always assisted me during my work. Thanks to my friend Thiago Silva.

Thanks to Suellen, Tina and Vera, and other Metallurgical and Materials Engineering staff. Thanks also to the Laboratory of Surface Phenomena (LFS) staff, who also assisted me with part of my experiments.

Thanks to Master in Engineering Paulo Konrad Vencovsky and staff at the HEF Durferrit, Brazil for allowing me to use their reactor for the deposition of the DLC thin films. Thanks to Filipe Estevao, Gustavo Bispo, and Anton Paar's staff for allowing me to use their AFM and Calotest equipment for my analysis. To Prof. Marco, who also assisted me with the deposition of my samples at the initial stage of my research. Thanks to Prof. Peter Hammer, from Photoelectron Spectroscopy Laboratory (LEFE), Departamento de Físico-Química, Instituto de Química – UNESP for the XPS analysis. Thanks to Dr. Jefferson Bettini and other staffs of Laboratório Nacional de Nanotecnologia (LNNano) in Centro Nacional de Pesquisa em Energia e Materiais (CNPEM), Campinas, Sao Paulo, Brazil.

I sincerely acknowledge Prof. Giorgio De Tomi, Prof. E. A. Ajayi, and Simone Lau for making it possible for me to arrive in Brazil to start my research. Thanks to Petroleum Technology Development Funds (PTDF) and staff for the scholarship opportunity. To Conselho Nacional de Desenvolvimento Científico e Tecnológico (CNPq) for the scholarship given to me.

ABSTRACT

CrN/DLC with Cr interlayer and DLC-W with WC interlayer were deposited using a hybrid Physical Vapour Deposition and Plasma Enhanced Chemical Vapour Deposition (PECVD) reactor on Ford Ka 1.0 model mechanical valve tappets. The PVD / PECVD reactor has a 700 mm planetary table with rotational movement around two axes. Characterization of the chemical composition, microstructure and topography of the coatings was performed using X-ray Photoelectron Spectroscopy (XPS), Raman Spectroscopy, Scanning Electron Microscopy, and Energy Dispersive Spectroscopy (SEM/EDS), Atomic Force Microscopy (AFM), Transmission Electron Microscopy (TEM), Selected Area Electron Diffraction (SAED), Energy Dispersive Spectroscopy (EDS) and Electron Energy Loss Spectroscopy (EELS). The mechanical properties of the coatings were analyzed using microindentation and nanoindentation to evaluate the fracture toughness, hardness, and elastic modulus of both coatings. The adhesion properties of the coatings to the substrate were examined using CETR-UMT Multi-Specimen Test System equipment and Hysitron TI-950 TriboIndenter for micro-scratch and nano-scratch respectively. Rockwell C indentation was used to determined acceptable failure according to VDI 3198 standard. Reciprocating Wear tests were performed for the uncoated, CrN/DLC, and DLC-W coated valve tappet using an Optimol SRV® v4 device with a ball on plane configuration under dry conditions at 25 ^{o}C, 150 ^{o}C, 200 ^{o}C, and 250 ^{o}C. The load used was 20N for a total duration of 30 min, 10 Hz of reciprocating frequency, and a stroke of 2 mm with a contact body of AISI 52100 steel sphere balls. Scanning Electron Microscopy was used to observe the wear tracks and scars on the uncoated and coated valve tappets. The chemical composition of the wear tracks was analysed by energy-

dispersive X-ray spectroscopy (EDS) integrated with the SEM equipment, while the wear volumes were measured using 3D Optical Profilometry. Both CrN/DLC and DLC-W coatings showed good adhesion to the metallic substrate at the micro and nanoscale. The COF range was 0.061 to 0.133 for the valve tappet, 0.045 to 0.11 for CrN/DLC, and 0.049 to 0.12 for DLC-W. The Rockwell C test showed a failure mode of HF1 for the CrN/DLC and HF2 for the DLC-W, both within the acceptable failure mode. CrN/DLC had a better fracture toughness compared to the DLC-W. The Hardness values were measured as 11.04±1.91 GPa, 18.85±042 GPa, and 9.88±1.76 GPa for the substrate, CrN/DLC, and DLC-W, respectively, while the Elastic moduli were measured as 199.79±4.31 GPa, 154.93±3.21 GPa and 101.94±8.13 GPa for the substrate, CrN/DLC and DLC-W respectively. During the reciprocating wear tests, the COF for the uncoated valve tappet increased from 0.82 to 1.37 at 25^{o}C to 250^{o}C, respectively. The CrN/DLC COF increased from 0.18 at 25°C to 0.46 at 250^{o}C. The DLC-W COF increased from 0.28 at 25^{o}C to 0.69 at 250^{o}C. The CrN/DLC coating showed the lowest wear rates, ~0.53 x 10^{-5} mm^3/N.m at 25°C and 6.2 x 10^{-5} mm^3/N.m at 250^{o}C. The wear rate for DLC-W were, ~0.6 x 10^{-5} mm^3/N.m and 23 x 10^{-5} mm^3/N.m at 25^{o}C and 250^{o}C respectively. The results showed that CrN/DLC had excellent wear resistance at all temperatures (25 ^{o}C, 150 ^{o}C, 200 ^{o}C, and 250 ^{o}C), while DLC-W had excellent wear resistance at 25 ^{o}C and 150 ^{o}C. At higher temperatures, 200 ^{o}C, and 250 ^{o}C, the wear rates for DLC-W were very high. Both CrN/DLC and DLC-W coatings had better wear resistance than the uncoated valve tappet (substrate). Furthermore, the wear track's hardness and elastic moduli revealed a reduction in hardness and elastic moduli of CrN/DLC and DLC-W as the temperature increased, which corresponds to an increase in the ID/IG ratio. The study implies a great

improvement of the wear resistance of the valve tappet using both CrN/DLC and DLC-W coatings at 25 ^{o}C and 150 ^{o}C. For 200 ^{o}C and 250 ^{o}C temperatures, only the CrN/DLC coating system performed well.

Keywords: Chromium Nitride, Diamond-like Carbon and Tungsten Doping. Thin Film. Mechanical and Tribological Behaviour, Physical Vapour Deposition. Plasma Enhanced Chemical Vapour Deposition.

RESUMO

Filmes DLC foram depositados em tuchos mecânicos de válvulas de motor à combustão interna, do veículo Ford modelo Ka 1.0, foram recobertos com filmes DLC. Dois tipos de deposição forma utilizados: DLC depositado sobre uma intercamada CrN de suporte mecânico ao DLC e DLC-W com intercamada de adesão rica em W e C. Esses filmes foram depositados em reator híbrido de Deposição Física de Vapor e Deposição Química de Vapor Assistido por Plasma (PECVD) O reator PVD/PECVD possui uma mesa planetária de 700 mm com movimento rotacional em torno de dois eixos. A caracterização da composição química, microestrutura e topografia dos revestimentos foi feita por meio de Espectroscopia de Fotoelétrons de Raios-X (XPS), Espectroscopia Raman, Microscopia Eletrônica de Varredura e Espectroscopia de Energia Dispersiva (SEM/EDS), Microscopia de Força Atômica (AFM), Microscopia Eletrônica de Transmissão (TEM), Difração de Elétrons em Área Selecionada (SAED), Espectroscopia de Dispersão de Energia (EDS) e Espectroscopia de Perda de Energia de Elétrons (EELS). As propriedades mecânicas dos revestimentos foram analisadas usando microindentação e nanoindentação para avaliar a tenacidade à fratura, dureza e módulo de elasticidade de ambos os revestimentos. As propriedades de adesão dos revestimentos ao substrato foram examinadas usando equipamento CETR-UMT Multi-Specimen Test System e Hysitron TI-950 TriboIndenter para ensaios de microesclerometria instrumentada e nanoesclerometria instrumentada, respectivamente. O ensaio de indentação Rockwell C foi usado para determinar a a adesão dos revestimentos ao substrato, de acordo com o padrão VDI 3198. Testes de desgaste reciprocante foram realizados para os tuchos de válvula revestidos com CrN/DLC e DLC-

W e sem revestimento usando um dispositivo Optimol SRV® v4 com uma configuração de esfera no plano sob condições secas a 25 °C, 150 °C, 200 °C e 250 °C. A carga utilizada foi de 20 N por um tempo total de 30 min, 10 Hz de frequência e trajeto de 2 mm. O contracorpo utilizado foi uma esfera de aço AISI 52100. A Microscopia Eletrônica de Varredura foi usada para observar as marcas de desgaste, sulcos e crateras nos tuchos de válvula revestidos e não revestidos. A composição química das trilhas de desgaste foi analisada por espectroscopia de energia dispersiva de raios X (EDS) integrada ao microscópio eletrônico de varredura, enquanto os volumes de desgaste foram medidos por perfilometria óptica 3D. Ambos os revestimentos CrN/DLC e DLC-W apresentaram boa adesão ao substrato metálico em micro e nanoescala. A faixa de variação dos coeficientes de atrito foi de 0,061 a 0,133 para o tucho de válvula, 0,045 a 0,11 para CrN/DLC e 0,049 a 0,12 para DLC-W. O teste Rockwell C mostrou um modo de falha de HF1 para o CrN/DLC e HF2 para o DLC-W, ambos dentro do modo de falha aceitável. O CrN/DLC teve uma melhor tenacidade à fratura em comparação com o DLC-W. Os valores de dureza medidos foram 11,04±1,91 GPa, 18,85±042 GPa e 9,88±1,76 GPa para o substrato, CrN/DLC e DLC-W, respectivamente, enquanto os módulos elásticos medidos foram de 199,79±4,31 GPa, 154,93± 3,21 GPa e 101,94±8,13 GPa para o substrato, CrN/DLC e DLC-W, respectivamente. Durante os testes de desgaste reciprocante, o coeficiente de atrito para o tucho de válvula sem revestimento aumentou de 0,82 para 1,37 a 25 °C para 250 °C, respectivamente. O revestimento CrN/DLC apresentou coeficientes de atrito de 0,18 a 25°C e 0,46 a 250° C. O revestimento DLC-W apresentou coeficientes de atrito de 0,28 a 25 °C para 0,69 a 250 °C. O revestimento CrN/DLC apresentou as menores taxas de desgaste, ~0,53 x 10^{-5} mm^3/N.m a 25°C e 6,2

x 10^{-5} mm^3/N.m a 250 °C. A taxa de desgaste para o revestimento DLC-W foi de ~0,6 x 10^{-5} mm^3/N.m e 23 x 10^{-5} mm^3/N.m a 25 ºC e 250 ºC, respectivamente. Os resultados mostraram que o CrN/DLC apresentou excelente resistência ao desgaste em todas as temperaturas (25 °C, 150 °C, 200 °C e 250 °C), enquanto o DLC-W apresentou excelente resistência ao desgaste a 25 °C e 150 °C. Em temperaturas mais altas, 200 °C e 250 °C, as taxas de desgaste para DLC-W foram muito altas. Ambos os revestimentos CrN/DLC e DLC-W tiveram melhor resistência ao desgaste do que o tucho de válvula não revestido (substrato). Além disso, a dureza e os módulos elásticos da trilha de desgaste revelaram uma redução na dureza e nos módulos elásticos de CrN/DLC e DLC-W com o aumento da temperatura, o que corresponde a um aumento na relação ID/IG. O estudo implica em uma grande melhoria da resistência ao desgaste do tucho da válvula usando ambos os revestimentos CrN/DLC e DLC-W a 25 °C e 150 °C. Para temperaturas de 200 °C e 250 °C, apenas o sistema de revestimento CrN/DLC teve um bom desempenho.

Palavras-chave: Nitreto de Cromo, Carbono em forma de Diamante e Tungstênio. Filme Fino, Mecânico e Tribológico. Deposição Fiscia de Vapor. Deposição Química de Vapor Assistida por Plasma.

LIST OF FIGURES

LIST OF TABLES

CONTENTS

1.0 INTRODUCTION

Diamond-like carbon (DLC) is an amorphous carbon (a-C) or hydrogenated amorphous carbon (a-C:H) thin film material with a high fraction of metastable four-fold coordinated sp^3 carbon bondings, as in diamond, and three-fold coordinated sp^2 carbon bonds, as in graphite, with hardness varying in the range 10 – 80 GPa (DEARNLEY et al., 2010; ROBERTSON, 2002; GRILL, 1993). The non-hydrogenated DLCs have unpassivated carbon atoms at their surfaces with dangling carbon bonds, making them hydrophilic, while the hydrogenated DLCs have their surface carbon atoms passivated (saturated), making their surface hydrophobic (DEARNLEY et al., 2010). The non-hydrogenated DLCs are produced using Physical Vapour Deposition (PVD) methods by physical evaporation of graphitic sources, while the hydrogenated DLCs are produced using plasma assisted/enhanced Chemical Vapour Deposition (PACVD/PECVD) methods by plasma pyrolysis of carbonaceous chemical vapours like acetylene, methane, propane or butane or a combination of PVD and PECVD methods, which can be referred to as hybrid deposition technology (DEARNLEY, P. A., et al., 2010; CINIVIZ et al., 2016).

Diamond-like carbon have widespread applications as protective coatings in areas such as cutting tools, automotive engines, biomedical implants, micro-electromechanical devices (MEMS) due to the high mechanical hardness, chemical inertness, optical transparency and a wide band gap semiconductor they possess. DLC coatings are commonly used for automotive engine parts (cylinder head, cylinders, crankshaft, connecting rods, pistons, sparks plug, fuel injectors, intake and exhaust valves, camshaft, and belt) (SNIDERMAN, 2016). The main reason DLC coatings are used in automotive engine parts are simply because they are low friction and high wear resistance coatings

(CHA; ERDEMIR, 2015). Figure 1 gives a schematic of the breakdown of the energy consumed by a passenger car, which indicates that 33% of energy is lost to friction and 11.5% of this energy is lost in the engine.

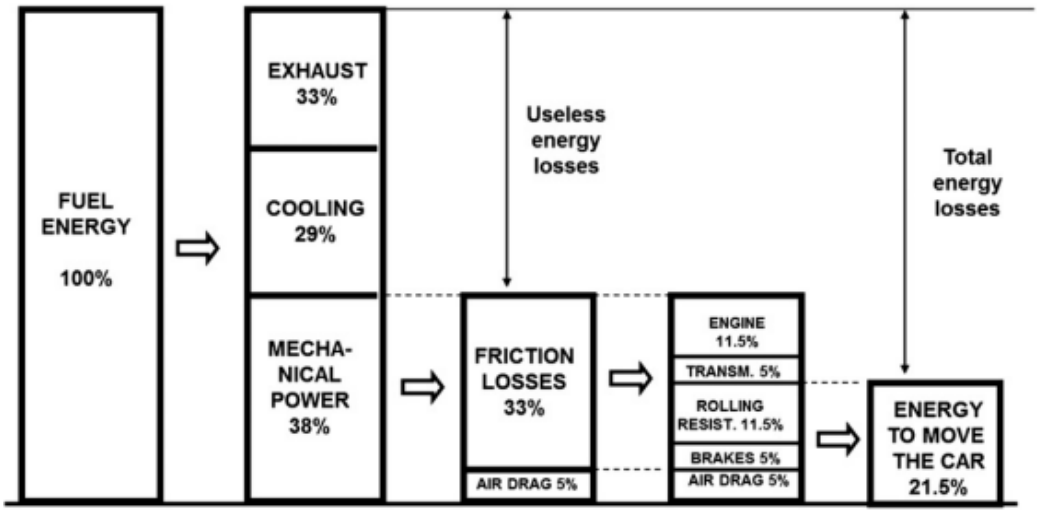

Figure 1: Breakdown of passenger car energy consumption (HOLMBERG; ANDERSSON; ERDEMIR, 2012).

In the automotive industry there is an increasing desire to improve environmental friendliness, reliability, durability, and energy efficiency. The transportation sector consumes a lot of energy and this accounts for 13.5% of the total global warming (IBRAHIM et al., 2017). Wear and friction reduction are the key factors to reducing energy losses in combustion engines, which can be achieved by surface treatments and coatings (MOBARAK; CHOWDHURY, 2014). Many automotive industries are attracted to the use of DLC coatings as protective films for engine components due to its high hardness, ultra-low friction, and good wear resistance under dry or lubricated contacts (BEWILOGUA et al., 2009; LAWES; FITZPATRICK; HAINSWORTH, 2007).

In automotive engines, rolling contact fatigue, micro-pitting, oxidation, and scuffing as presented in Figure 2 are the tribological challenges encountered during operations.

The use of DLCs can overcome these challenges except for the issue of oxidation. This is due to the high temperatures (150 to 180^{o}C) involved, if exposed to high temperatures at operating conditions of the engine, they would be prone to oxidation (DEARNLEY et al., 2010). A decrease in friction coefficient and wear of DLC films occurs with increase in temperature between 100 – 300^{o}C (GRILL, 1993), however, above 300^{o}C, the friction coefficient and wear of the DLC film begin to increase gradually. This is the reason why DLC films are reliable coatings from room temperature up to 300^{o}C.

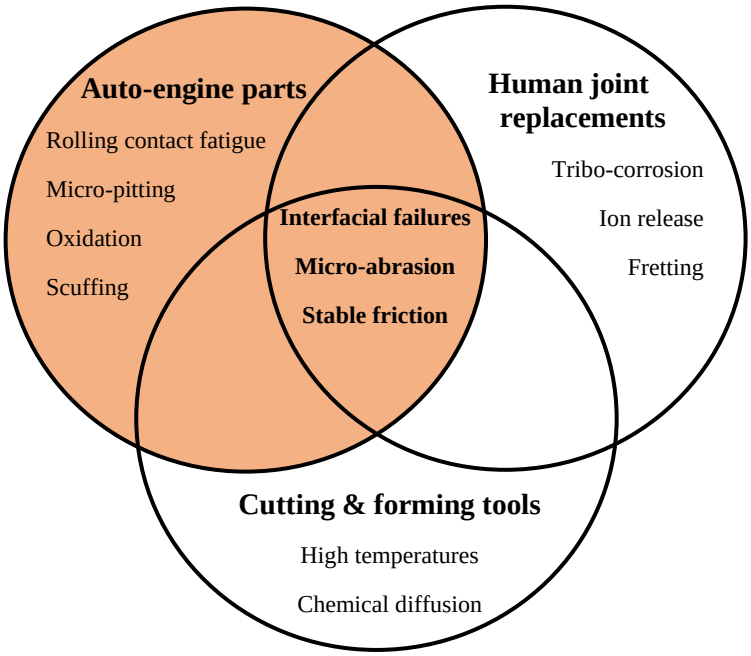

Figure 2: Tribological challenges for carbon coated components and devices (DEARNLEY et al., 2010).

Doping helps to improve the performance of DLC coatings. The advantages of non-metal and metal doped DLC coatings are that they increase the surface energies and ability to interact with lubricants to form surface protective films, good adhesion with substrate, increased wear resistance, improved electrical conductivity, decreased internal compressive stresses during deposition and improve thermal stability. It reduces the wear

rates and coefficient of friction as it generates a transfer layer on the counter surface, which forms a tribofilm with lubricants (MOBARAK; CHOWDHURY, 2014). Presently, these coatings are used in engine and powertrain components in passenger cars, those under boundary lubricated conditions are not left out. The interaction of DLC coatings in oil lubricants and various lubricant additives are complex due to the variety of DLC (non-hydrogenated and hydrogenated) coatings and lubricants which affects their tribological performance (ABDULLAH et al., 2014). Hydrogen content, doping elements and sp^2/sp^3 ratio are the intrinsic factors that affect the tribological performance of DLC coatings under lubricated conditions and their interaction with lubricant additives strongly depends on them (ABDULLAH et al., 2014; PODGORNIK; JACOBSON; HOGMARK, 2003).

Si-doped DLC (Si-DLC) is a common example of metal doped DLC and has been reported to resist oxidation, it would promote the formation of a protective Si-rich surface passive film in aqueous corrosion wear environments that are like the automotive engine operating conditions. The Si-doped DLC has an excellent tribo-oxidation resistance, high hardness (50GPa) and micro-abrasion resistance to carbonaceous combustion particulates (DEARNLEY et al., 2010). Hardness and internal compressive stress increase with increasing sp^3 content (sp^2/sp^3) ratio in DLCs. Internal compressive stress for DLC coatings (> 1GPa) in tribological applications is not good, due to the elastic strain energy that drives fractures along the coatings/substrate interface, leading to delamination through blistering (DEARNLEY et al., 2010). Doping DLC coatings with metals increases the interfacial fracture toughness and moderates the internal stress by improving the bond layer of the coatings. High internal stress can also be reduced by doping with metals or non-metals (DEARNLEY et al., 2010; NAKAO et al., 2017). DLC

coatings have numerous advantages due to the unique properties and have been doped with metals. Several research has been carried out on their tribological, biomedical, mechanical, optical, and electrical properties. However, there is limited studies carried out on the thermal properties of DLC coatings doped with metals (FU et al., 2005). Using W doping is an effective way to reduce the thermal induced stress or increases the critical load of failure in the scratch-test of DLC coatings (TANG et al., 2014).

Some authors have published their findings on the thermal stability of DLC coatings and it has been reported that DLC films could not retain their diamond-like properties at high temperature due to the changes in their structure, during the transformation of sp^3 bonds to sp^2 bonds (LI et al., 2006; ZHANG; BUI; LI, 2006). Elements such as Si or N or nanoparticles-dispersed composites have been used as dopant for DLC to improve their thermal stability (CHOI et al., 2009; ER; SO, 2010; ZOU et al., 2009). Poor adhesion is also another problem associated with DLC film when deposited on metallic substrates, due to residual stresses (BORGES; PFENDER; HEBERLEIN, 2001). However, to overcome these, different interlayers between the substrate and DLC film (e.g. SiH_4 or Cr) have been used. Furthermore, diffusion treatments of the substrates, like plasma nitriding, have been tried (BORGES; PFENDER; HEBERLEIN, 2001). Controlled metal ions incorporated into solid are very important for research and industrial applications (SCHMID, 1998; WANG et al., 2006). Metal ion-doped solid films combine the properties of the metal ion particles, especially nanoparticles, and the bulk of the host material (SHIRAKURA et al., 2006; TAKAHARA et al., 2001).

Pure DLC coatings are specifically known for their poor adhesion on metallic substrates, doping of DLC with metallic elements helps to reduce residual stress and interfacial difference between the film and metallic substrate. DLC-W have been reported by researchers to have improved adhesion properties, excellent wear resistance, corrosion resistance, and high hardness. The properties of DLC doped with tungsten is altered when this carbide forming transition metal modify the amorphous structure to form a nanocomposite with nanosized carbide embedded into the carbon matrix (FU et al., 2005; TANG et al., 2014; HOVSEPIAN et al., 2016; MÜLLER et al., 2017; MUTAFOV et al., 2014). Tungsten is also a metallic element that has been used to improve the adhesion properties of DLC coatings deposited on metallic substrate. W-doped DLC coatings can be deposited using PECVD or PVD methods, this can be achieved by using CH_4/Ar gas, W or WC target (BANERJI; BHOWMICK; ALPAS, 2014; BHOWMICK; BANERJI; ALPAS, 2015; KRŽAN; NOVOTNY-FARKAS; VIŽINTIN, 2009).

It is generally known that the hardness, Young's modulus, and adhesion of DLC-W improves significantly resulting in low wear rate and higher load capacities, giving rise to the excellent tribological and mechanical properties of DLC-W (BANERJI; BHOWMICK; ALPAS, 2014; BHOWMICK; BANERJI; ALPAS, 2015; KRŽAN; NOVOTNY-FARKAS; VIŽINTIN, 2009). DLC-W films has been deposited using several techniques such as, DC magnetron sputtering (MUTAFOV et al., 2014; BANERJI; BHOWMICK; ALPAS, 2014; BHOWMICK; BANERJI; ALPAS, 2015; KRŽAN; NOVOTNY-FARKAS; VIŽINTIN, 2009), high power impulse magnetron sputtering technique (HiPIMS) (WANG; LI; KUANG, 2018), conventional DCMS and hybrid DCMS-HiPIMS (EVARISTO; FERNANDES; CAVALEIRO, 2020). As an example, Mo–W doped DLC was deposited

using industrial sized Hauzer HTC 1000-4 PVD coating machine which combines UBM (unbalanced magnetron) and HIPIMS (high power impulse magnetron sputtering) (MÜLLER et al., 2017).

Only very limit study on thermal stability and high temperature tribological behavior of CrN/DLC and DLC-W deposited by PVD and PECVD has been carried out. Therefore, this research will focus on the characterization of CrN/DLC and DLC-W and studying the mechanical behavior and thermal stability using temperature-dependent tribological analysis of CrN/DLC and DLC-W coating deposited by hybrid Physical Vapour Deposition and Plasma Enhanced Chemical Vapour Deposition. This study offers to investigate the mechanical behavior and thermal stability using temperature-dependent tribological analysis of DLC-W and CrN/DLC coatings deposited on mechanical valve tappets from an automobile engine.

2.0 RESEARCH HYPOTHESIS

Poor adhesion of DLC to metallic substrate is a well-known issue, that affects the tribological behavior of DLC, especially in the internal combustion engine of an automobile due to elevated temperatures. Focusing on the need to improve the adhesion and tribological behavior of DLC deposited on metallic substrate, applying interlayers and doping with metals would help in solving this problem. The use of interlayers improve adhesion by creating an adhesion layer, between the metallic substrate and DLC coating. While, metallic doping improves the adhesion properties by reducing the residual stress of the coatings and creating an interfacial bonding between the metallic substrate and the

DLC coating, making the doped DLC coating adhere properly to the surface of the metallic substrate.

Since, the addition of W to DLC coatings improves the adhesion properties, one research hypothesis would be to compare DLC and DLC-W, to determine the effect of the addition of the tungsten to the mechanical properties and tribological behavior of the coatings at high temperatures mentioned in literature. Another research hypothesis suggests that the use of Cr interlayer and WC interlayer would improve the adhesion properties of DLC coatings. In addition, doping DLC with W would further improve the adhesion properties and tribological behavior at high temperatures. Based on literature the tungsten added would form a solution in the DLC coating forming a single layer coating, leading to an increase in hardness and Young's modulus. Also, this hypothesis further suggests that WC present in the DLC coating, would promote graphitization (sp^3 to sp^2) at elevated temperatures during tribological tests, acting as a solid lubricant. The main contributions of this research are the study of the high temperature tribological behavior of CrN/DLC and DLC-W from 25 ^oC to 250 ^oC using SRV equipment in the ball on disk configuration. Analysing the wear mechanisms and worn surface using SEM, EDS mapping, Raman analysis and nano-indentation.

2.1 Objectives of the study

2.1.1 General objectives

The aim of this research is to deposit CrN/DLC and DLC-W coatings on mechanical valve tappet substrates, study the chemical composition, morphology, structure, mechanical and temperature-dependent tribological behavior of the as-deposited coatings, at various temperature operational conditions. To study the effect of CrN layer and W at different temperatures on the mechanical and tribological behavior of the CrN/DLC and DLC-W coated, respectively, on automotive valve tappet substrates.

2.1.2 Specific objectives

The specific objectives of this research will be to achieve the following:

- To deposit CrN/DLC and DLC-W coatings on valve tappet substrates using hybrid Physical Vapour Deposition (PVD) and Plasma Enhanced Chemical Vapour Deposition (PECVD) reactor.
- To examine the structure and morphology of the as-deposited CrN/DLC and DLC-W coatings on valve tappets (substrate).
- To characterize the as-deposited CrN/DLC and DLC-W coatings.
- To determine the mechanical and adhesion properties of the as-deposited CrN/DLC and DLC-W coatings.

- To evaluate the temperature-dependent tribological behavior of the as-deposited CrN/DLC and DLC-W coatings at room temperature (RT), 150^{o}C, 200^{o}C and 250^{o}C.

  *250^{o}C corresponds to an extreme working temperature of internal combustion engine

2.2 Justification of the study

Fuel economy is the topmost consideration manufacturers give when designing automotive engines parts (engine block, cylinder head, cylinders, tappet, crankshaft, connecting rods, pistons, sparks plug, fuel injectors, intake and exhaust valves, camshaft, and belt). Some of these parts undergo very high contact pressures (>800 MPa) and maintain low friction coefficient (< 0.1) without degradation. A lot of stress cycles are also involved, leading to high cycle fatigue durability which is also a design requirement. The use of metal doped DLC coatings reduces friction by almost 30% in automotive engines (CHA; ERDEMIR, 2015; HOLMBERG; ANDERSSON; ERDEMIR, 2012). This will in turn reduce the amount of fuel energy required to overcome friction in automotive engines, transmission, tires, and brakes. In 2009 the worldwide estimate of fuel used to overcome friction in a passenger car was 208 billion litres. On the average one passenger car uses approximately 340 litres of fuel per year to overcome friction, this is equivalent to 610 Euros according to average European gas price in 2022. Improvement in fuel economy can be achieved by threefold if friction losses are reduced (CHA; ERDEMIR, 2015; HOLMBERG; ANDERSSON; ERDEMIR, 2012; BEWILOGUA et al., 2009).

3.0 LITERATURE REVIEW

In the course of this work, hybrid Plasma Enhanced Chemical Vapour Deposition (PECVD) and Physical Vapour Deposition (PVD) systems will be used to deposit CrN/DLC and DLC-W coatings on valve tappets used for automobile engines application. The resultant CrN/DLC and DLC-W coatings will be subjected to high temperature tribological and mechanical test. Therefore, an overview of the techniques used to deposit CrN/DLC and DLC-W will be made in this section, as well as the valve tappet (substrate).

3.1 Diamond-like carbon coatings

Diamond-like carbon coatings are amorphous carbon material that exhibit some of the typical properties of diamond and are characterized based on the content of sp^3 bonded carbon and structure, which ranges from those that do not contain hydrogen such as, graphite-like carbon (GLC), amorphous carbon (a-C), tetrahedral amorphous carbon (ta-C) to hydrogenated amorphous carbon (a-C:H) and hydrogenated tetrahedral amorphous carbon (ta-C:H) (MORIGUCHI; OHARA; TSUJIOKA, 2016). The major precursors of carbon for DLCs are ethane (C_2H_6), methane (CH_4), acetylene (C_2H_2), iso-butane (C_4H_{10}), propane (C_3H_8), benzene (C_6H_6), n-butane (C_4H_{10}) and graphite targets (ZAHID et al., 2015). DLC coatings have the potential to be used on automobile part´s interface to decrease the friction coefficient (COF). The most efficient method used to evaluate the friction coefficient in DLC coatings is the use of tribological pin-on-disk testers. Yasuda et al. (2003) used DLC coatings on automobile parts and their work showed a reduction in friction for PECVD deposited DLC coatings. According to Louda,

(2007) the use of thin coatings in automotive parts brings about eco-friendly environments and economic savings.

3.1.1 Types of diamond-like carbon coatings

There are seven different types of DLC films, which all vary in mechanical, physical and tribological behavior. DLC coatings are used in automotive engines due to their ability to decrease friction, wear resistance, increase durability, and chemically inert nature. The proportion of sp^2 (graphite-like) and sp^3 (diamond-like) determines the properties they possess, although such properties can usually be influenced by adding non-metals (hydrogen, nitrogen, silicon, fluorine and sulphur) or metals (tungsten, titanium and molybdenum) as shown in Figure 3 (LAWES; FITZPATRICK; HAINSWORTH, 2007).

- Non-hydrogenated amorphous carbon (a-C),
- Non-hydrogenated tetrahedral amorphous carbon (ta-C) films,
- Hydrogenated amorphous carbon (a-C:H),
- Hydrogenated tetrahedral amorphous carbon (ta-C:H) films,
- Non-hydrogenated metal-doped amorphous carbon (a-C:Me) films,
- Hydrogenated metal doped amorphous carbon (a-C:H:Me) films,
- Hydrogenated non-metal doped amorphous carbon (a-C:H:X) films (BEWILOGUA; HOFMANN, 2014).

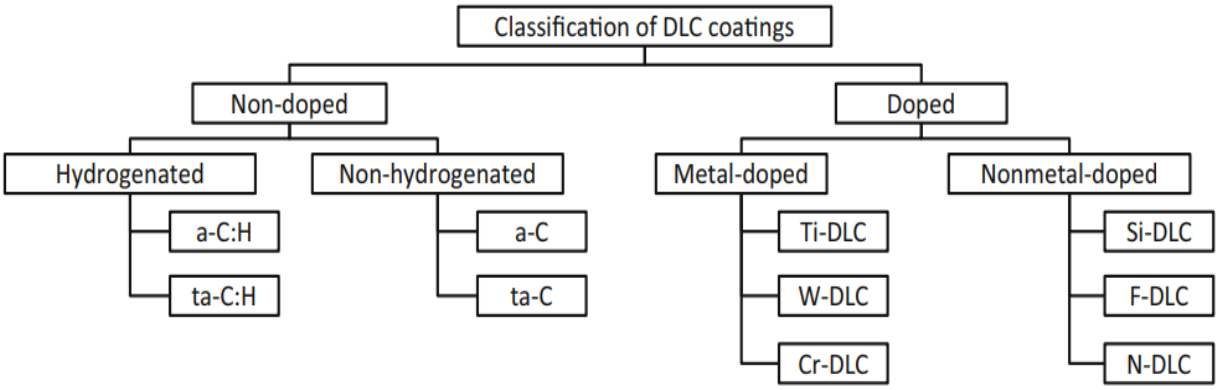

Figure 3: Classification of DLC coatings (ZAHID et al., 2015).

3.2 Deposition methods of DLC coatings

DLCs, can be produced by a wide range of deposition methods and these methods can be categorised based on their suitability for laboratory experimental or industrial application (ROBERTSON, 2002; MEMMING; TOLLE; WIERENGA, 1986). Deposition methods have been developed to produce DLCs with an increase in sp^3 bonding, depending on the type of application. DLC coatings are produced by two (2) main methods, namely; physical vapour deposition (PVD) and chemical vapour deposition (CVD). PVD methods makes use of solid graphite as carbon source, while, on the other hand CVD methods use gases such as methane, acetylene, propane, etc, as hydrocarbon sources. The sputtering (JANSEN et al., 1985; SAVVIDES, 1984), arc ion plating (LIFSHITZ, 1996), ion vapor deposition (LIFSHITZ, 1996), ion beam (AISENBERG; CHABOT, 1971), laser abrasion (COLLINS; DAVANLOO, 1992), cathode arc (MCKENZIE; MULLER; PAILTHORPE, 1991), deposition methods are known as PVD techniques, while the radio frequency (RF) plasma-assisted deposition (CATHERINE, 1991; MCKENZIE, 1996), microwave and Electron Cyclotron Resonance (ECR)-assisted

discharges (CATHERINE, 1991), plasma enhanced chemical vapour deposition (PECVD) (CATHERINE, 1991; BUBENZER et al., 1983; WILD; KOIDL, 1989) methods are known as the CVD techniques (MORIGUCHI; OHARA; TSUJIOKA, 2016). DLC coatings produced by CVD contains hydrogen, while those produced by PVD do not contain hydrogen (MORIGUCHI; OHARA; TSUJIOKA, 2016).

If the sp^3 fraction increases to a high degree, then a-C is denoted as tetrahedral amorphous carbon (ta-C), to distinguish it from sp^2 a-C according to McKenzie, (1996). Deposition methods, such as PECVD are able to reach into the interior of the ternary phase diagram between sp^3, sp^2 and H bonding. Different type of DLC films regions can be represented in the ternary diagram depending on the contents of the nature of the carbon bonds and dangling bonds (KOIDL et al., 1991) as represented in Figure 4. The PECVD technique is based on glow discharge processes, and gases, such as acetylene (C_2H_2), supply hydrogen to form a-C:H (hydrogenated amorphous carbon gases, with a negatively biased substrate working at radio frequencies (13.56 MHZ) or mid frequencies (10 to 100 KHZ). It is important to note that the PECVD process allows depositing DLC coatings at low substrate temperatures (<200^{o}C).

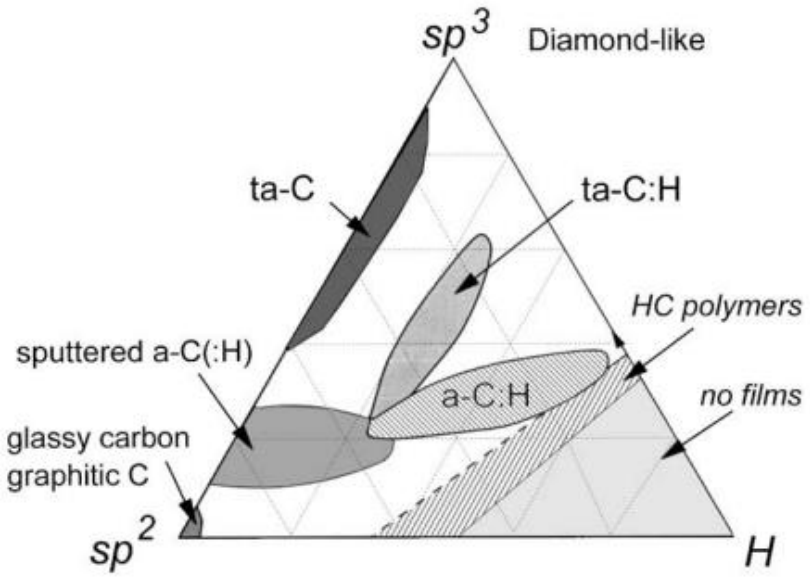

Figure 4: Ternary phase diagram for various forms of diamond-like carbon (ROBERTSON, 2002; BEWILOGUA; HOFMANN, 2014).

3.2.1 Plasma Enhanced Chemical Vapour Deposition

RF-PECVD is the most widely used laboratory deposition technique (CATHERINE, 1991; BUBENZER et al., 1983; KOIDL et al., 1991). This reactor consists of two electrodes varying in area. The rf power is mostly coupled in a capacitive like manner to a smaller electrode where the substrate is placed, the other electrode and the reactor walls are connected to the earth. Plasma is generated in between the electrodes by the rf power. Electrons in the plasma creates a sheath next to the electrodes with an excess of ions due to the high movement of electrons. This creates a positive space charge, developing a positive voltage for the plasma in conjunction to the electrodes, make it equal to the mean electron and ion current to the wall (LIEBERMAN; LICHTENBERG, 2005), as shown in Figure 5.

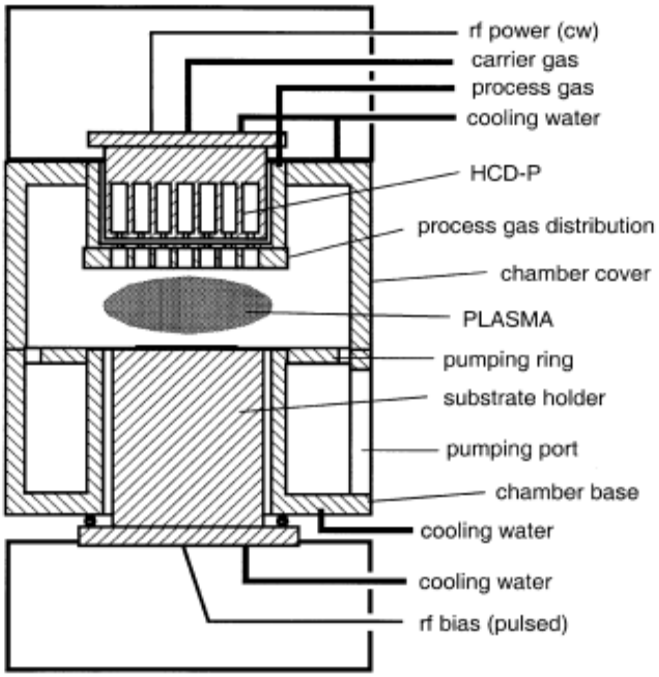

Figure 5: Schematic cross-section of a 13.56-MHz RF PECVD for diamond like carbon deposition (FEDOSENKO et al., 2002).

The PECVD technique can also be carried out in a pulsed DC source that consists of a discharge in low pressure plasma using a pulsed switched source for the plasma generation as seen in Figure 6. Through this technique, different films type (a-C:H and ta-C:H) can be obtained. The structure of the obtained films is composed of the sp^2 hybridization clusters inter-connected by carbon atoms bonded with sp^3 hybridization. Several mechanisms are involved in the deposition of films a-C:H, and the strong dependence on the properties of a-C:H films deposited by PECVD with the polarization voltage (bias-voltage) and the bombardment ions, indicate that the latter have a fundamental role in the deposition of films, which makes it necessary to describe the physical process of ionic sub-implantation (BONETTI et al., 2006; CAPOTE et al., 2008; TRAVA-AIROLDI et al., 2007).

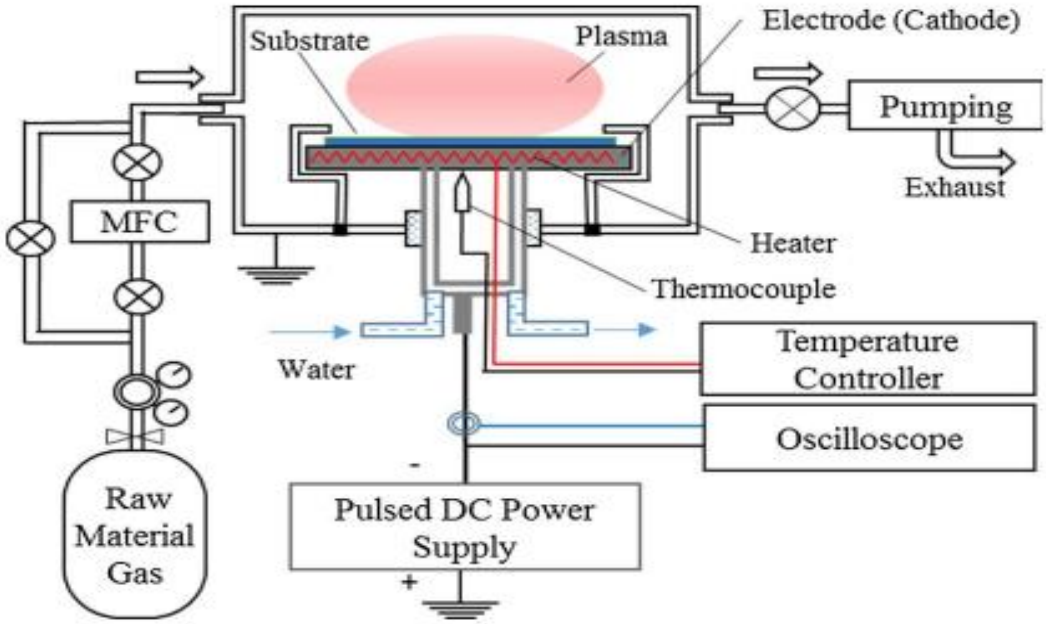

Figure 6: Schematic of Pulsed DC PECVD system (Mamun; Furuta; Hatta, 2018).

The sheaths act as a diode, making the electrodes obtain DC self-bias voltages equivalent to their peak rf voltage. The rf voltage divided between the sheaths of the two electrodes as in a capacitive divider based on their inverse capacitance as represented in Figure 7. Consequently, the DC self-bias voltage varies inversely with the electrode area as represented in equation 1 (ROBERTSON, 2002; CATHERINE, 1991; LIEBERMAN; LICHTENBERG, 2005).

$$\frac{V_1}{V_2} = \left(\frac{A_2}{A_1}\right)^2 \qquad (\mathbf{1})$$

The smaller electrode with smaller capacitance acquires the large bias voltage and becomes negative as regards to the large electrode, making it the substrate electrode. The negative sheath voltage accelerates the positive ions to give the bombardment needed to create the sp^3 bonding. In low pressure rf plasmas, the plasma is excited by a rf coupling to the sheaths. At higher pressures, the plasma is excited by Joule heating of the bulk plasma. During the deposition of diamond-like carbon films, the plasma is usually operated at the lowest pressure, so as to maximize the ion to radical fraction of the plasma. However, even at a pressure of 50 mtorr, the flux forming the film is made up of only ~10% of the ions. The energy of the ions may be lost as a result of collisions during acceleration across the sheath. If this occurs, then the ion energy ceases to be the sheath voltage. Therefore, in order to reduce the collisions that will occur it is necessary to use low pressure so as to restrict the ion energy distribution. The sheath thickness decreases with increasing pressure (P), given by equation 2 (ROBERTSON, 2002; LIEBERMAN; LICHTENBERG, 2005).

$$d = kP^{-1/2} \quad \textbf{(2)}$$

(from the Debye length) while the ion mean free path decreases as A = k/P. Hence, the ratio λ/d scales as $P^{-1/2}$ and the mean free path becomes less than the sheath thickness at low enough pressures. A lower plasma pressure can be created by using a magnetic field to confine the plasma to increase the electron path length and increase the ionisation efficiency. This allows a capacitively coupled plasma to continue to operate at $5x10^{-4}$ torr. At this pressure, the ion mean free path exceeds the sheath thickness and ion energy now has a restricted distribution (ROBERTSON, 2002).

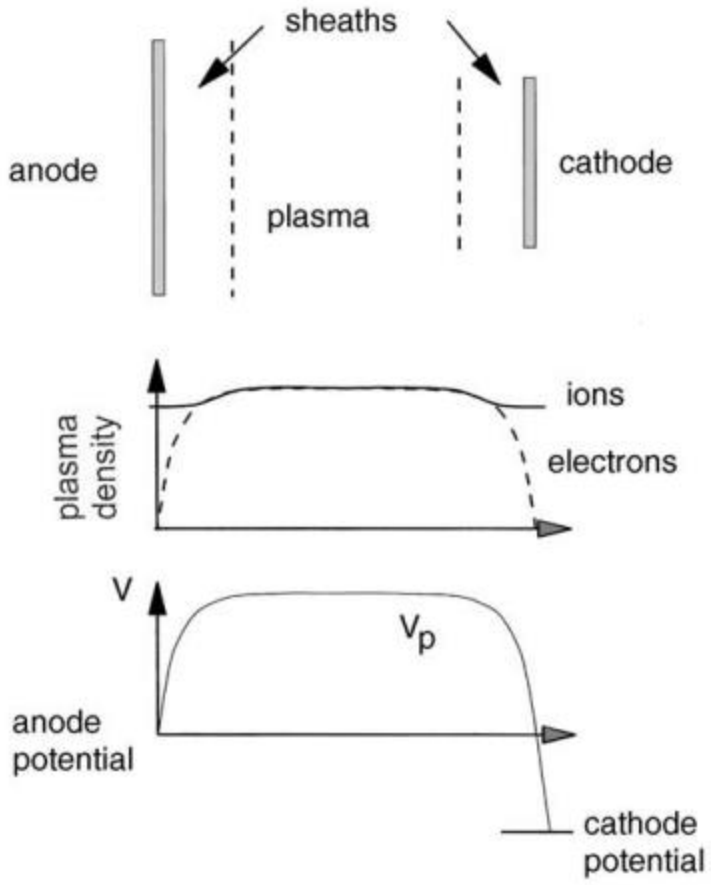

Figure 7: Electrons and ion distributions which create sheaths between the neutral plasma and the wall (ROBERTSON, 2002; LIEBERMAN; LICHTENBERG, 2005).

The principle behind the plasma beam source (PBS) (WEILER et al., 1996) is shown in Figure 8(a). The plasma beam source has a magnetic confinement of plasma through which the plasma leaves the grid at earth potential. The rf is applied to a moveable electrode whose area is larger than the grid, so that this electrode acquires the positive self-bias. This repels the positive ions through the grid to form a plasma beam which then condenses on the substrate to form DLC. The plasma beam is neutral so it can be used on insulating substrates. The most compact rf-powered, high plasma-density is the recently developed electron cyclotron wave resonance (ECWR) source (WEILER

et al., 1998) shown in Figure 8(b). The rf is inductively coupled to the plasma through a single turn coil. A transverse static magnetic field confines the plasma, causing the rf electromagnetic wave in the plasma to form left and right hand circular polarised waves and the refractive index of one of these waves increases dramatically. This decreases the wavelength of the rf, so the rf can form a half wavelength standing wave across the chamber, which allows a resonant coupling of power into the plasma bulk. A rf signal is also capacitively coupled to a rear electrode to provide a self-bias voltage to vary the ion energy. The plasma can exit the chamber as a neutral beam through a grounded grid electrode. The ECWR is equivalent to the helicon, except for a different orientation of the fields and antennas. The ECWR source produces an extremely high-density plasma of 1012 cm^{-3} or over with an independent control of the ion energy and ion current density (WEILER et al., 1998). The ECWR produces DLC at a much higher growth rate (1.5 nm per sec) than the PBS and gives uniform deposition over a diameter of 10 cm, which is scalable to large values (ROBERTSON, 2002).

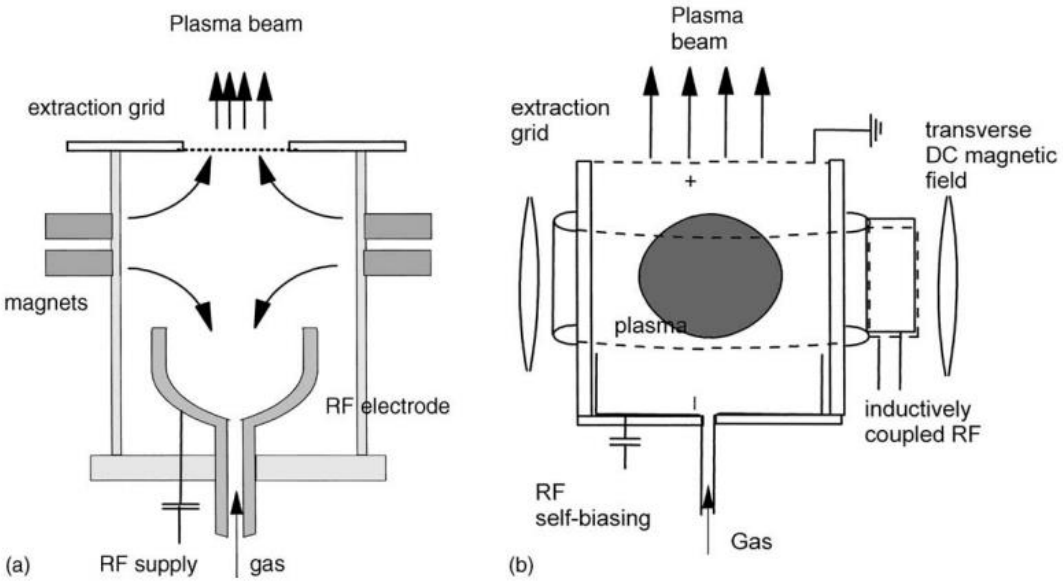

Figure 8: Schematic diagrams of the (a) plasma beam source and (b) ECWR source (WEILER et al., 1996; WEILER et al., 1998).

In recent years, it has become clear that high density plasma sources are possible (ROBERTSON, 2002; LIEBERMAN; LICHTENBERG, 2005). The two fundamental properties of the plasma are given in equation 3, which are the plasma density n_0 and the electron temperature T_e, k is the mean ion energy. The aim is to maximise n_0, and the plasma electrons have a Maxwellian energy distribution, N(E) which defines the electron temperature T_e.

$$N(E) = n_0 \exp\left(-\frac{E}{kT_e}\right) \quad (\mathbf{3})$$

Electrons with energy above some threshold energy colliding with a neutral species will ionise or dissociate it according to the convolution as seen in equation 4.

$$N_i = \int n_0 (E, T_e) f_i(E) dE \quad (\mathbf{4})$$

where f_i is the ionisation probability. This is shown schematically in Figure 9. Over a limited energy range, this gives

$$N_i = N_0 \exp\left(-\frac{E_i}{kT_e}\right) \quad (\mathbf{5})$$

Where E_i is the ionisation potential, a high T_e maximises the ionisation.

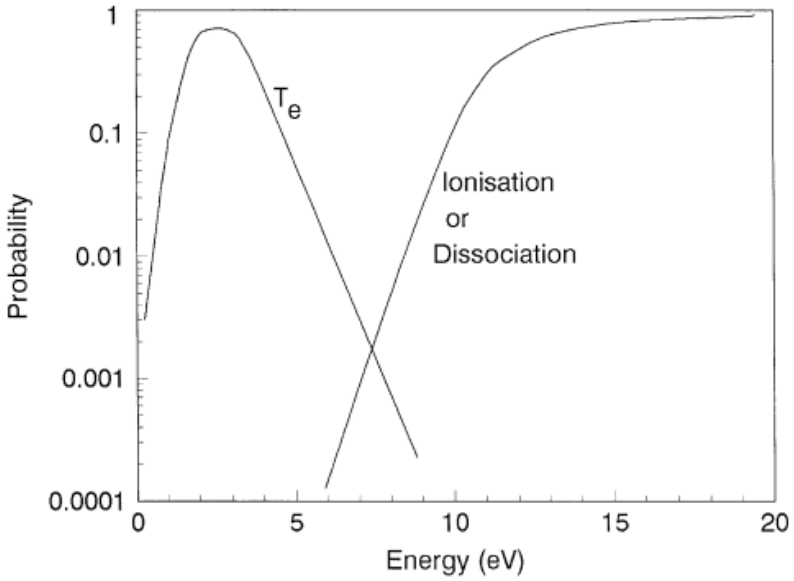

Figure 9: Electron temperature T_e (K) and the dissociation/ionisation probability of a species as a function of the threshold energy (ROBERTSON, 2002; LIEBERMAN; LICHTENBERG, 2005).

Similar relations hold for dissociated atomic species and excited species. N_p and T_e . are set by the requirements of energy and particle balance (LIEBERMAN; LICHTENBERG, 2005). The particle balance sets T_e by equating the rate of generation of ions in the bulk plasma to the rate of loss of radicals and ions to the walls.

$$K_i N_g n_0 V = n_0 u_B A \tag{6}$$

This gives

$$\frac{K_i(T_e)}{u_B(T_e)} = \frac{1}{N_g l} \tag{7}$$

where l is the effective plasma length, A and V are the surface area and volume of plasma respectively, n_0 is the plasma density, n is the density of atoms in the gas, K_i is the ionisation rate constant and u_B is the Bohm velocity of the electron. Here K_i and u_B are functions of T_e as shown in equation 6 and 7. The energy balance sets the plasma density

n_0 by equating the power absorbed by the plasma W to the energy loss per ion E_T as ion energy and as ion loss to the walls as presented in equation 8. This gives

$$n_0 = \frac{W}{eu_B A E_T} \quad (\mathbf{8})$$

The gas used in PECVD has a significant effect on the a-C:H properties. In the early days, precursors with low ionisation potentials such as benzene were chosen as this gave a much higher growth rate. The deposition rate increases roughly exponentially with decreasing ionisation energy (BUBENZER et al., 1983). For mechanical applications, it is desirable to maximise the hardness, minimising the incorporation of hydrogen. This requires using a precursor with small H/C ratio, such as acetylene, as this strongly affects the H/C ratio of the resulting film (ROBERTSON, 2002).

Acetylene is often more acceptable since just 200 V bias is required to reach 100 eV energy per carbon atom. Acetylene is very important in providing low pressure deposition due to its strong C=C bonds responsible for its simple dissociation pattern, giving mainly C_2H^{n+} ions (WEILER et al., 1996). Acetylene is preferred for mechanical purposes as a source gas, although it is not desirable for electronic applications due to its none availability in pure form, which can lead to doping effects especially when used in high density plasma. Methane has been used for electronic applications due to its high purity, however the growth rate is lower and the hydrogen content is higher (ROBERTSON, 2002).

3.2.2 Physical Vapour Deposition

Physical Vapor Deposition is a method used to deposit coatings on a substrate. This technique produces coatings when the materials to be deposited goes from condensed phase to a vapour phase then solidifies as a thin film in a condensed phase, this can be seen as transfer of material at the atomic level (FARAJI; KIM; KASHI, 2018). This process is described as follows; (1) The material to be deposited is converted into a vapor by physical means, (2) the vapor is transported to a region of low pressure from its source to the substrate, and (3) the vapor undergoes condensation on the substrate to form a thin film. PVD can be used to deposit films of a few nanometers to thousands of nanometers thick and also to form multilayer coatings, graded composition deposits, very thick deposits, and freestanding structures (FARAJI; KIM; KASHI, 2018).

The schematic of a typical physical vapour deposition process is shown in Figure 10. PVD process is divided into sputtering and evaporation. In sputtering the atoms or molecules are dislodged from the solid target through the impact of gaseous ions (plasma), whereas in evaporation, thermal sources are used to deposit thin films [60]. A wide range of deposition techniques can be used: Sputtering technique – Magnetron (Radio Frequency (RF), Direct Current (DC), Magnetically Enhanced Plasma (MEP), Unbalanced Magnetron Sputtering (UBMS), Dual Magnetron Sputtering (DMS) and High-Power Impulse/Pulse Magnetron Sputtering (HiPIMS/HPPMS)), Ion Beam, Diode, Triode and Reactive Sputter Deposition, Evaporation technique – Arc (Stirred, Random and Cathodic Arc Deposition), Electron Beam, Inductive and Resistive (BAPTISTA et al., 2018).

3.2.2.1 Sputtering and Evaporation Principles

The PVD techniques uses a thermal physical process of releasing or collision to transform the target (material) to be deposited into atomic particles, which are directed to the substrates in conditions of gaseous plasma in a vacuum environment, generating a physical coating by condensation or the accumulation of projected atoms (BAPTISTA et al., 2018). In sputtering processes, before the deposition takes place, the substrate can be cleaned by reversing the voltage polarity between the substrate and the target (cathodic cleaning).

The raw material to be deposited is usually in the form of a target, in which a magnetron is placed close by during the process. An inert gas is introduced into the vacuum chamber, and dissociates forming a plasma. The inert gas ions are accelerated by a high voltage being applied between the target and the substrate in the direction of the magnetron, and, as a result, atomic size particle is released from the target. The released particles are then projected due to the kinetic energy transmitted by gas ions which have reached the target going to the substrate and creating a solid thin film (BAPTISTA et al., 2018).

The principle for the evaporation process involves the use of a purely physical processes, in which the target acts as an evaporation source containing the material to be deposited, which works as a cathode. The material is heated at high vapour pressure by bombarding electrons in high vacuum, and the particles are released. Leading the collision between the atomic size released particles and gas molecules, inserted into the reactor, this accelerates the particles, by creating a plasma. This plasma proceeds

through the deposition chamber, being stronger in the middle position of the reactor (BAPTISTA et al., 2018).

Sputtering is a cleaner method and permits better densification of the film. Stress and deposition rate are also controlled by power and pressure. Figure 10 shows the schematic representing two conventional PVD processes: (a) sputtering and (b) evaporation using ionized Argon (Ar^+) gas. Table 1, shows a summarized comparison between sputtering and evaporation techniques (BAPTISTA et al., 2018).

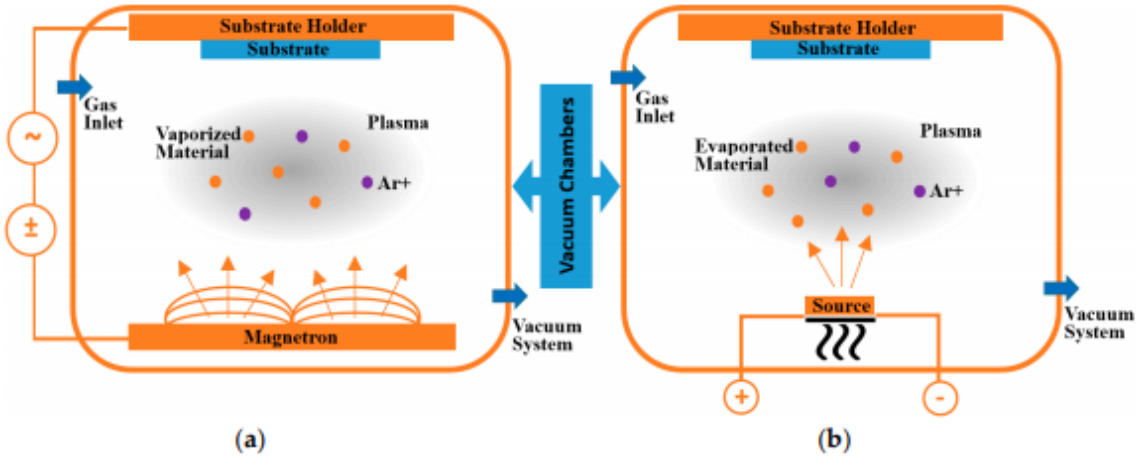

Figure 10: Schematic of two conventional PVD processes: (a) sputtering and (b) evaporation using ionized Argon (Ar^+) gas (BAPTISTA et al., 2018).

Table 1: Summarized comparison between sputtering and evaporation techniques.

Parameters	Sputtering	Evaporation
Vacuum	Low	High
Deposition rate	Low (expect for pure metals and dual magnetron)	High (up to 750,000 Å min^{-1})
Adhesion	High	Low
Absorption	High	Less absorbed gas into the film
Deposited species energy	High (1-100eV)	Low (~0.1-0.5 eV)
Homogeneous film	More	Less
Grain size	Smaller	Bigger
Atomized particles	More Dispersed	Highly directional

3.3 Diamond-like carbon (a-C:H) coatings

Diamond-like carbon is a metastable form of amorphous carbon (a-C) containing a four-fold coordinated sp^3 sites and three-fold coordinated sp^2 sites, with some terminal bonds of hydrogen (amorphous hydrogenated carbon, a-C:H (DLC-H)). It is known for its unique properties such as high wear resistance, low friction coefficient, high hardness and high chemical inertness, making their application suitable in several industries (ERBULUT; LAZOGLU, 2010; MA; RUYS; ZREIQAT, 2008; MAEDA; ENDO; HOTTA, 2015).

DLC can be deposited using various techniques including chemical vapour deposition, cathodic arc deposition, pulsed laser deposition, direct ion beam deposition, ion beam conversion of condensed precursor, magnetron sputtering, plasma source ion deposition and direct current/radio frequency sputtering. Different deposition techniques produce DLC with different properties. Therefore, it is important to note that the deposition parameters directly affect the chemical structures of DLC films such as the sp^3/sp^2 ratio and hydrogen content, changing the properties from polymer-like to diamond-like (ERBULUT; LAZOGLU, 2010; MAEDA; ENDO; HOTTA, 2015), as already shown in Figure 4.

As a coating material, DLC-H has high mechanical hardness, chemical inertness, wear resistance, corrosion resistance and optical transparency, and it is a wide band gap semiconductor. DLC coatings generally adhere well to various metallic and non-metallic substrates, especially when interlayers are used. DLC consists of a mixture of amorphous and crystalline phases, as seen in the ternary phase diagram for various forms of diamond-like carbon (Figure 4). The fraction of sp^3 sites, and the hydrogen content, are

the two key compositional parameters that determine the properties of DLC (MA; RUYS; ZREIQAT, 2008).

3.3.1 Characteristics of DLC-H Coatings

In considering improvement for surface modification, low wear friction coatings such as DLC-H can be used as a replacement for lubricants. Generally, DLC-H coatings graphitizes on the surface of the substrate at high pressures, so it transforms into a lubricant itself. Several researchers have shown continuous interest in DLC-H coatings due to their low COF, high mechanical hardness, chemical inertness, optical transparency, high wear resistance, and environmentally friendly characteristics (WANG; SHAN; GUO, 2015).

In DLC-H, carbon is able to exist in three hybridizations, sp^3, sp^2, and sp^1, as shown in Figure 11. The extreme physical properties of DLC-H derive from its mixture of carbon bonds. In DLC-H coatings, the sp^3, as in diamond, has a strong σ bond, which confers on it many beneficial properties, such as high mechanical hardness and chemical inertness. The sp^2, as in graphite, has a strong intralayer σ bond and a weak π bond between its layers. The great versatility of carbon materials arises from the strong dependence of their physical properties on the ratio of sp^2 (graphite-like) to sp^3 (diamond-like) bonds (WANG; SHAN; GUO, 2015).

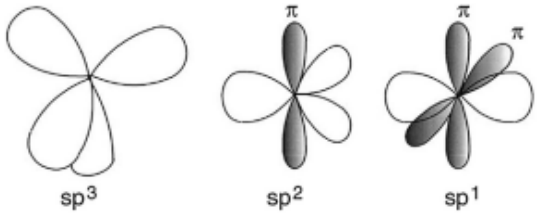

Figure 11: The sp^3, sp^2, and sp^1 hybridized bonding (ROBERTSON, 2002).

The hydrogenated amorphous carbons (a-C:H) have a rather small C-C sp^3 content. Amorphous carbons with the same sp^3 and H content show different mechanical properties according to the clustering of the sp^2 phase (WANG; SHAN; GUO, 2015). DLC-H coatings are characterized by high hardness and a high elastic modulus, but also by high internal stress. The hardness of DLC-H coating is between the range of 10-30 GPa, and Young's modulus of 100-300. The widest use of DLC coatings is mainly of the hydrogenated DLC (DLC-H) in applications exploiting the low friction coefficients and high wear resistance of these materials. The tribological behavior of DLC-H is controlled by an interfacial transfer layer which is formed by a friction-induced transformation of the top layer of the DLC-H coatings into a material of low shear strength. The low friction and ultra-low wear of DLC-H and its counterparts can be explained by the low shear strength of the transfer layer. In ambient air at relative humidity's of 20% < RH < 60%, the friction coefficients of DLC span a range of μ = 0.05-1.0. The large spread in the values of the friction coefficient is due to variations in the structure and composition of the coatings (WANG; SHAN; GUO, 2015).

All DLCs structures will transform into graphite-like carbon either by thermal activation or irradiation with energetic photons or particles. Heating DLC-H coatings leads to loss of hydrogen and CH_x species, from approximately 400 ^oC or lower, depending on the deposition parameters and doped elements contained in the DLC-H. This causes changes in the dimensions and properties of the material and limits the use of DLC-H in applications involving temperatures above 400 ^oC or lower, where thermal activation can cause the conversion of some sp^3 carbon bonds into sp^2 bonds (WANG; SHAN; GUO, 2015). Bewilogua et al. (2014) reported some properties of DLC-H which includes, sp^3

content – 20 – 60%, Hydrogen content - 10 – 50 at.%, Hardness - 10 -45 GPa, friction coefficients in dry air - 0.02 – 0.2, thermal stability in air - 300 – 350 °C.

3.3.2 Mechanical Properties of DLC-H Coatings

The mechanical properties of several surfaces are improved by the use of DLC-H coatings, due to their low friction and wear resistance. Therefore, it is necessary to discuss the residual stress, hardness, Young's modulus and fracture toughness of the DLC-H coatings.

3.3.2.1 Residual stress of DLC-H Coatings

High internal compressive stress in DLC-H can be explained through the structure of hydrogenated amorphous carbon coating seen as a random covalent network. The four-fold sp^3 carbon, the three-fold sp^2 carbon, and the singly coordinated hydrogen atoms, randomly bond together with each other, which forms a full constrained network. The mean coordination number of the network is equal to ~2.45 in order to maintain its constraints (FRANCESCHINI, 2002). Whenever, the networks are higher than the mean coordination number, it is referred to as over-constrained. The high sp^3-carbon atom fraction of hard a-C:H films leads to mean coordination numbers that are very often near 3 (FRANCESCHINI, 2002). Resulting in forming a chemical bond with considerable distortion in chemical bond length and angle, causing a strained amorphous network, which is known to be the origin of high internal compressive stress in DLC-H (FRANCESCHINI, 2002). Conversely, networks with mean coordination numbers less than 2.45 are referred to as under-constrained, are mechanically soft. The lower sp^3

fraction and the presence of a relatively high concentration of hydrogen atoms in their composition, make them less rigid and stressed than other kinds of DLC.

According to Robertson, (2002) the sp^2-carbon atoms in DLC coatings tend to cluster in the form of condensed six-fold aromatic rings, which also tend to cluster in the form of graphitic islands. The structure of a-C:H films may be seen as sp^2-carbon atoms in condensed aromatic clusters, dispersed in a sp^3-rich matrix, which confers to the network its characteristic rigidity. This situation can also be regarded as a random covalent network in which the sp^2 clusters of a defined size take part in the structure as an individual composed "atom" with its corresponding coordination number (FRANCESCHINI, 2002). DLC-H coatings were deposited using an asymmetrical bipolar pulsed-DC plasma enhanced chemical vapor deposition (PECVD) system and an active screen that worked as an additional cathode. Relatively low stress values, between -0.5 and -1.0 GPa, were obtained for all coatings. The reduction in the stress values favours the increase in the adherence of the DLC-H coatings to steel surfaces, due to the fact that the stress strongly affects the atomic interlinking bonds, and consequently the adhesion of the coating (CAPOTE; MASTRAPA; TRAVA-AIROLDI, 2015).

3.3.2.2 Hardness, Young's Modulus and Fracture Toughness of DLC-H Coatings

DLC-H coatings are known for their high hardness, Young's modulus and fracture toughness, it has been reported by several authors that high hydrogen content increases friction and wear of DLC coatings. Therefore, lowering the hydrogen to carbon ratio increases the hardness, Young's modulus and fracture toughness of the DLC coatings, leading to a reduction in the friction coefficient and lower wear volume. This occurs

because when the hydrogen to carbon ratio of the DLC coating is decreased, the degree of sp^3 bonding shifts from more C-H to more C-C bonds resulting into a stronger network of the DLC coating (JENG et al., 2017), high hardness, Young's modulus and fracture toughness are the properties that enhances the friction and wear behavior of the hydrogenated DLC coatings in open air (JENG et al., 2017).

Wei et al. (1999) caried out a study of the mechanical properties of DLC coatings deposited by pulsed laser deposition; nanoindentation measurements showed a hardness of 40 GPa and Young's modulus of 200 GPa (DEARNLEY et al., 2010). Conde et al. (2019) said that a thicker layer having higher hardness compared to a thinner layer, results to a better wear resistance and adhesion. DLC coatings with high thickness usually possess hard layers, leading to low wear rate, high critical load during spallation, high elastic modulus and low initial coefficient of friction, ensuring stability at high temperatures. However, various film properties change as the thickness changes. The "eggshell" effect, is usually observed when dealing with thinner layers of films due to the high residual stress and steep mechanical properties gradient and can affect the thermal stability of DLC coatings (CONDE et al., 2019).

Solis et al. (2016) reported the hardness and elastic modulus of DLC-H to be approximately 22 GPa and 180 GPa respectively, when deposited by PECVD. Scratch tests indicated excellent adhesion at a critical load of 80 N (SOLIS et al., 2016). The hardness values for DLC-H coatings were observed to increase according to the amount of argon in the acetylene atmosphere, reaching a maximum of 23 GPa at an argon-acetylene ratio of 50% Ar / (Ar + C_2H_2)). The highest reduction of hardness (16 GPa) was observed in the film deposited with the greatest acetylene dilution (70% Ar / (Ar + C_2H_2))

(CAPOTE; MASTRAPA; TRAVA-AIROLDI, 2015). Penetration depths for maximum applied load and elastic moduli measurements, during the nanoindentation tests as a function of the amount of argon in the acetylene atmosphere were carried out. The elastic moduli values in the films also increased with the amount of argon in the acetylene atmosphere and reached a maximum (240 GPa) at the same argon-acetylene ratio (50% Ar / (Ar + C_2H_2)). On the contrary, the penetration depth decreased with the argon dilution and reached a minimum at 155 nm for 50% Ar / (Ar + C_2H_2). The hardness and elastic modulus are proportional to the density of the deposited film (CAPOTE; MASTRAPA; TRAVA-AIROLDI, 2015).

3.3.3 Tribological Properties of DLC-H Coatings

The friction and wear performance of amorphous hydrogenated carbon coatings strongly depends on the method and parameters of deposition. DLC-H coatings usually provide low friction performance in sliding conditions (RONKAINEN et al., 2001). Low coefficient of friction observed for DLC-H has been explained by a tribolayer formation on the wear surface. This formation of a graphitic transfer layer (tribolayer) is responsible for lowering the friction coefficient between the coating and the counterbody. The increase in normal load and sliding velocity has a decreasing effect on the friction coefficient of a-C:H coatings against a counterpart (RONKAINEN et al., 2001). Increasing the applied load and velocity enhances a graphitisation process, in turn influencing the frictional behavior. Higher sliding velocities increase the contact frequency and the rate of temperature rise that facilitates the release of hydrogen atoms from the sp^3 structure.

Furthermore, higher load enhances the shear deformation and transformation of the weakened hydrogen-depleted DLC structure into graphite (RONKAINEN et al., 2001).

In dry conditions, hydrogen from the coating is needed in the tribocontact for reducing the friction performance of the a-C:H coatings. Hydrogen is present in the structure, which can provide very low friction performance in dry conditions. This verifies that the graphite formation is the most evident explanation for the low friction performance on these DLC coatings, since graphite requires humidity for low friction performance. Showing the importance of hydrogen for the low friction performance of DLC coatings (RONKAINEN et al., 2001).

Djoufack et al. (2015) studied the wear behavior of hydrogenated diamond like-carbon coating using a pin-on-disc test under lubrication with two diesel fuels. Results obtained from the investigation of the effect of load, speed and temperature on the DLC and steel counterbody wear showed that the steel counterbody wear volume was not affected by pressure, temperature, speed and lubricant, whereas the DLC-coating revealed correlation between these parameters and wear rate (DJOUFACK et al., 2015).

Cemin et al. (2016) deposited DLC on AISI 4140 low-alloy steel on top of a silicon-containing interlayer. Scratch tests were performed by using a nanotribometer with a conical diamond tip to analyze the failure mechanism to delaminate the DLC and quantify the adhesion of DLC on steel through the delamination critical load. By analyzing the shear stress distributions, the innermost interface, between the silicon containing interlayer and the substrate, seems to be more strengthening than the outermost interface, between the silicon containing interlayer and the DLC film. Therefore, the delamination of both the DLC and the silicon-containing interlayer occurs at a higher

shear stress than the delamination of DLC only. Thus, the adhesion energy due to Si–Fe chemical bonds plus defects (innermost interface) is greater than C-Si and C–C chemical bonds plus defects (outermost interface) (CEMIN; BOEIRA; FIGUEROA, 2016).

The effect of normal load on the friction and wear behaviors were investigated, with steel pins sliding against the actual coating, under dry conditions at room temperature (20 ± 2 ^{o}C) and 35–50% RH. The results show that the coefficient of friction of the coating decreased from 0.21 to 0.13 values with the increase in the applied loads (10–50N). Specific wear rates of the surface coating also decreased with the increase in the same range of applied loads. Maximum and minimum values were 14×10^{-8} and 5.5×10^{-8} mm^3/Nm, respectively (SOLIS et al., 2016).

The average surface roughness (R_a) and the coefficients of friction (COF) of the DLC-H coatings as a function of the amount of argon in the acetylene atmosphere was studied. Low values of roughness (R_a), between 22 and 35 nm, were observed for all sample surfaces, having COFs between 0.09 and 0.13 respectively. The highest roughness values were observed on the surfaces of the films that were deposited using the greatest acetylene dilution (50 - 70% Ar / (Ar + C_2H_2)). The fact that a surface with relatively high hardness will usually have low wear resistance was confirmed by these results (CAPOTE et al., 2015; LUKASZKOWICZ; PARADECKA; WIŚNIEWSKA, 2013).

3.3.4 Structure and Properties of CrN/DLC-H coatings

Mulligan et al. (2014) studied the CrN/DLC-H coating system, and described it as being a duplex coating with durable properties against wear. They reported that the microstructure of the CrN layer consisted of fine crystallites columnar grains with average

diameter of 10 nm and height in the order of hundreds or thousands of nanometer. The CrN/DLC-H coatings had its COF between 0.03 to 0.06 and the critical load value, L_{C1} and L_{C2} were 9 N and 39 N respectively (LUKASZKOWICZ; PARADECKA; WIŚNIEWSKA, 2013). The hardness and elastic modulus of CrN/DLC were found to be 23±5 GPa and 230 ± 60 GPa respectively, while, the COF and wear rate were determined to be 0.07 ± 0.01 and 7.32 x 10^{-7} mm^3 /N m respectively (MULLIGAN et al., 2014).

Conde et al. (2019) carried out a study on the dependence of wear and mechanical behavior of nitrocarburized/CrN/DLC layer on film thickness. Their findings showed that the duplex CrN/DLC coating had excellent adhesion to the substrate, irrespective of the thickness (CONDE et al. 2019). It was observed that the thicker CrN and DLC layers displayed higher hardness and better wear resistance compared to the lower thickness (CONDE et al. 2019).

Bujak and Michalczewsk, (2011), in their research work, carried out the characterization of multi-layered Cr-doped diamond-like carbon coatings. In their findings they reported that the Cr/CrN/DLC coatings deposited by pulsed biased filtered arc method exhibited hardness in range 8 – 11 GPa and Young's modulus from 95 to 130 GPa. Increasing the bias voltage, resulted in both hardness and elastic modulus decrease. The drop in mechanical properties of the Cr/CrN/DLC coatings was probably due to the increase of chromium concentration in the DLC top layers from 2 to 4 at.%, due to the fact that the incorporation of Cr decreases the DLC coating hardness. The COF was between 0.13 and 0.15, while the spallation failure of the DLC layers was observed after approximately 200–300 load cycles (BUJAK; MICHALCZEWSKI, 2011).

3.4 Tungsten doped Diamond-like carbon (a-C:H-W) coatings

Diamond-like carbon coatings can be doped with metals (C:H-Me) to improve the adhesion properties and reduce the internal stress in the coating. Metal doped DLC are being increasingly used as low friction coatings for various automotive components. Most C:H-Me coatings are known to form high strength carbides in DLC films (KRŽAN; NOVOTNY-FARKAS; VIŽINTIN, 2009). Tungsten doped diamond-like carbon (a-C:H-W) coatings have been identified as one of the metal doped DLC coatings, which possesses excellent adhesion to the metallic substrate, reduced residual stress, high hardness, high wear resistance and low friction, making these coatings suitable for mechanical parts (YUE et al., 2015).

DLC-W coatings have been deposited on various substrate using several methods such as PVD, conventional DCMS and hybrid DCMS-HiPIMS configurations (EVARISTO; FERNANDES; CAVALEIRO, 2020), radio-frequency plasma enhanced chemical vapor deposition (RF-PECVD) and DC magnetron co-sputtering of tungsten metal target (TAKENO et al., 2008; TAKENO et al., 2009), direct-current plasma enhanced chemical vapor deposition (DC-PECVD) (BAI et al., 2021) and ion beam assisted deposition (IBAD) (LIU et al., 2015).

3.4.1 Characteristics of DLC-W Coatings

Doping of DLC with tungsten metals provides an inclusion of tungsten nanoclusters into the DLC matrix. The DLC-W coatings structure was observed by Transmission Electron Microscopy (TEM), and found to be structured as metal clusters of several nanometers sized, dispersed into the amorphous carbon host matrix (TAKENO et al.,

2009). Previous studies have shown that the addition of W enhances the formation of sp^2 bonded carbon sites in the amorphous DLC matrix. Therefore, the W atoms would preferentially react and bond with sp^2 carbon which possesses relative lower bond energy as compared with sp^3 carbon which is likely to form WC or W_2C (EVARISTO; FERNANDES; CAVALEIRO, 2020). It is important to note that tungsten will form carbide precipitates when doped with diamond-like carbon coatings (HOVSEPIAN et al., 2016). WC_x is the general chemical composition in which tungsten carbide can exist in DLC doped with tungsten (DAI et al., 2015). Figure 12, shows the morphology of a DLC-Me coatings containing metal carbides as in the case with tungsten carbide in DLC-W coatings.

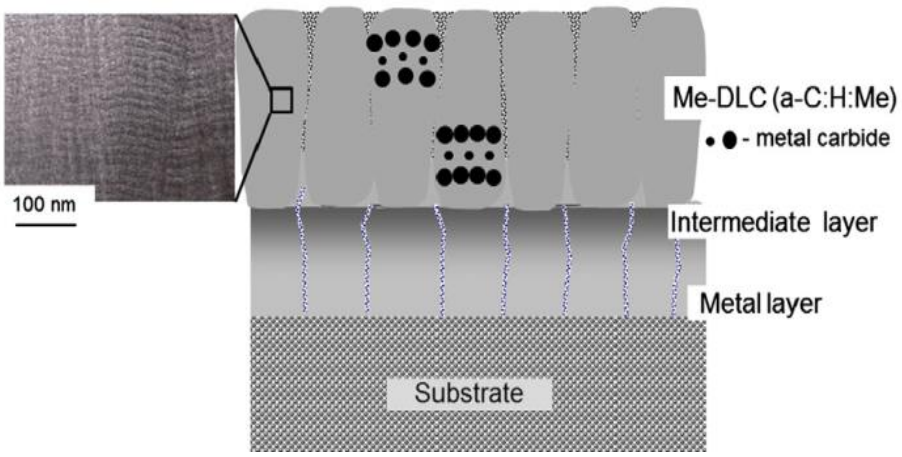

Figure 12: Scheme morphology of a Me-DLC coating grown in a sputter machine with rotating substrates (BEWILOGUA; HOFMANN, 2014).

3.4.2 Mechanical Properties of DLC-W Coatings

The mechanical properties of DLC-W are very important when considering their use in the tribology area to improve the surface of any part. In this section the residual stress, hardness, Young's modulus and fracture toughness of the DLC-H coatings will be discussed.

3.4.2.1 Residual stress of DLC-W Coatings

Takeno et al. reported a reduction on the level of residual stresses of DLC-W due to the formation of tungsten metal clusters in the DLC coating (TAKENO et al., 2009). The dispersive metal clusters lead to a reduction of the stress in the DLC coating and helped to achieve a good adherence to stainless-steel substrates (TAKENO et al., 2009). Generally, several authors have reported the reduction of residual stresses due to the doping effect of tungsten comparing with the residual stresses in DLC-H. DLC-W also plays an important role in multilayer DLC composites by reduction of residual stress and improving adhesion to metallic substrate, the doped tungsten form carbide nano-clusters in the amorphous carbon matrix of the DLC coatings, resulting into a multilayer structure of DLC-W, which is an alternating hard and soft layer and is responsible for accommodating load by shearing in the soft layer, which significantly reduces the stress concentration at the coating–substrate interface (GU et al., 2019).

3.4.2.2 Hardness, Young's Modulus and Fracture Toughness of DLC-W Coatings

Bai et al. (2021) measured the hardness and Young modulus of DLC-W coatings using nano-indentation at 10 mN load. The hardness and Young modulus were 13 GPa and 140 – 160 GPa respectively for W doped DLC, resulting in a decrease in the hardness/reduced elastic modulus (H/Er) ratio. W-DLC coating had a higher H and Er scattering compared to pure DLC, caused probably by the roughness of the coating surface (S_a = 52.6 nm) covered in micro-bumps of the DLC-W (BAI et al., 2021). DLC-W deposited using magnetron sputtering showed good adhesion and hardness (15 GPa), having nanometric tungsten carbide grains embedded in carbon matrix, with sp^2/sp^3 ratio, 80%. The coating surface had a tribolayer 2-4 nm thick formed during sliding of the contact ball on the coating (MUTAFOV et al., 2014).

An increase in the W content within the DLC coatings, leads to an increase in WC and free W contents in the film, and an increase in hardness and elastic modulus, while there was a decrease in the sp^3-C content. At 3.08 at. % W the critical load increased to above 100 N, while, the coefficient of friction varied depending on the type of lubricant used. The friction coefficients and wear rates evaluated using a ball-on-disc friction test (MS-T3000) under dry friction with a load of 1.96 N or PAO lubrication with a load of 9.80 N; the counter-body used was Si3N4 ball with a diameter of 3 mm was used. Generally, it is worth noting that an increase in sputtering current leads to an increase in W content and decrease in the carbon content during deposition. The intensity of the D peak/ intensity of the G peak ratio (ID/IG ratio) increases with increasing sp^2 content, increase in W content for the DLC coatings shifts the G peak position to the right and

increases the ID/IG ratio. Formation of sp^2 bonded carbon sites is enhanced by the incorporation of W in the amorphous DLC matrix, meaning that W atoms would preferentially react and bond with sp^2 carbon which possesses relative lower bond energy as compared with sp^3 carbon (CAO et al., 2020; SÁNCHEZ-LÓPEZ; FERNÁNDEZ, 2008; YONG et al., 2016; MIKI; TAKENO; TAKAGI, 2008; ARSLAN et al., 2019).

3.4.3 Tribological Properties of DLC-W Coatings

BANERJI; BHOWMICK; ALPAS, (2014) reported low COF and wear rate during the tribological experiment of W-DLC coating against Ti–6Al–4V alloy at 25 °C, which was as a result of the formation of carbon rich transfer layer on the Ti–6Al–4V alloy counter-body. They also reported high COF and wear rate at temperature between 200^{o}C and 300^{o}C, due to the absence of transfer layer on the Ti–6Al–4V alloy counter-body. However, between 400^{o}C and 500^{o}C, very low and wear rates were reported, which were attributed to WO_3 layer formed on the DLC-W surface (BANERJI; BHOWMICK; ALPAS, 2014).

According to EVARISTO; FERNANDES; CAVALEIRO, (2020) the deposition of three different DLC-W coatings using direct current magnetron sputtering (DCMS), a hybrid direct current magnetron sputtering + high power impulse magnetron sputtering (DCMS-HiPIMS) and a hybrid direct current magnetron sputtering + high power impulse magnetron sputtering (DCMS-HiPIMS) with CH_4 configuration possessed excellent adhesion, hardness and reduced Young's modulus. Three types of failure were observed in the DLC-W coating during scratch tests: first cracking (L_{c1}), first coating shipping (L_{c2}) and more than 50% coating failure (L_{c3}) (EVARISTO; FERNANDES; CAVALEIRO, 2020).

There was a reduction in Young's modulus from approximately 200 to 193 GPa due to a change in the type of bonds in the material. The reduction of the modulus can be related with the presence of C–H bonds, which avoids establishing sp^3 bonds between C atoms, thus lowering the bonding energy (EVARISTO; FERNANDES; CAVALEIRO, 2020).

EVARISTO; FERNANDES; CAVALEIRO, (2020) observed that the DLC-W coatings avoided the detachment of larger hard W–C particles, which are responsible for abrasive wear of the coatings. The tribological performance of the films was governed by a W–C, C and W–O rich tribolayer that adheres to the ball counterpart (EVARISTO; FERNANDES; CAVALEIRO, 2020). Bai et al. (2021) reported that W-doped DLC had a COF which was relatively more stable at 1 Hz and 36 Hz than at 6 Hz, which for the analysed sample shows a nearly 50 % drop of COF after ~2000 cycles. There was a decrease in the average COF of DLC-W from 0.18 at 1 Hz, to 0.13 at 6 Hz and 0.09 at 36 Hz (BAI et al. 2021). The specific wear rate was higher for DLC-W than pure DLC at 1 Hz and 6 Hz and significant wear and debris were found on the W-DLC compared to the pure DLC coatings. The W-DLC wear tracks also exhibit deep grooves at different frequencies indicating an abrasive wear mechanism against the Al_2O_3 counter-body balls. Wear debris around the wear tracks was seen in the form of sub-micron particles. In addition, a network of cracks was observed at the bottom of the wear-tracks that appear to preferentially propagate along the boundaries of the original coarse surface bumps of the W-DLC (BAI et al. 2021).

The reduction of wear rate of DLC-W at the highest sliding velocity 36 Hz may be due to the formation of a thicker, protective tribo-film containing WS_2, which is a solid lubricant and act similarly as graphite. At a constant normal load, at lower sliding velocities

tribo-films may be thin, leading to their easy displacement by the reciprocating ball. However, at high velocities, and increased surface temperature, the faster build-up of a thicker tribofilm can act as a protective mechanism, reducing subsequent wear rate as observed for the DLC-W. The reduction in wear rate of DLC-W at 36 Hz via a stable tribofilm containing graphitic carbon also correlates with the reduction in COF at higher sliding velocities (BAI et al. 2021).

According to Takeno et al. (2008) the rolling effect of tungsten oxide debris makes the friction coefficient unstable. Proposing that the mechanism was due to the reaction of tungsten and oxygen, tungsten oxide debris formed. The debris comes in and out of the sliding track, which causes unstable friction. Mutafov et al. (2014) observed unstable friction of DLC-W during dry tests of the samples, deducing that the formation of the transfer layer is responsible for friction variation in dry sliding conditions (MUTAFOV et al., 2014). According to the work of Arslan et al. (2019) textured samples show lower average COF and wear than un-textured samples, this is because of wear debris (solid lubricants) entrapped in the grooves (ARSLAN et al., 2019).

3.5 Application of DLC and DLC-W Coatings on Automobile Engine Components

The use of DLCs as coatings for automobile engine parts has assisted to reduce friction and wear, which could not be achieved by the use of lubricants alone, this has improved engine performance and transmission components (MOBARAK; CHOWDHURY, 2014). Lawes et al. (2007) reported diamond-like carbon to have reduced fuel consumption of automobiles, chemical stability and weight reduction. The excellent tribological properties (low friction, wear resistance, corrosion resistance, high hardness, high thermal and chemical stability) of DLC, since their discovery in 1971 has made them widely used in the automotive industry. Different types of DLC films vary in mechanical, physical and tribological properties which is usually determined by the proportion of sp^2 (graphite-like) and sp^3 (diamond-like) bonding in the DLC coating (MATTHEWS; ESKILDSEN, 1994; TREUTLER, 2005). Although, addition of non-metals (hydrogen, nitrogen, silicon, fluorine and sulphur) or metals (tungsten, titanium, molybdenum) can be used to influence their tribological properties (LAWES; FITZPATRICK; HAINSWORTH, 2007).

The Stribeck curve in Figure 13 can be used to explain how DLC-H and DLC-W coatings greatly improves the tribological behavior surfaces of the automobile components. Coatings such as DLC-H and DLC-W shift the Stribeck curve to the left (by changing the behavior from the red line to the dashed blue line). Thus, the contact is preserved, since the permanence of the friction system in regions 1 and 2 is reduced and entered into the hydrodynamic regime is advanced. In practice this means that the mechanical components of the system will wear out less or, in other words, have their durability extended. Another important effect of this behavior is that the friction in the

system is reduced for a longer time, since the level of friction in regions 2 and 3 is lower than in region 1.

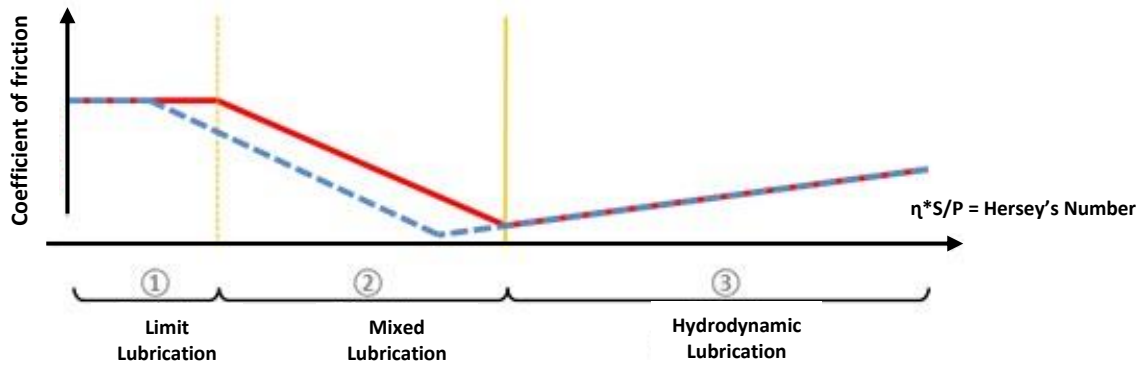

Figure 13: The Stribeck curve, (DLC-H and DLC-W shift the Stribeck curve to the left (by changing the behavior from the red line to the dashed blue line)

The Stribeck curve explains that the friction in lubricated environments depends on contact load, lubricant viscosity and relative speed which are factors affecting the Hersey number (equation 9).

$$Hersey\ number = \frac{\eta\ .N}{P}, \tag{9}$$

Where η is the dynamic viscosity of the fluid, N is the entrainment speed of the fluid and P is the normal load per length of the tribological contact.

The curve is divided into 3 main regions with the following behavior in contact between surfaces:

Region 1 – Limit lubrication is when the solid surfaces come into contact, mostly through roughness.

Region 2 – Mixed lubrication is when in addition to contact via the roughness of solid surfaces, the load is also supported by the lubricant.

Region 3 – Hydrodynamic lubrication is when there are almost no interactions occurring between the roughness, as hydrodynamic pressure is predominant in the load-bearing role.

The reduction in friction occurs due to the superfinished surface of DLC-H and DLC-W coated components which leads to a strong reduction in the roughness of the system. Thus, the required lubricant film thickness for separation from solid surfaces will be smaller. This contributes to making rough contact difficult, leading to the shift in the Stribeck curve. Worldwide, several engine components such as pins and piston rings, rocker arm pins and shafts, valve tappets and camshafts, fuel injection system components fuel, floating rocker arms, etc., have already been tested using these coatings to reduce the friction levels and allowing them to operate under higher contact pressures without failure, which ensures high performance, reduced fuel consumption and pollutant emissions, as well as gains in durability and engine reliability (BEWILOGUA; HOFMANN, 2014).

The mechanical and tribological properties have been analysed by nano-indentation, scratch, wear and friction testing of an instrumented cam-tappet testing rig in a study of evaluation of the tribological properties of DLC coatings for engine applications (ZAHID et al., 2015; FERRARI, 2004). Success has been recorded over recent years with the application of DLC coatings to a number of automotive engine components (piston, tappet, camshaft, piston rings, gudgeon pin, valve stem and head, and rocker arm) as

seen in Figure 14 (HEF, 2021). DLC coatings applied to automobile parts possess thickness ranging between 1 – 30 µm (LAWES; FITZPATRICK; HAINSWORTH, 2007). DLC coatings in engines need careful selection of required surface finishing, mechanical properties, and tribological behavior of the coatings with engine oils (LAWES; FITZPATRICK; HAINSWORTH, 2007). The coatings hardness and stiffness are needed to determine the wear resistance. Friction is controlled by hardness, topography of the surface and tribo-chemical interactions of the dopants with the DLC coatings (LAWES; FITZPATRICK; HAINSWORTH, 2007).

Figure 14: Selected engine parts coated with DLC: a. piston, b. finger roller follower, c. tappet, d. valve, camshaft sprocket, f. camshaft and g. piston ring (HEF, 2021).

Tribological properties of DLC coatings are affected by adhesion promoter (interlayer), substrate roughness, hydrogen incorporation and coating deposition parameters such as bias voltage, etching, current, precursor gas, time and substrate temperature (AL MAHMUD et al., 2014). Service conditions such as temperature, sliding speed, load, relative humidity, counter surface and lubrication affects the tribology of

DLC-coated parts. Although there has been success in the application of DLC coatings for mass production of engine components there is still need for sufficient tribological test especially at high temperature (KANO, 2015). The behavior of DLC coatings vary in service under lubricating conditions. Diverse applications are currently making use of DLC coatings without lubrication, due to their ability to exhibit high wear resistance, corrosion resistance and low friction in dry conditions (RÜBIG et al., 2017). Increase in thickness of the DLC coatings improves the tribological and mechanical properties. Rubig et al. (2017) carried out an experiment using water and engine oil as lubricants for hard, soft and multilayer film deposited on a metallic substrate and tested them using a pin-on-disc tribometer. Their experiments revealed that under same tribological parameters all lubricated soft DLC coatings on polished substrate suffered under strong fatigue wear on the surface. Which was contrary to the rough DLC surfaces which showed no fatigue wear at all but they caused high counterpart wear and higher COFs. The occurrence of fatigue wear was due to stress related to rapture of the oil film (RÜBIG et al., 2017; GANGOPADHYAY, 2015).

3.6 Effect of Temperature on DLC-H and DLC-W Coatings

During the application of DLC-H and DLC-W in automobile engines, they are subjected to temperatures between room temperature (RT) to around 200 ^{o}C and sometimes could even be much higher 250 ^{o}C or above (extreme conditions) depending on the type of automobile. The conditions are sometimes regarded as harsh conditions and can affect the integrity of the coatings during use. Raman spectroscopy can be used to evaluate the coatings after being subjected to harsh conditions. Usually, Raman

spectroscopy curves display the presence of the two main peaks, D and G bands. The high degree of crystallographic disorder is the cause of the wide band gap of the peaks at centre of the D and G bands. The amorphous nature of DLC coatings explains the less coherency of the photons scattered during the Raman process (FERRARI et al., 1999). The D peak usually appears at 1350 cm^{-1} and represents the breathing vibration mode of disordered graphite, while the G peak, around 1580 cm^{-1} is sensitive to all sp^2 sites vibrations, whether in aromatic rings or chains.

The I(D)/I(G) ratio obtained during Raman analyses makes it possible to indicate the presence of the hydrocarbon compounds that forms the films. Lower ratio values mean the presence of less aromatic rings inside the film instead of sp^2 or sp^3 chain bonds. The higher I(D)/I(G) found in the DLC coating suggests higher graphite formation (FERRARI et al., 1999). Surface-Enhanced Raman Scattering (SERS) and Tip Enhanced Raman Scattering (TERS) provide a fast, convenient and non-destructive molecular detection to analyse tribological properties of DLC films. X-ray Photoelectron Spectroscopy (XPS) can also be used to determine the bonding structure of DLC coating, before and after tribological analysis, this will enable the determination of change in the structure caused by increase in temperature loading pressure (FERRARI et al., 1999).

Friction and wear are strongly affected by high temperatures causing an increase in coefficient of friction. The effect of high temperature on DLC coatings has been studied by some researchers. Increase in temperature above 500^oC causes transformational change from sp^3 diamond-like bond to sp^2 graphite-like bond. However, as the temperature increases further there is a gradual increment of COF due to the evaporation of water molecules attached to the coating surface. At temperature ranges between 350

– 400^{o}C, thermo gravimetric analysis (TGA) has been used to observe the occurrence of severe oxidations on DLC coated surface, which affects the COF (GHARAM et al., 2011; WANG et al., 1999). Frictional properties vary in the case of a-C:H and a-C, according to Gao et al. the COF increases due to thermal distortion of a-C:H structures to 147^{o}C causing significant detachment of hydrogen from a-C:H coating surface.

Generally, at high temperatures, there is an increase in wear rate and a reduction in the COF. Transformation (graphitization) requires higher temperatures, when DLC is doped with non-metals and metals. Usually, the temperatures at which phase transformation and oxidation takes place for a-C is much higher than that for a-C:H. Therefore, the friction coefficient of a-C will remain stable at higher temperatures compared to a-C:H. When a ta-C film is annealed in vacuum, the structure remains stable until 727^{o}C. However, when annealed in air, the film gets oxidized between 450–500^{o}C (ROBERTSON, 2002). Normally, a-C behaves differently from ta-C, and a-C film deposited by magnetron sputtering have been reported to have thermal stability till 300^{o}C. A drastic drop in hardness caused by graphitization of the coating structure occurs above 300^{o}C. Friction coefficients increases at elevated temperature, which is due to the absence of water on the tribo-contact surface (KONCA et al., 2005).

Relatively low wear rates at 25^{o}C are usually caused by the transfer layer formed on the metal counterface (GHARAM et al., 2011). The layer is usually lubricious due to atmospheric moisture, dissociating into H and OH radical, so the dangling bonds on the surface get passivated consequently minimizing C-C interactions existing between the sliding interface and the layers. Moisture evaporation will usually take place between 25^{o}C to 100^{o}C, leading to a rapid increase of wear rate. The increase at this temperature

range is due to moisture evaporation which harms the passivation. Adhesion on the metal - carbon interfaces will be enhanced; this step hinders the transfer layer from forming on the counterface. Above 400ºC, there is a decrease in the wear rate which may be due to a temperature effect, enhancing a graphitization process through sp^3 to sp^2 bonds transformation (PODGORNIK; JACOBSON; HOGMARK, 2003; WEILER et al., 1996; SATTEL; ROBERTSON; EHRHARDT, 1997). Annealed a-C coating will wear more rapidly than the 25ºC as-deposited a-C coating, due to oxidation, which occurs on the coated surface during the annealing process. Konca et al. (2006) confirmed it from EDS results which showed that for a 300°C annealed sample a higher oxygen content was detected. The comparison of the as-deposited DLC-W coating tested at 25ºC and 300ºC showed that at the higher temperature, the wear rate was also higher (Veverkova; Hainsworth, 2008). Typical friction–temperature regimes are shown in Figure 15.

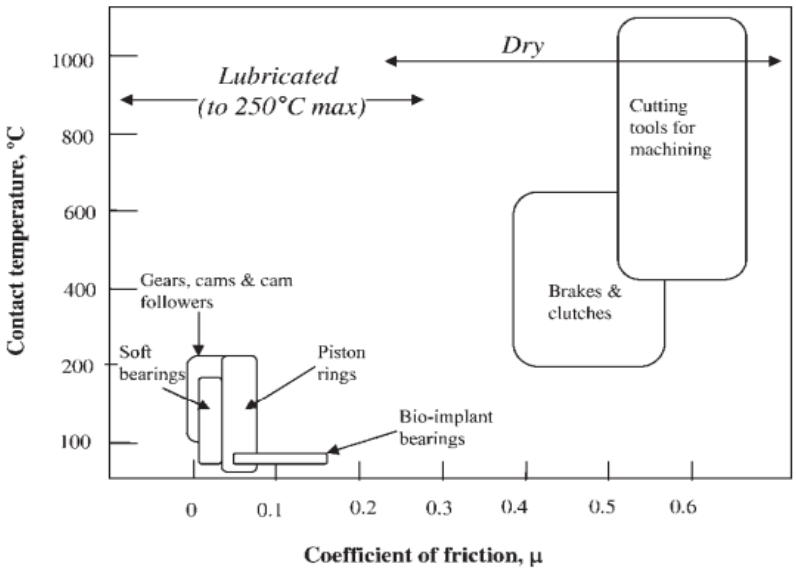

Figure 15: Typical friction–temperature regimes (DEARNLEY et al., 2010).

During tribological experiments the initial wear mechanism in wear testing is usually adhesive, which occurs by galling and cracking of superficial material, removing small pieces of material. The loosen particles begin to act as abrasive and scratch the tested specimen, initiating a three-body abrasive wear mechanism along the DLC coating. This leads to thermal instability of DLC coated engine parts. However, increasing DLC coating thickness increases wear resistance, as this will compensate for the loss in thickness at high temperature, thereby improving the thermal stability of DLC coatings. The wear rates of DLC-W coatings and the counterface are affected at temperatures between 200^{o}C to 300^{o}C. An increase in wear rate from 0.5 x 10^{-5} mm^3/Nm to 8.5 x 10^{-5} mm^3/Nm as the temperature increases from room temperature to 100^{o}C respectively, which gradually decreased at 400^{o}C (HOVSEPIAN et al., 2016; GHARAM et al., 2011; YANG et al., 2014).

Tribological tests were used to analyse a-C, a-C:H, and Ti–C:H, both in a vacuum and in air environment at 450^{o}C. No hardness loss occurred after testing in vacuum (KRUMPIEGL et al., 1999). However, after testing in air, a significant hardness loss occurred due to oxidation. DLC films are unstable during deposition and tend to change structures when subjected to high temperature (ERDEMIR; FENSKE, 1996; WU; HON, 1999). There is usually a change in wear and frictional behavior, due to the changes that occurs in the chemical and structural morphology (ERDEMIR; DONNET, 2006).

Several authors have reported low COF and wear rate of DLC-W coated components at room temperature forming a transfer layer on the ball counterpart rich in C with traces of W-O. The presence of W-C, C and W–O oxides forms tribolayer which provides some lubrication due to their recognized lubricious properties at elevated

temperatures (300ºC to 500ºC) (BANERJI; BHOWMICK; ALPAS, 2014; EVARISTO; FERNANDES; CAVALEIRO, 2020; GHARAM et al., 2011). At high temperature, the presence of WO_3 is observed during tribological test of DLC-W coatings. Similar wear debris were found to have adhered to the ball counterparts for the DLC-W at room temperature. The wear debris oxidizes easily due to the temperature and will adhere to the ball or free sliding at the surface of the film. The oxidation of these particles is faster accelerated by the temperature, which in the contact will promote the polishing type wear mechanism. Despite the less severe wear mechanism at this temperature, the wear rates at high temperatures are higher than at RT tests. Which is due to softening of the films with temperature, making the removal of the material easier, graphitization of carbon through the transformation of sp^3 (diamond like) to sp^2 (graphite-like) and absence of humidity, which will not passivate the dangling carbon bonds and will not minimize C/C interactions of the free C particles, thus, C will not provide low friction as for RT (EVARISTO; FERNANDES; CAVALEIRO, 2020). Figure 16 shows a reciprocating Optimol SRV tribometer which is very effective in measuring wear at different temperatures.

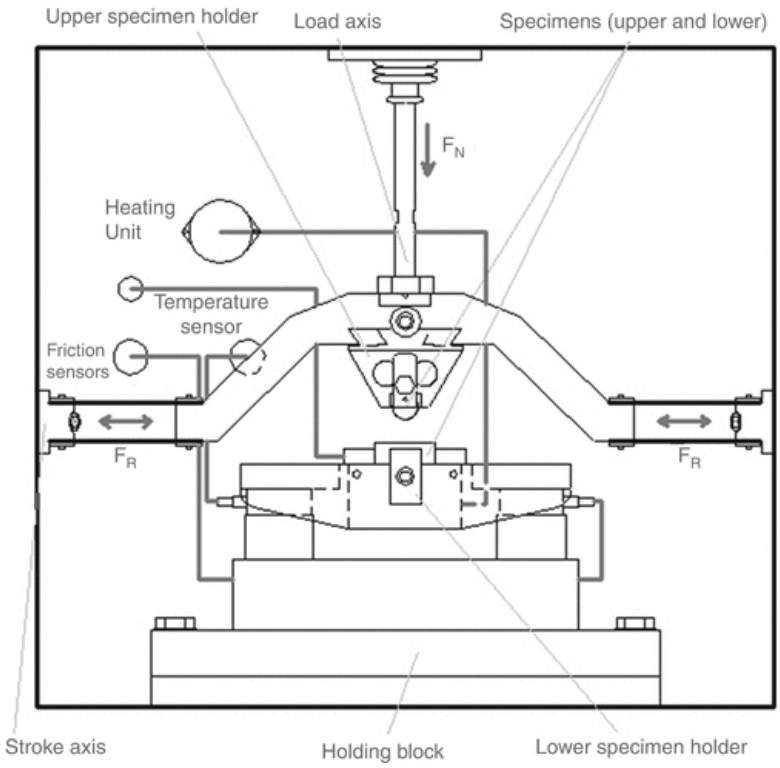

Figure 16: Scheme of the reciprocating Optimol SRV tribometer (RIGO & FEINLE, 2014).

4.0 MATERIALS AND METHODS

4.1 Materials

The substrate used in this experiment is a cylinder head valve tappet used in the Ford Ka 1.0 3cc 3150 mm 2014 model, which was purchased in a commercial store in São Paulo, Brazil as seen in Figure 17.

Figure 17: Commercial cylinder head valve tappet Ford Ka 1.0 3cc 3150 mm 2014.

4.1.1 Substrate characterization

A cross section of the valve tappet was cut, using a cut-off. The cross section was mounted in a phenol formaldeid resin (Bakelite), in a mounting press, under 28 MPa, at 150°C. The mounted valve tappet sample was then ground using semi-automatic grinder with different grades of silica paper and polished using automatic polishing machines. Finally, the polished valve tappet sample was etched using 2% Nital solution and analysed for chemical composition, microstructure, and microhardness. The chemical composition and microstructure were analysed using Scanning Electron Microscopy in a field effect gun - FEG - Inspect 50 microscope, with a secondary electron detector, a dedicated backscatter electron and a Silicon Drift Detector EDS X-ray spectrometer. A Shimadzu hardness tester was used to carry out microhardness measurements on the sample using a load of 980.7 mN (0.1_{HV}) for 15 seconds.

4.2 Deposition of CrN/DLC and DLC-W coatings

4.2.1 Substrate preparation for CrN/DLC and DLC-W coatings deposition

The valve tappets were polished to obtain an average surface roughness value (R_a) of 0.05. The surface roughness for unpolished and polished valve tappet were measured using a 3D CCI Taylor Hobson Profilometer, surface roughness data was analysed to the least square line, with Gaussian filter, 0.25 mm upper cut off and bandwidth. Thereafter the valve tappets were ultrasonically cleaned in ethanol and acetone for 20 minutes.

4.2.2 Deposition process of CrN/DLC and DLC-W coatings

The CrN/DLC and DLC-W coatings were deposited, on 16MnCr5 steel valve tappets, using an hybrid Physical Vapour Deposition (PVD) and Plasma Enhanced Chemical Vapour Deposition (PECVD) reactor at HEF DURFERRIT, São Paulo, Brazil. The coating chamber has a working diameter of 750 mm and a working height of 1000 mm. During the deposition for CrN/DLC, the reactor was first pumped and heated to a final temperature of 180 ^{o}C and final pressure of 2.5E^{-6} mbar for a duration of 120 minutes. Plasma etching was carried out for 10 minutes, followed by deposition of a Cr adhesion interlayer for 5 minutes using a Cr target and thereafter a CrN layer, using a Cr target (99.99% purity) and N_2 gas (99.99%) for 60 minutes. Finally, the deposition of a DLC layer was performed, using C_2H_2 gas for 60 minutes. The deposition of the Cr adhesion interlayer and CrN layer were deposited by Magnetron sputtering process, while the DLC layer was deposited by PECVD process.

For the deposition of the DLC-W coating, the reactor was first pumped and heated to a final temperature of 180 °C and pressure of 2.5E-6 mbar for 120 minutes. Plasma etching was carried out for 40 minutes. The deposition of the DLC-W coating was done using a WC target (99.99% purity) to deposit WC adhesion interlayer for 5 minutes followed by DLC-W multi-layer using WC target (99.99% purity) and C_2H_2 gas for 180 minutes. The valve tappets were positioned on a twofold planetary rotating table. The table rotating speed was 5 rpm, while the vertical trees around the table had a rotating speed of 22.5 rpm. The WC target was positioned in the 12 o'clock position, while the 3 o'clock, 6 o'clock, and 9 o'clock positions were empty or contained Cr targets for the deposition of an adhesion Cr layer before the DLC-W coating. Microwave guns were

responsible for extending the range of ionization of the acetylene gas. The temperature and pressure were constant throughout the deposition and the reactor was allowed to cool for 30 minutes after the deposition of both coatings. Figure 18 shows the uncoated and CrN/DLC and DLC-W coated valve tappets. Figure 19a presents the coating architecture, for the CrN/DLC as Cr interlayer/CrN layer/top DLC layer (Cr/CrN/DLC), and Figure 19b presents the coating architecture for the DLC-W as WC interlayer/top DLC-W layer (WC/DLC-W). The deposition parameters are summarized in Table 2:

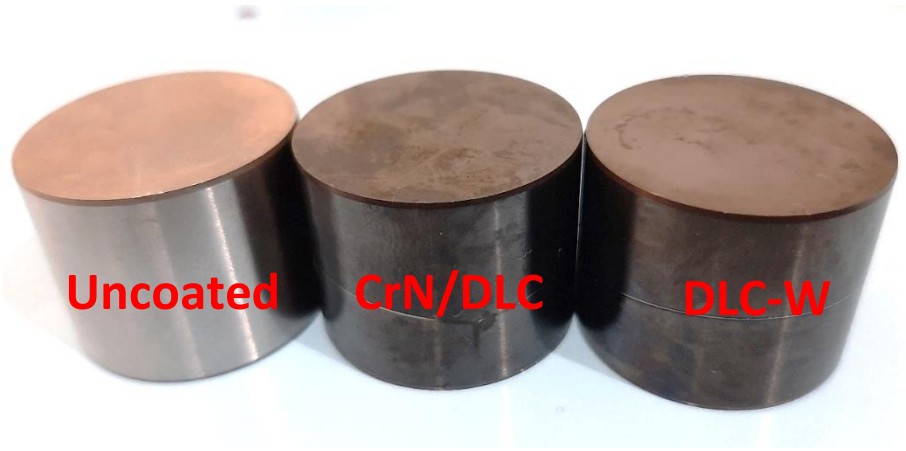

Figure 18: Image of Uncoated, CrN/DLC and DLC-W coated valve tappet.

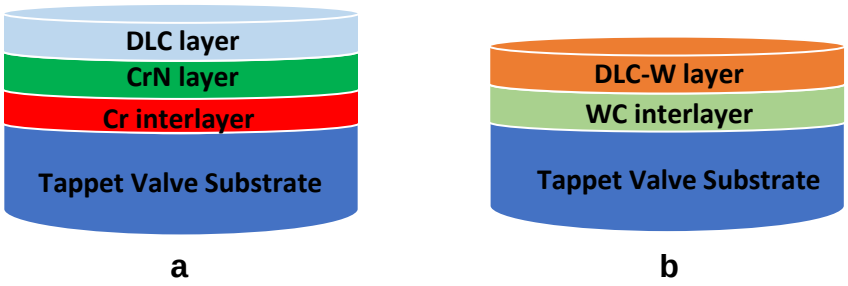

Figure 19: Architecture of valve tappet coated with (a) CrN/DLC (b) DLC-W.

Table 2: Deposition Parameters for CrN/DLC and DLC-W coatings

Coating	Process	Frequency (KHz)	Gas flow rate (sccm)	Bias (V)	Power (W)	Time (min)
CrN + DLC	Plasma etching	150	Ar flow 100	150		10
	Cr adhesion interlayer	150	Ar flow 150	100	19kW	5
	CrN coating	150	N_2 flow 300 Ar flow 110	150	15 KW	60
	DLC coating	150	C_2H_2 flow 1400	330	Microwave Guns 3 KW	60
DLC-W	Plasma etching	150	Ar flow 110	150		40
	WC adhesion interlayer	150	Ar flow 550	150	Sputtering 17 KW	5
	DLC-W coating	150	Ar flow 300 C_2H_2 flow 600	100	Sputtering 17 KW	180

4.3 Coating characterization

4.3.1 Raman spectroscopy

Raman spectroscopy, (confocal Horiba® Xplora One™) having a 532 nm excitation wavelength laser source, with an 1800 grating per mm diffraction mesh, a 50 µm slit and a 100X objective lens, allowing measurement of D and G bands of the Raman spectra in regions up to 1 µm in diameter with a spectral resolution of 2 cm^{-1} (Figure 20). Characterization of the carbon bonds and the ID/IG intensity ratio at the surface for CrN/DLC and DLC-W were carried out. The extended and static modes were used to detect chemical compound formation and the carbon peaks (disorder, D and amorphous graphitic, G peaks) for the coating deposited on a silicon substrate structure. The scan range for the identification of the carbon peaks were, 400 to 2400 cm^{-1}. Origin v9.5 software was used to process all acquired Raman spectra, using a Gaussian non-linear

curve fit with a R^2 higher than 0.95 to deconvolute the D and G shift positions. The ratio ID/IG was considered as an indicator of the carbon sp^2/sp^3 structure.

Figure 20: Raman spectroscopy (confocal Horiba® Xplora One™).

4.3.2 X-ray excited photoelectron spectrometer (XPS)

XPS is based on the photoelectric effect, where electron binding energy is determined by measuring the kinetic energy of electrons emitted from the material after X-ray illumination with known energy. As the binding energies are specific for each element and orbital, the XPS can be used for elemental identification (BRIGGS; WILEY, 1983; MOULDER; STICKLE; SOBOL, 1992; *NIST,* n.d.; SCOFIELD, 1976; SMITH, 1994). Furthermore, the exact binding energy is influenced by the chemical bond in which the element participates. This makes it possible to obtain chemical information from XPS spectra. In the present study, most chemical information is obtained in the region of the C1s, O1s and W4f electronic level. The positions of the relevant peaks found in the literature similar to this present work are presented in Table 3.

The chemical composition is determined by the relative peak intensities, corrected by experimentally determined sensitivity factors. As XPS analyses photoelectrons, the mean free path of the electron in matter will determine the depth of analysis. The XPS analysis was performed at Photoelectron Spectroscopy Laboratory (LEFE), Departamento de Físico-Química, Instituto de Química – UNESP. The XPS analysis was carried out using a commercial UNI-SPECS UHV spectrometer with base pressure below $5x10^{-7}$ Pa. The ionization source used was Mg Kα line (hν = 1253.6 eV) and the energy throughput of the analyzer was set to 10 eV. Shirley's method was used to subtract the inelastic noise of the high-resolution spectra of O1s and C 1s and W 4f.

Table 3: Values of electron binding energies (E) for energy levels by XPS.

Coatings	Electronic level	Bonding	E(eV)	References
DLC	C1s	C-H	283.5	(WANG; LI; KUANG, 2018; BUJAK; MICHALCZEWSKI, 2011; MAHMUD et al., 2014; *NIST, n.d.;* HUMPHREY et al., 2020; KHANMOHAMMADI et al., 2022; LI; MIAO; ZHU, 2018; MÜLLER et al., 2011; RAO et al., 2020).
		C-O	286.45	
		C=O	288.38	
		O-C=O	291.05	
		sp^2C	284.02, 284.7	
		sp^3C	284.9, 285.8	
	O1s	O=C	531.20	
		O-C	532.15	
		O-C=O	533.60	
DLC-W	C1s	C-W	284.2,	(TAKENO et al., 2009; MIKI, H., TAKENO, T., & TAKAGI, 2008; *NIST, n.d.;* KHANMOHAMMADI et al., 2022; FU et al., 2013; TAKENO et al., 2009; YUE et al., 2012).
		C-H	285.2	
		C-O	287.0	
		C=O	287.65	
		O-C=O	288.95	
	O1s	O-W	530.40 – 531.00	
		O=C	531.25	
		O-C	532.10	
	W4f	W 4f7/2	31.10 -37.00	
		W 4f5/2	33.40	
		W-C 4f7/2	31.50 – 32.00	
		W-C 4f5/2	34.10	
		WO34f5/2	37.40 – 37.90	
		WO34f7/2	35.40 – 36.40	

The composition of the surface layer (<5 nm) was determined by the relative proportions of the peak areas corrected by Scofield atomic sensitivity factors with an accuracy of ±5%. The binding energy of the spectra was corrected using the hydrocarbon component (C-H) fixed at 284.9 eV. The deconvolution analysis of the spectra was carried out using a Voigtian-like function, with a combination of 70% Gaussian and 30% Lorentzian. The width at half height ranged between 1.2 and 2.1 eV, and the position of the peaks was determined with an accuracy of ±0.1 eV.

4.4 Microstructural Observation

4.4.1 Optical microscope (OM)

The microstructure and morphology of the uncoated valve tappet, CrN/DLC and DLC-W were examined using a BX60M – Olympus optical microscope coupled to a 5MP digital camera.

4.4.2 Scanning electron microscope (SEM)

Microstructure, morphology, cross-section of the CrN/DLC and DLC-W films, backscattered electron images and EDS composition were obtained using Scanning electron microscopy (Figure 21) with field emission gun - FEG - Inspect F50, with secondary electron detector, backscatter detector, EDS X-ray spectrometer and EDAX backscattered electron diffraction chamber EBSD.

Figure 21: Scanning electron microscope (SEM) with field emission gun - FEG - Inspect F50

4.4.3 Atomic force microscope (AFM)

The atomic force microscopy (AFM) technique, using a model Tosca 400, Anton Paar, under tapping mode and place on an active anti-vibration table (Figure 22) was used to obtain images of the surface topography, surface roughness and nano-scratch of the uncoated valve tappet, CrN/DLC and DLC-W coatings. All the data were processed by Talysurf-Mountains Technology®, which generated 2D and 3D images and provided the surface amplitude parameters (Ra, Rq, Rp, Rv), according to the ISO 25178 standard. Each measurement was performed in triplicates.

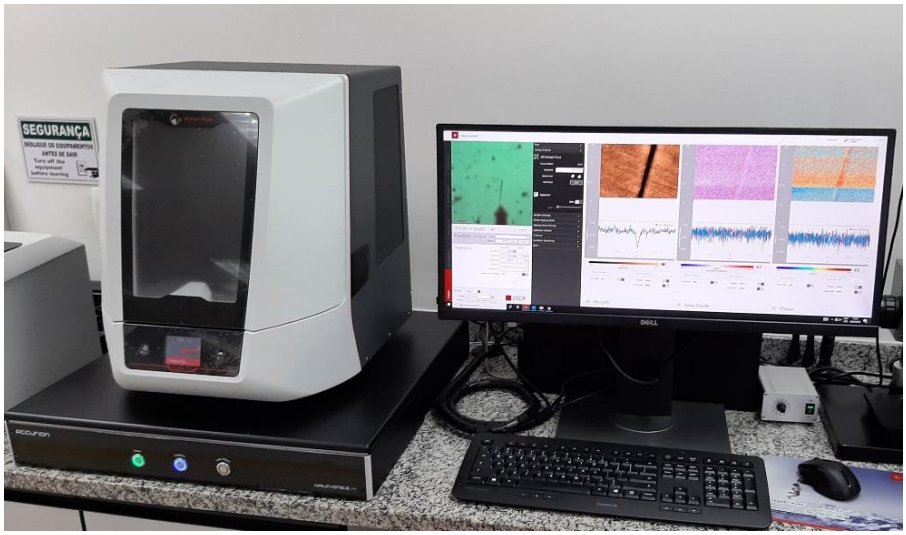

Figure 22: Atomic force microscope (AFM), Anton Paar, model Tosca 400**.**

4.4.4 Transmission electron microscope (TEM)

The microstructure of the CrN/DLC and DLC-W coatings were examined by TEM. The microscope used in this work was the JEOL JEM 2100F HRP high resolution (200 KeV), located at the Laboratory of Electron Microscopy at the National Center for Research in Energy and Materials (CNPEM). The equipment has a field effect emission gun (FEG) and operates both in transmission mode and Scanning Transmission Electron Microscopy (STEM) mode and Selected Area Electron Diffraction (SAED). The chemical

composition of the CrN/DLC and DLC-W was confirmed from the elements present in the coatings using Energy Dispersive Spectroscopy (EDS) and Electron Energy Loss Spectroscopy (EELS).

4.5 Mechanical Properties

4.5.1 Rockwell C indentation tests

The adhesion of the CrN/DLC and DLC-W coatings on the valve tappet substrate was analysed by using the Rockwell C indentation test according to the VDI 3198 standard (VIDAKIS; ANTONIADIS; BILALIS, 2003). The 120º conical Rockwell C adhesion test (Daimler Benz test) was carried out, using a diamond cone indenter, 200 µm tip radius, under an applied load of 150 Kgf, thrice on each coated surface. The stresses around the rim of a normal Rockwell C indent may cause microcracking and delamination of the coating. Once the load has been removed, the surface of the specimen was observed in an optical microscope to classify the coating adhesion as HF 1 to HF 6 according to the amount of cracking or spallation around the indent, as reported in VDI 3198 standard (VIDAKIS; ANTONIADIS; BILALIS, 2003), Figure 23. The morphologies and distribution of the crack faults associated with the names HF1 to HF4, represent typical morphologies of good adhesion coatings. The cracks represented in HF5 and HF6 show an aspect of film delamination.

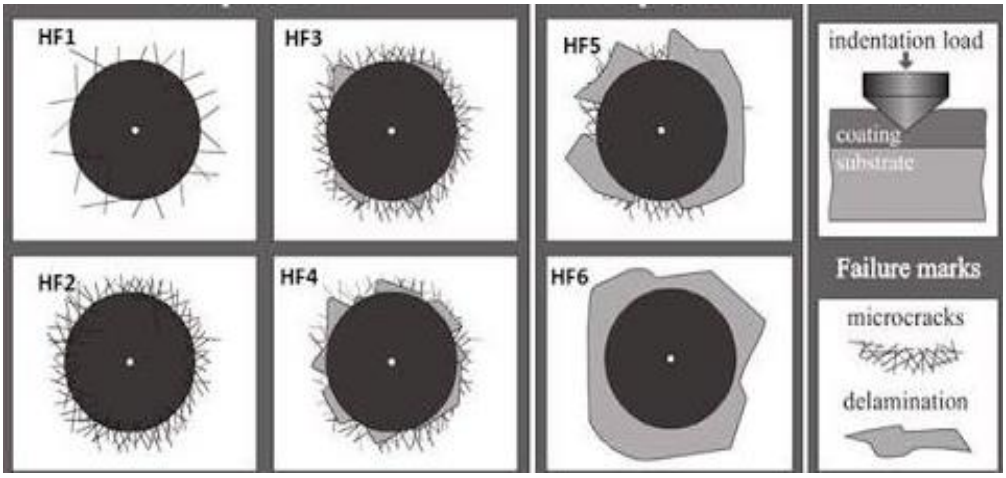

Figure 23: Morphology of failures obtained in Rockwell C adhesion tests (HEINKE et al., 1995).

4.5.2 Scratch test

Scratch test were performed on the uncoated valve tappet, CrN/DLC and DLC-W coatings according to ASTM C1824, (2005) in a CETR-UMT Multi-Specimen Test System equipment, shown in Figure 24. The CETR-UMT Multi-Specimen equipment with a conical diamond indenter with an angle of 120° and a tip radius of 200 µm (ASTM, 2009). At the beginning of the test, a preload of 1 N was applied for 10 seconds and then, a linearly increasing load was applied from 1 N to 50 N with displacement of the indenter, with displacement speed of 0.1 mm/s during 90 seconds, obtaining 5 mm long scratches. The scratch tracks were observed under an optical microscope. The experiment was performed in triplicate under the same conditions.

Figure 24: CETR-UMT Multi-Specimen Test System equipment.

The scratch hardness of the coating was determined using equations 10 and 11 (LI, 2014; MARSHALL; LAWN, 1985; LAWN; FULLER, 1975; ANSTIS et al., 1981; HARDING; OLIVER; PHARR, 1995). The average width of the scratch track is determined, and the scratch hardness number, HS is determined using equation 10, where HS is the scratch hardness number, P is the normal force, and w is the scratch width.

$$HS = \frac{8P}{\pi w^2} \qquad (\mathbf{10})$$

Substituting π gives equation 11

$$\mathrm{HS} = \frac{\mathrm{K} \times \mathrm{F_N}}{\mathrm{w}^2} \qquad (\mathbf{11})$$

Where K is a constant referring to the known geometry of scratching tip (Berkovich indenter k=2.55), F_N is the applied normal (vertical) force, w is the width of scratch.

4.6 Nano-indentation test

Hysitron TI 950 TriboIndenter with a Berkovich indenter was used to measure the hardness and reduced modulus of elasticity (Young's modulus) of the CrN/DLC and DLC-W thin coatings at the Laboratório de Fenômenos de Superfície (LFS), USP (Figure 25). The max load used was 10 mN at a load and unload rate of 5 mN/min. The indenter is pressed against a film surface while the force and displacement of the indenter are recorded. The hardness is given by the ratio between the peak load and the contact area between the indenter and the film. The elastic modulus is given by the slope of the unloading curve, following the Oliver and Pharr method (OLIVER; PHARR, 1992). The indentation depth should be less than 10% of the film thickness to minimize any substrate effect.

Figure 25: Hysitron TI 950 TriboIndenter.

4.6.1 Determination of hardness by nanoindentation

From the calibration of the equipment using the projected contact area, Ar, the hardness and reduced modulus of elasticity (module E) are determined through the load-displacement curve. A typical load-displacement curve and strain pattern are given in Figure 26.

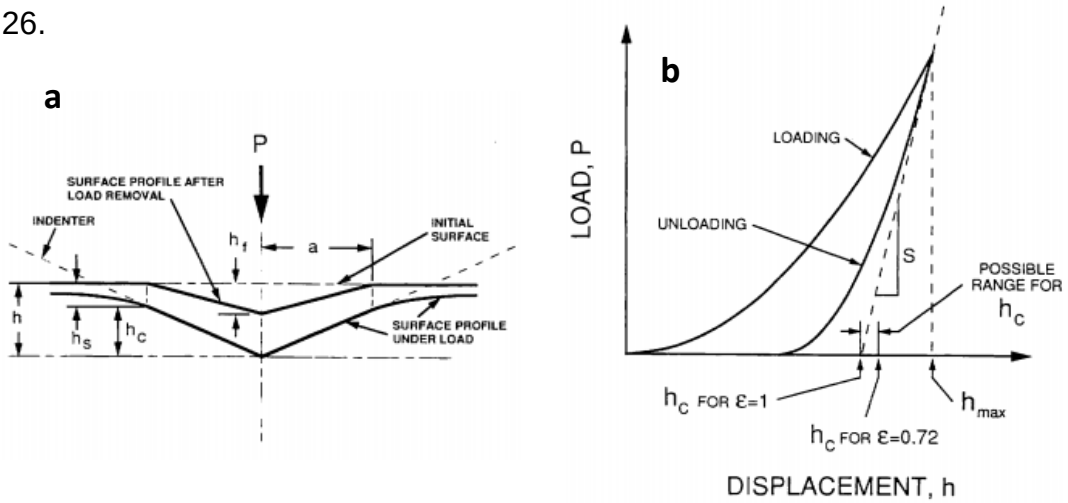

Figure 26: (a) Elastic-plastic deformation pattern during and after nano-deformation (b) Typical load curve (OLIVER; PHARR, 1992).

The procedure for calculating both H hardness and E modulus is not straightforward. The method commonly used for the analysis of indentation data is the "Oliver and Pharr" method. In this work, the method (or procedure) developed by Oliver and Pharr (OLIVER; PHARR, 1992) in 1992, was used in data processing. The procedure consists of a first step where the unloading section of the load-displacement data is adjusted. The mathematical equation that describes the unloading is described by Equation 12:

$$P = A(h - h_f)^m \qquad (\mathbf{12})$$

For the applied load in Newtons, h is the surface penetration depth and the final displacement. A_{em} are empirical constants, dependent on the geometry and the material

used (FISCHER-CRIPPS, 2000). The contact stiffness S=dP/dh can be calculated by deriving P and evaluating it for $h=h_{max}$, being described by Equation 13.

$$S = \frac{dP}{dh} = mA(h_{max} - h_f)^{m-1} \quad (\mathbf{13})$$

The contact stiffness corresponds to the initial part of the unloading curve, as shown in Figure 27b.

The contact depth can be determined by calculating the value of S (equation 13) and substituting in Equation 14:

$$h_c = h_{max} - \varepsilon \frac{P_{max}}{S} \quad (\mathbf{14})$$

Where c is a geometric constant that depends on the indenter (c=0.75 for indenter Berkovich). h_c is in turn used to calculate the contact area. A= 24.58hc for a perfect Berkovich indenter, these values should be calibrated for a non-ideal tip through a calibration procedure, using an area function, described by Equation 15.

$$A_c = C_0 h_c^2 + \sum_{i=0}^{n} C_i (h_c)^{\left(\frac{1}{2}\right)i} \quad (\mathbf{15})$$

Where Ci (also Ca) are constants determined by the curve fitting procedure.

Using S, Ac, the reduced elastic modulus E can be determined by Equation 16:

$$E_r = \frac{\sqrt{\pi} S}{2\beta A_c} \quad (\mathbf{16})$$

β is a constant that will depend on the geometry of the indenter (1.034 for Berkovich indenter). The reduced modulus is correlated with the elastic modulus of the indenter and the elastic modulus E of the sample, being calculated from Equation 17:

$$\frac{1}{E_r} = \frac{1 - v^2}{E} + \frac{1 - v_{ind}^2}{E_{ind}} \quad (\mathbf{17})$$

Where the symbols v and v_{ind} are the Poisson ratio of the sample and the indenter.

The elastic recovery value (*We*) represents the elasticity recovery capacity of the coating. High elastic recovery helps in stoppage of crack formation. The *We* value (equation 18) can be derived from the load-displacement curves, defined as

$$The\ elastic\ recovery\ (W_e) = \frac{[d_{maximum} - d_{residual}]}{d_{maximum}} x\ 100\% \quad (\mathbf{18})$$

where $d_{maximum}$ and $d_{residual}$ are the maximum indentation depth during loading and the residual indentation depth after unloading, respectively (OLIVER; PHARR, 1992).

4.6.2 Nano-scratch

Nano-scratch tests were performed using the LFM (Lateral Force Measurement) option of the Nano Indenter XP on a Hysitron Ti950 tribo-indenter (Figure 27) with a cono-spherical tip of 10 μm in diameter and load of 300 mN. The experiment was performed under dry condition in a ramping load configuration. The total scratch length was 300 μm at Laboratório de Fenômenos de Superfície (LFS), USP.

4.7 Wear reciprocating test

Wear reciprocating test was performed on the plane surface of the uncoated, CrN/DLC and DLC-W coated valve tappet using an Optimol SRV® v4 device with a ball on plane configuration under dry condition (Figure 27) at Laboratório de Fenômenos de Superfície (LFS), USP. Tests were performed at 20 N for total duration of 30 min, 10 Hz of reciprocating frequency and a stroke of 2 mm at temperatures (25 ºC, 150 ºC, 200 ºC and 250 ºC). The contact body used were AISI 52100 steel sphere balls (848 Vickers hardness) with a diameter of 10 mm. The wear tracks and scars of the uncoated and coated tappets valve were observed by SEM. The chemical composition of the wear track was analysed by energy-dispersive X-ray spectroscopy (EDS) integrated with the SEM equipment. The specific wear rate (Ws) of the uncoated, CrN/DLC and DLC-W coated valve tappet tested at 25ºC, 150ºC, 200ºC and 250ºC were calculated using equation 19:

$$Ws = \frac{\Delta V}{(F_n . S)} \qquad (\mathbf{19})$$

Where, ΔV is the wear volume, F_n is the normal load and S is the sliding distance.

Figure 27: Optimol SRV® v4 device.

4.8 3D Optical Profilometry

The 3D coherence correlation interferometry (CCI) - Taylor Hobson profilometer (Figure 28) was used to assess the surface roughness of the uncoated valve tappet. The micro-scratch and nano-scratch depths along the scratch track were also assessed. Finally, the wear volume of the wear tracks was also determined.

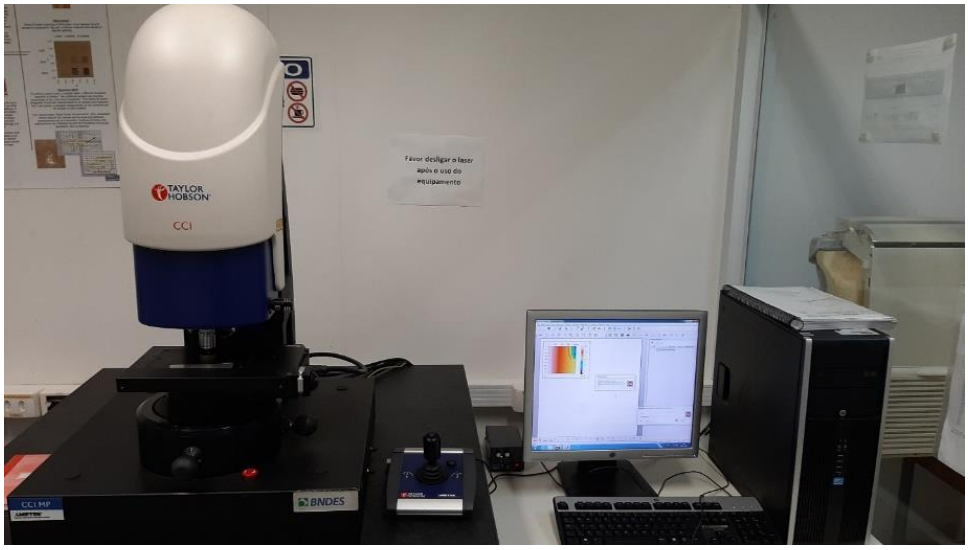

Figure 28: 3D coherence correlation interferometry (CCI) - Taylor Hobson profilometer.

5 RESULTS AND DISCUSSION

5.1 Substrate characterization

The valve tappets used in this study were manufactured using DIN 16MnCr5 steel. The nominal chemical composition of the steel is shown in Table 4. The valve tappets were carburized to obtain a wear resistant hardened surface layer. Figure (29-30) presents optical image of cross-section of valve tappet showing the diffusion layer (case), core, and bottom. SEM images showing the diffusion layer (case), core, and bottom of the cross-section of the valve tappet can also be seen in Figure 31. The plot of the microhardness against depth is presented in Figure 32.

Table 4: Nominal chemical composition of the valve tappets (wt.%)

C	Mn	Si	Cr	P	S
0.14 – 0.19	1.05 – 1.30	0.4 max	0.85 – 1.10	0.025 max	0.035 max

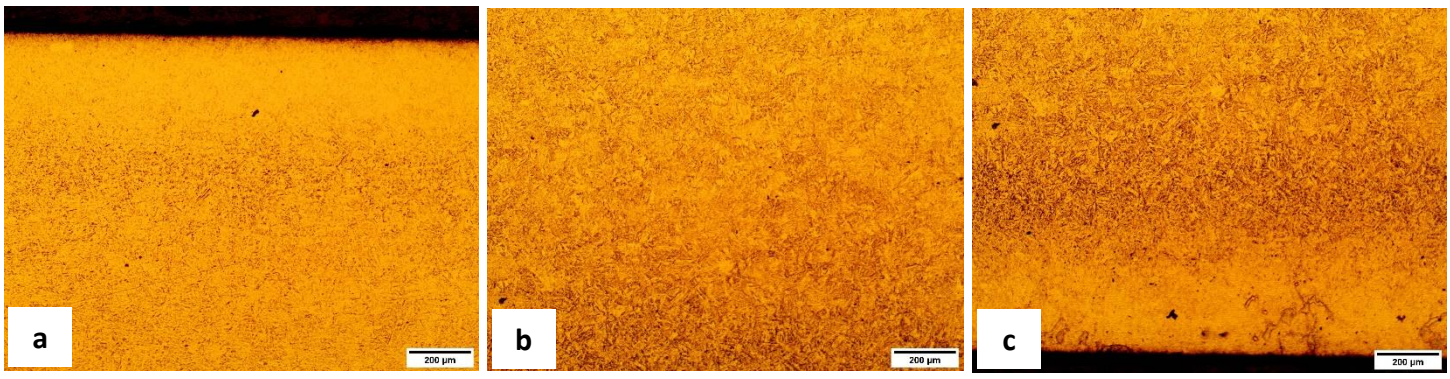

Figure 29: Optical image of cross-section of the carburized valve tappet at 100x (a) carburized layer (b) core (c) bottom.

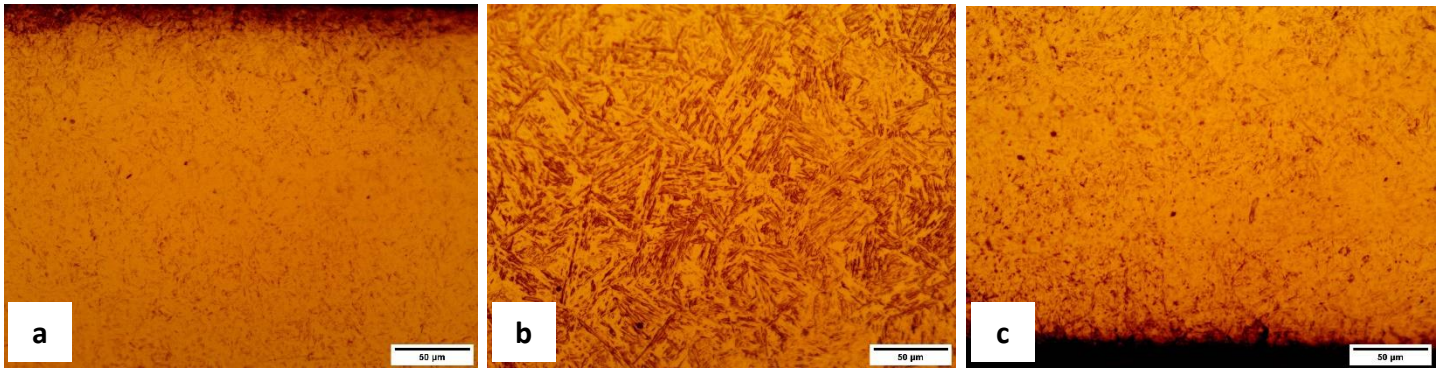

Figure 30: Optical image of the cross-section of the carburized valve tappet at 500x (a) carburized layer (b) core (c) bottom.

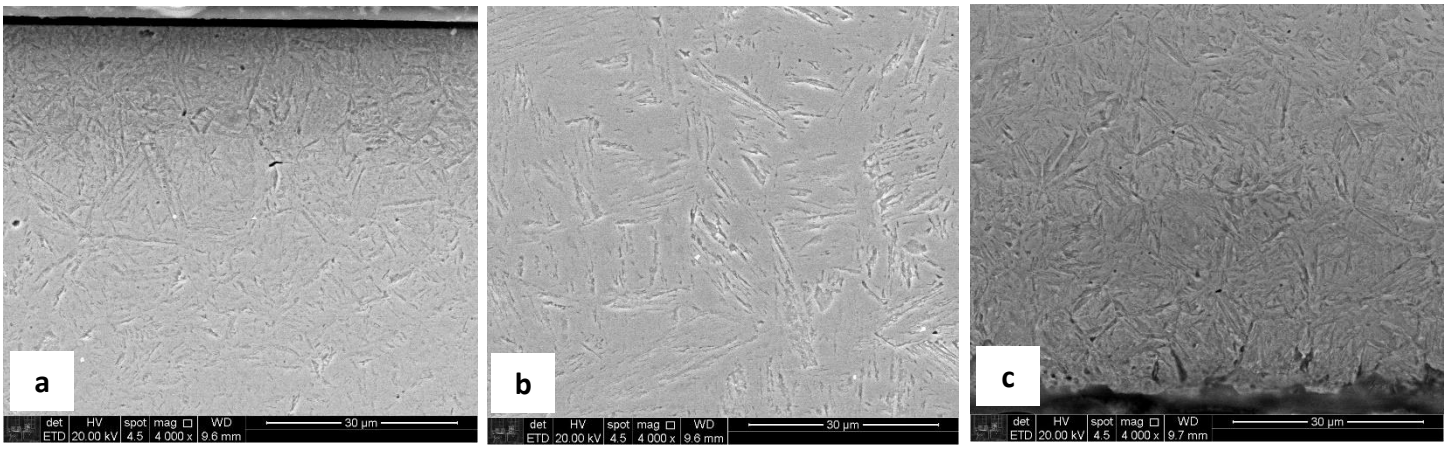

Figure 31: SEM image of cross-section of the carburized valve tappet (a) carburized layer (b) core (c) bottom.

The carburized layer (case) of the valve tappet contains high carbon martensite, while the core contains a mixture of martensite and bainite as seen from the microstructure obtained from both optical and SEM images in Figure (29-31). Microhardness measurements made on the cross section of the valve tappet indicate a maximum hardness of 929 $HV_{0.1}$ at 3200 µm and 917 $HV_{0.1}$ at 100 µm both taken on the carburized layer (case). Hardness decreases towards the core with increasing depth down to around to 400 $HV_{0.1}$ at 2100 µm and increases again from about 2200 µm with hardness of 418 $HV_{0.1}$ to 3200 µm with hardness of 929 $HV_{0.1}$. The microhardness variation indicates a carburized depth of approximately 450 µm on both sides, measured by the EHT criterion EN ISO 2639 standard. It correlates with the observed changes in the microstructure after carburizing, quenching and tempering the valve tappets. The presented results are similar to those obtained from similar studies (MARRAY et al., 2014; KULA et al., 2014; PILCH et al., 2016). The valve tappet was manufactured by been drawn from a steel strip and thermochemically treated by carburizing, quenching and tempering. The surface roughness (Ra) of the unpolished and polished valve tappet were measured as 0.1611 µm and 0.007962 µm, respectively, as seen in Figure 33.

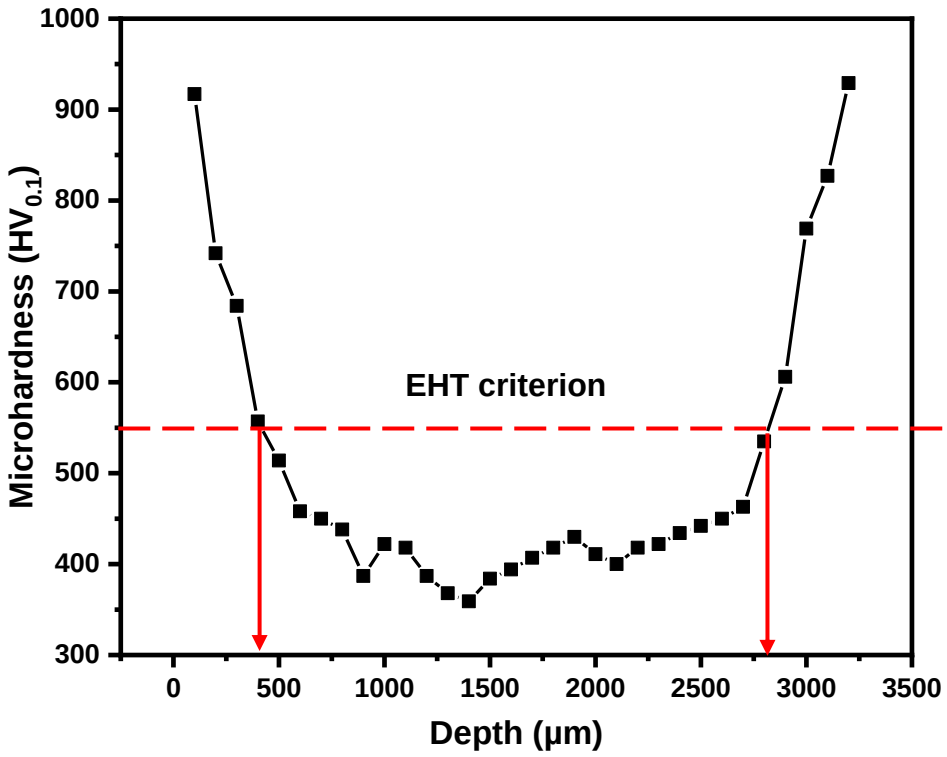

Figure 32: Microhardness profile of valve tappet for determination of the carburizing depth.

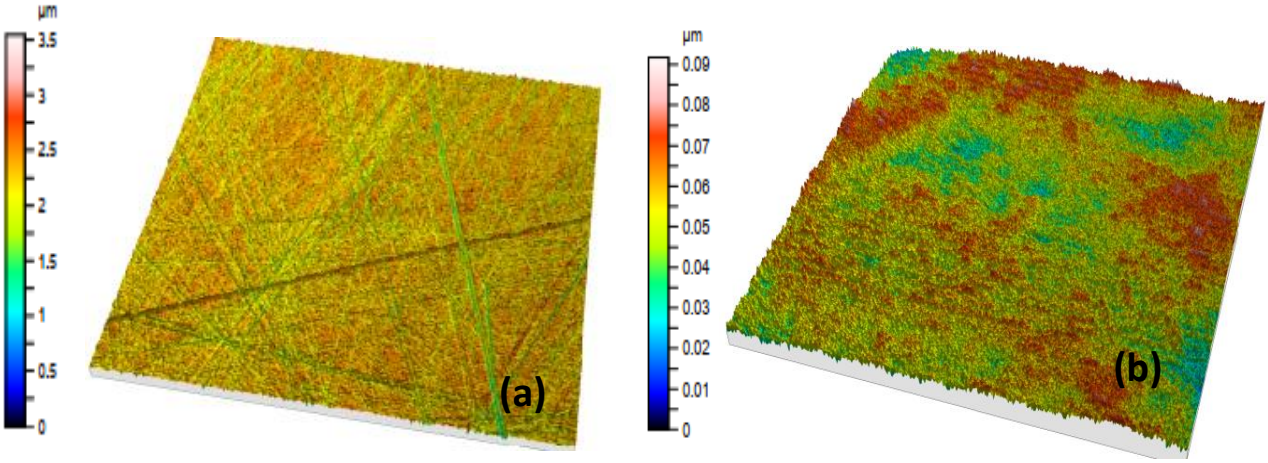

Figure 33: 3D Profilometry surface roughness of valve tappet (a) unpolished (b) polished.

5.2 Coating characterization

5.2.1 Thickness of deposited films

The CrN/DLC with Cr interlayer and DLC-W with WC interlayer were successfully grown by a hybrid PVD/PECVD system. The thickness of CrN/DLC and DLC-W coatings were measured on the cross-section of the coatings deposited on the metallic substrate (valve tappet). The CrN/DLC coating has a duplex layer coating architecture, with an underlying 0.35 µm thick Cr adhesive layer, followed by a 0.75 µm CrN reinforcing layer and finally, a 1.85 µm thick DLC layer. The DLC-W coating is preceded by a WC adhesion interlayer 0.58 µm in thickness. The DLC-W coating is 6 µm thick. Details of the layer thickness measurements of CrN/DLC and DLC-W coatings are listed in Table 5.

Table 5: Coating thickness measurement of CrN/DLC and DLC-W

Layer	CrN/DLC	DLC-W
Cr adhesion interlayer (µm)	0.35	
CrN layer (µm)	0.75	-
DLC layer (µm)	1.85	-
WC adhesion interlayer (µm)	-	0.58
DLC-W layer (µm)	-	6
Total thickness (µm)	2.95	6.58

5.3 Chemical Composition

The surface region atomic concentrations (< 5 nm) obtained during the XPS analysis from high-resolution spectra for the samples are listed in Table 6. The spectra composition contains mainly elements of C, O, and W. The CrN layer was not presented in these results because XPS analysis is majorly superficial.

Table 6: Chemical composition of the surface region of coatings

Samples / Elements	[% atom] DLC	DLC-W
Oxygen (O 1s)	2.6	3.2
Carbon (C 1s)	97.4	95.4
Tungsten (W 4f)	-	1.4

The CrN/DLC coating contains 14.6 at. % of oxygen and 84.4 at.% of carbon; on the other hand, the DLC-W coating contains 15.2 at.% of oxygen, 83.4 at.% of carbon and 1.4 at. % of tungsten. The oxygen content in both coatings is insignificantly different; the oxygen obtained was mainly from the surface during the XPS analysis.

5.3.1 Structure and chemical bonds of coatings

5.3.1.1 X-ray Photoelectron Spectroscopy (XPS) analysis

The chemical bonds and binding energies of CrN/DLC and DLC-W coatings are summarized in Table 7. Figure 34(a-c) presents the XPS spectra for DLC total, C1s and O1s of CrN/DLC coatings, while Figure 35(a-d) presents the XPS spectra for DLC-W total, C1s, O1s and W4f of DLC-W coatings.

Carbon, C 1s, as seen in the high-resolution spectra, the tuned components of CrN/DLC correspond to carbons in different chemical environments. The main peaks were the sp^2 and sp^3 at 283.37 eV and 284.82 eV respectively which are associated with carbon DLC (a-C:H), also at 286.28 eV and 288.50 eV the peaks of C-O and C=O, respectively were revealed, which corresponds to the oxygenated groups of the small concentration (Figure 34b) similar to the results found in literature (BUJAK; MICHALCZEWSKI, 2011; AL MAHMUD et al., 2014). Oxygen, O 1s, for the CrN/DLC sample the components at low binding energy associated with surface O=C, followed by a peak of O-C and O-C=O which suggests that oxygen could be incorporated into the DLC layer from the gaseous contamination of the reactive chamber and from the surface layer exposure to ambient atmosphere during the XPS analysis (Figure 34c).

The chemical bonds obtained for DLC-W were mainly sp^2 and sp^3 at 283.78 eV and 284.75 eV, respectively. Other peaks obtained were W-C and C-O at 285.29 eV and 287.26 eV, respectively. The W-C corresponds to the presence of tungsten carbide (Figure 35b), which corroborates those found in literature (FU et al., 2013; YUE et al., 2012). In the DLC-W sample, the component at low energy is related to O-W bonds at the tail of spectrum W 4f as seen in Figure 35c. Also, a small component associated with C-W bonds appears at 283.0 eV. Tungsten, W 4f, the spectrum of the spin-orbit pair (W 4f7/2 and W 4f5/2) was fitted with 4 spin-orbit pairs of components that correspond with increasing binding energy to metallic W, WC, $W_{18}O_{49}$ (W^{5+}) and WO_3 (Figure 35d). The XPS peaks which were deconvoluted imply that there exist free W, WC, and WO in the top layers (5 nm) of the coatings. The presence of tungsten carbide (WC) in the DLC coatings causes the formation of the nanocomposite structure composed of nanocrystalline WC phase dispersed in amorphous carbon matrix, which is beneficial to the improvement of the coating's properties. A reduction in the sp^3 bond and an increase in the sp^2 bond occurs in the DLC-W coating, due to the presence of tungsten, which forms WC and W_2C nanoclusters in amorphous carbon matrix (DAI et al., 2015), leading to an increase in disorder and increasing the spacing between the carbon atoms, reducing the number of coordinated carbon atoms and the atomic density, thereby causing a decrease in the density (BAI et al., 2021; LIU et al., 2015 DAI et al., 2015), which is also responsible for the reduction in the hardness of the DLC-W. These results corroborate previous works (HOVSEPIAN et al., 2016; KRŽAN; NOVOTNY-FARKAS; VIŽINTIN, 2009; EVARISTO; FERNANDES; CAVALEIRO, 2020; TAKENO et al., 2008; TAKENO et al., 2009; BAI et al., 2021; LIU et al., 2015 DAI et al., 2015). While CrN/DLC coatings

possess higher sp^3 and lower sp^2 than DLC-W due to the high number of coordinated carbon atoms and higher atomic density. W atoms would prefer to react and bond preferentially with sp^2 carbon due to their relative lower bond energy compared with sp^3 carbon (CAO et al., 2020).

Table 7: Chemical species and corresponding binding energies.

XPS Peaks	Chemical species and corresponding binding energies		
	C1s	**O1s**	**W4f**
CrN/DLC	sp^2 – 283.37 eV sp^3 – 284.82 eV C-O – 286.28 eV C=O – 288.50 eV	O=C – 531.21 eV O-C – 532.11 eV O-C=O – 533.43 eV	-
DLC-W	sp^2 – 283.78 eV sp^3 – 284.75 eV W-C – 285.29 eV C-O – 287.26 eV	O-W – 530 eV O=C – 531.26 eV O-C – 532.10 eV O-C=O – 533.50 eV	W4f 7/2 – 31.17 eV W4f 5/2 – 33.32 eV W-C 4f 7/2 – 31.89 eV W-C 4f 5/2 – 34.04 eV W18O49 4f 7/2 – 34.56 eV W18O49 4f 5/2 – 36.71 eV WO3 4f 7/2 – 35.61 eV WO3 4f 5/2 – 37.76 eV

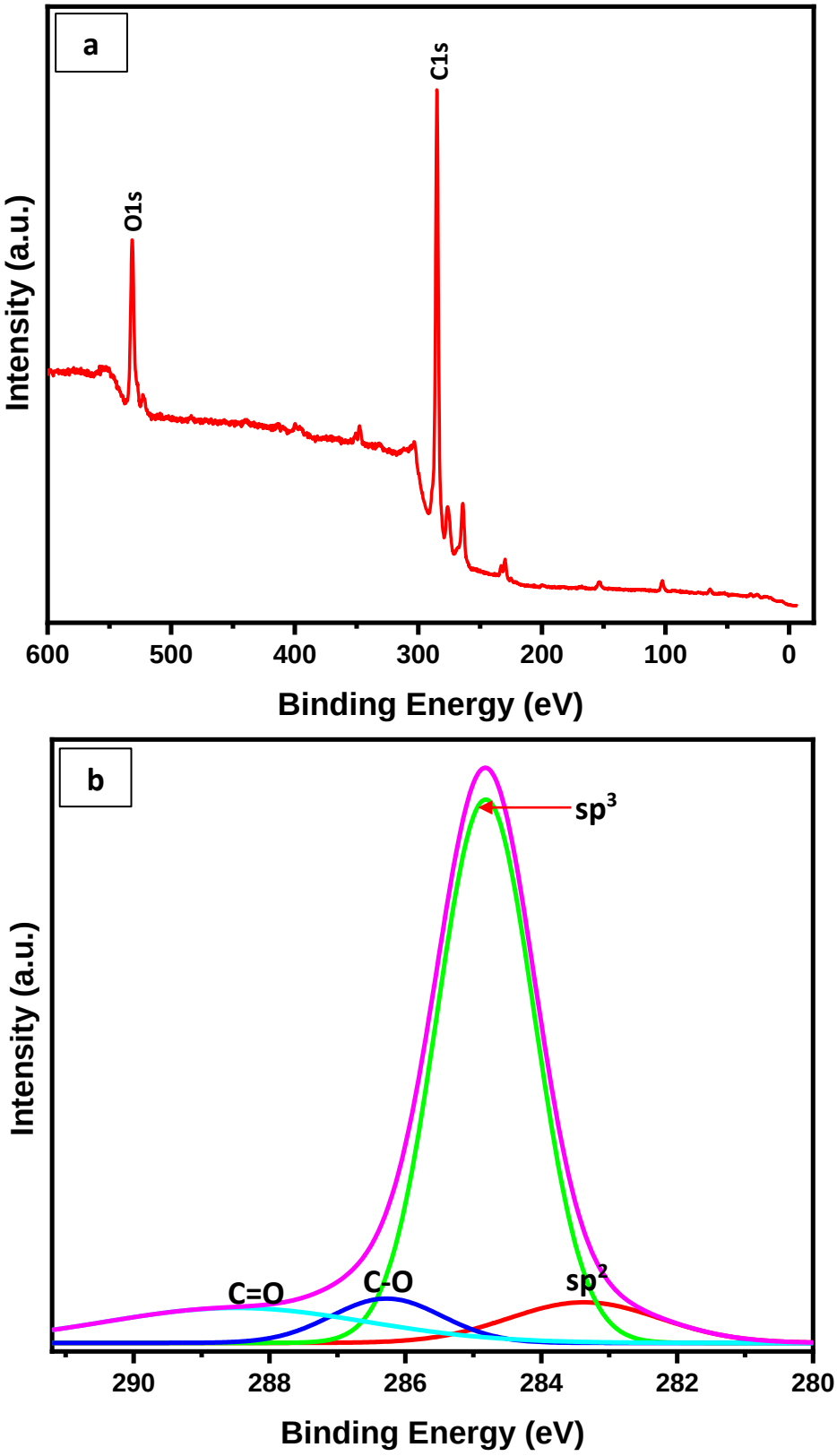
a
C1s
O1s
Intensity (a.u.)
600
500
400
300
200
100
0
Binding Energy (eV)
b
sp3
C=O
C-O
sp2
Intensity (a.u.)
290
288
286
284
282
280
Binding Energy (eV)

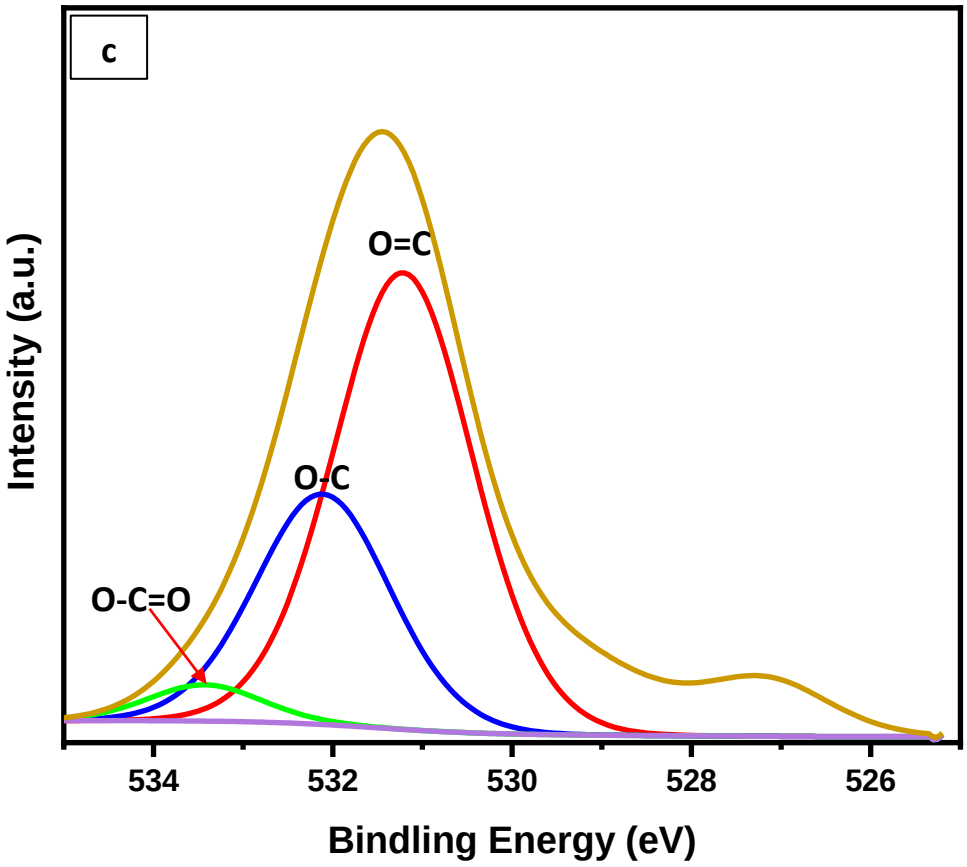

Figure 34: XPS spectra of CrN/DLC coatings (a) DLC total (b) C1s (c) O1s.

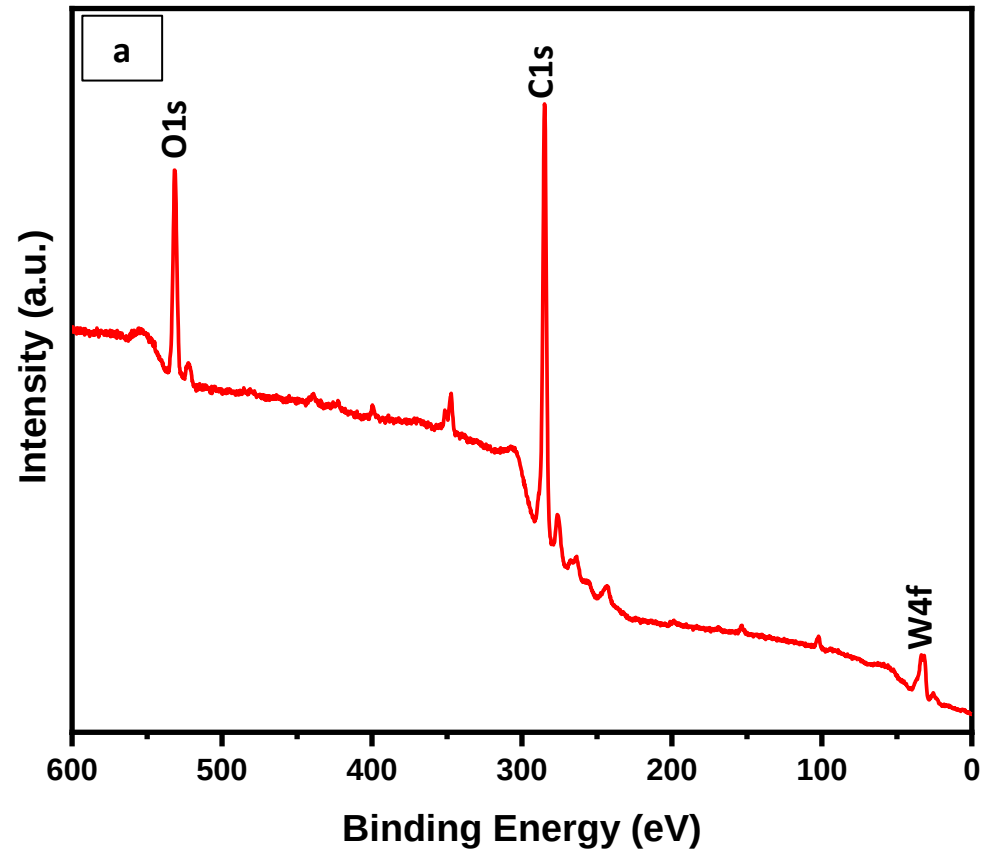
a
O1s
C1s
W4f
Intensity (a.u.)
600
500
400
300
200
100
0
Binding Energy (eV)

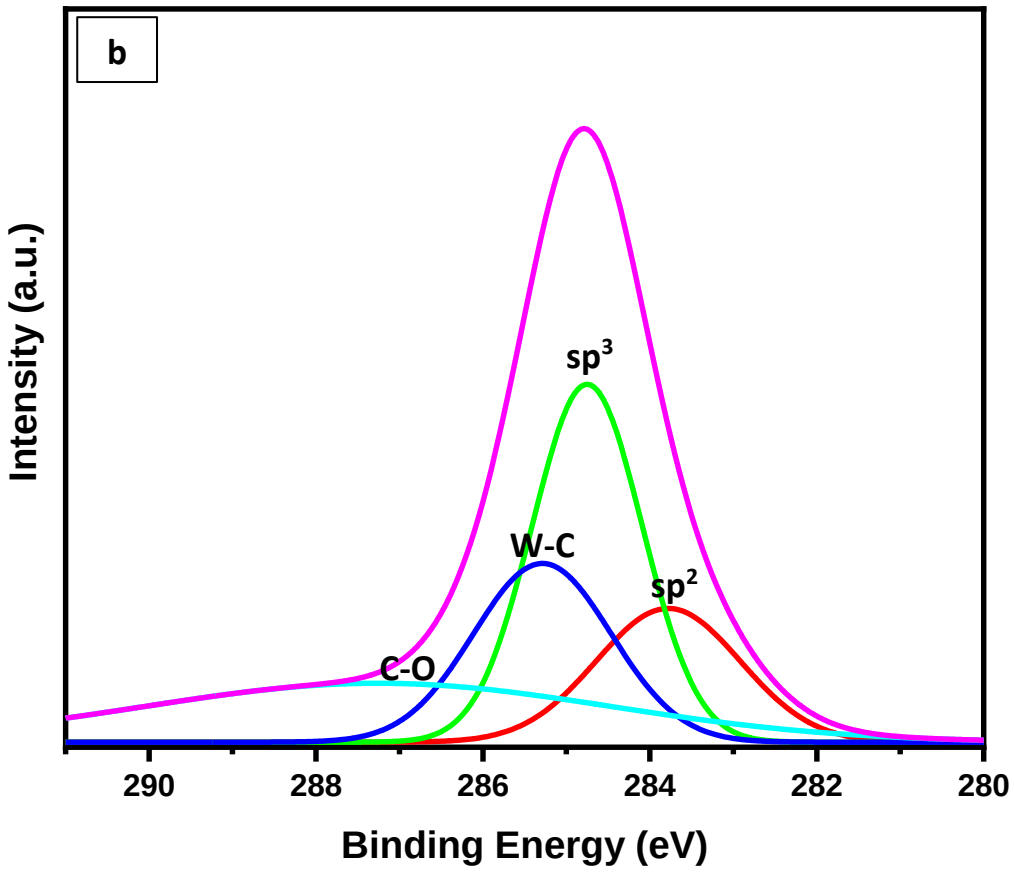
b
Intensity (a.u.)
sp3
W-C
sp2
C-O
290
288
286
284
282
280
Binding Energy (eV)

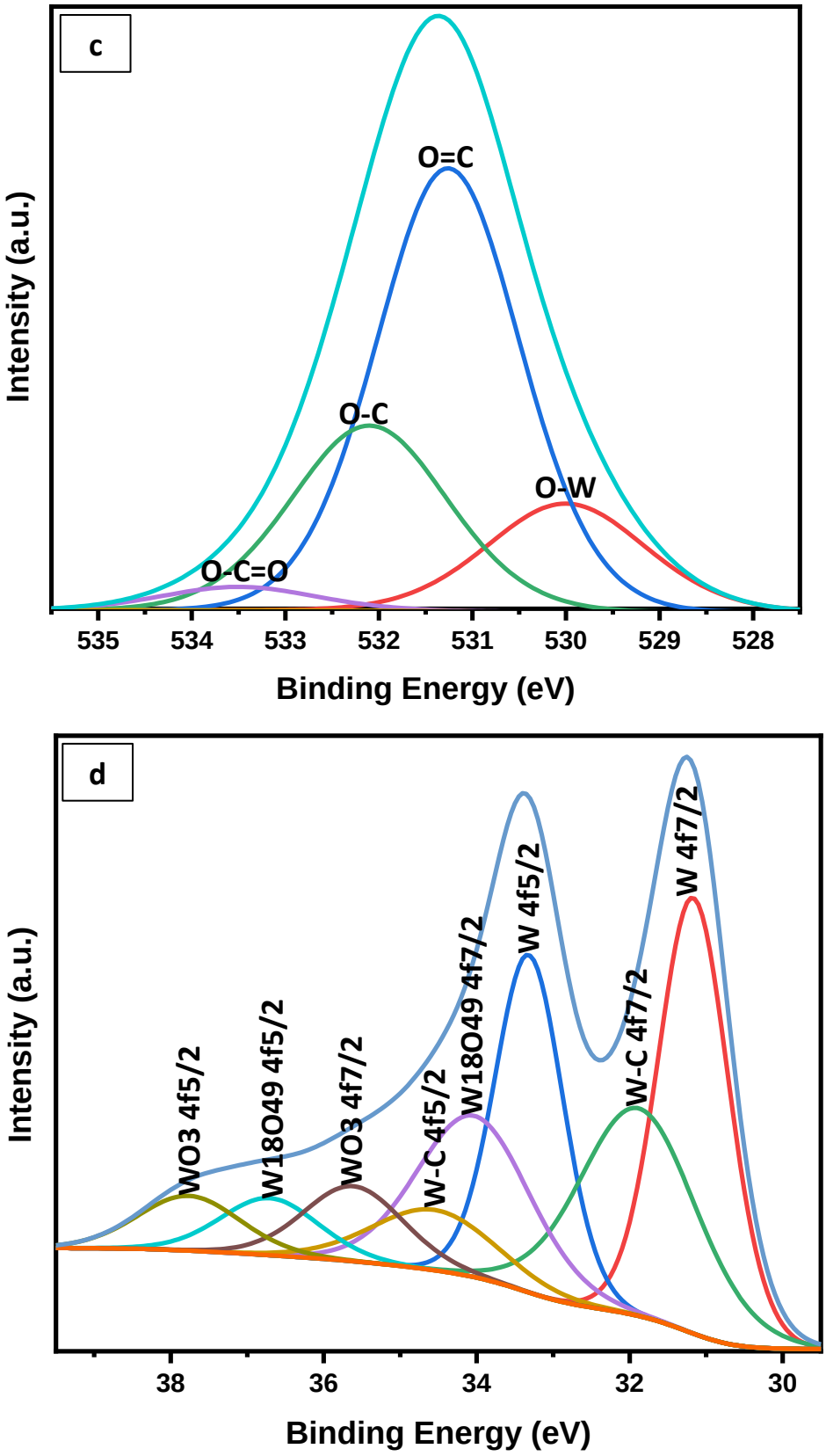

Figure 35: XPS spectra of DLC-W coatings (a) DLC-W total (b) C1s (c) O1s (d) W4f.

5.3.1.2 Raman analysis

The structural properties and chemical composition of the DLC films can be determined by Raman spectroscopy. The Raman spectrum for DLC is typically composed of two broad peaks (G band at 1560 cm^{-1} and D band at 1380 cm^{-1}). The G peak is attributed to the bond stretching of all pairs of sp^2 carbon atoms in both rings and chains, and the D peak is due to the breathing modes of sp^2 carbon atoms in rings. Previous studies have shown that the ratio between the I(D) and the I(G) intensities of the D and G bands, I(D)/I(G), can be used to characterize the sp^2/sp^3 ratio (CASIRAGHI; FERRARI; ROBERTSON, 2005; FERRARI; ROBERTSON, 2000; IRMER; DORNER-REISEL, 2005). The D and G peaks are obtained by deconvolution of the spectra using Gaussian line fitting to obtain all the relevant information from the Raman spectra using the Origin 2019 software. The D and G peaks are results obtained due to the vibration of sp^2 sites. Information relating to the sp^2/sp^3 ratio can be obtained from ID/IG ratio, G peak position and FWHM (full width at half maximum) of the G peak, summarized in Table 8.

The presence of H in DLC has been reported to be responsible for promoting sp^3 bond formation because they possess random covalent network bonding between fourfold sp^3 carbon, threefold sp^2 carbon, and single coordinated H atoms (EVARISTO; FERNANDES; CAVALEIRO, 2020). The Raman spectra for CrN/DLC and DLC-W coating are represented in Figures (36-37). The DLC-W shows a D band shifted to the left and a G band slightly shifted to the right due to the addition of tungsten. The ID/IG ratio increases due to an increase in the amount of sp^2 bonding due to tungsten addition. These results agree with previous works (WANG et al., 2006; VIJAI BHARATHY et al., 2012; LI; KE; WANG, 2015; XUEMIN et al., 2009), indicating that the incorporation of W

enhances the formation of sp^2 bonded carbon sites in the amorphous DLC matrix (WANG et al., 2006; VIJAI BHARATHY et al., 2012; LI; KE; WANG, 2015; XUEMIN et al., 2009). This reaction is enhanced due to the addition of W to DLC coating, leading to a decrease in the intensity of the Raman spectra for DLC-W because WC is Raman inactive (CAO et al., 2020). The results obtained by Raman analysis agree with those from the XPS analysis and corroborate those published in the literature (VIJAI BHARATHY et al., 2012; LI; KE; WANG, 2015; XUEMIN et al., 2009). Also, Bai et. al. reported an increase in the I(D)/I(G) ratio in Raman spectra from 0.52 to 1.11 due to the addition of tungsten (BAI et al., 2021).

Table 8: Raman analysis of the coatings .

Coatings	D Position (cm^{-1})	G Position (cm^{-1})	I_D/I_G	D FWHM (cm^{-1})	G FWHM (cm^{-1})
CrN/DLC	1375.73	1544.13	0.84	271.20	170.82
DLC-W	1368.05	1546.53	1.69	282.12	138.19

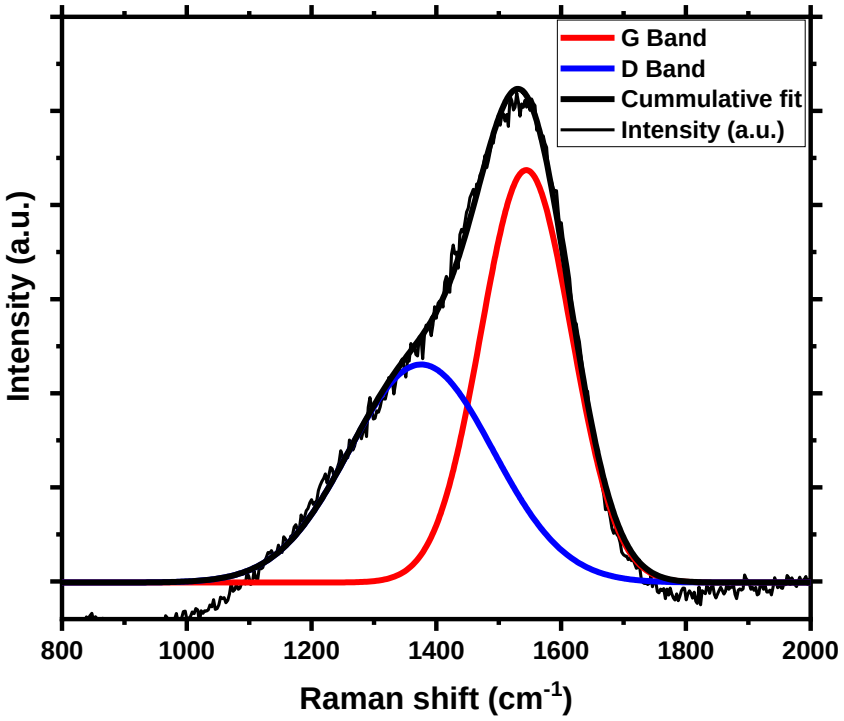

Figure 36: Raman spectra of CrN/DLC coatings.

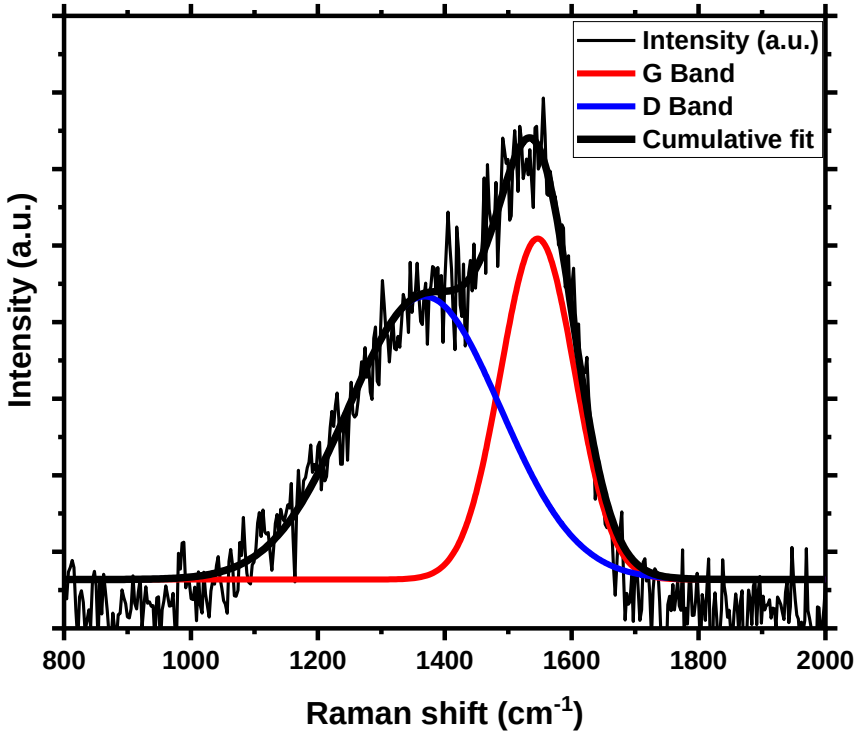

Figure 37: Raman spectra of DLC-W coatings.

5.4 Morphology and Topography of CrN/DLC and DLC-W Coatings

The surface morphology and topography of the both coatings were analyse using SEM and AFM. Figure 38 shows the surface morphology and cross-section of the CrN/DLC and DLC-W coatings on the valve tappet substrates. The CrN/DLC coatings have a duplex layer coating architecture with Cr adhesion interlayer, a total thickness of 2.95 µm. The DLC top layer has a smooth surface, although deposited on top of a CrN columnar structure and of a Cr interlayer. On the other hand, shows a multilayer columnar structure with a 6.58 µm total thickness. Both coatings were observed to possess micro-bumps, but DLC-W had coarser micro-bumps resulting in a higher roughness than CrN/DLC. The columnar structure of the CrN layer is observed below the top DLC layer in the secondary electrons image (Figure 38c), and the backscattered electrons image shows a bright Cr interlayer due to the presence of chromium which is a heavy metal having an adhesion layer, intermediate layer and transition layer (Figure 38d). The DLC-W has bright WC adhesion interlayer followed by a DLC-W coating with a columnar structure, observed from both secondary electrons image (Figure 38e) and backscattered electrons image (Figure 38f). The WC adhesion interlayer shows a compositional gradient, being richer in W at the interface and containing more carbon as it grows. The corresponding EDS Elemental mapping images of CrN/DLC and DLC-W coatings are presented in Figures 39 and 40, respectively, showing the presence of C, O, N, and Cr in the CrN/DLC and C, W, and O in DLC-W.

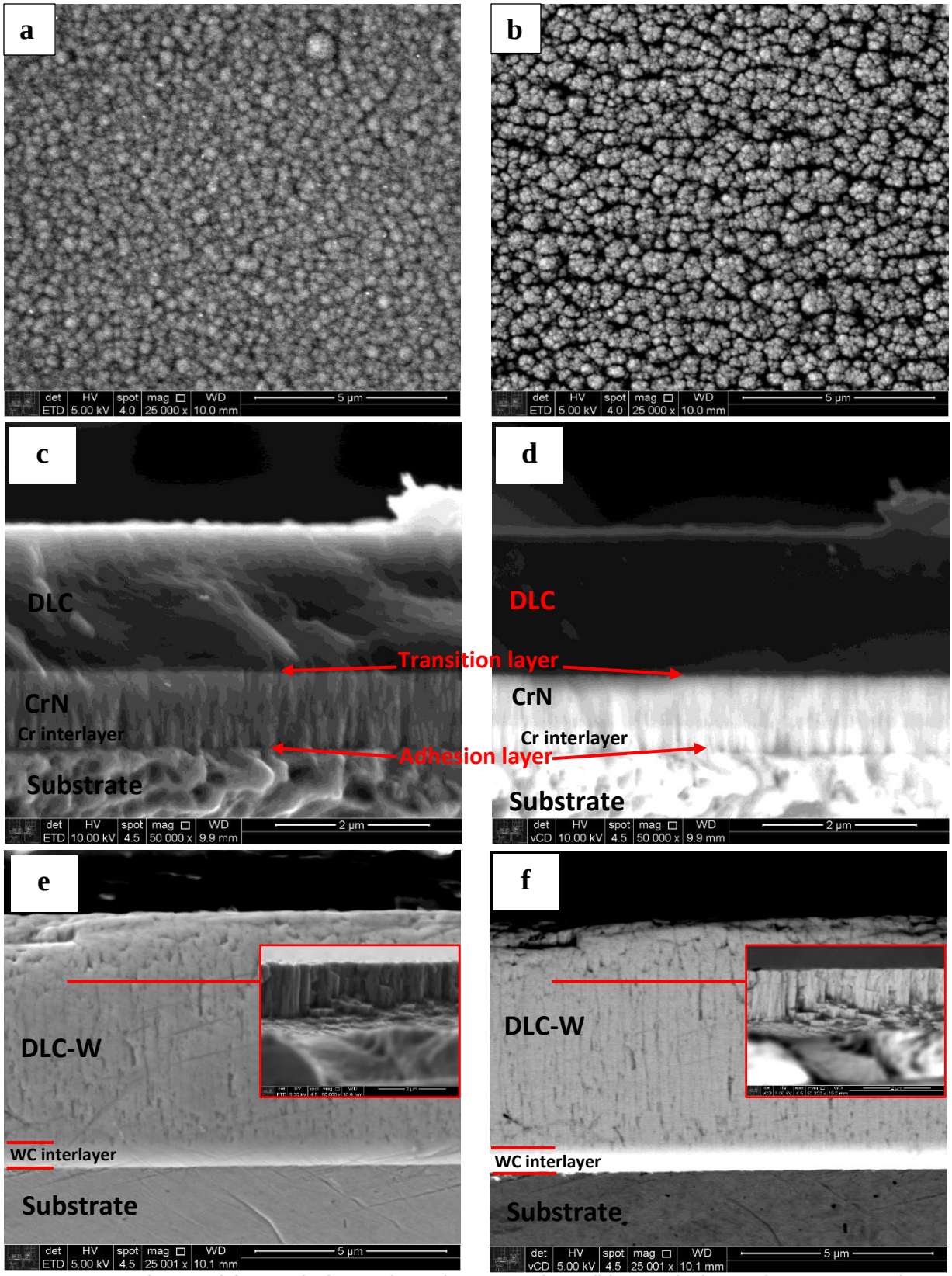

Figure 38: SEM image (a) morphology of CrN/DLC coatings (b) morphology of DLC-W coatings (c) CrN/DLC secondary electrons image (d) CrN/DLC backscattered electrons image (e) DLC-W secondary electrons image (e) DLC-W backscattered electrons image.

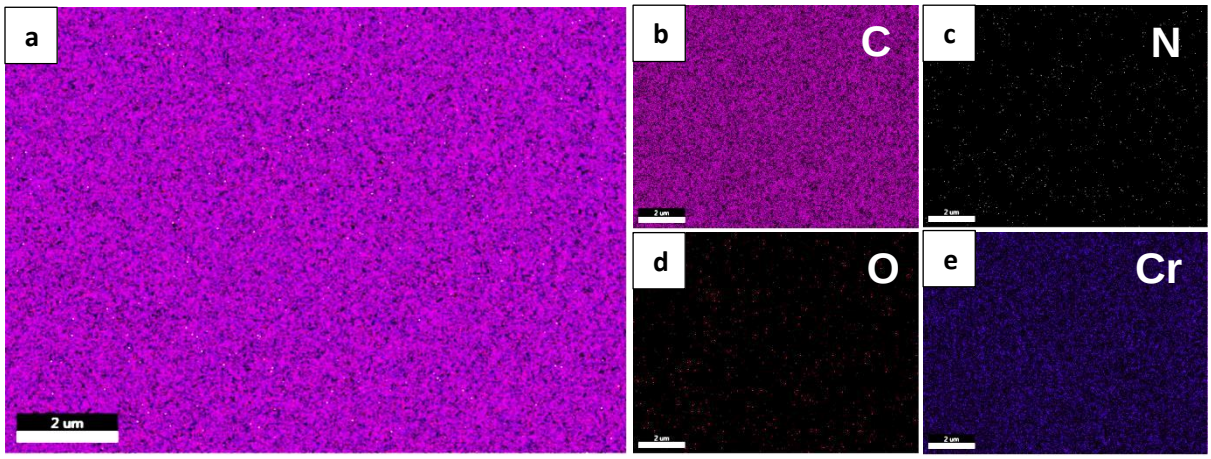

Figure 39: EDS mapping of CrN/DLC coating (a) overlay elements (b) 97 % at. C Kα2 (c) 0.5 % at. N Kα1 (d) 1 % at. O Kα1 (e) 2.5% at. Cr Kα2.

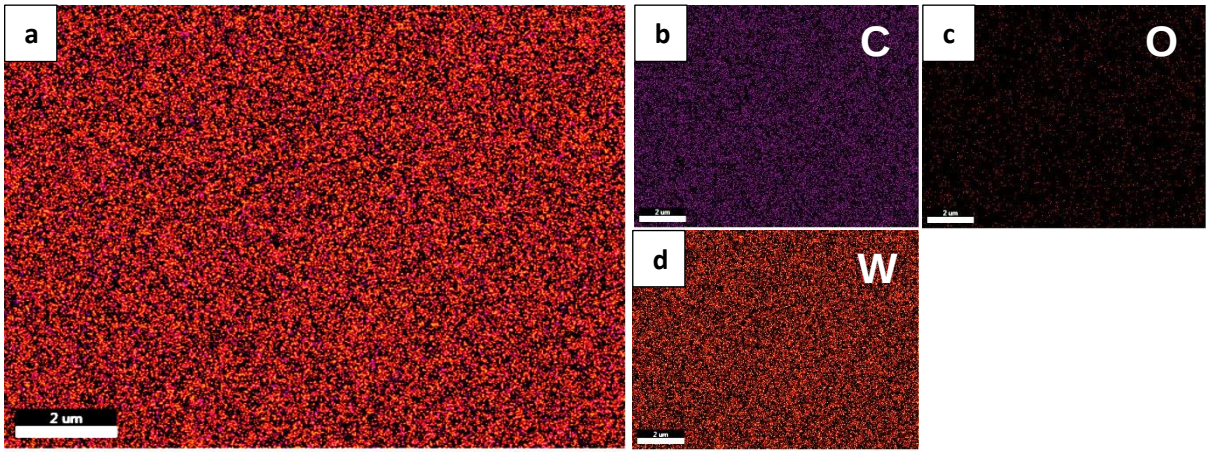

Figure 40: EDS mapping of DLC-W coating (a) overlay elements (b) 31% at. C Kα2 (c) 4% at. O Kα1 (d) 65% at. W M α1.

Figure 41(a-f) presents the 2D and 3D AFM images of the uncoated, CrN/DLC and DLC-W coated valve tappet with the scan size of 5 µm x 5 µm for surface topography. The uncoated, CrN/DLC and DLC-W coated valve tappet showed fine-grained structure and relevant smoothness, there were no visible voids, defects and cracks on the surface. The measured values of the average roughness (R_a) – 2.73 nm and root mean square roughness (R_q) – 4.37 nm for the uncoated valve tappet. While, for the CrN/DLC coating, the average roughness (R_a) – 5.77 nm and root mean square roughness (R_q) – 7.34 nm

and the DLC-W coating had an average roughness (R_a) – 13.63 nm and root mean square roughness (R_q) – 17.49 nm. The structure of the coatings is smooth in a nanocluster formation. The AFM results shows that CrN/DLC has finer grains than DLC-W, this is indicated in the columns of CrN/DLC having smaller diameter compared to DLC-W with coarser grain structure. The topography also shows that DLC-W possesses a rougher surface compared to CrN/DLC. The topography of both coatings can also be described as having globulitic particles formed due to nucleation and growth of the coatings and can be seen as a cauliflower structure. The morphology and topography of CrN/DLC and DLC-W are similar to those published in literature (LUKASZKOWICZ; PARADECKA; WIŚNIEWSKA, 2013; MULLIGAN et al., 2014; XUEMIN et al., 2009; CAVALEIRO; HOSSON, 2006; CZYZNIEWSKI et al., 2011)

(a) **(b)**

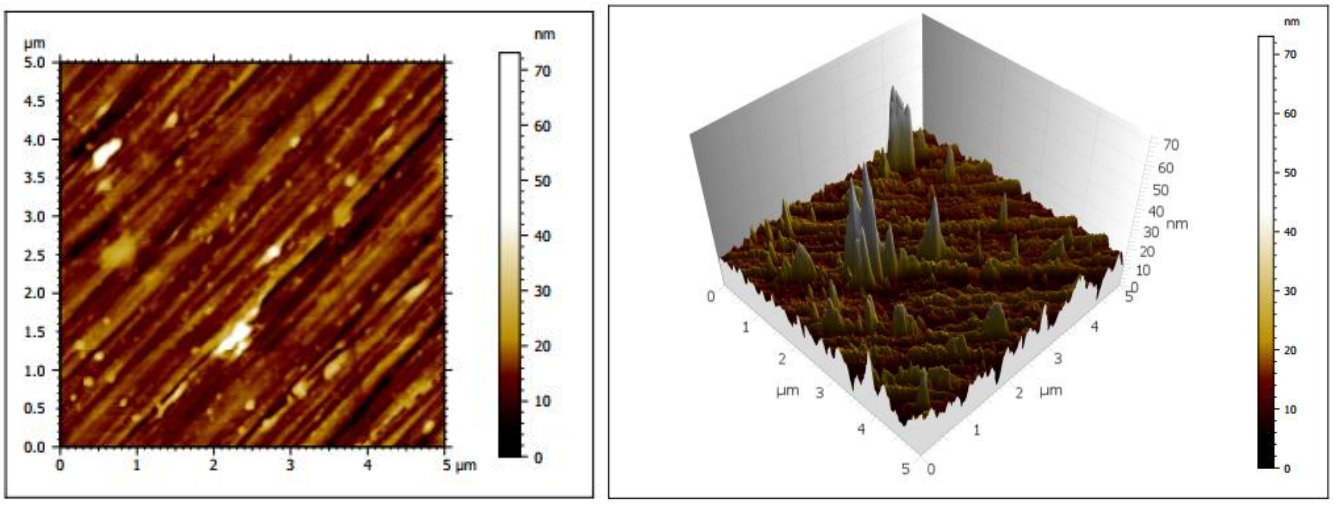

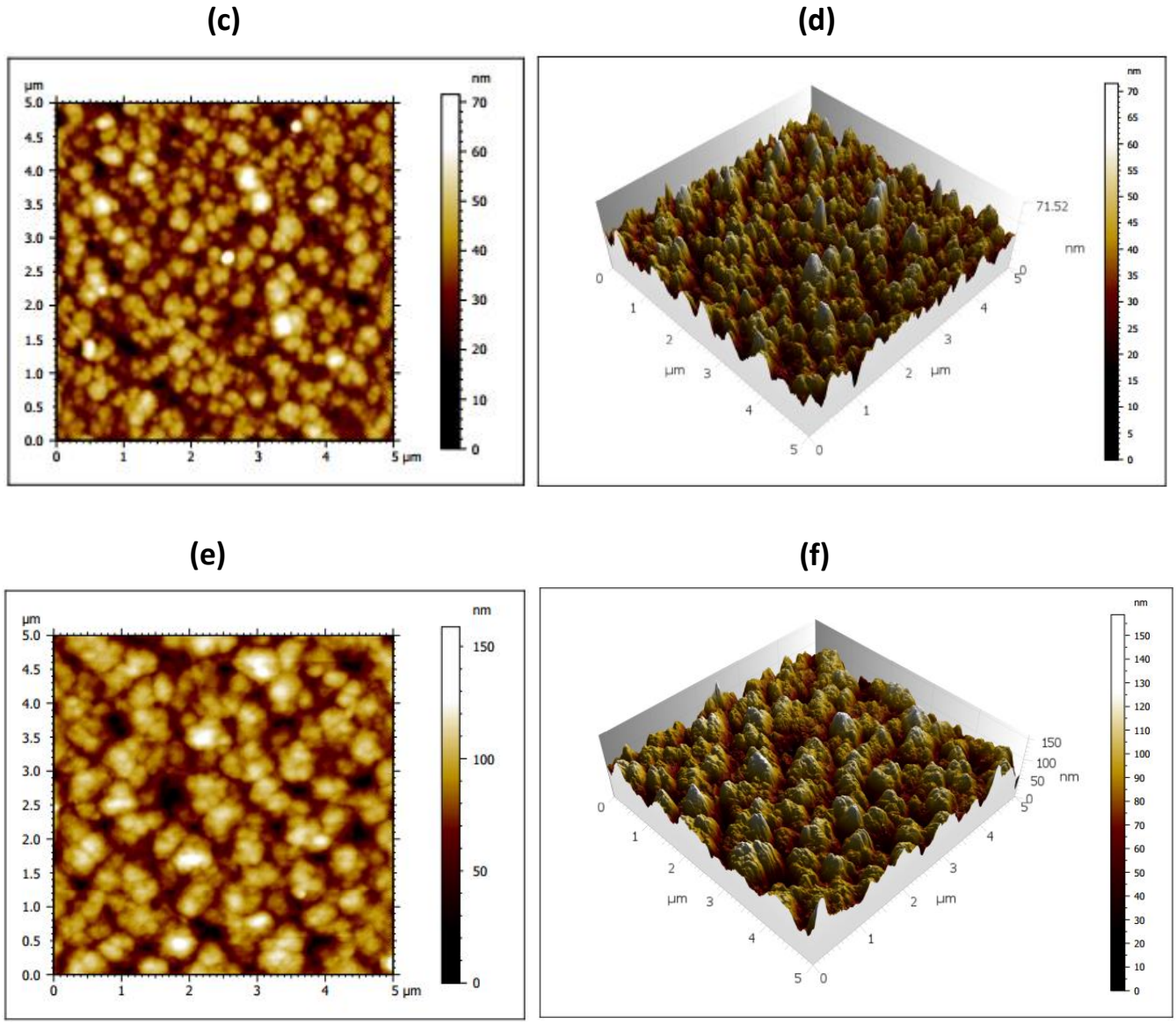

Figure 41: Atomic Force Microscopy images of (a-b) valve tappet (c-d) CrN/DLC (e-f) DLC-W.

5.5 Transmission Electron Microscope (TEM)

A thin layer of platinum was deposited on the coatings surface for protection during focused ion beam milling of the cross-sections. Figure 42a shows a TEM image of CrN/DLC coating obtained in STEM mode with a dark top layer of DLC (dark), grey CrN layer and a lighter grey Cr adhesion interlayer. The CrN layer, which has a dense columnar structure, shows a rough cauliflower morphology on the top. The interfacial region is made up of a high-atomic-density Cr interlayer, giving allowance for excellent adhesion of the chromium nitride layer to the steel substrate. On the other hand, the interphase initially has a higher contrast, composed of a higher mass corresponding to the metallic chromium interlayer deposited before the chromium nitride layer deposition. Here is where the amorphous layer with the columnar structure must have been nucleated. According to Bewilogua; Hofmann, (2014) and Cavaleiro; Hosson, (2006), the CrN coating structure is constituted by a body-centered cubic chromium columnar interlayer (BEWILOGUA; HOFMANN, 2014; CAVALEIRO; HOSSON, 2006). The EDS and EELS results of the CrN/DLC coating (across the red line) is presented in Figure 42b and 42c, respectively, which displays the elements present in the CrN/DLC coating such as C, N, Cr, O, while Fe and other elements are from the substrate. One can see the variation of Fe, Cr, and N across the deposited layers. The adhesion Cr interlayer extends for approximately 200 to 350 nm. After that the columnar CrN layer extends for additional 750 nm. The outermost DLC layer shows a very low concentration of Cr, Fe and N and a very high C concentration.

Figure 43a shows the TEM image of DLC-W obtained in STEM mode with a single type multilayer, which has a columnar structure. The DLC-W multilayers with an

approximate periodicity of 14 to 16 nm consist of light layers (richer in W) and darker layers (richer in C). The DLC-W structure also grew as columnar grains; however, it was possible to observe the formation of a multilayer structure of nanometric thickness with a periodicity of 14 to 16 nm. The multilayer may consist of an amorphous matrix with WC nanoclusters of crystalline particles embedded, which is approximately 2 nm in the WC lamellae and are equally distributed within the multilayer, similar to that described by Cavaleiro; Hosson, (2006). The image obtained in STEM HAADF mode presents layers of lighter tone (atoms with higher atomic number), interspersed with layers of darker tone formed by atoms of lower atomic number. Therefore, the coating structure seems to be formed by regions richer in W and poorer in W, giving rise to the multilayer structure obtained in the hybrid rotary table PVD/PECVD deposition reactor. The deposition process is similar to that described by Czyniewski et al. (2011). Cavaleiro; Hosson, (2006) mentioned that the coatings are primarily amorphous, but containing crystalline particles grouped as clusters of cubic β-WC1-*x* phase in the WC lamellae (BEWILOGUA; HOFMANN, 2014; CAVALEIRO; HOSSON, 2006). The EDS and EELS results of the DLC-W coating (across the red line) is presented in Figure 43b and 43c, respectively, which displays the elements present in the DLC-W coating such as C, W and O. During the deposition process, tungsten is deposited in the sub-layers when the rotating substrate passes close to the tungsten carbide target; at this stage, the PVD process is dominant. As the substrate rotates away from the tungsten carbide target the PECVD process becomes dominant, allowing for the deposition of an amorphous carbon due to the proximity of the acetylene gas. This is responsible for the compositional fluctuation

which is observed from the EDS and EELS analysis, which occurs at approximately 14 to 16 nm.

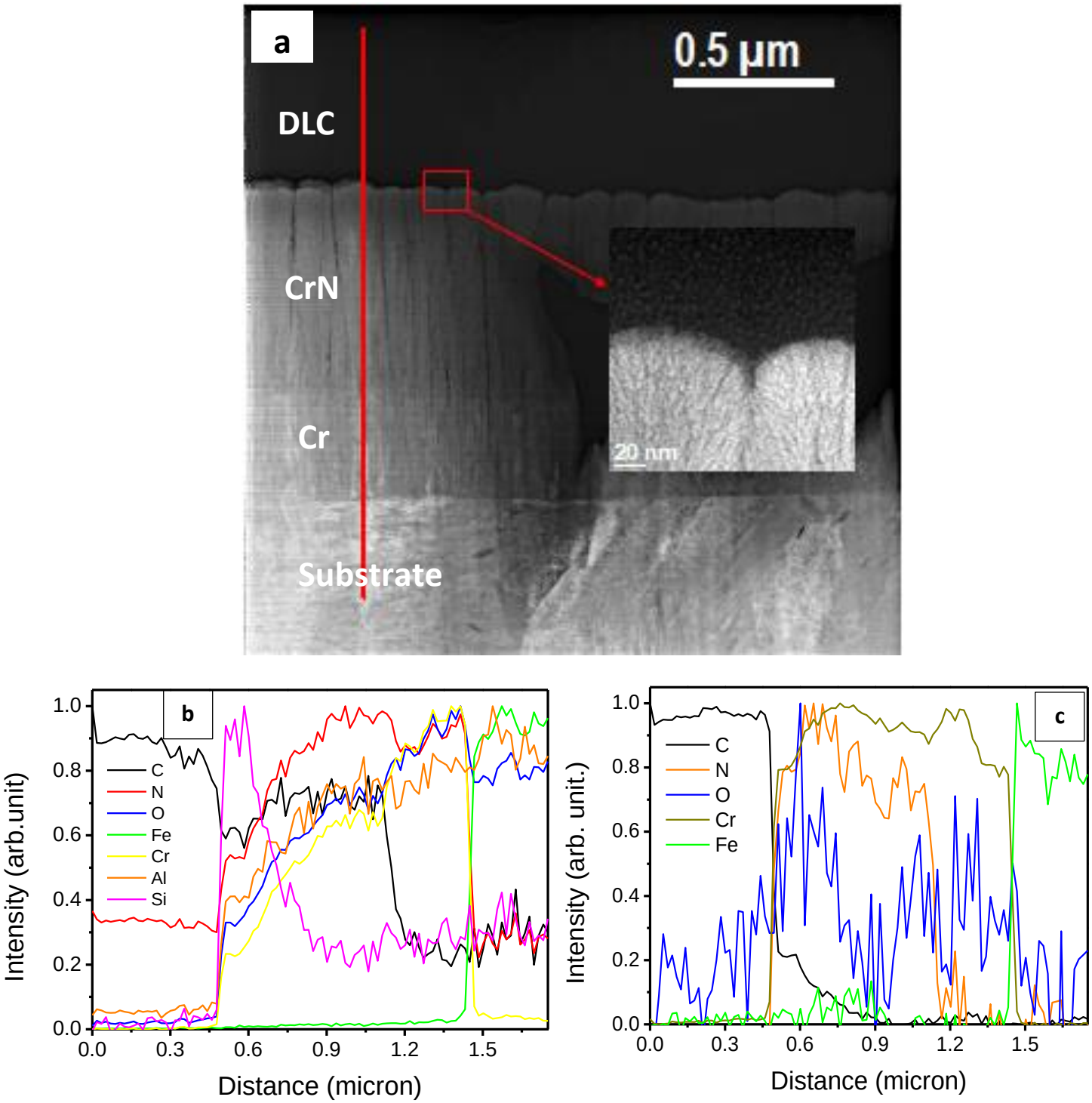

Figure 42: Cross section of CrN/DLC (a) TEM image (b) EDS analysis (c) EELS analysis.

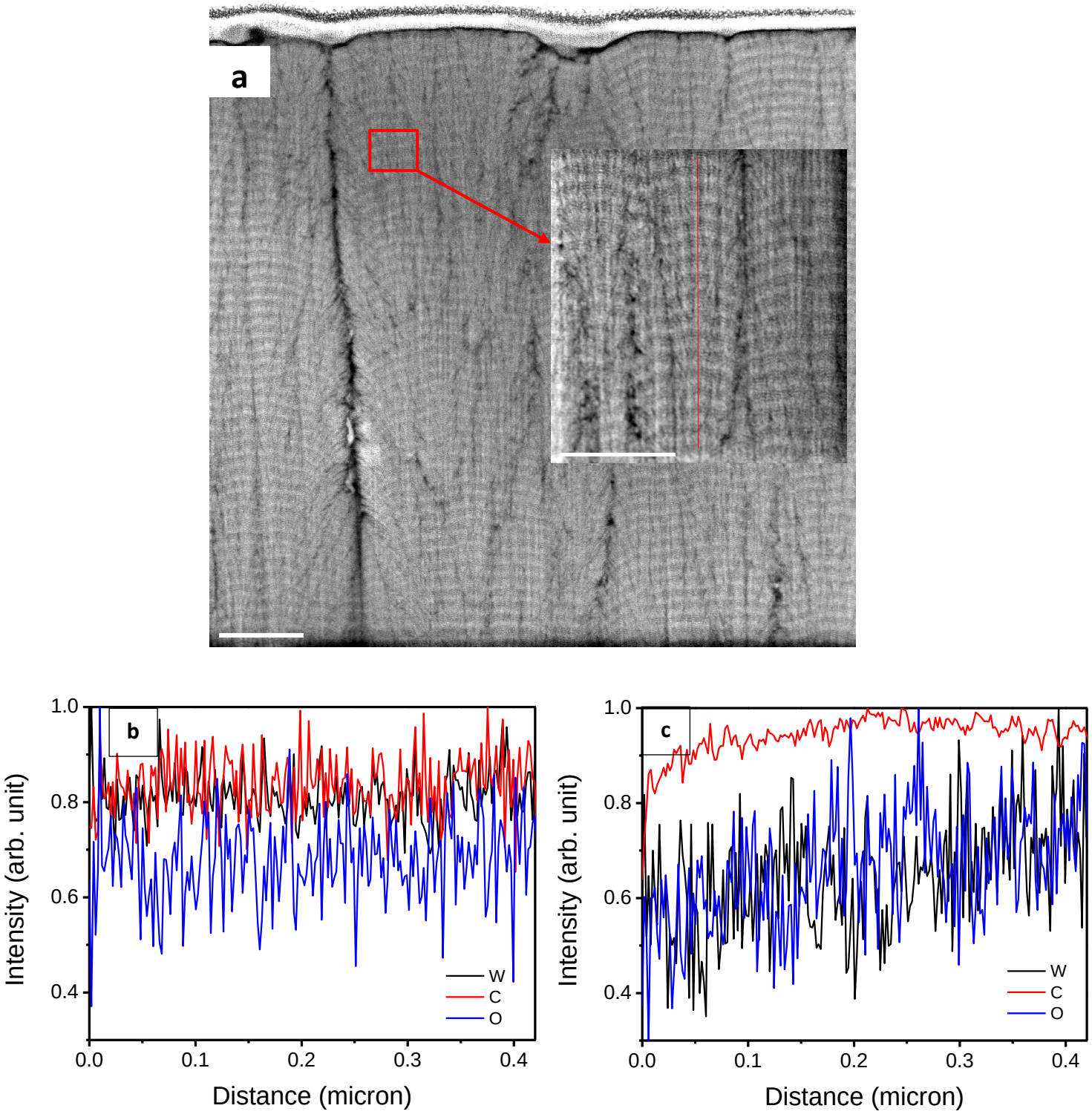

Figure 43: Cross section of DLC-W (a) TEM image (b) EDS analysis (c) EELS analysis.

Figure 44 shows the selected area electron diffraction (SAED) patterns of the DLC-W coating for dark and light sublayers of STEM image. The brighter layers (richer in W) are more crystalline than, the darker layers (poorer in W), as revealed in the SAED images. It is almost impossible to get the Miller indexes since the planes' distances are close. The sample is practically amorphous, and the diffraction error can be higher than 5% without a standard sample as a reference. Therefore, the multilayer DLC-W coatings can be described as WC nano-crystallite embedded in amorphous carbon matrix. The coherency strain and moduli-mismatch of the soft-hard layers or the presence of a low amount of cross-linked bonds at the interface between the WC_{1-x} and amorphous carbon layer are possible reasons for the reduction in the internal stress in the DLC-W (PU; HE; WANG, 2015).

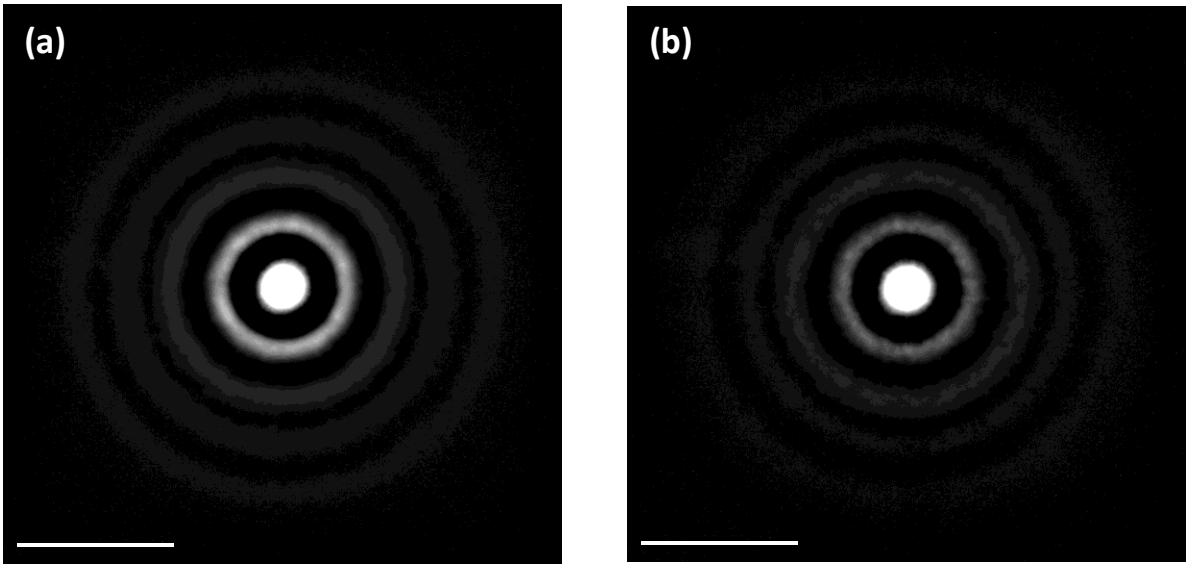

Figure 44: Selected Area Electron Diffraction (SAED) (a) dark sub-layer (b) bright sub-layer.

5.6 Mechanical Properties of Substrate, CrN/DLC and DLC-W coating

5.6.1 Nano-indentation

The nanoindentation technique was used to measure the mechanical properties of the uncoated, CrN/DLC and DLC-W coated valve tappets. Oliver & Pharr (OLIVER; PHARR, 1992; FISCHER-CRIPPS, 2000) evaluation of the indentation curve was used to extract the hardness and reduced elastic modulus (force and displacement) summarized in Table 9. The hardness for CrN/DLC and DLC-W were measured as 18.85 ± 0.42 GPa and 9.88 ± 1.76 GPa, respectively. While, the Young modulus for CrN/DLC and DLC-W were measured as 154.93 ± 3.21 GPa and 101.94 ± 8.13 GPa, respectively. A high variation in the hardness and elastic modulus of the DLC-W was observed, possibly due to the compositional difference between the W rich layer and W poor layer. Figure 45, presents load-displacement curves at a maximum indentation load of 10,000 µN for the coatings based on the thickness to avoid the effect of approximation to the substrate. The loading and unloading curves indicate a shift to the right of the load-displacement nanoindentation curve and an increase in the maximum depth due to the presence of tungsten, which is responsible for the decrease in hardness and reduced elastic modulus of DLC-W, which has also been reported by other authors (KRŽAN; NOVOTNY-FARKAS; VIŽINTIN, 2009; BAI et al., 2021; TAKENO et al., 2009; BEAKE et al., 2015). The DLC-W curve reveals higher hysteresis between loading-unloading curves compared to the CrN/DLC, which is as a result of higher plastic deformation (larger penetration depth) caused by reduction in hardness of the DLC-W coating (KRŽAN; NOVOTNY-FARKAS; VIŽINTIN, 2009; BAI et al., 2021; TAKENO et al., 2009; BEAKE et

al., 2015; SHAHSAVARI et al., 2016). The uncoated valve tappet showed more plastic deformation than both coatings.

The improvement in mechanical properties of CrN/DLC compared to DLC-W relates to the presence of higher sp^3 content in CrN/DLC (BEAKE et al., 2015). The H/E or H^3/E^2 ratio (plasticity index) are very important parameters which correlate with the wear resistance and is related to the plastic deformation resistance of the coatings as shown in Table 9. The elastic properties are controlled by the amount of sp^3 carbon bonding present, because of its high directional σ bond sum to the short-range ordering of sp^2, while the sp^2 clusters are joined as chains or rings with delocalized π bonds (MÜLLER et al., 2017; KONCA et al., 2006). The hardness and elastic modulus indicate that the wear behavior and adhesion strength of CrN/DLC coatings may perform better than DLC-W coatings. It can be confirmed that the lowest ratio H/E for DLC-W showed higher plastic deformation, as seen in Table 9. Increase in the H/E ratio reduces the plasticity, because the failure mechanism of thin coatings begins with plastic deformation, as confirmed in literature (SHAHSAVARI et al., 2016; CAO et al., 2021).

The elastic recovery was calculated for the different surfaces using equation 18, which reveals that CrN/DLC coatings had the higher recovery, followed by DLC-W coating and, lastly, the uncoated valve tappet; this is strongly in agreement with the plastic deformation of the uncoated, CrN/DLC and DLC-W coated valve tappet surfaces. The multilayer structure of DLC-W, which is an alternating hard and soft layer can accommodate the load by shearing in the soft layer, which significantly reduces the stress concentration at the coating–substrate interface. On the other hand, the multilayer DLC-W reduces hardness, lowers the residual stress, lowers the COF and improves the

adhesion to the metallic substrate. The addition of tungsten changes the bonding, due to the new C-W and C-C bonds (MÜLLER et al., 2017; KONCA et al., 2006), which in turns affects the mechanical properties as confirmed from the nanoindentation results. The architecture and properties (tungsten content and thickness of sub-layers) can be controlled by the deposition system geometry, substrate rotation speed and flow of carbon carrying reactive gas (CZYZNIEWSKI et al., 2011).

Cao et al. (2021) reported an increase in hardness when tungsten was added to DLC from 14.4 ± 1.6 GPa to 17.3 ± 1.9 GPa and increase elastic modulus from 168.3 ± 10.3GPa, but increase to 195.4 ± 13.4 GPa when 0.9 at %W was added to DLC coating (CAO et al. 2021). However, decreased as the W content increased in the DLC, furthermore, there was a decrease in hardness to 9.6 ± 1.4 GPa and 6.5 ± 0.8 GPa when 3.1 at% W and 15.1at%W was added to DLC coatings, respectively. The elastic modulus also decreased to a low value of 101.4 ± 5.9 GPa when the tungsten addition was increased to 15.1 at.% [149]. In the case of Pu et al., pure DLC coating had the highest hardness and elastic modulus, which gradually decreased as the W content increased from 1.54 at.% to 7.39 at. % [149]. Bai et. al. reported a decrease in hardness for DLC doped with W. This strongly implies that very low W content addition in DLC can increase the hardness and elastic modulus and decreases when the W content decreases in the DLC due to the breaking of C-C bonds when W-C bonds are formed during the addition of W in DLC matrix.

Table 9: Hardness and Reduced elastic modulus.

Surface	Hardness (GPa)	Reduced elastic modulus (GPa)	h_c(nm)	H/E ratio	H^3/E^2 ratio (GPa)	Elastic recovery (%)
Substrate	11.04 ± 1.91	199.79 ± 4.31	164.99 ± 3.32	0.055 ± 0.003	0.034 ± 0.004	31.65
CrN/DLC	18.85 ± 0.42	154.93 ± 3.21	121.30 ± 9.18	0.122 ± 0.001	0.279 ± 0.001	71.04
DLC-W	9.88 ± 1.76	101.94 ± 8.13	183.15 ± 9.13	0.097 ± 0.005	0.093 ± 0.002	67.12

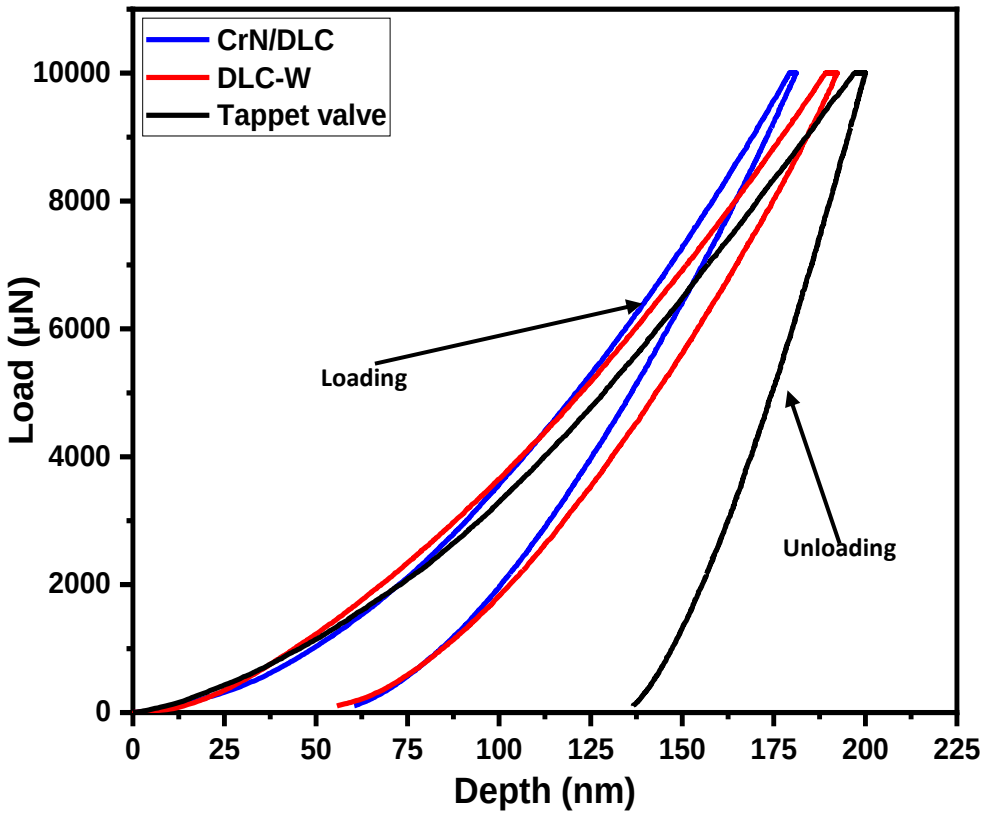

Figure 45: Load-displacement curve for nano-indentation of the uncoated, CrN/DLC and DLC-W coated valve tappet.

5.6.2 Nano-scratch

The nano-scratch tests were performed on the coated samples to characterize their tribological behavior and investigate the adhesion of CrN/DLC and DLC-W coating to the valve tappet substrates at the nano-scale. The nano-scratch tests were performed at a ramping load of 300 mN for each coating. Figure 46(a-b) shows the plot of coefficient of friction against scratch distance which corresponds to the tip penetration profile during testing, the variation in the COF observed in the coatings could be due to the substrate effect during penetration of the indentation tip caused by the difference between the substrate and the CrN/DLC and DLC-W. From the nano-scratch results it was observed that the depth linearly increased as the scratch distance increased. There was no significant change in the curve for the CrN/DLC, which implies that there was no Lc_1 and Lc_2, and no coating peeled off during the nano-scratch. The COF increased steadily from 0.002 to 0.13 for CrN/DLC, while for DLC-W, there was a steady increase in the COF from 0.004 to 0.15, Lc_1 was 98mN, and no region of delamination was observed. Figure 47(a-b) shows the optical images of the scratch track obtained from the CrN/DLC and DLC-W coatings. According to Zhang; Huan, (2005) the scratch depth increases linearly as a function of the ramping, which increases as the load and scratch distance increases (ZHANG; HUAN, 2005). Figures 48(a-b) and 47(c-d) show the SEM image of the nano-scratch of CrN/DLC and DLC-W coatings, respectively.

The OM images revealed no region of crack or delamination for CrN/DLC as seen in Figure 47a; on the other hand, DLC-W revealed a region of tiny cracks encircled red, as seen in Figure 47b. The SEM images revealed the part of the nanoscratch track for CrN/DLC and DLC-W, which revealed the nanoscratch pattern for CrN/DLC and DLC-W.

The displacement between the coatings grains was narrower for the CrN/DLC coating compared to the DLC-W, which could be attributed to the higher hardness, denser and smaller grain columnar structure of the CrN/DLC, while the DLC-W coatings had a wider displacement which is mainly due to lower highness, less dense and larger grain structure of DLC-W.

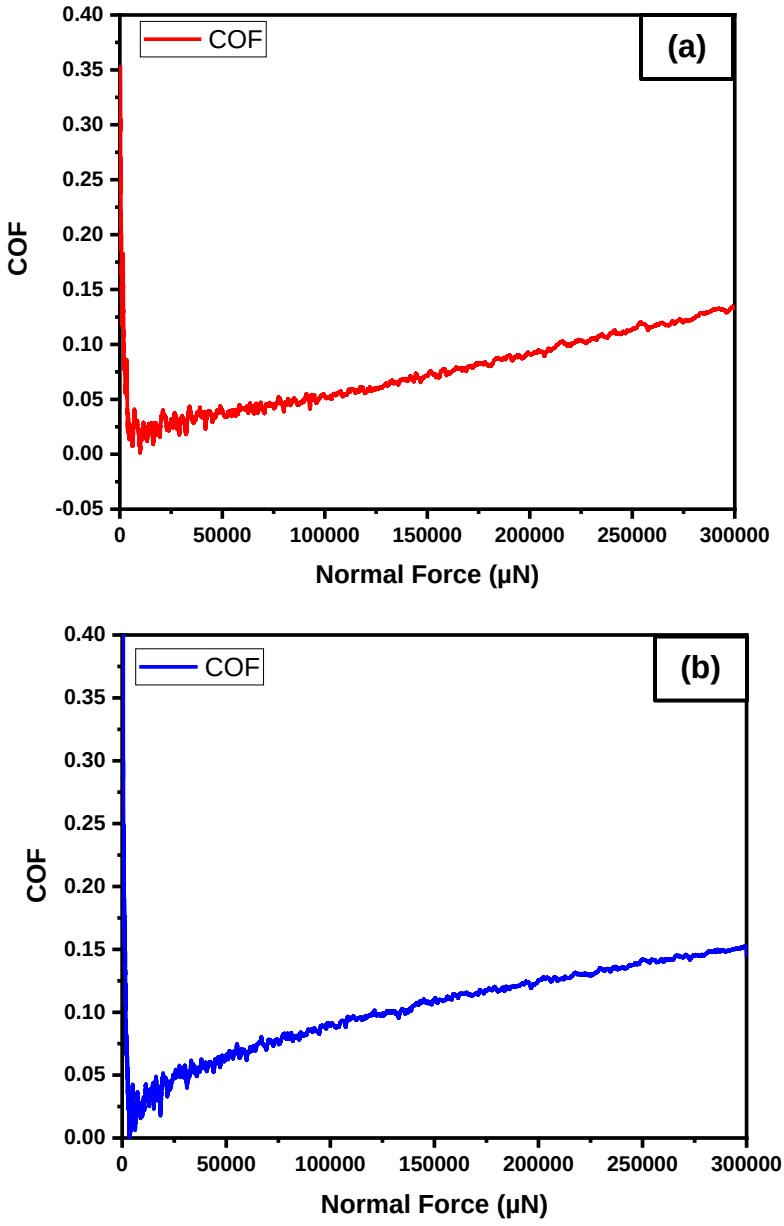

Figure 46: Coefficient of friction against normal load (a) CrN/DLC and (b) DLC-W.

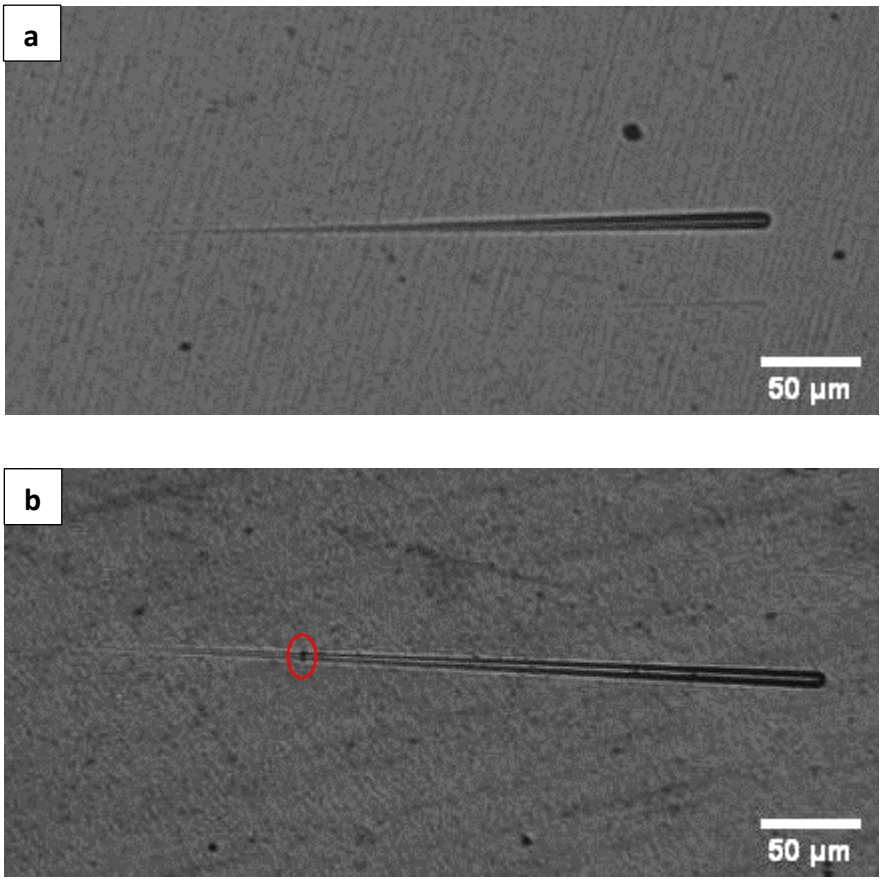

Figure 47: Optical image of a nano-scratch track (a) CrN/DLC and (b) DLC-W.

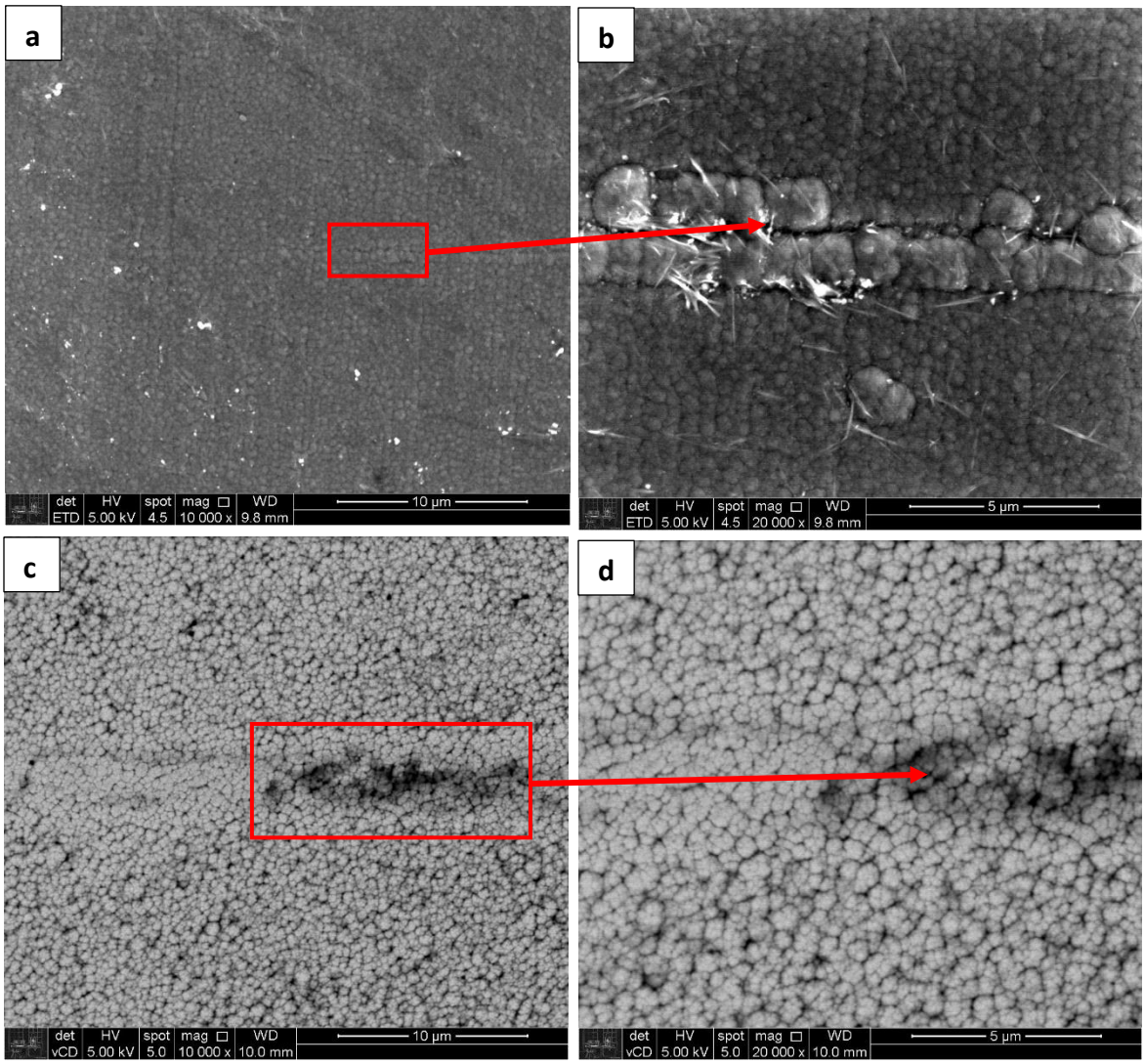

Figure 48: SEM image of a nano-scratch track (a, b) CrN/DLC and (c, d) DLC-W.

Figures 49 and 50 show the AFM 2D images, 3D longitudinal cross-sections, and depth profiles of the nano-scratches made at 300 mN for CrN/DLC and DLC-W, respectively. The depth and height profile were obtained from the data for each nano-scratch part (start, middle, and end) which are summarized in Table 10. It can be observed from the results obtained that the depth and height of the nano-scratch increase as the scratch distance increases for both coatings. Additionally, a significant increase in scratch depth and height was observed for the DLC-W compared to CrN/DLC, mainly due to the lower hardness of the DLC-W coating.

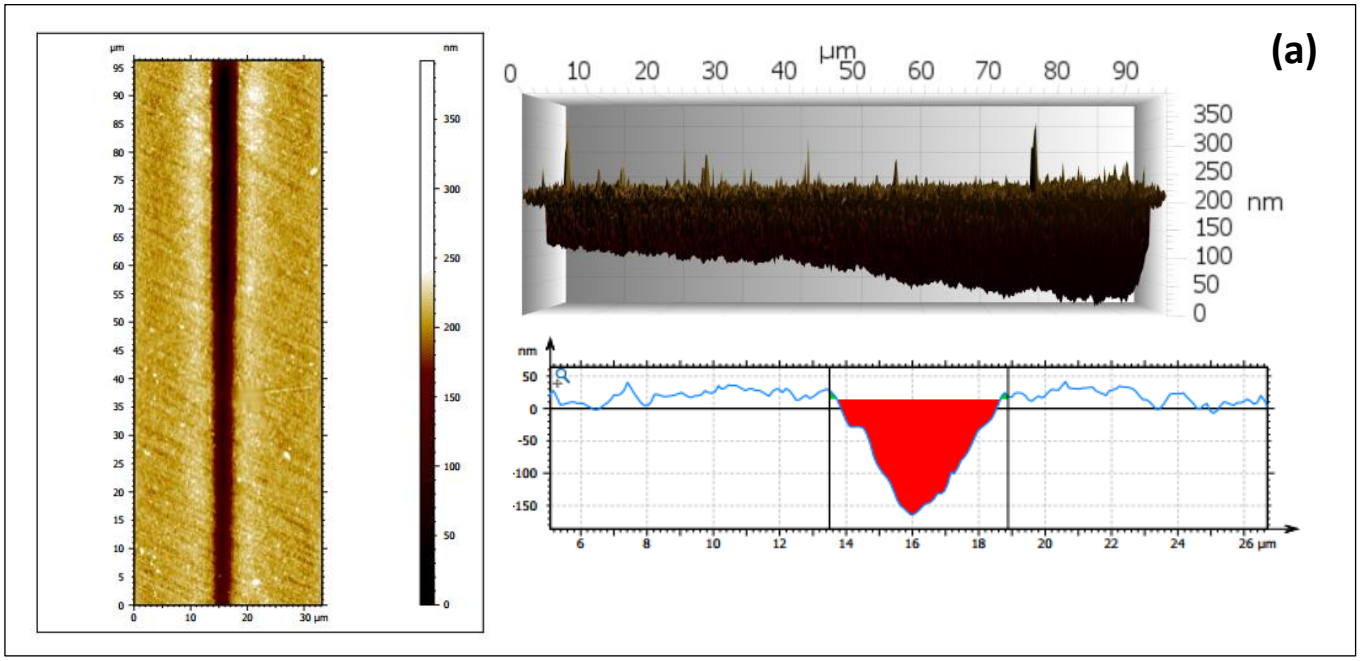

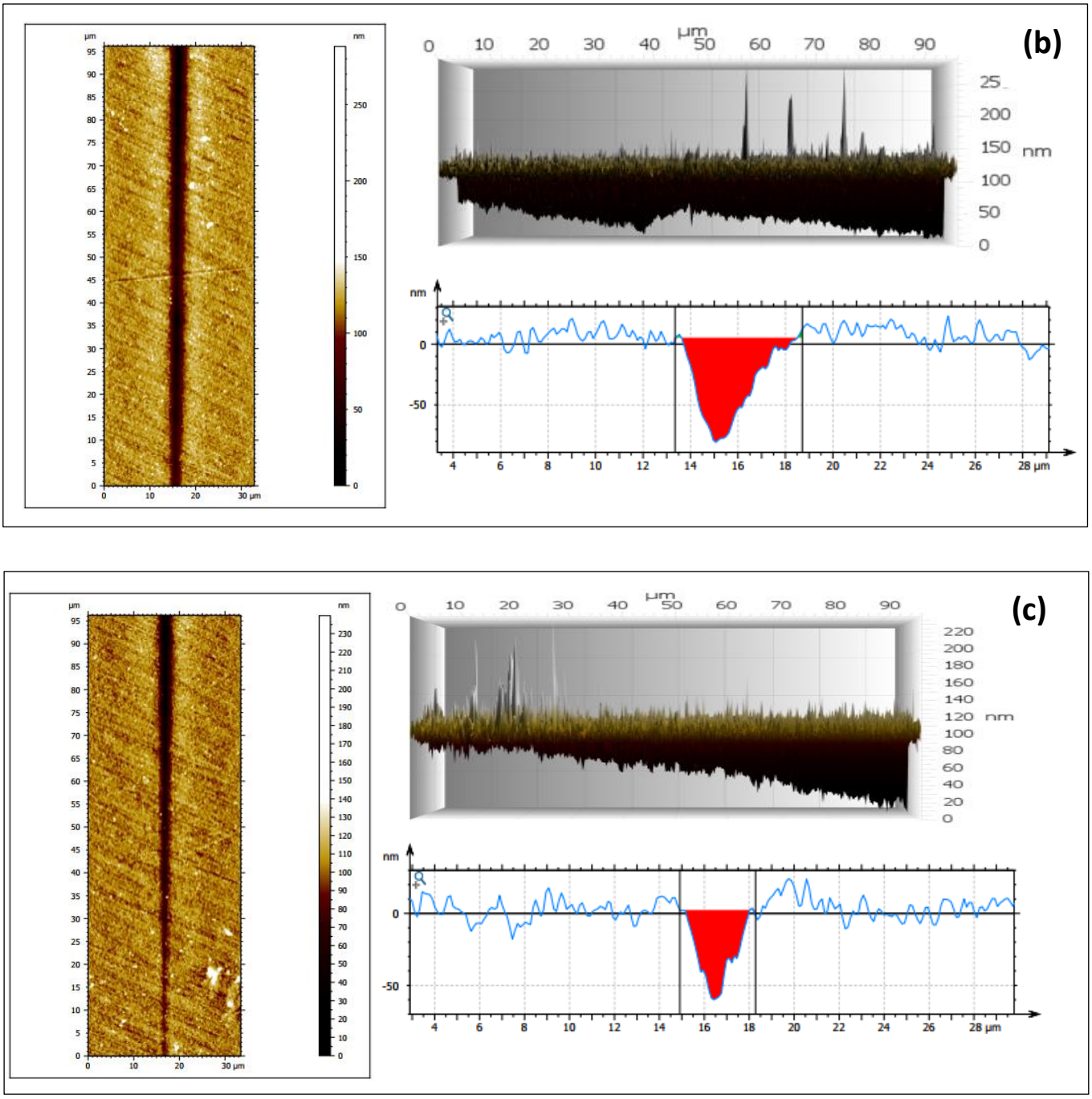

Figure 49: AFM for nano-scratch of CrN/DLC (a) end (b) middle (c) start.

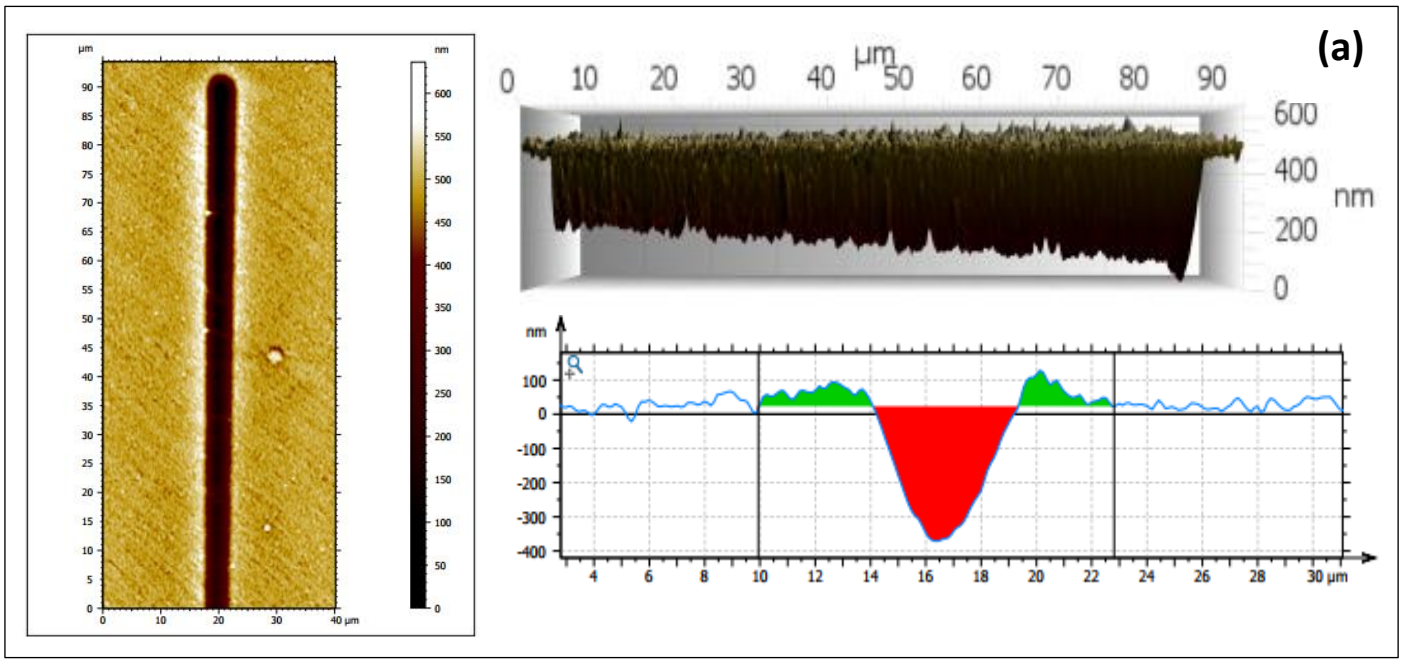
(a)
µm
nm
0 10 20 30 40 50 60 70 80 90
600
400
200
0
100
0
-100
-200
-300
-400
4 6 8 10 12 14 16 18 20 22 24 26 28 30 µm

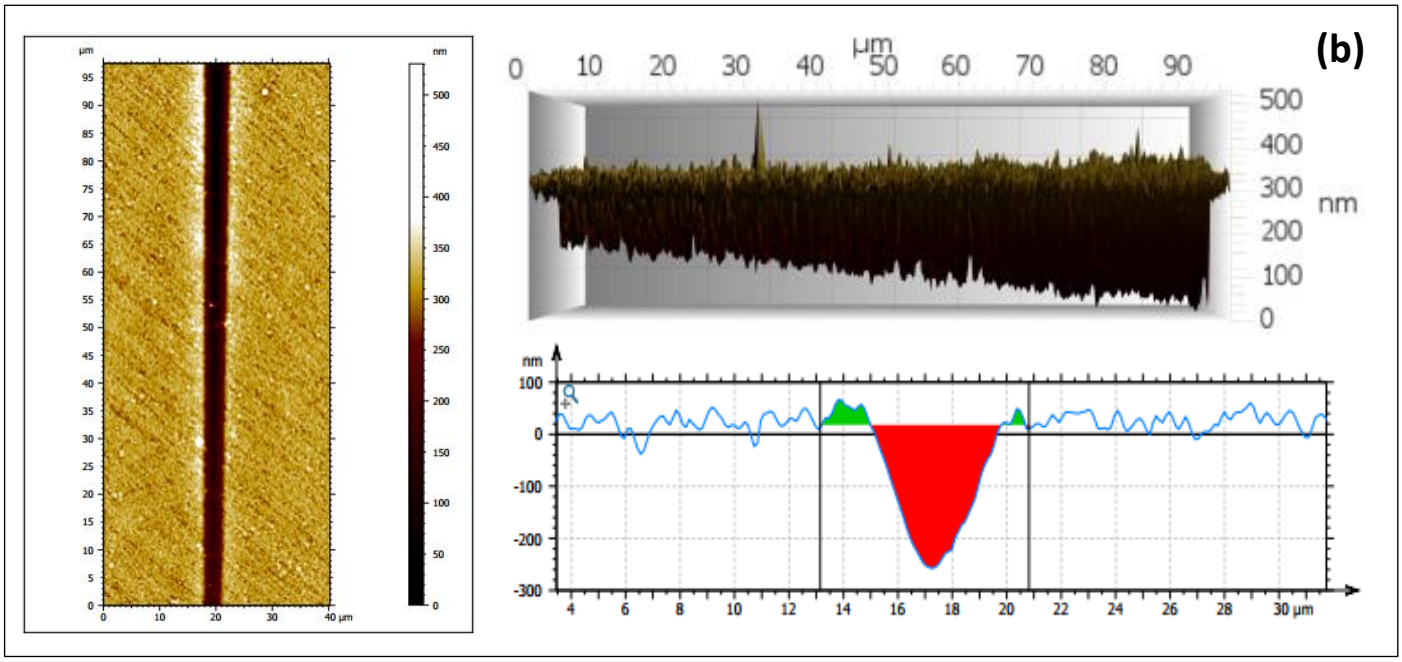
(b)
µm
nm
0 10 20 30 40 50 60 70 80 90
500
400
300
200
100
0
100
0
-100
-200
-300
4 6 8 10 12 14 16 18 20 22 24 26 28 30 µm

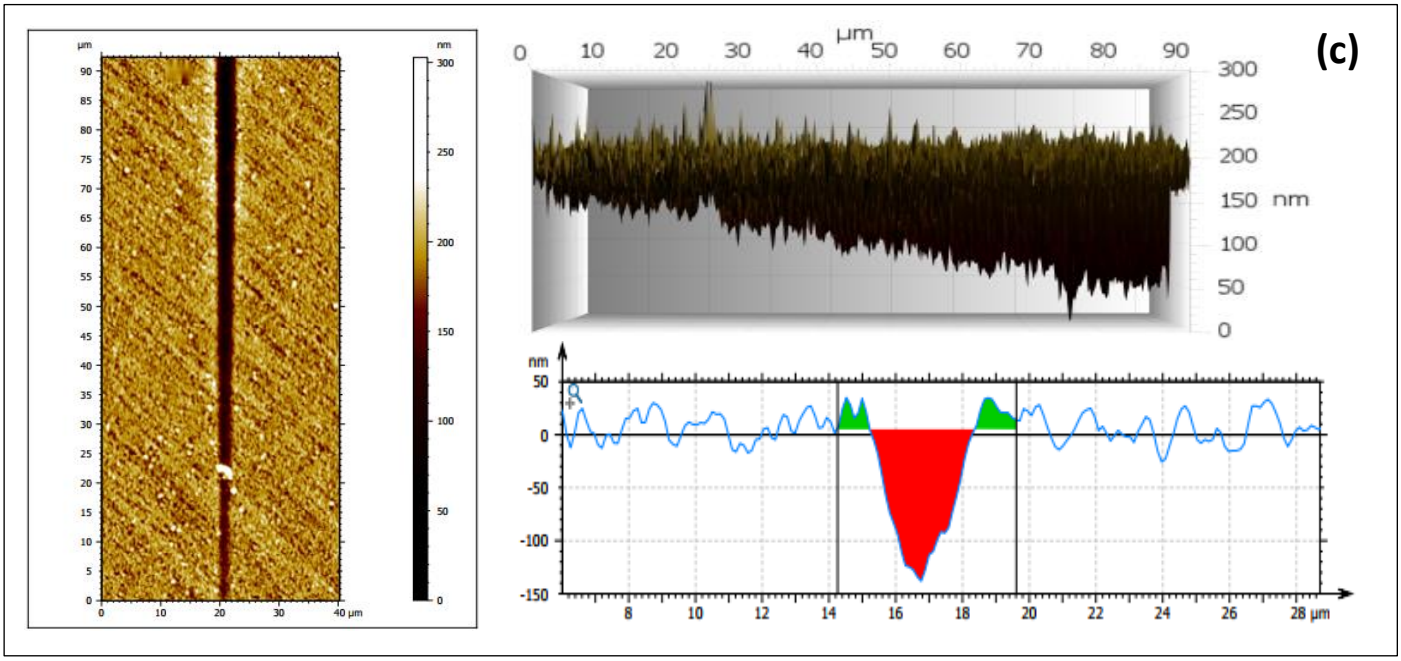

Figure 50: AFM for nano-scratch of DLC-W (a) end (b) middle (c) start.

Table 10: Nano-scratch depth and height variation at different positions of the scratch track.

Sample/Position	Max. depth (nm)	Max. height (nm)	Coating Thickness (µm)
CrN/DLC - Start	63.18	0.62	
CrN/DLC - Middle	87.13	5.44	2.95
CrN/DLC - End	180.30	11.79	
DLC-W - Start	144.70	28.39	
DLC-W - Middle	278.60	46.12	6.58
DLC-W - End	399.00	100.80	

5.7 Adhesion of CrN/DLC and DLC-W coatings

The adhesion properties of the CrN/DLC and DLC-W coatings were assessed by macro-scratch test using CETR-UMT Multi-Specimen test system equipment and observed under optical microscopy (OM). Figures (51-53) presents the plot of COF against applied load. Figures (54-56) displaying OM micrographs obtained for the starting, middle and ending points of the scratch track show the critical loads and different failure modes. The critical loads (Lc_1 and Lc_2) were determined by comparing the curves of friction coefficient and applied load against the scratch length. Lc_1 represents the load at which the first tiny cracks appear on the coating surface and Lc_2, the load at which the first delamination occurs on the coating, which is usually caused by buckling or wedging failure modes (HEDENQVIST; HOGMARK, 1997).

The adhesion strength of the DLC coating to the valve tappet plays an important role in evaluating the service life, the critical loads which are summarized in Table 11. The COF range was 0.061 to 0.133 for the valve tappet, COF range was 0.045 to 0.11 for CrN/DLC, COF range was 0.049 to 0.12. Both CrN/DLC and DLC-W coating show excellent adhesion to the valve tappet substrate due to the presence of Cr and WC interlayers, respectively. Cao et al. (2021) reported that the critical load depends mainly on the content of W addition to DLC. In their work they measured the L_{C2} valve as 33N for DLC, and increased to 42 N for 0.94 at.%W addition of W, however reduced to 19 N and 14 N for 3.1at%W and 13.1at%W addition to DLC coating, respectively. This trend is consistent with other results published in the literature (WANG et al., 2006; CAO et al., 2020; IRMER; DORNER-REISEL, 2005).

Table 11: Critical load for CrN/DLC and DLC-W coatings

Critical load (N)	CrN/DLC	DLC-W
Lc_1	6.51	7.29
Lc_2	37.9	32.1

Using the Bull, (1991) methods of determining cohesive and adhesive failure, the CrN/DLC and DLC-W coatings displayed an adhesive failure mode as seen from the morphologies of Lc_1 failure, and the values for both coatings were close. The failure type shown in Figures (57-58) is adhesive, followed by delamination caused by spallation, tiny cracks, buckling, and wedging failure modes (HEDENQVIST; HOGMARK, 1997; BULL, 1991; MALKOW; BULL, 2001; BURNETT; RICKERBY, 1987). It can also be noted that the DLC-W coatings show brittle failure mode towards the end of the scratch track.

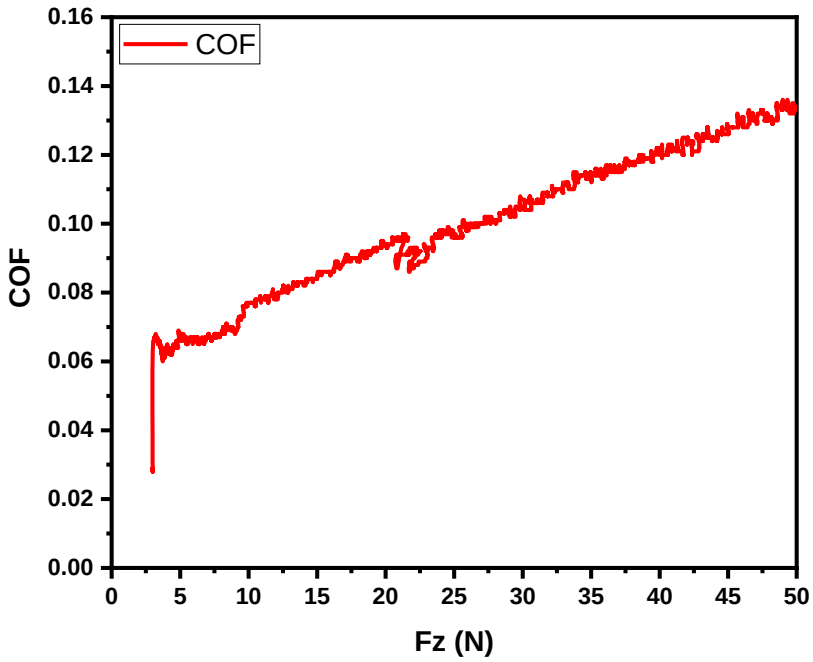

Figure 51: Plot of COF against applied load for valve tappet.

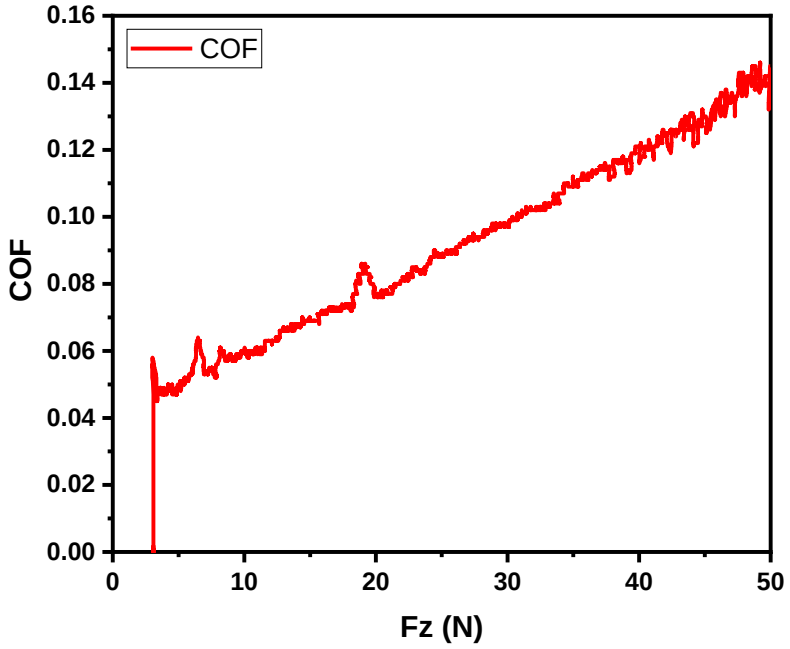

Figure 52: Plot of COF against applied load for CrN/DLC coatings.

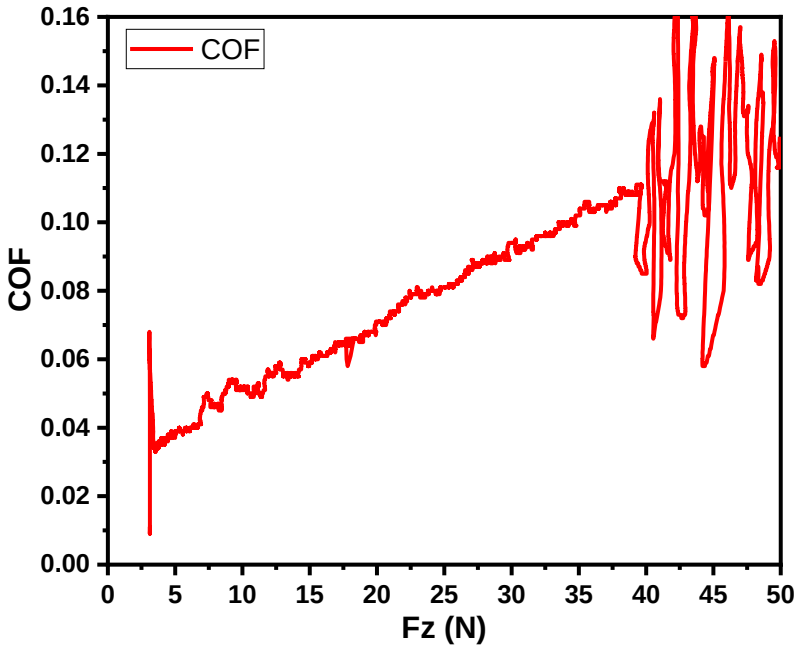

Figure 53: Plot of COF against applied load for DLC-W coatings.

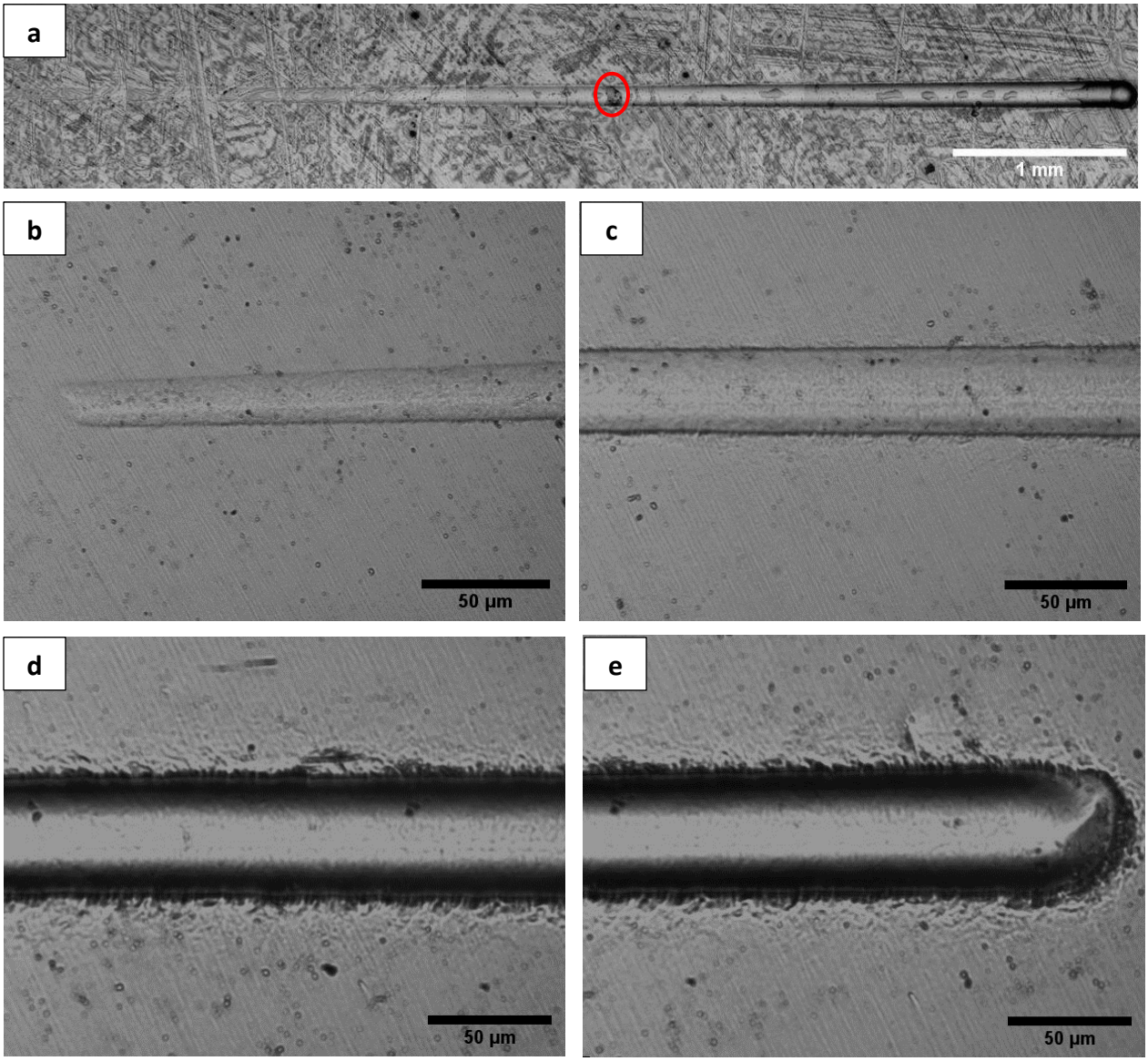

Figure 54: OM images of the scratch tracks for determining the critical loads for uncoated valve tappet (a) full scratch track (b) start of scratch track (c) middle of scratch track (d) middle of scratch towards the end (e) end of the scratch track.

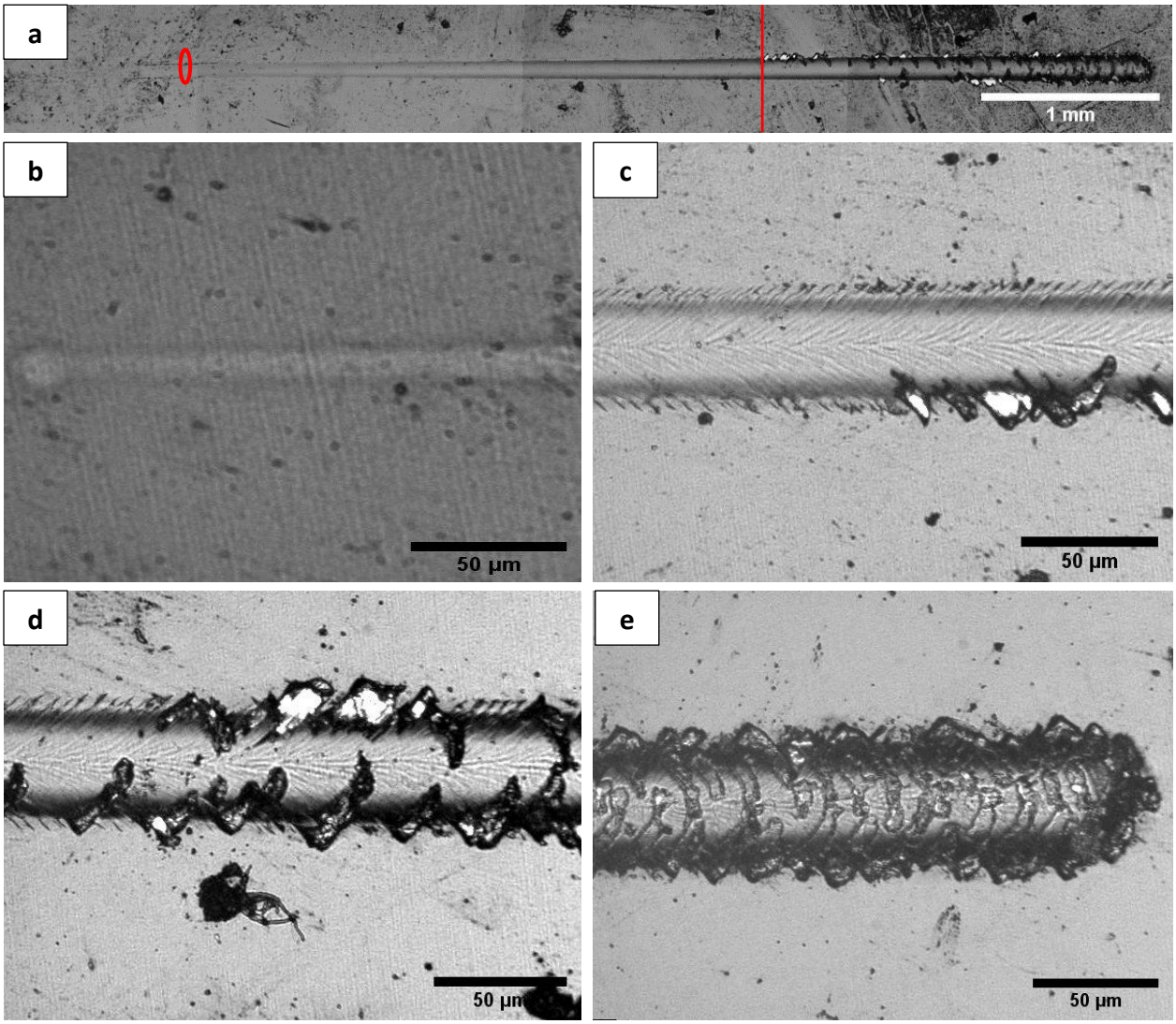

Figure 55: OM images of the scratch tracks for determining the critical loads for CrN/DLC coated valve tappet (a) full scratch track (b) start of scratch track (c) middle of scratch track (d) middle of scratch towards the end (e) end of the scratch track.

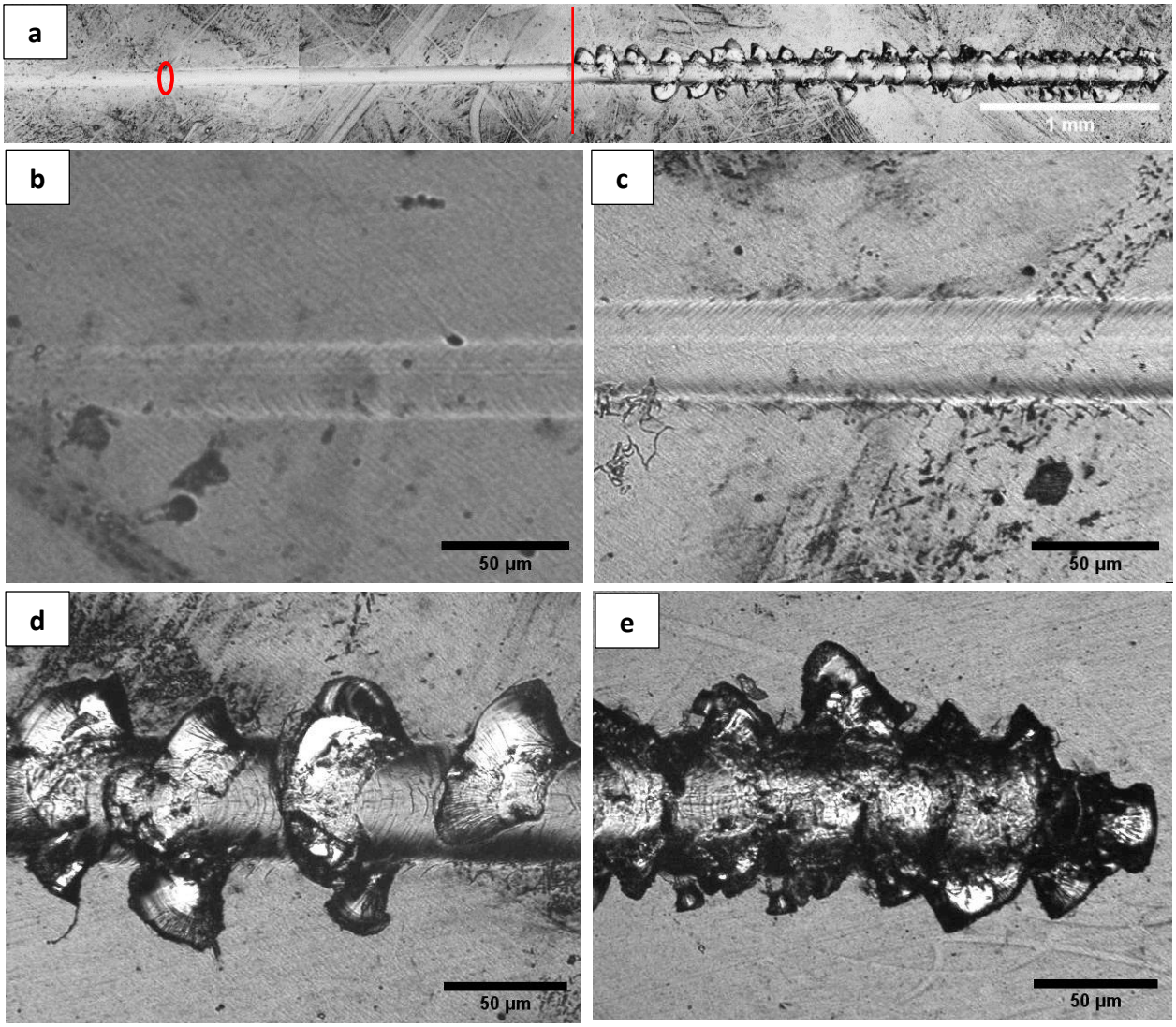

Figure 56: OM images of the scratch tracks for determining the critical loads for DLC-W coated valve tappet (a) full scratch track (b) start of scratch track (c) middle of scratch track (d) middle of scratch towards the end (e) end of the scratch track.

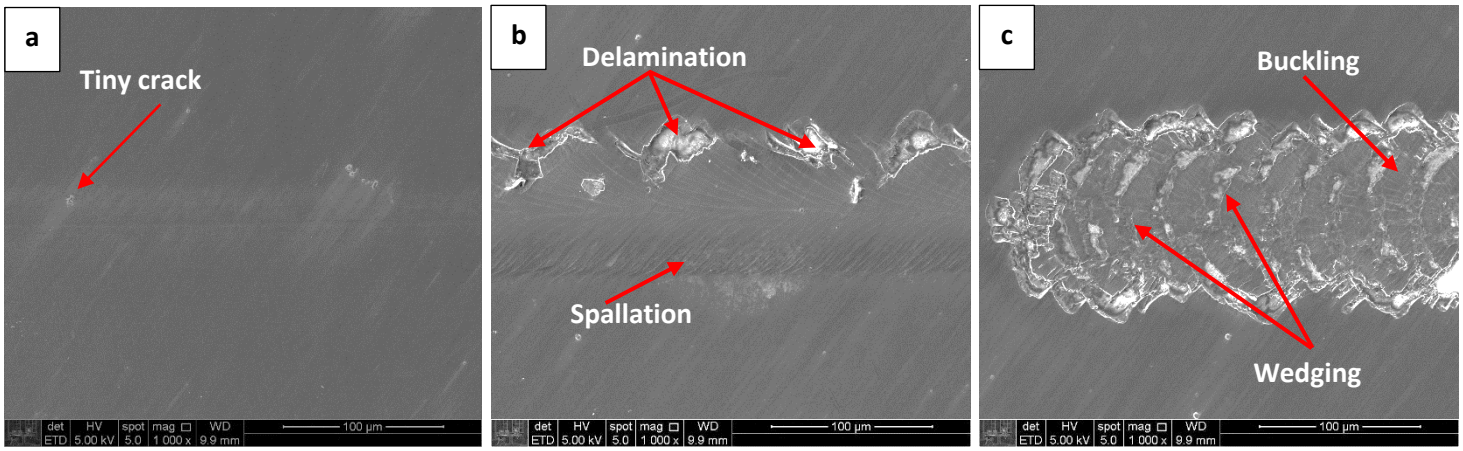

Figure 57: The SEM image of the different failure modes of the CrN/DLC coating.

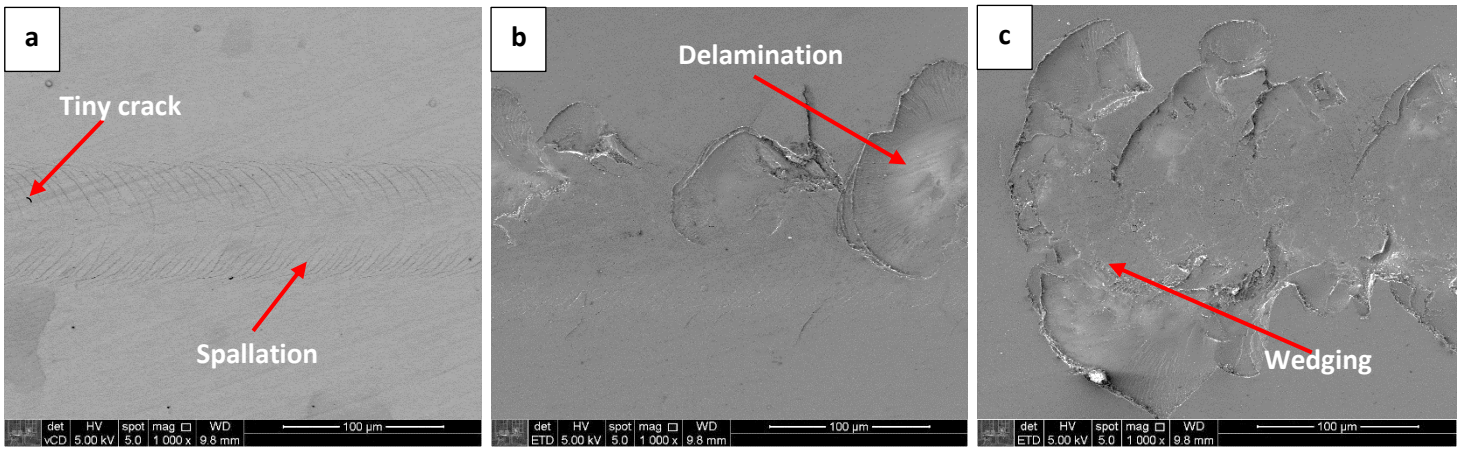

Figure 58: The SEM image of the different failure modes of the DLC-W coating.

The scratch hardness was measured using the standard ASTM G171-03. The average width of the scratch track was used to calculate the scratch hardness using equation 11 (LI, 2014). Figure 59 shows the plot of scratch hardness values for the uncoated valve tappet, CrN/DLC and DLC-W coating. The results show that the uncoated, CrN/DLC and DLC-W coated valve tappet decrease in hardness as the normal force increases along the scratch track which is as a result of local deformation. The CrN/DLC had the highest scratch hardness throughout the scratch test. This reveals that the CrN/DLC coating deforms lesser than DLC-W coating, which is consistent with the

hardness measurement obtained from nanoindentation measurements. The scratch hardness was accessed at every 1 mm of the scratch track, this result shows that as the load increases along the scratch track the scratch hardness reduces. The lower hardness of DLC-W coating is as a result of the addition of tungsten, which is expected.

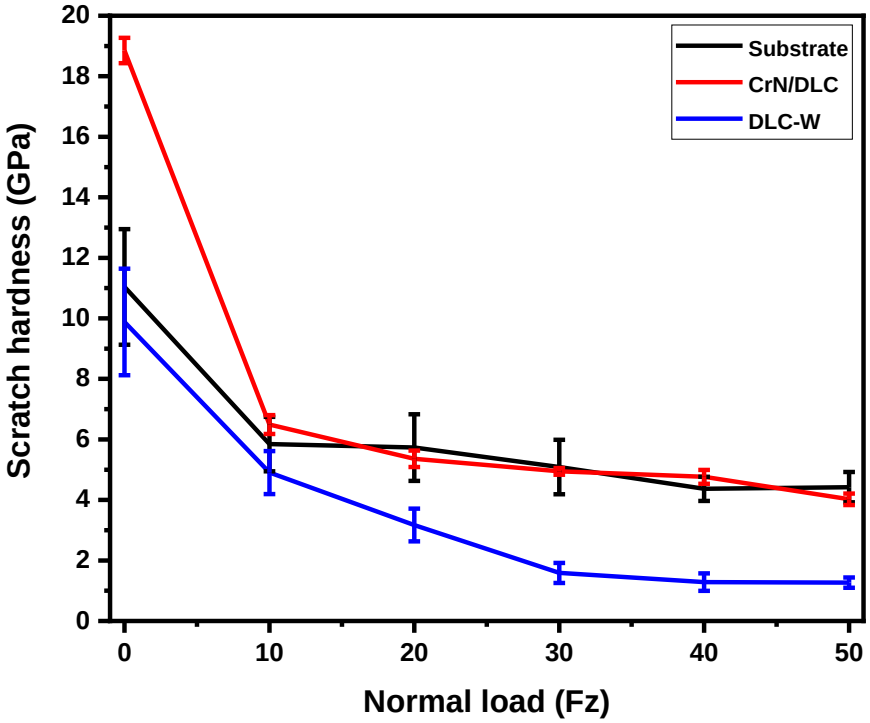

Figure 59: Plot of scratch hardness against normal load for valve tappet, CrN/DLC and DLC-W.

The 3D images, 2D transversal and longitudinal profiles of the scratch tracks for the uncoated, CrN/DLC and DLC-W coated valve tappet obtained using 3D profilometry are presented in Figures (60-62). Figure 61a, shows that the scratch track for the uncoated valve tappet had the smoothest track, the CrN/DLC coated valve tappet showed regions of spallation and mild delamination towards the end, while the DLC-W coated valve tappet showed regions of spallation and heavy delamination from mid-way of the scratch track on. The 2D transversal and longitudinal profiles showed that the DLC-W

had the widest and deepest scratch, which is strongly related to the hardness properties of the coatings. The scratch depth for the valve tappet, CrN/DLC and DLC-W coated valve tappet was 1.0 µm, 1.6 µm and 2.9 µm, indicating each surface's penetration depth. The results indicates that the indenter penetrated the CrN/DLC coating, reaching the substrate at about 4.4 mm (Figure 61c), while the indenter penetrated DLC-W coating, reaching the substrate at about 3.4 mm (Figure 62c).

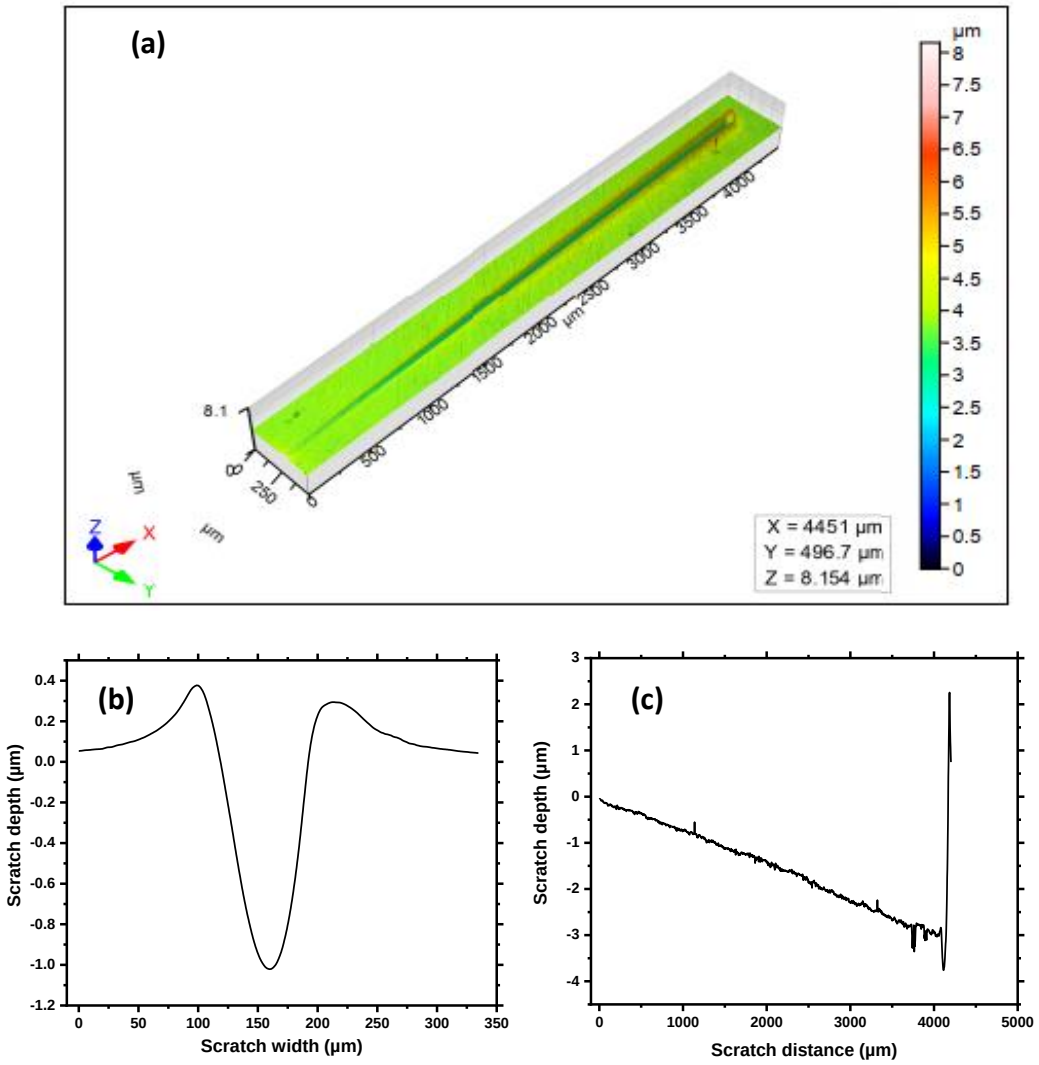

Figure 60: Scratch track of valve tappet (a) 3D image (b) plot of transversal profile (c) plot of longitudinal profile.

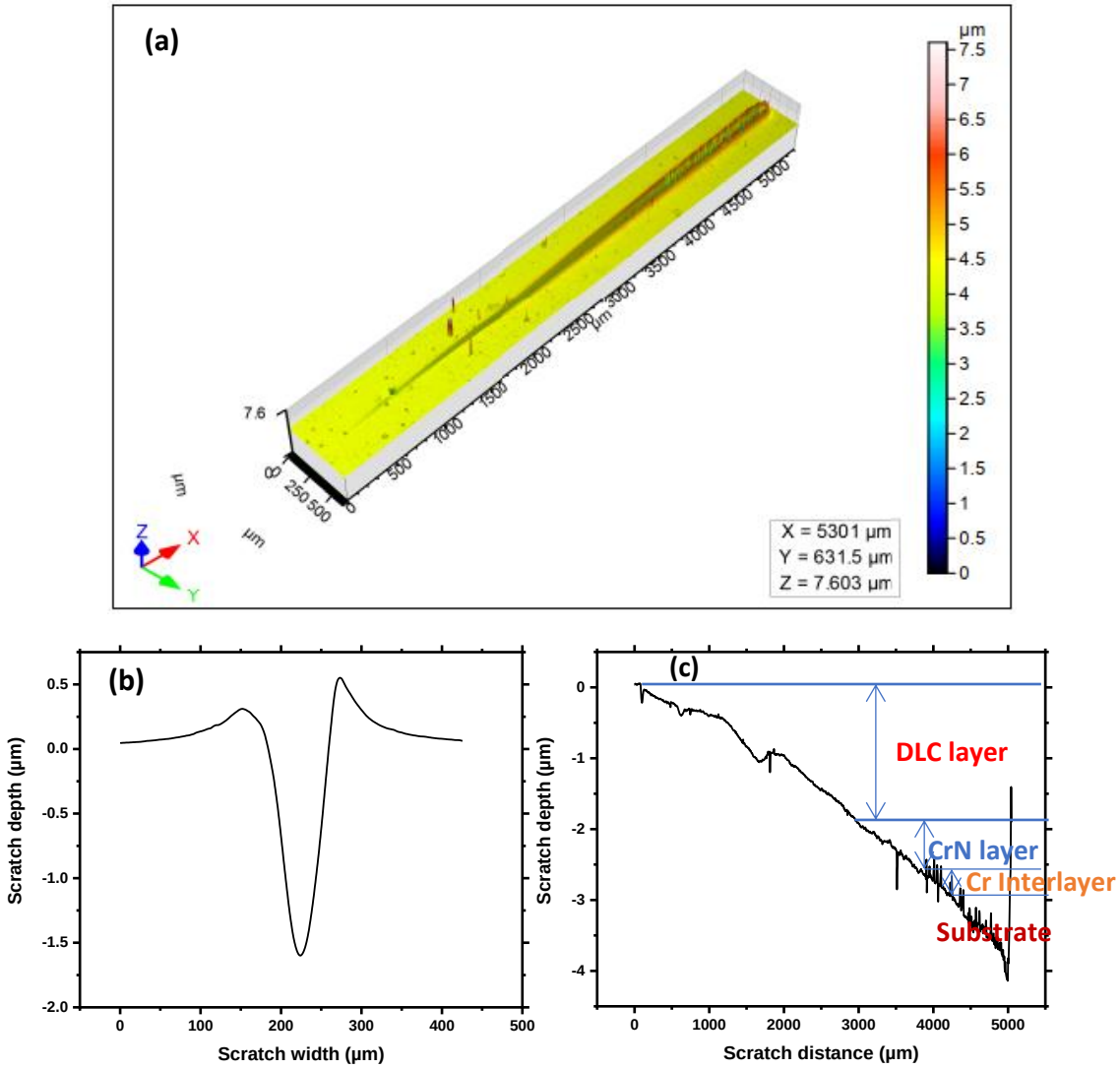

Figure 61: Scratch track of CrN/DLC (a) 3D image (b) plot of transversal profile (c) plot of longitudinal profile.

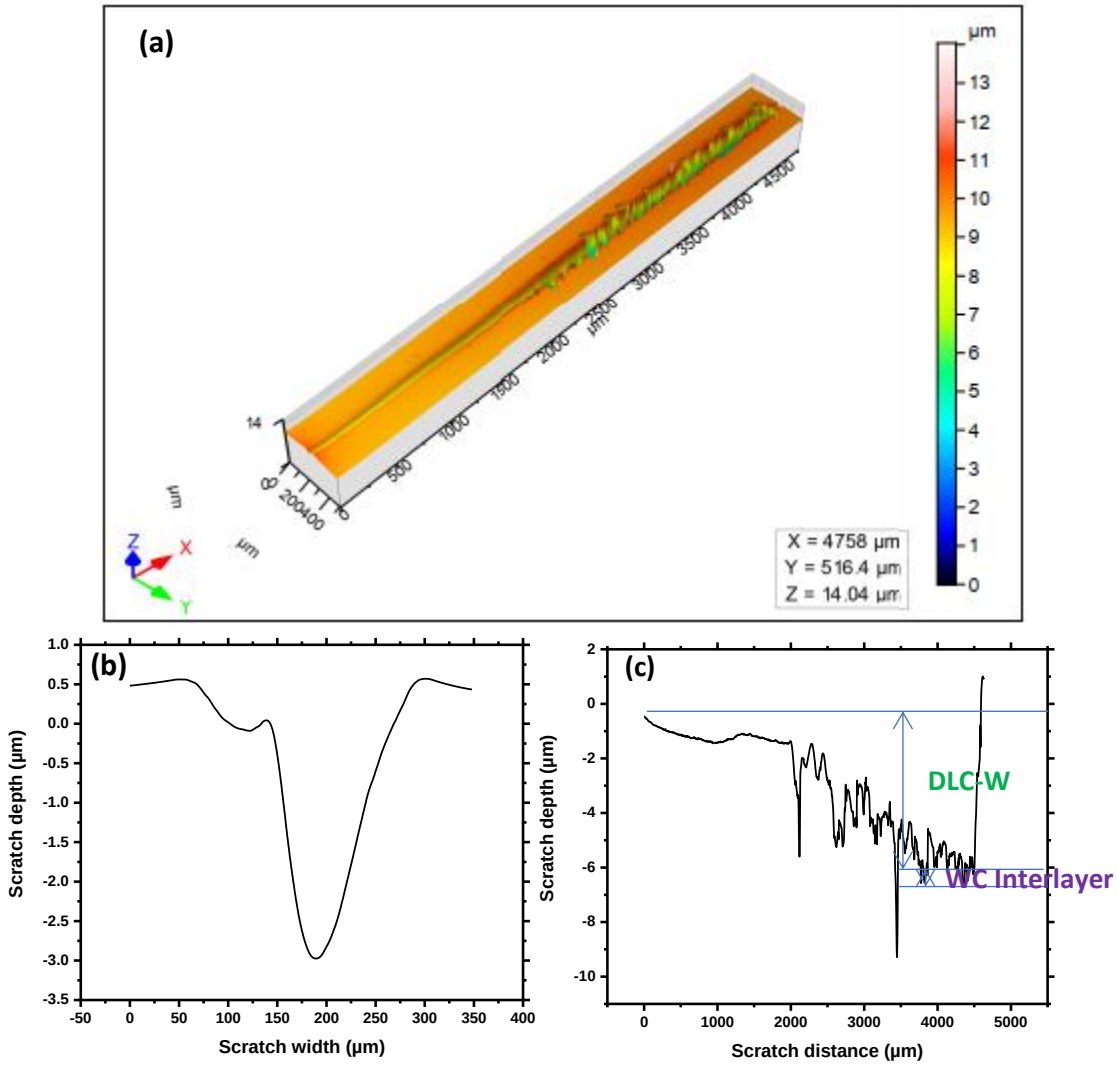

Figure 62: Scratch track of DLC-W (a) 3D image (b) plot of transversal profile (c) plot of longitudinal profile.

5.8 Rockwell-C adhesion test

Figure 63 shows the images of the indented surface during the adhesion test carried out using a Rockwell C adhesion test (Daimler Benz test) with a diamond cone indenter, 200 µm tip radius, under an applied load of 1471 N on the uncoated, CrN/DLC and DLC-W coated valve tappet. The indented surface of the uncoated, CrN/DLC and DLC-W coated valve tappet was observed under an optical microscope for proper classification of the coating adhesion as HF1 to HF6 according to the amount of cracking or spallation around the indent, as reported in VDI 3198 standard for coating assessment (VIDAKIS; ANTONIADIS; BILALIS, 2003) as shown in Figure 25. The CrN/DLC coated valve tappets can be classified as HF1 due to its excellent adhesion and the absence of delamination or spallation was observed, while, the DLC-W coated valve tappet can be classified as HF2 due to its good adhesion and the presence of little spallation being observed. The WC interlayer was also responsible for the good adhesion of DLC-W. Overall, the failure mode of both coatings based on VDI 3198 standard are acceptable failure (HF1 and HF2). The results are in agreement with those published elsewhere for CrN/DLC (CONDE et al., 2019) and DLC-W (CZYZNIEWSKI et al., 2011).

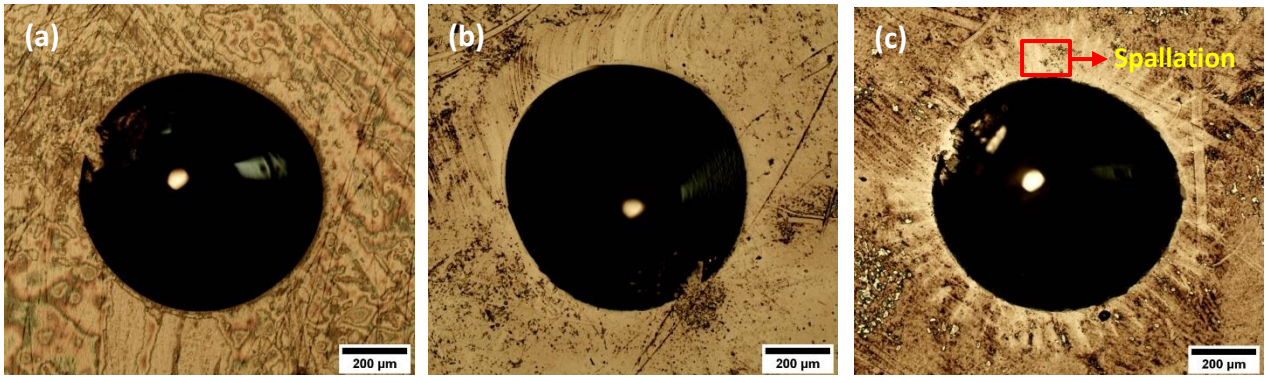

Figure 63: Images of the indented (a) valve tappet surface (b) CrN/DLC coatings (c) DLC-W coatings.

5.9 Tribological properties of CrN/DLC and DLC-W coating

5.9.1 Coefficient of friction and wear rate of substrate and coatings

The tribological properties of CrN/DLC and DLC-W were determined using SRV reciprocating test at 25^{o}C, 150^{o}C, 200^{o}C and 250^{o}C. Figure 64(a) shows the average COF values of the steady state stage at the different temperatures (25^{o}C, 150^{o}C, 200^{o}C and 250^{o}C). The COF of the coatings were quite stable at 25^{o}C and 150^{o}C for CrN/DLC and DLC-W coatings displaying very insignificant friction fluctuations compared to 200^{o}C and 250^{o}C, however, significant fluctuations was observed for the uncoated valve tappet (substrate) at all the different temperatures. The coefficient of friction stabilized few seconds after the running in period for the uncoated, CrN/DLC and DLC-W coated valve tappet for all temperatures. The COF at 25^{o}C for CrN/DLC was much lower than the DLC-W and the uncoated valve tappet at all temperatures. The COF for both CrN/DLC and DLC-W were lower than the uncoated valve tappet at all temperatures, indicating an improvement of the substrate by the CrN/DLC and DLC-W coatings. At 25^{o}C the CrN/DLC coating had a COF of 0.18, which increased gradually to 0.27 as the temperature increased to 150^{o}C, increasing the temperature to 200^{o}C further increased the COF to 0.35 and lastly, at 250^{o}C, the highest COF of 0.46 was reached for the CrN/DLC. Similarly, increase in COF was observed for the DLC-W coating as the temperature increased from 25^{o}C to 250^{o}C. The COF for the DLC-W was 0.28, 0.39, 0.53 and 0.69 at 25^{o}C, 150^{o}C, 200^{o}C and 250^{o}C respectively. The uncoated valve tappet had COF of 0.82, 1.03, 1.05 and 1.37 at 25^{o}C, 150^{o}C, 200^{o}C and 250^{o}C respectively.

The low COF of CrN/DLC was due to the improvement in the adhesion of the coating to the substrate by the use of Cr interlayers and secondly, the high sp^3 content which is responsible for the high hardness (lower deformation), helped to reduce the friction coefficient of CrN/DLC coating, even up to 250ºC. But as the temperature increases from 25ºC to 250ºC the COF increases due to an increase and the presence of oxidation at higher temperatures. On the other hand, DLC-W coating had a slightly higher COF than CrN/DLC due to lower sp^3 content (BANERJI; BHOWMICK; ALPAS, 2014) and lower hardness. DLC-W coating also experiences an increase COF as the temperature increased from 25ºC to 250ºC. It has been reported in literature that tungsten oxides formed due to oxidation, can be harmful below 300ºC leading to a higher COF before the formation of more lubricious graphitic tribo-layers (LE HUU et al., 1996). The higher fluctuation in the DLC-W can be as a result of the alternating soft and hard sub-layers present in the multilayer DLC-W. The results obtained can be corroborated by those in published in literature (BANERJI; BHOWMICK; ALPAS, 2014; BHOWMICK; BANERJI; ALPAS, 2015; EVARISTO; FERNANDES; CAVALEIRO, 2020; CONDE et al., 2019; LUKASZKOWICZ; PARADECKA; WIŚNIEWSKA, 2013; BAI et al., 2021; CAO et al., 2020; CZYZNIEWSKI et al., 2011).

Figure 64(b) shows the specific wear rate (Ws) of the uncoated, CrN/DLC and DLC-W coated valve tappet tested at 25ºC, 150ºC, 200ºC and 250ºC which was calculated using equation 19. The uncoated valve tappet had the highest wear rate compared to the coated valve tappets. The uncoated valve tappet displayed a wear rate of ~5.9 x 10^{-5} mm^3/N.m, ~25 x 10^{-5} mm^3/N.m, ~35 x 10^{-5} mm^3/N.m and ~38 x 10^{-5} mm^3/N.m at 25ºC, 150ºC, 200ºC and 250ºC respectively. While, CrN/DLC coatings had the lowest

wear rate at all temperatures, ~0.53 x 10^{-5} mm^3/N.m, ~1.8 x 10^{-5} mm^3/N.m, ~2.8 x 10^{-5} mm^3/N.m and ~6.2 x 10^{-5} mm^3/N.m at 25ºC, 150ºC, 200ºC and 250ºC respectively. DLC-W coatings also displayed similar wear rates to CrN/DLC at 25ºC and 150ºC, but increased drastically at 200ºC and 250ºC. Lastly, the wear rate for DLC-W were, ~0.6 x 10^{-5} mm^3/N.m, ~3.6 x 10^{-5} mm^3/N.m, ~20.5 x 10^{-5} mm^3/N.m and ~23 x 10^{-5} mm^3/N.m at 25ºC, 150ºC, 200ºC and 250ºC respectively. The high hardness of CrN/DLC coatings also contributes to the low wear rate at all temperatures compared to DLC-W. The wear results clearly indicates that the CrN/DLC and DLC-W coatings exhibited apparently different wear properties at different temperatures. Nevertheless, the variation in the wear rate of the CrN/DLC and DLC-W coatings at 25ºC, 150ºC, 200ºC and 250ºC correlates with the friction characteristics.

The 3D and 2D profiles represented in Figure (65 – 67) are in agreement with the wear rate of all the different surfaces at various temperatures. The wear resistance of CrN/DLC at all temperature was strongly due to high hardness and the excellent adhesion promoted by the Cr interlayer. The wear resistance of DLC-W at 25ºC and 150ºC was mainly due to the addition of tungsten and the excellent adhesion promoted by the WC interlayer, however, exhibited low wear resistance at 200ºC and 250ºC due to the low hardness demonstrated by the coatings. As the temperature increased there was a corresponding increase in depth and width of the wear track for both uncoated and coated valve tappet. Additionally, increasing wear rate for both uncoated and coated valve tappet as temperature increases corroborates the decrease of coatings hardness. The wear rate and COF obtained here are similar to those reported in literature (BANERJI; BHOWMICK; ALPAS, 2014; BHOWMICK; BANERJI; ALPAS, 2015).

It is well understood that DLC coatings show low friction and high wear resistance at ambient temperature due to formation of graphitic tribo-layer at the asperity contacts at this point sp^3 begins to transform into sp^2 (HOVSEPIAN et al., 2016; TAKENO, et al., 2009; BAI et al., 2021; ARSLAN et al., 2019). The wear rates continue to increase as the temperature increases due to an increase in the sp^2 content in the CrN/DLC coatings, resulting in a softer coating at higher temperature which easily wears out. An increase of wear rate for DLC-W with tungsten is more likely as a result of the presence of WC nano-clusters acting as abrasive component (CZYZNIEWSKI et al., 2011). At 25ºC the wear rate is slightly higher than CrN/DLC due to lower sp^3 content and as the temperature increase the sp^2 content continues to increase reducing the hardness of the DLC-W and oxidation also begins to occur. Graphitization is delayed up to 300ºC and above by the presence of tungsten in DLC-W (MÜLLER et al., 2017; BANERJI; BHOWMICK; ALPAS, 2014; KONCA et al., 2006), therefore between 25ºC to below 300ºC the friction coefficient is higher, caused by the delay in graphitization which serves as self-lubricant (transfer layer) while in CrN/DLC coating graphitization occurs at temperatures as low as 40ºC (MÜLLER et al., 2017; KONCA et al., 2006). Since graphitization occur at lower temperatures for CrN/DLC coatings and at higher temperatures for DLC-W, it is expected that both COF and wear rates of CrN/DLC would be lower.

In the work performed by Banerji et al. (2014), the authors reported that at 25ºC, the low COF (0.10) and wear rates of DLC-W was similar to pure DLC, which could be attributed to the formation of a carbon rich transfer layer on the Ti–6Al–4V alloy counterface. However, between 200ºC and 300ºC, there was a high COF (0.46-0.51) and wear rates due to lack of formation of transfer layer on the substrate. At 400 °C and 500

°C, very low COF (0.07–0.08) and wear rates were obtained due to the formation of a tungsten trioxide layer on the W-DLC surface (BANERJI; BHOWMICK; ALPAS, 2014). According to Banerji et al. tungsten addition was shown to be particularly beneficial for the high temperature tribological behavior of DLC coatings (BANERJI; BHOWMICK; ALPAS, 2014). Pu et al. (2015) evaluated the tribological properties of DLC-W having tungsten of 0 at.%, 1.54 at.%, 3.57 at.%, 5.43 at.%, 6.38 at.% and 7.39 at. % at 25ºC and 200ºC. Their work revealed that at 25ºC and 200ºC the lowest COF and wear rates were at 5.43 at.%. The tungsten content below and above possessed higher COF and wear rates, which was attributed to low WC_{1-x} phase content in DLC-W for tungsten content below 5.43 at.% forming too little transfer layers for protecting the DLC-W, and to high WC_{1-x} phase content in DLC-W for tungsten content above 5.43 at.% forming hard WC_{1-x} transfer layers, which acts as abrasive particles causing severe wear (PU; HE; WANG, 2015).

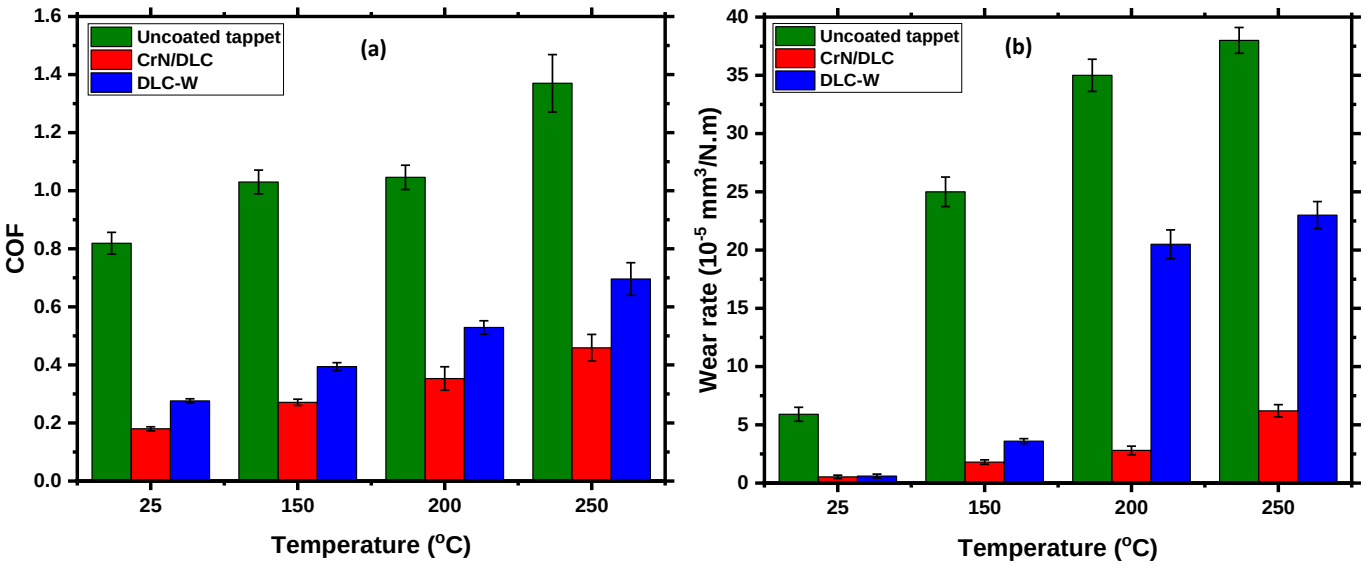

Figure 64: Uncoated and coated valve tappet tested against AISI 52100 balls at 25, 150, 200 and 250ºC (a) Average coefficient of friction (b) specific wear rate.

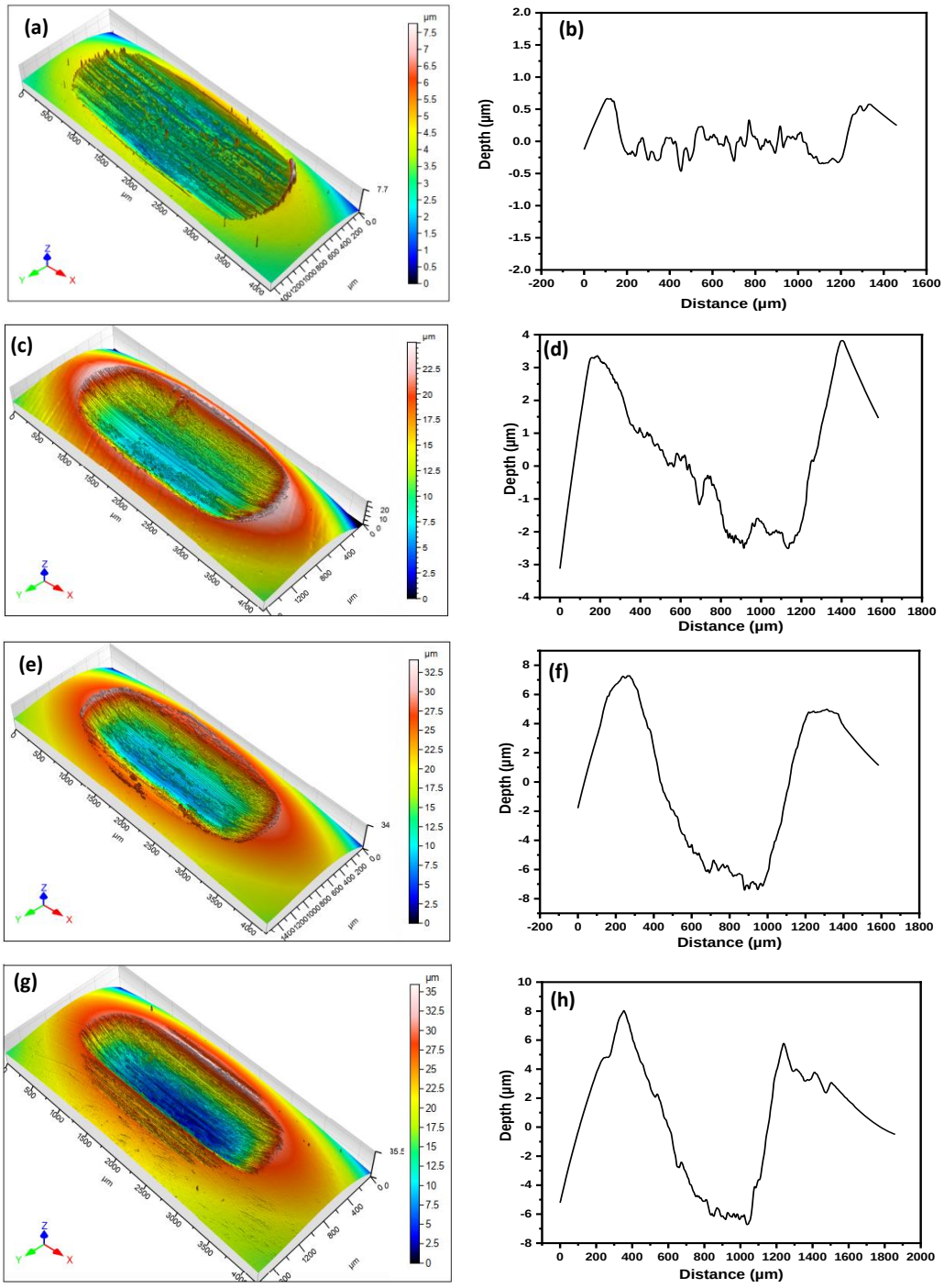

Figure 65: 3D and 2D image of wear track for uncoated tappet (a) (b) 25^{o}C (c) (d) 150^{o}C (e) (f) 200^{o}C (g) (h) 250^{o}C.

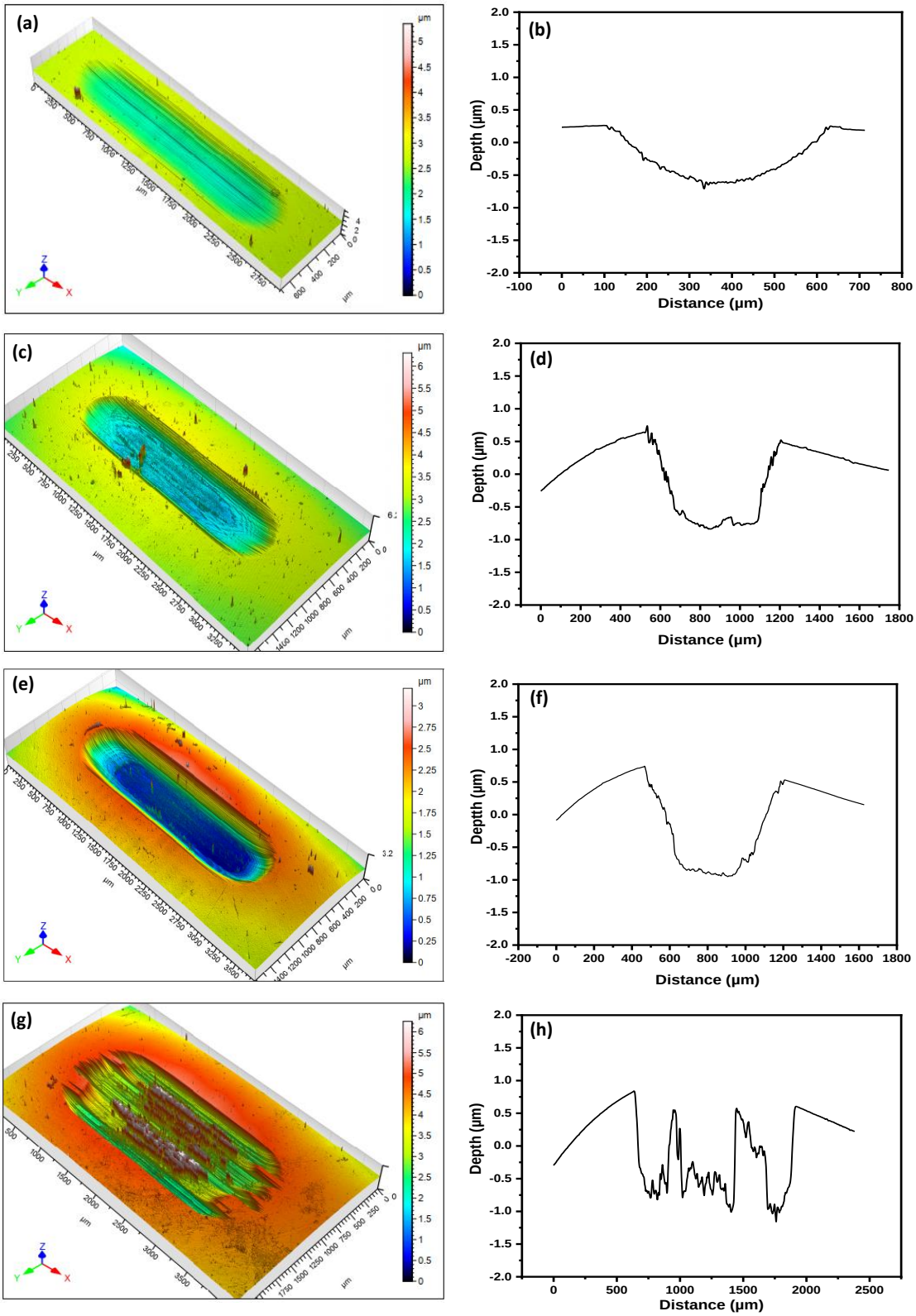

Figure 66: 3D and 2D image of wear track for CrN/DLC coated tappet (a) (b) 25^{o}C (c) (d) 150^{o}C (e) (f) 200^{o}C (g) (h) 250^{o}C.

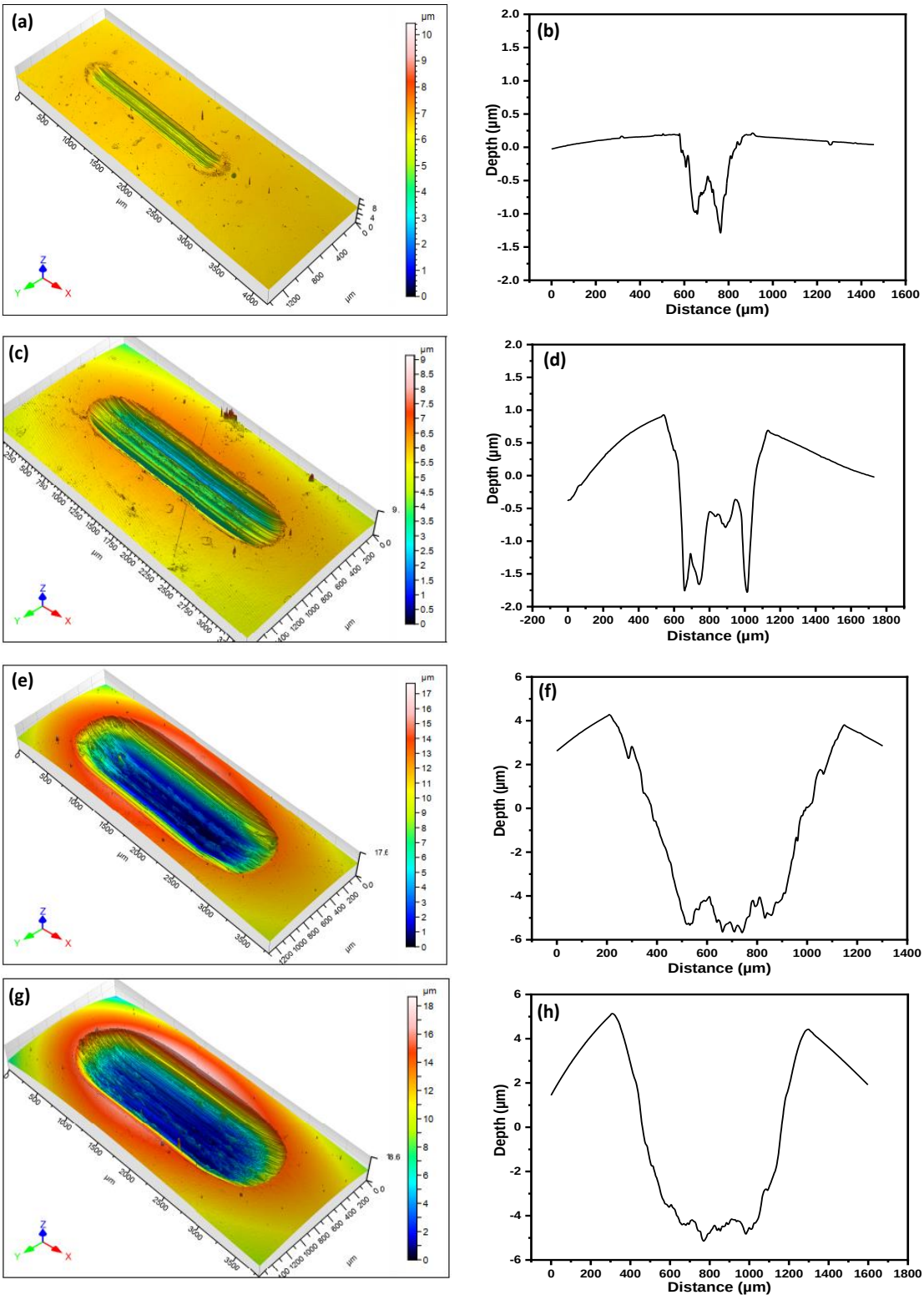

Figure 67: 3D and 2D image of wear track for DLC-W coated tappet (a) (b) 25ºC (c) (d) 150ºC (e) (f) 200ºC (g) (h) 250ºC.

5.9.2 Wear mechanisms and surfaces analysis

The investigation of the wear mechanisms (interaction between the uncoated, coated surfaces and contact ball) on the different surfaces are important due to the changes that occurs in the COF and wear rate of the coatings, which are partially related to factors, such as chemical composition, mechanical properties, physical properties of the materials, temperature change, wear mechanisms taking place in the wear track and the applied load. Scanning electron microscopy with energy dispersive X-ray spectroscopy (SEM–EDS), Raman spectroscopy and nano-indentation were used to analyse the worn surfaces and wear debris that originated during the tribological testing to understand the wear mechanisms.

5.9.2.1 Wear mechanisms and surfaces analysis at various temperature

To further investigate the friction and wear behaviors of the CrN/DLC and DLC-W coatings, the morphology of the wear tracks for the uncoated, CrN/DLC, and DLC-W coated valve tappet tested, and wear scars for the contact steel balls at 25^{o}C, 150^{o}C, 200^{o}C and 250^{o}C were observed by SEM/EDS. The results are shown in Figures (68 – 78). The wear track of the uncoated valve tappet at 25^{o}C had adhered material and scratches aligned in the slide direction of the contact ball, as seen in Figure 68(a). This could be the result of mixed abrasion and adhesion wear mechanisms. EDS compositional analysis revealed that the adhered materials of the uncoated valve tappet was rich in C, O, Fe and a trace of Mn, which were contributions from both the valve tappet and contact ball see Figures 68(a) & 69(a). The SEM image and EDS

compositional analysis revealed that the contact ball had adhered materials consisting of C-O, Fe-O and N-O (Figure 74). These were responsible for the high friction and wear rates.

The wear track of the CrN/DLC coating at 25^{o}C depicted adhered material, detached particles, and fine scratches aligned in the sliding direction of the contact ball, suggesting that the wear mechanisms were a mixture of abrasion and adhesion, see Figure 70(a). Accumulated materials removed from the coatings were observed at the end of the wear track. The corresponding EDS elemental mapping showed the distributions of the elements on the wear track, namely, Cr, O, N and C as seen in Figure 70(b-e). However, Fe-O was absent at 25^{o}C in the wear track. Figure 75(a), shows the SEM image of the contact ball, while Figure 76, shows the EDS compositional analysis which revealed that the contact ball surface comprising of a mixture of high C-containing wear debris, together with N-O and Fe–O. The O observed was due to oxidation during the sliding of the contact ball on the surface of the coating. The presence of C-rich particles which were observed on the contact ball from the coating aided the reduction of friction and wear at 25^{o}C. The wear tracks of the DLC-W coating at 25^{o}C depict similar behavior as CrN/DLC coating at 25^{o}C, with wear mechanisms exhibiting a mix abrasion and adhesion wear mechanisms consisting of adhered material, detached particles and fine scratches aligned in the slide direction of the contact ball as can be observed in Figure 72(a). Removed materials from the coatings were observed at the end of the wear track. The adhered materials on the contact ball which was analysed using EDS compositional analysis suggests that the material was rich in C-O, Fe-O, N-O, W-C and W-O (Figure 78). The corresponding EDS elemental mapping showed the distributions of the elements

on the wear track namely, W, O, Fe and C as seen in Figure 72(a-e). The C-rich and W-rich particles, presence of O was due to oxidation, was observed on the contact ball from the coating, suggesting a poor WC or WC1-x layer, which forms abrasive particles and can be responsible for the slightly increase in friction and wear rate compared to CrN/DLC coating.

Detached particles that were observed in the wear track could be a mixture of non-oxidized and oxidized particles from the coatings and the contact ball during sliding. Wear debris were found to adhered to the contact ball which were similar to those on the wear track. At the protuberances of the contact, a local increase in temperature usually arises due to the friction generated by the sliding of the contact ball against the surface of the coatings. During the continuous sliding of the contact ball, asperities from both the ball and the surface of the coating usually break away, generating free wear debris particles, which are oxidized and adhere to the surfaces. This continuous process leads to scratching of the surfaces and coating removal. The majority of the wear debris were ejected out of the wear track as the movement of the ball continued. A decrease in hardness and fracture toughness (see H/E ratio in Table 6) caused by W addition made it easier for the material removal from the DLC-W coatings compared to CrN/DLC, which is in agreement with the increased wear rate observed in Figure 64(b). The wear track was also observed to increase in width and depth for DLC-W compared to CrN/DLC coatings.

The test conducted at higher temperatures (150^{o}C, 200^{o}C and 250^{o}C) had evidence of deformation at the edge of the wear track, deeper and wider wear track with fine scratches in the slide direction, suggesting abrasive wear as the active mechanism

for uncoated, CrN/DLC and DLC-W coated valve tappet (Figure 68(b-d), Figure 69(f,k,p) and Figure 70(f,k,p) respectively. Here the wear scar on the contact ball had smoother and shallower scratches and there were small oxidized wear debris found adhered to the wear scar (Figure 73(b-d), Figure 75(b-d) and Figure 77(b-d). In contrast, there was very high amount of adhered material observed at the surface of the uncoated and coated valve tappet formed by oxides. The wear track had rough and deeper scratches in the slide direction due to mixed adhesion and abrasion mechanisms. At these temperatures the coatings will oxidize spontaneously due to their low oxidation resistance (EVARISTO; FERNANDES; CAVALEIRO, 2020). The wear tracks were also observed to increase in width and depth which was as a result of the increase in temperature as seen in Figure (65-67).

In the test conducted at 150^{o}C for uncoated, CrN/DLC and DLC-W coated valve tappet, the wear track was wider than that of 25^{o}C. The scratch size increased with increase in temperature due to the increase in the severity in the abrasion. In all cases the amount of wear debris, adhered materials and detached particles which were found on the wear track and contact ball surface increased with increase in temperature. The wear track of the uncoated valve tappet at 150^{o}C had smoother adhered material, finer scratches than that of 25^{o}C, caused by sliding of the contact ball and the hot pressing of the contact ball on the valve tappet. It also exhibited a mixed abrasion and adhesion wear mechanisms. EDS compositional analysis suggests that the adhered materials of the uncoated valve tappet was rich in C-O, N-O and Fe-O which was contributed from both the valve tappet and contact ball (see Figure 69b). An increase in wear rate and COF corresponds to the material removal observed in Figure 68(b).

For CrN/DLC coatings at 150^{o}C, depicted a mixture of abrasion and adhesion wear mechanisms with adhered material, detached fine particles and fine scratches in the slide direction of the contact ball (Figure 70f). More material removal occurred compared 25^{o}C and contained more adhered materials, analysis from EDS elemental mapping showed the distributions of the increased elements on the wear track namely, Cr, O, N and C as seen in Figure 70(g-i). The corresponding EDS compositional analysis revealed that the contact ball surface comprised of a mixture of high C-containing wear debris, N-O and Fe–O. Figure 75(b) is in agreement with the wear rate and COF. The DLC-W coating at 150^{o}C had a mix abrasion and adhesion wear mechanisms with adhered material, detached fine particles and fine scratches in the slide direction of the contact ball. More removed materials from the coatings were observed at the end of the track as seen in Figure 72(f). The adhered materials analysed by EDS compositional analysis showed that the material was rich in C-O, Fe-O, W-C and W-O. The corresponding EDS elemental mapping showed the distributions of the increased elements on the wear track namely, W, O, Fe and C as seen in Figure 72(g-j). The compositional SEM/EDS analysis revealed that the contact ball surface comprised of a mixture of high C-containing wear debris with Fe–O, predominantly W-O and W-C (see Figure 77(b)&78). The presence of O was due to oxidation, a C-rich and W-rich transfer layer was observed on the contact ball from the coating, suggesting a rich WC layer, which were responsible for slightly increasing the COF and wear rate as compared to CrN/DLC. Figure 72(f) is in agreement with the wear rate and COF.

The wear track of the uncoated valve tappet at 200 and 250^{o}C had smoother adhered material, finer scratches caused by sliding of the contact ball at elevated

temperature and hot pressing of the contact ball on the valve tappet, which exhibited an adhesion wear mechanism (Figure 68(c-d)). EDS compositional analysis revealed that the adhered materials of the uncoated valve tappet was rich in C-O, N-O and Fe-O which were from both the valve tappet and contact ball (see Figure 69(c-d) & 73(c-d). The increase in hard particles oxide were responsible for increase in COF and wear rates. For CrN/DLC coatings at 200 and 250^{o}C, depicted a mixture of lesser abrasion and adhesion wear mechanisms with adhered material, detached fine particles and fine scratches. An increase in material removal occurred at 200 and 250^{o}C exposing the substrate (valve tappet) partially and contained more adhered materials as seen in Figure 70k & 70p. The adhered material was rich in C-O, Cr-O, Fe-O and N-O. The corresponding EDS elemental mapping showed the distributions of the increased elements on the wear track, namely, Cr, O, N and C as seen in Figures 70(i-o) & 70(q-t)). The detection of Cr on the wear track indicates that the DLC coating is been removed, leaving the CrN layer on the surface EDS compositional analysis revealed that the contact ball surface comprised of a mixture of high C-containing wear debris, N-O, Fe-O and predominantly C–O (see Figure 71(c-d)). Regions of deformation were also observed around the edge of the coatings. The DLC-W coating at 200^{o}C and 250^{o}C had mixed abrasion and adhesion wear mechanisms with adhered material, detached fine particles and fine scratches. More removed materials from the coatings were observed at the end of the track exposing the substrate (valve tappet) partially at 200^{o}C and severely at 250^{o}C, as seen in Figures 72k & 72p. They contained adhered materials that were rich in C-O, Fe-O, W-C and W-O. The corresponding EDS elemental mapping showed the distributions of the increased elements on the wear track, namely, W, O, Fe, and C as seen in Figures 72(i-o) & 72(q-

t)). The compositional SEM-EDS analysis revealed that the contact ball surface comprised a mixture of high C-containing wear debris, W-O and predominantly Fe–O (see Figure 77(c-d)). Regions of deformation were also observed around the edge of the coatings. An increase in hard WC1-x particles increases the COF and wear rate at 250^{o}C.

It was noticed for all the EDS mapping images that as the temperature increased the Fe content increased, meaning that at higher temperature there was an increase in the Fe-O transfer from the contact ball to the surface of the coatings as seen in Figures 71(a-d) and Figures 72(e,j,o&t). The increase in the presence of iron on the surface of the coatings as the temperature increase was due to increase wear of the ball, during the sliding of the ball, it losses iron which, adheres to the surface of the coatings being tested. As the iron content increases on the surface of the coatings, they get oxidized with increase in temperature, forming hard iron oxide particles which increases the wear rate with increase in temperature.

Oxidation which is known to occur on the wear track due to the flash temperature increase is induced by the movement of the ball. The removal of oxides takes place and its continuous removal from the wear track simply explains the high specific wear rate of the coatings when compared to experiments at 25 ^{o}C and 150 ^{o}C. Since the CrN/DLC and DLC-W coated valve tappet is protected by the C-rich transfer layer (for CrN/DLC) and WC-rich transfer layer (for DLC-W), the wear in the contact ball is much lower at 25 ^{o}C and 150 ^{o}C, giving rise to narrower, shallower wear tracks. The CrN/DLC coating showed the best wear resistance at all temperatures due to its enhanced oxidation resistance, and increased hardness, as reported in previous work published elsewhere (BANERJI; BHOWMICK; ALPAS, 2014; EVARISTO; FERNANDES; CAVALEIRO, 2020).

The DLC-W coatings, however, showed poor wear resistance at 200 ºC and 250 ºC, due to the presence of hard oxides particles. The sliding contact between the adhered debris at the ball and the coating surface, from which the oxides are being removed, lead to similar COF, regardless of the composition of the films.

The combined oxides of iron and tungsten carbide lead to the formation of a transition layer, causing a strong bonding of DLC-W onto the metallic substrate at 25ºC and 150ºC. However, as the temperature increase to 200ºC and 250ºC, there is an increase in the removal of WC which fails to form transfer layers and become very hard (PU; HE; WANG, 2015), thereby increasing the abrasive wear at these temperatures and causing a rise in COF and wear. The analysis of friction that occurred suggests that the initial phase is dominated by graphitization accompanied by tribo-oxidation of the coating (CZYZNIEWSKI et al., 2011). It has been reported that the governing mechanisms of the low friction of W-DLC observed at 500ºC are transfer layers that consist of mainly of tungsten trioxide (WO_3) that formed on W-DLC's surface, ensuring low wear rates and friction, whereas at 25ºC the transfer layers were rich in carbon (BANERJI; BHOWMICK; ALPAS, 2014; EVARISTO; FERNANDES; CAVALEIRO, 2020; PU; HE; WANG, 2015). Tungsten addition has been proven to be particularly beneficial for the high-temperature tribological behavior of DLC coatings for temperatures of 300°C and above, whereby the sliding-induced graphitization of DLC-W occurs (MÜLLER et al., 2017; BANERJI; BHOWMICK; ALPAS, 2014; KONCA et al., 2006). The DLC-W easily consumed under mild conditions and low wear rates (CAVALEIRO; HOSSON, 2006), is the main reason why it performed slightly worse than the CrN/DLC coatings at 25ºC and 150ºC and severely worse at 200ºC and 250ºC.

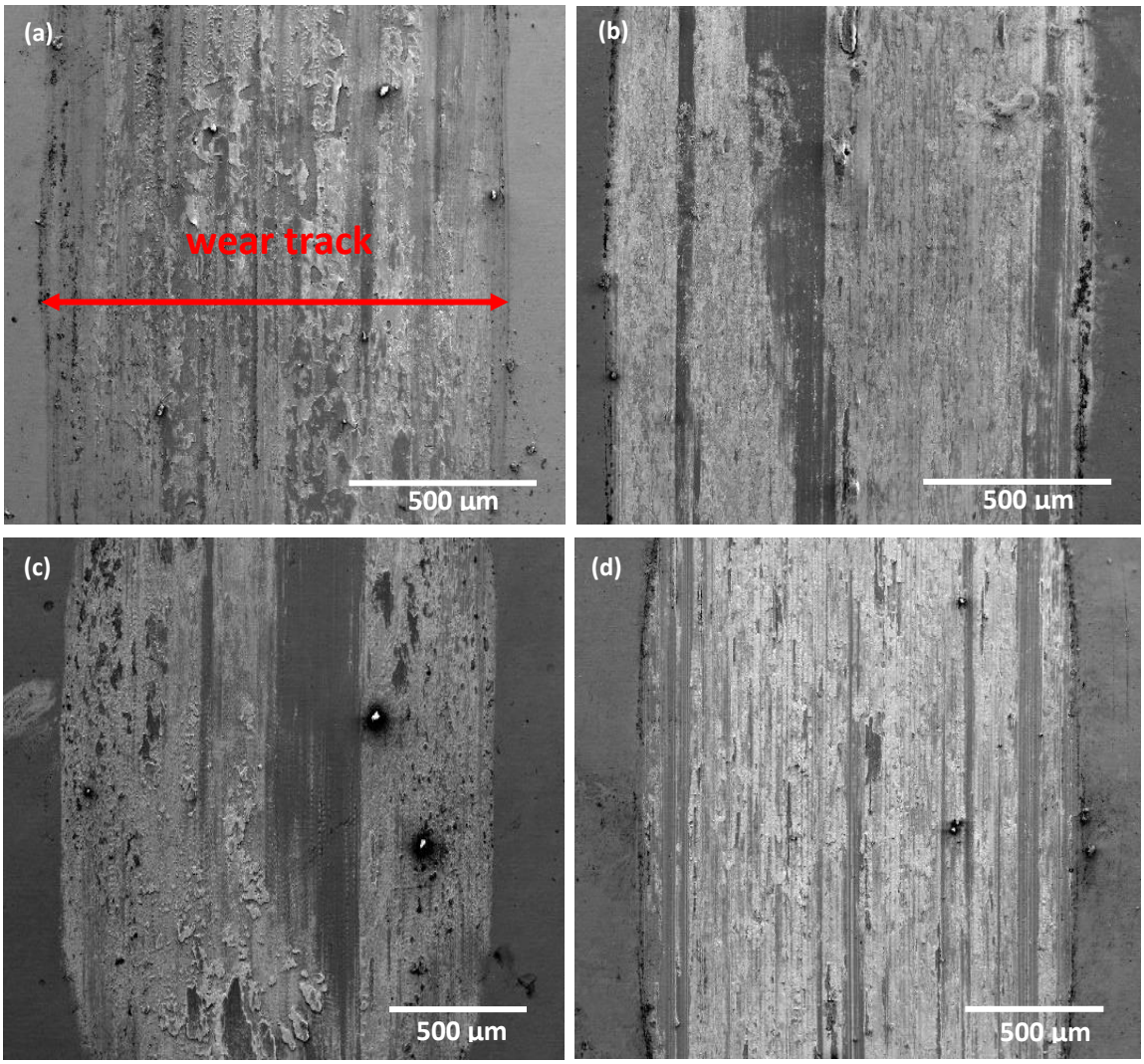

Figure 68: SEM images of wear track for uncoated tappet (a) 25ºC (b) 150ºC (c) 200ºC (d) 250ºC.

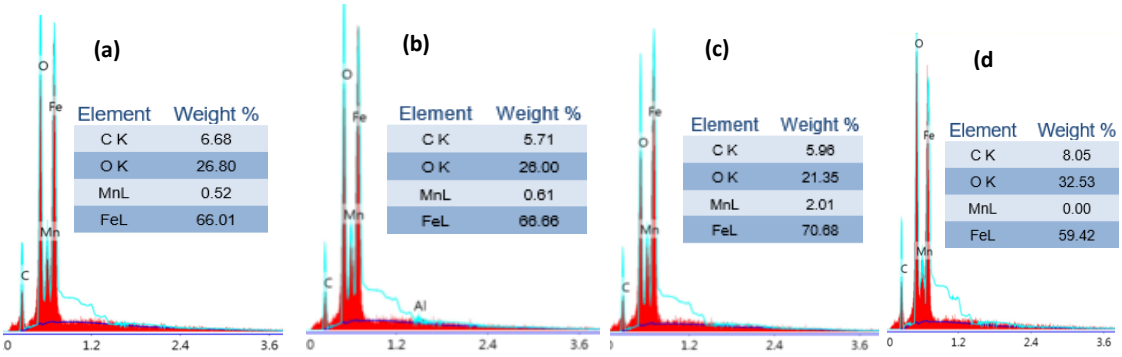

Figure 69: EDS composition for wear track for uncoated tappet (a) 25ºC (b) 150ºC (c) 200ºC (d) 250ºC.

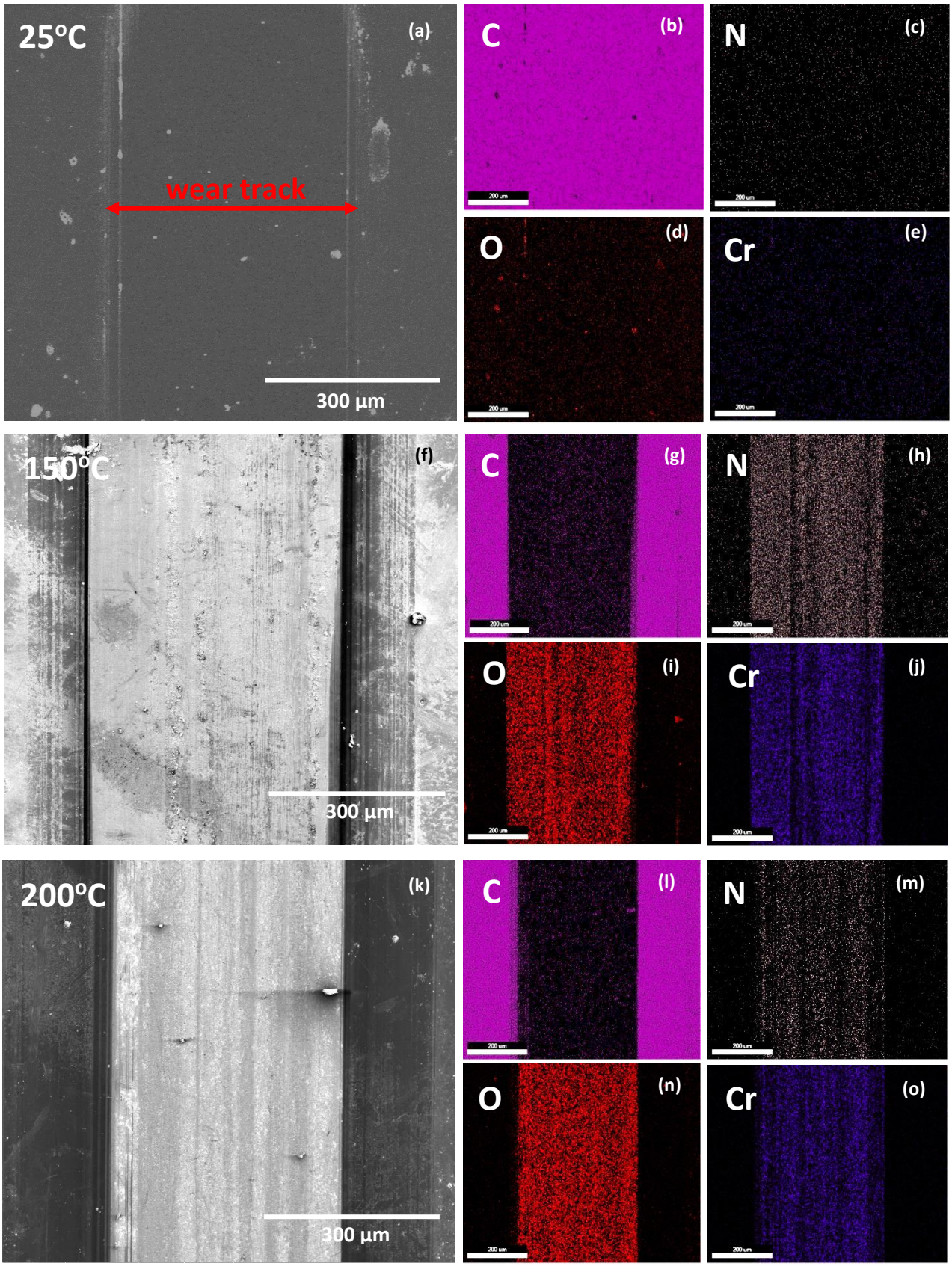
25°C
(a)
wear track
300 µm
C
(b)
N
(c)
O
(d)
Cr
(e)
150°C
(f)
300 µm
C
(g)
N
(h)
O
(i)
Cr
(j)
200°C
(k)
300 µm
C
(l)
N
(m)
O
(n)
Cr
(o)

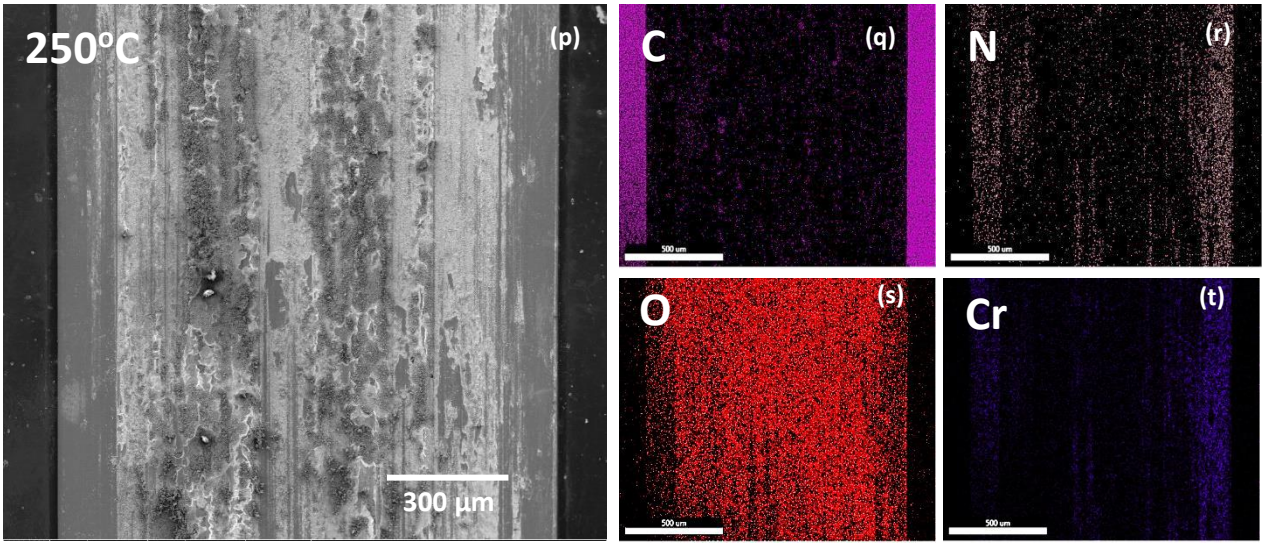

Figure 70: SEM images of wear track for CrN/DLC coated tappet at (a) 25°C (f) 150°C (k) 200°C (p) 250°C. Elemental EDS mapping at 25°C (b) C (c) N (d) O (e) Cr, at 150°C (g) C (h) N (i) O (j) Cr, at 200°C (l) C (m) N (n) O (o) Cr, at 250°C (q) C (r) N (s) O (t) Cr.

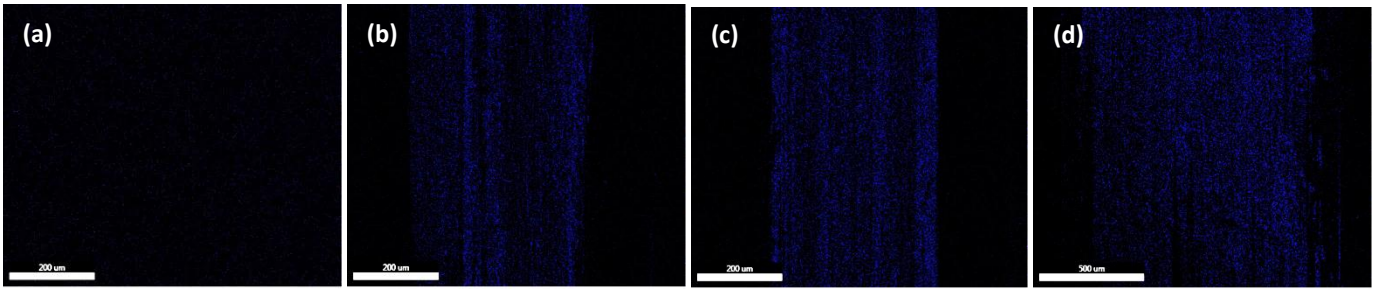

Figure 71: Elemental EDS mapping for Fe of wear track for CrN/DLC coated tappet at (a) 25°C (b) 150°C (c) 200°C (d) 250°C.

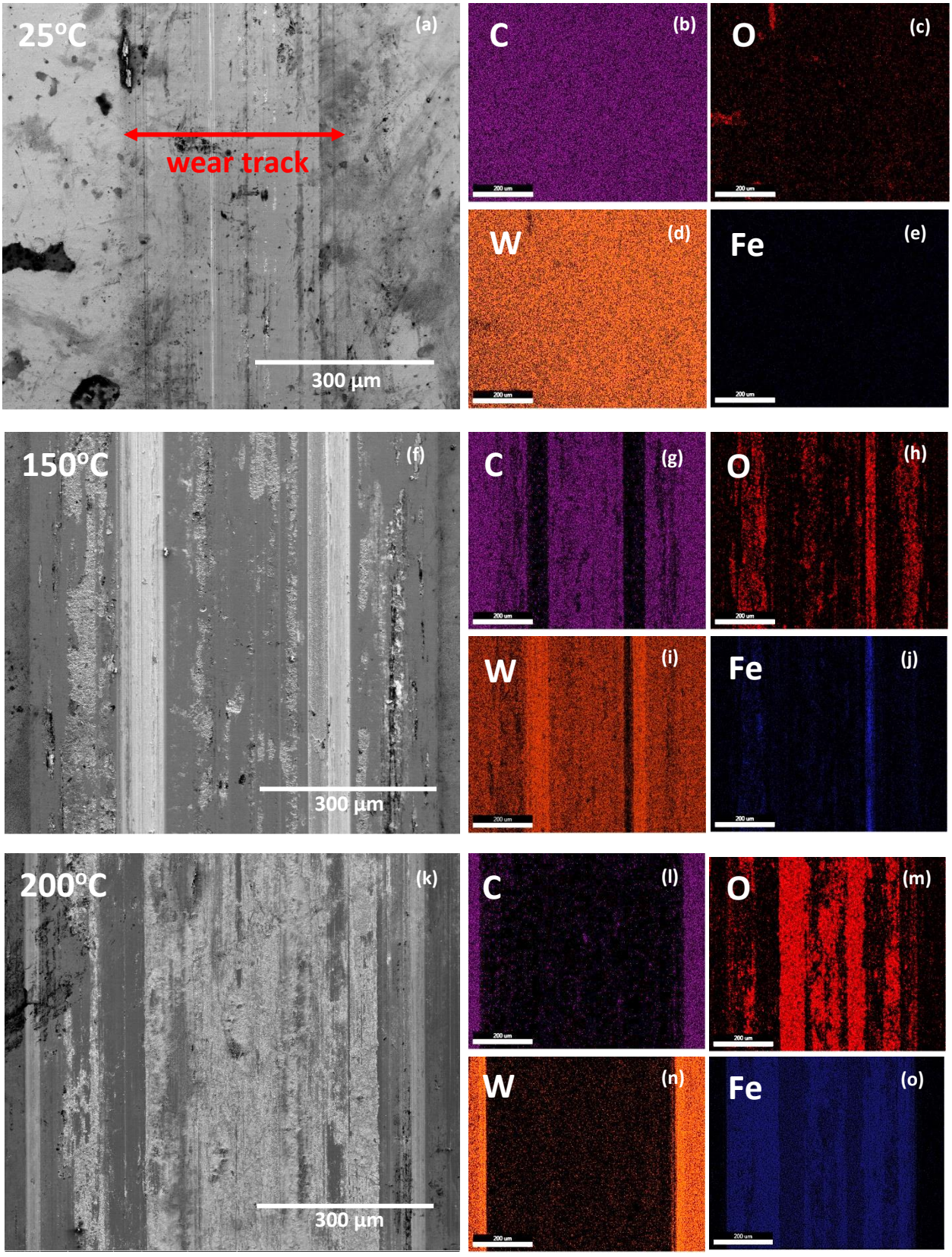
25°C
(a)
wear track
300 µm
C
(b)
O
(c)
W
(d)
Fe
(e)
150°C
(f)
300 µm
C
(g)
O
(h)
W
(i)
Fe
(j)
200°C
(k)
300 µm
C
(l)
O
(m)
W
(n)
Fe
(o)

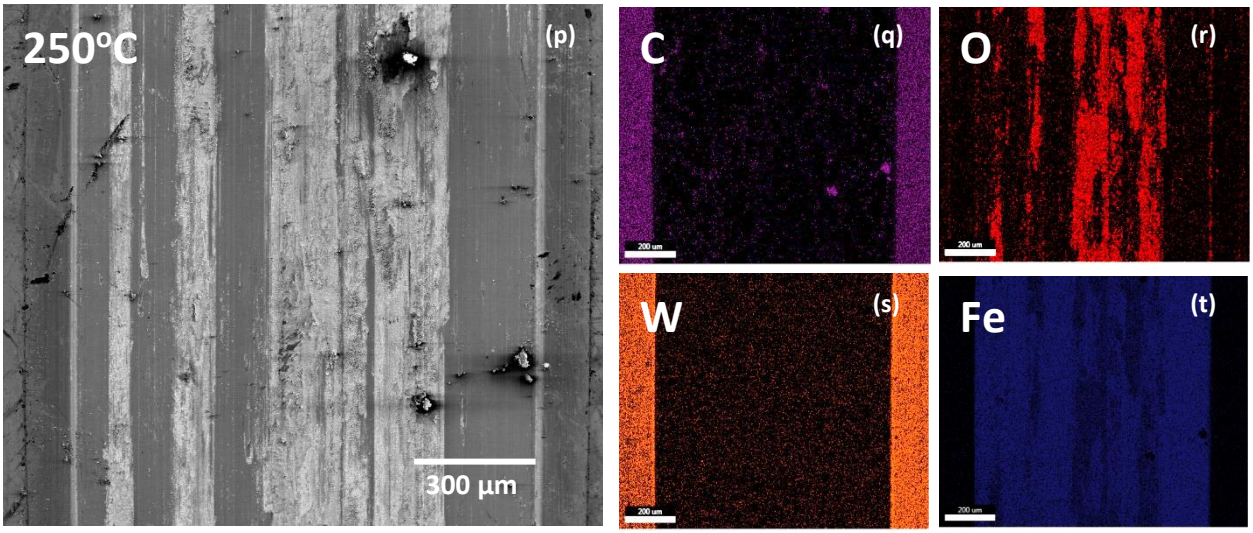

Figure 72: SEM images of wear track for DLC-W coated tappet at (a) 25°C (f) 150°C (k) 200°C (p) 250°C. Elemental EDS mapping at 25°C (b) C (c) O (d) W (e) Fe, at 150°C (g) C (h) O (i) W (j) Fe, at 200°C (l) C (m) O (n) W (o) Fe, at 250°C (q) C (r) O (s) W (t) Fe.

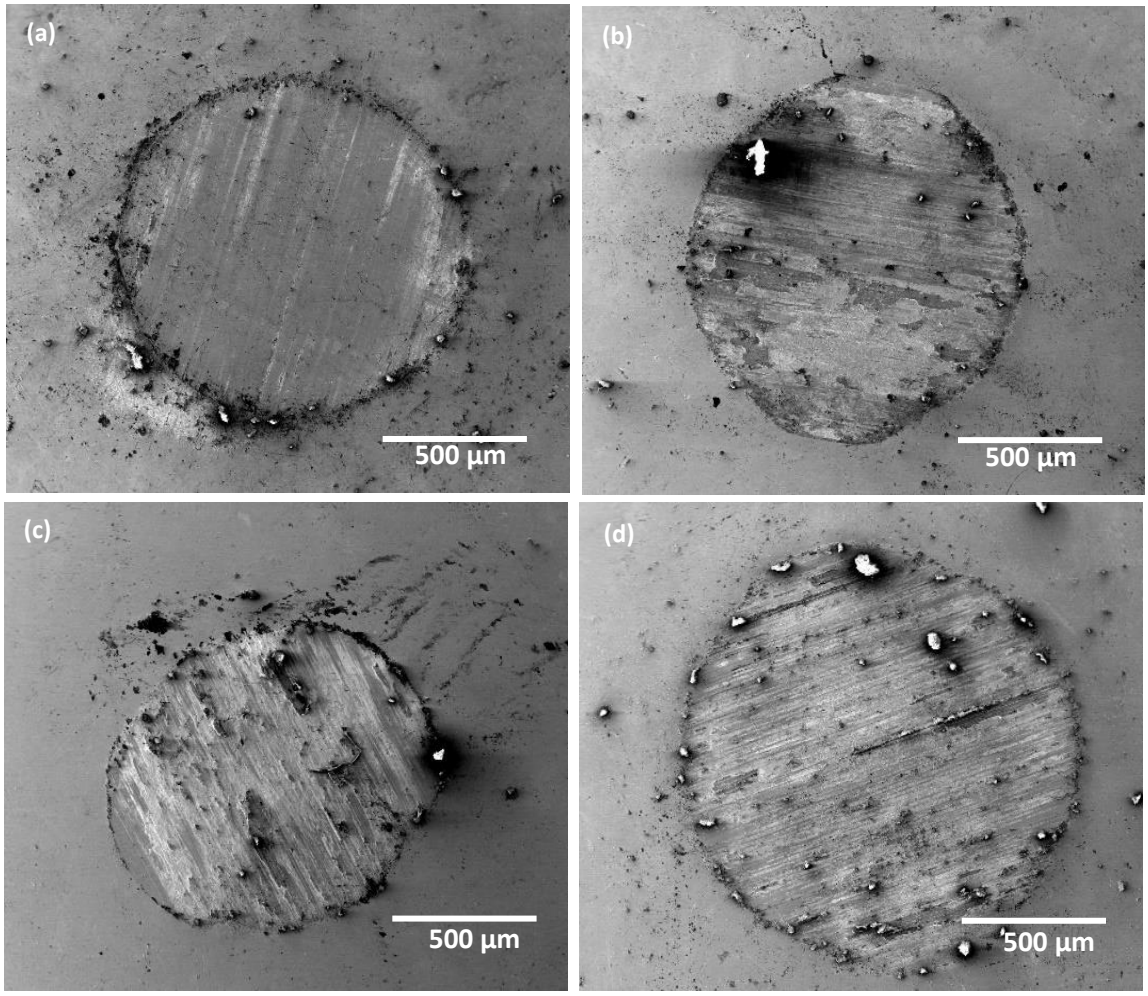

Figure 73: SEM images of wear scar for contact ball on uncoated tappet (a) 25ºC (b) 150ºC (c) 200ºC (d) 250ºC.

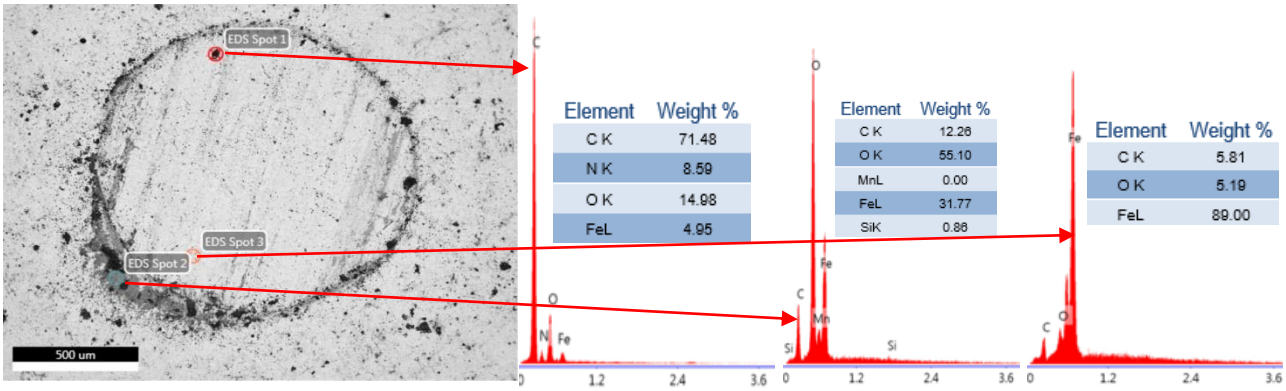

Figure 74: SEM image and EDS composition for contact ball on uncoated tappet (a) 25ºC (b) 150ºC (c) 200ºC (d) 250ºC.

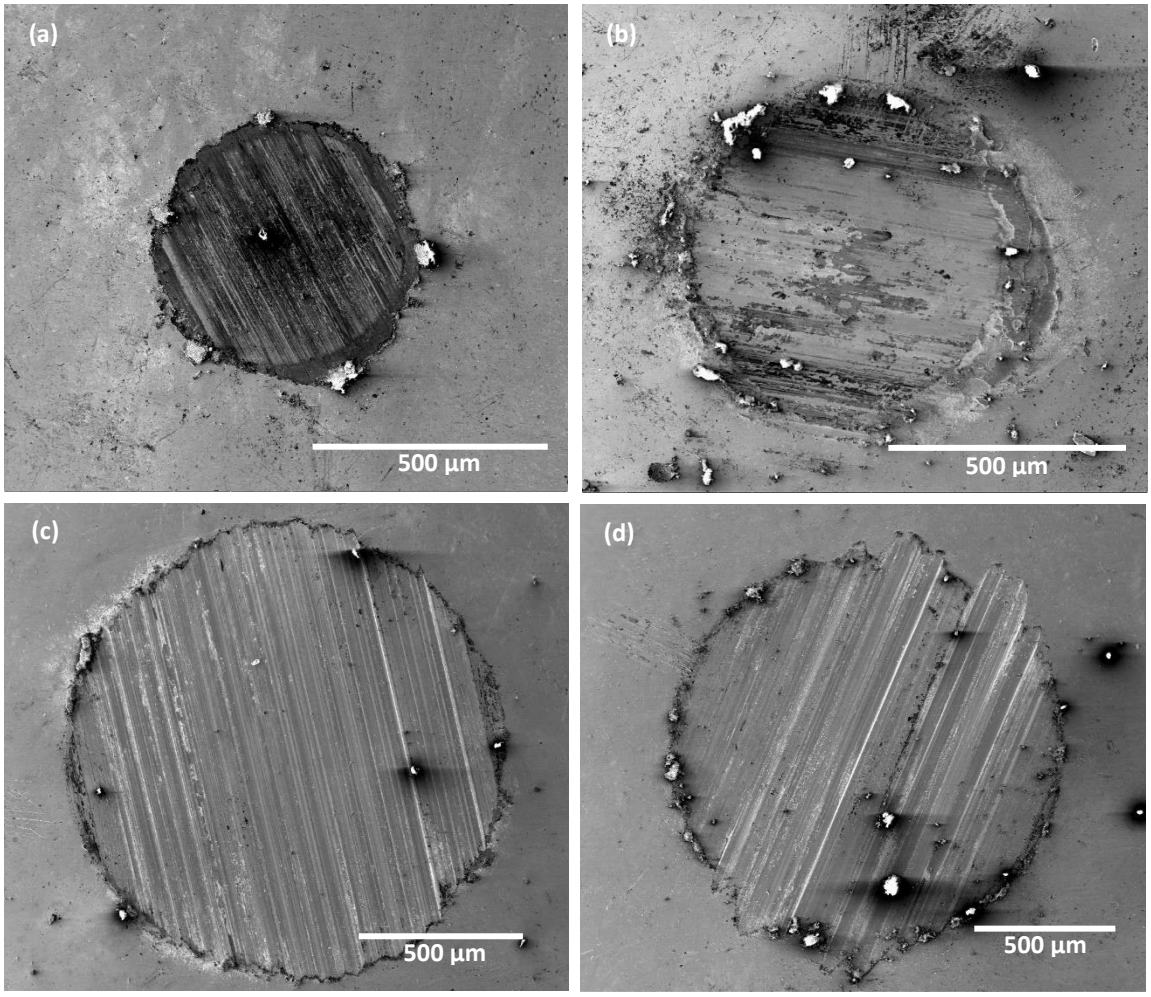

Figure 75: SEM images of wear scar for contact ball on CrN/DLC (a) 25ºC (b) 150ºC (c) 200ºC (d) 250ºC.

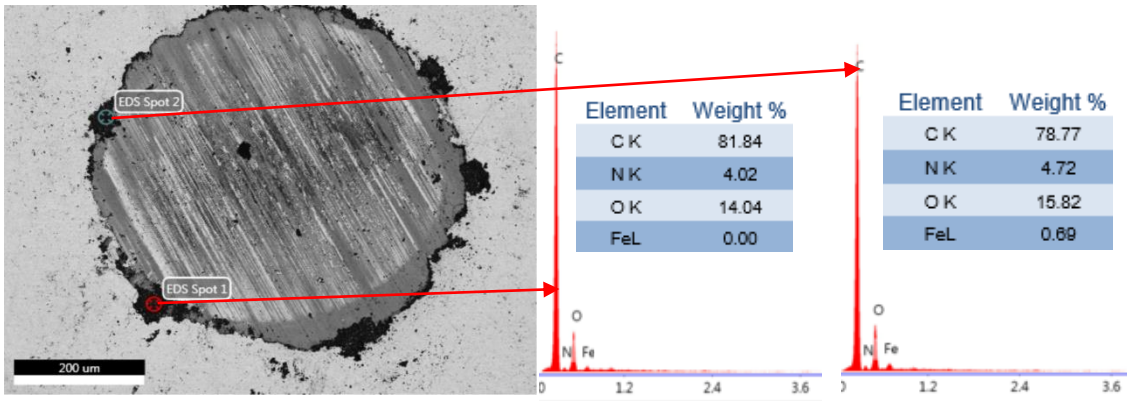

Figure 76: SEM image and EDS composition of wear scar for contact ball on CrN/ DLC coatings.

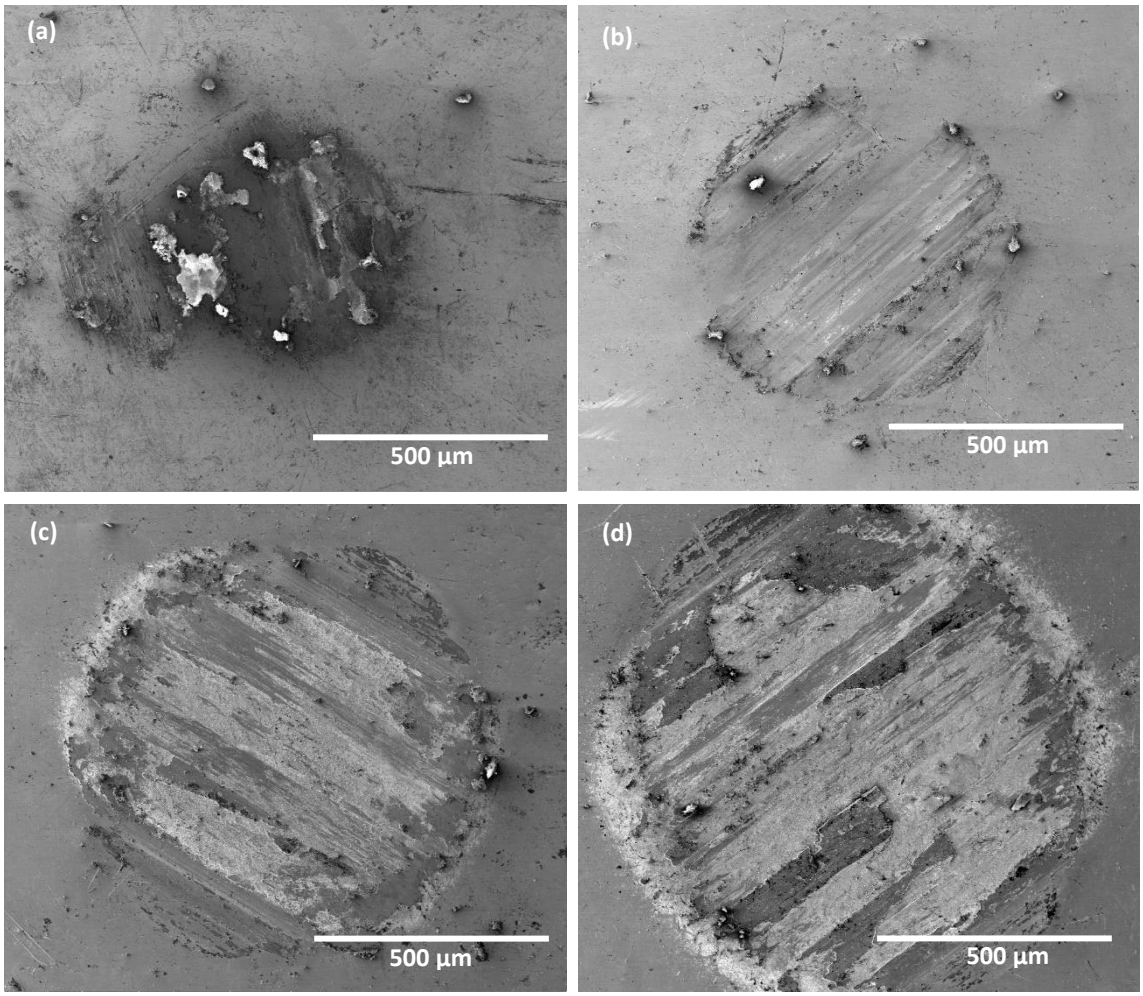

Figure 77: SEM images of wear scar for contact ball on DLC-W (a) 25ºC (b) 150ºC (c) 200ºC (d) 250ºC.

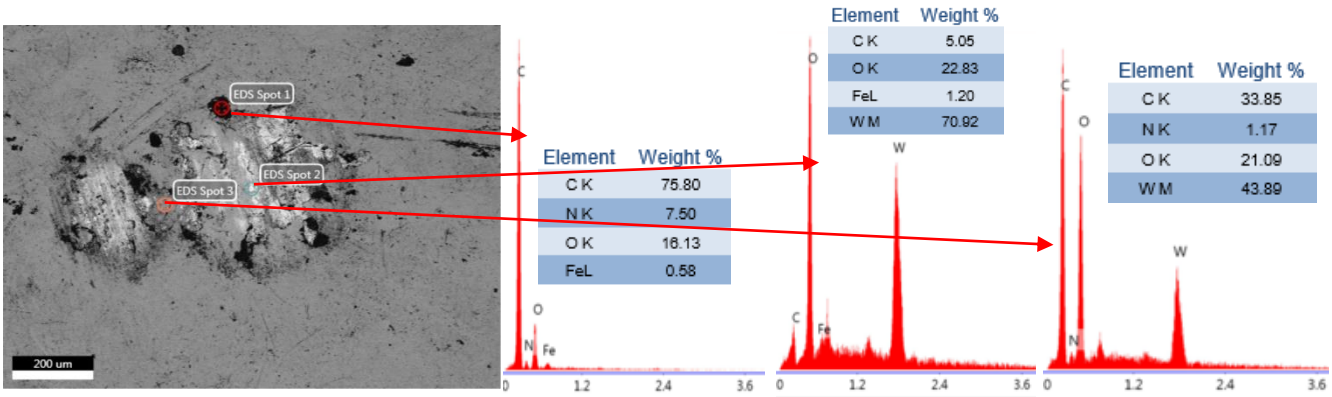

Figure 78: SEM image and EDS composition of wear scar for contact ball on DLC-W coatings.

5.9.2.2 Raman analysis of the wear track

Further investigation of the wear track (inside and outside) of CrN/DLC and DLC-W at 25 ^{o}C, 150 ^{o}C, 200 ^{o}C and 250 ^{o}C by Raman spectroscopy are shown in Figures 79 and 80. The G and D peaks, G position, ID/IG ratio were determined at 25 ^{o}C, 150 ^{o}C, 200 ^{o}C and 250 ^{o}C. The results presented in Figure 81 shows the G position (cm^{-1}) and ID/IG ratio for inside and outside the wear track at different temperatures. The result shows that for both CrN/DLC and DLC-W coatings, there were very few differences in the ID/IG and G Positions outside of the wear tracks, which may be due to the effect of small changes caused by the rise in temperature alone on the coatings, giving rise to a fluctuation in hardness and elastic modulus values at various temperatures and is in agreement with Figure 82. According to the literature, no significant phase transformation from sp^3 to sp^2 can occur until about 400^{o}C for DLC (LE HUU et al., 1996). In contrast, the ID/IG and G Positions for inside the wear tracks showed significant changes for both CrN/DLC and DLC-W coatings, which could be due to the combined effect of temperature and plastic deformation taking place simultaneously on the surface of the coatings. An increase in the ID/IG ratio and G Positions were observed for CrN/DLC and DLC-W coatings at 150 ^{o}C, 200 ^{o}C and 250 ^{o}C. At 25^{o}C, the changes that occurred were little due to possible plastic deformation during the sliding of the contact ball on the coated valve tappet. In addition, the DLC-W coatings displayed a higher increase in ID/IG ratio and G Positions at various temperatures, implying a lower hardness and elastic modulus than CrN/DLC coatings at all temperatures.

Furthermore, the appearance of an additional peak at 343 cm^{-1} (BANERJI; BHOWMICK; ALPAS, 2014) indicates the presence of iron oxide for the CrN/DLC, which

is responsible for abrasive wear in the CrN/DLC coating. On the other hand, the appearance of additional peaks at 347 cm^{-1} and 457 cm^{-1} (BANERJI; BHOWMICK; ALPAS, 2014) indicates the presence of tungsten oxide for the DLC-W coating. Sliding contact triggered the formation of a tungsten oxide rich layer, especially the formation of WO_3 (BANERJI; BHOWMICK; ALPAS, 2014; PU; HE; WANG, 2015). Therefore, the formation of tungsten oxide occurred when W particles during the sliding process become oxidized. In addition, the transfer layers containing graphitized carbon and lubricative WO_3 are responsible for the low friction at 25ºC and 150ºC, with the graphitized carbon dominating at 25ºC and while WO_3 dominates at higher temperatures (200 to 500ºC) (BANERJI; BHOWMICK; ALPAS, 2014; PU; HE; WANG, 2015).

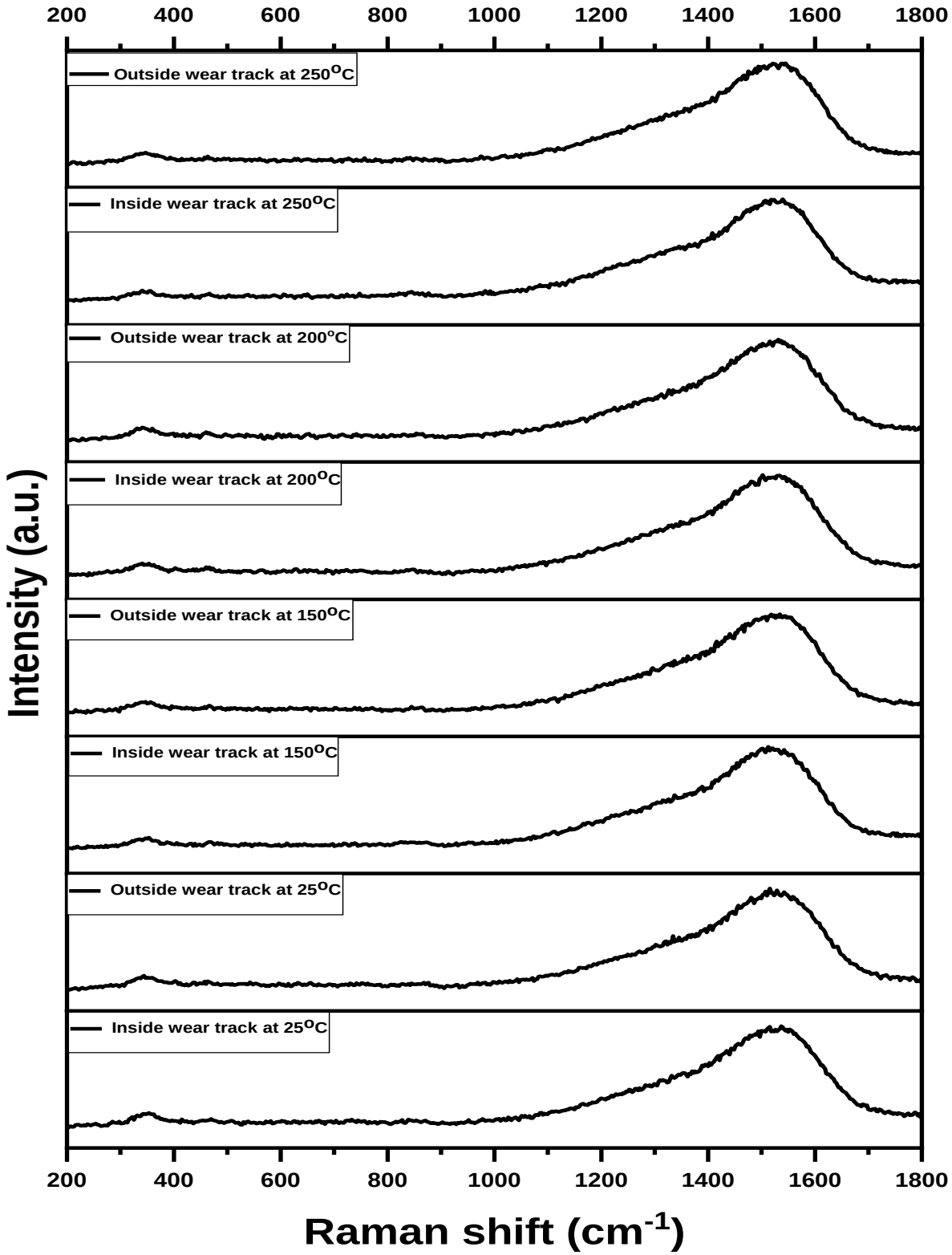

Figure 79: Raman spectra for worn CrN/DLC coatings.

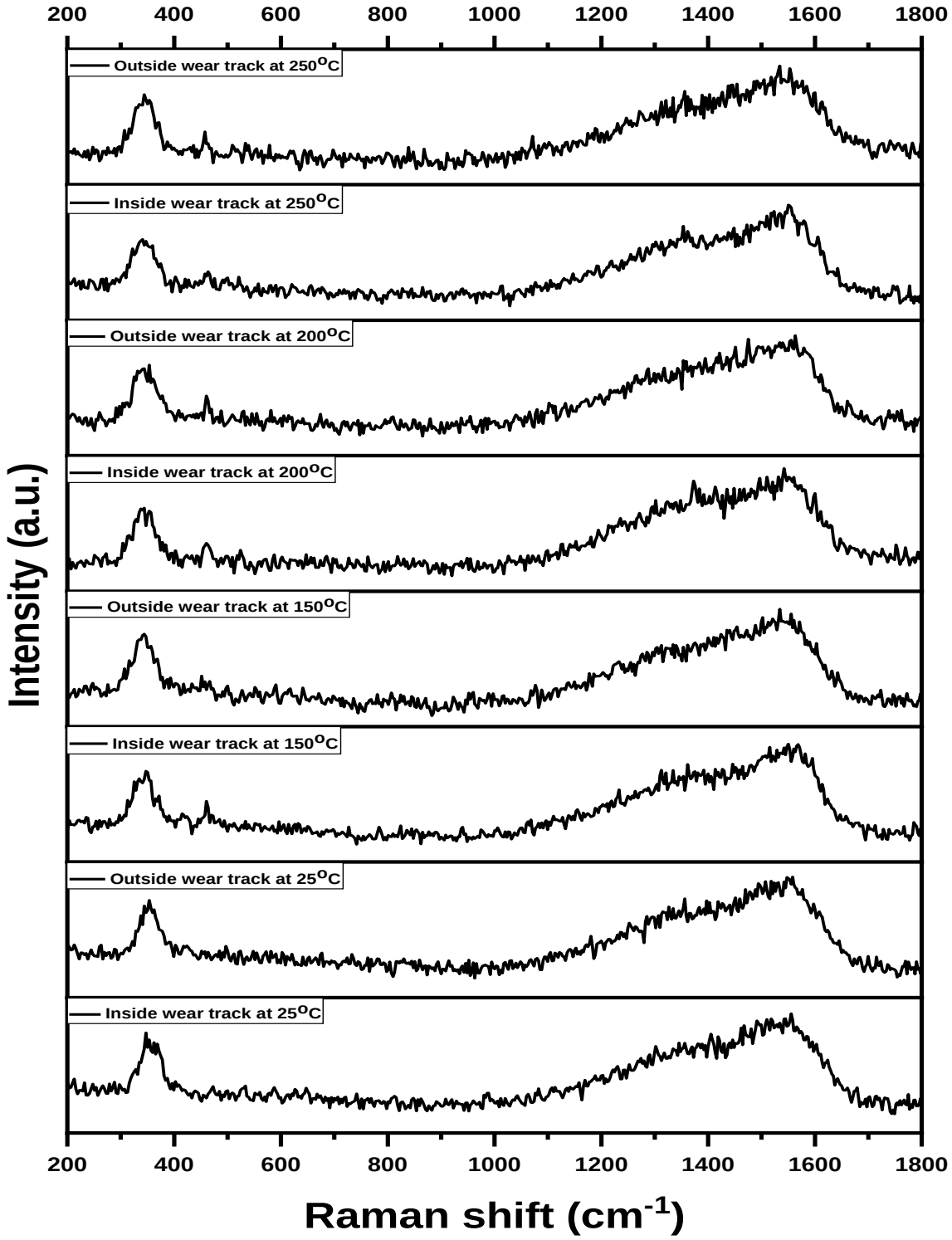

Figure 80: Raman spectra for worn DLC-W coatings.

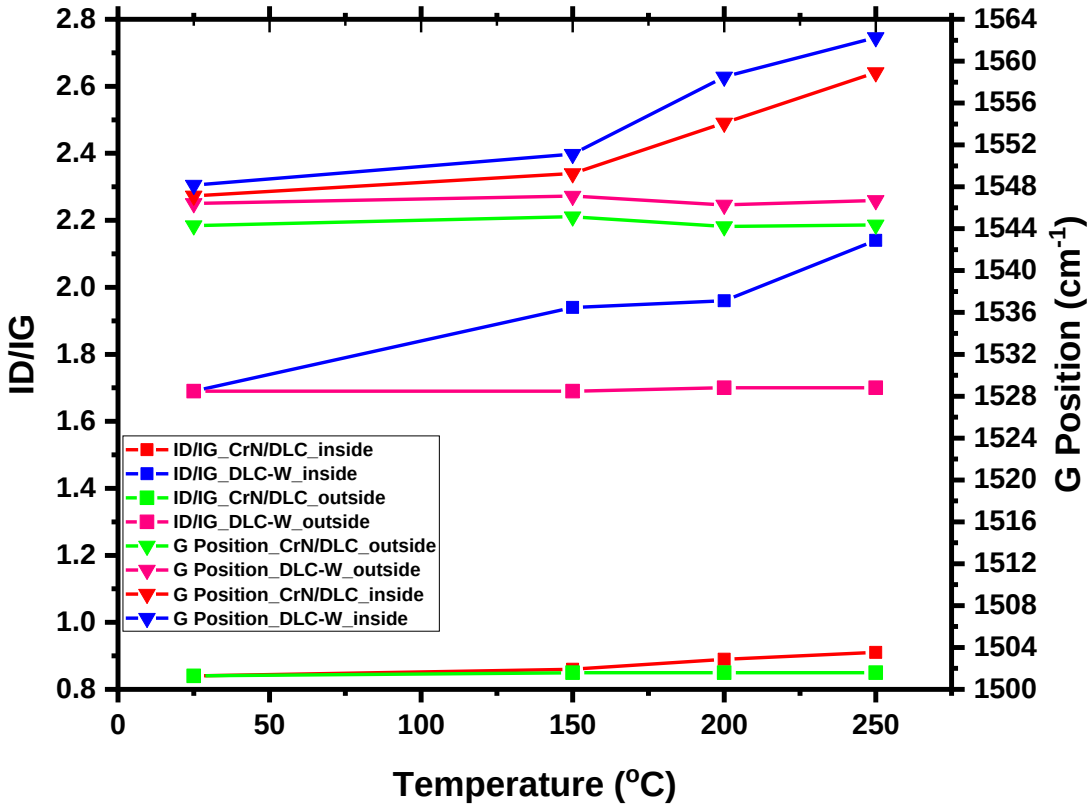

Figure 81: Effect of temperature on ID/IG ratio and G Position for CrN/DLC and DLC-W coatings.

5.9.2.3 Mechanical properties of the wear track

The mechanical properties of the wear track were further investigated for CrN/DLC and DLC-W at various temperatures as presented in Figures 82 and 83. The hardness and elastic modulus inside and outside the wear track is presented. In addition, the H^3/E^2 ratio inside and outside the wear track of the coatings at various temperatures were estimated. The H/E and H^3/E^2 values of the material reflect the elastic behavior and resistance to plastic deformation, respectively (ER YANG et al., 2019). The higher H^3/E^2 value of CrN/DLC indicates that it has a better resistance to plastic deformation. The H^3/E^2 values of the coatings are in agreement with the hardness and elastic modulus presented in Figure 82 for both inside and outside the wear track. These properties help in improving the wear rate of the coatings. There was insignificant change in the hardness, elastic modulus and H^3/E^2 for the outside of the wear track. Conversely, a reduction in the hardness value occurred inside the wear track, which was as a result of deformation during sliding of the contact ball and transformation of sp^3 to sp^2 due to the increase in temperature. The hardness values continue to decrease as the temperature increased. While, the elastic modulus increased to 200^{o}C and began to decrease. The H^3/E^2 ratio decreased drastically from 25^{o}C to 200^{o}C, and then increased slightly upto 250^{o}C. The change in mechanical properties for the CrN/DLC coatings at different temperatures maybe due to deformation, to an increase in temperature, and to an increase in the amount of C-rich transfer layers.

On the other hand, for DLC-W coatings, the hardness value inside the wear track reduced rapidly from 25^{o}C to 250^{o}C, a consequence of deformation as the temperature increased, while the elastic modulus decreased to 150^{o}C, increased to 200^{o}C and finally

decreased to 250^{o}C and H^3/E^2 ratio decreased drastically from 25^{o}C to 200^{o}C, and then increased slightly up to 250^{o}C. The change in mechanical properties for the DLC-W coatings at different temperatures may be due to deformation, increased temperature, increased amount of WC-rich transfer layers, and the presence of WO_3.

At low temperature and ambient atmosphere, DLC films saturated with hydrogen are found to be stable and inert; however, at higher temperatures and high vacuum conditions, the hydrogen present is gradually desorbed thereby creating a hydrogen free phase. At about 400^{o}C, DLC experience phase transition from sp^3 to sp^2. During sliding contacts, combined heat generated during friction and contact pressure, the critical temperature can also be dependent on the Hertzian contact pressure and internal stress of the coatings. Hydrogen desorption which arises due to friction, occurs particularly at contact asperities because of the flash temperature inducing a modification of the structure and mechanical properties of the coatings. The tribological behavior and wear rate differences of these films seem to come from the difference in sp^2/sp^3 bonding ratio and from the hydrogen and metals/non-metals incorporated in these structures (LE HUU et al., 1996).

The friction and wear performance of hydrogenated DLC coatings is due to the following properties: hydrogen present in the coatings, terminating dangling bonds in the contact, reduces the adhesion of the surface; hardness of the coating, limiting deep penetration during slide contact; sp^3 to sp^2 phase transition, consuming a large part of the friction energy in the contact and create a thin graphite layer on the surface; cleavage and softness of the graphite created on rubbing surface lubricating the sliding contact (LE HUU et al., 1996). The increasing flash temperatures at the contact asperities promotes

local chemical reactions and increases the amount of desorbed hydrogen. In this case, edge sites are multiplied and increase the adhesion between the friction surfaces, which also increases the COF. However, desorption of hydrogen from the surface continues. If hydrogen remains present on the friction track during sliding, these sites are inactive, and the COF decreases and remains low for a long period. Simultaneously, carbon atoms which co-exist on the same active sites are extremely unstable, trying to become stable structures. Active surface can also be dislocated due to the influence of the contact Hertzian pressure. It is important to note that whenever two active carbon atoms close to one another, a common sp^2 or π bond can exist in between. A reaction step by step may occur, leading to the transformation of sp^2 structure on the coatings surface. If desorption of the entire hydrogen takes place on the friction surface, the friction track will become unlubricated. The transformation of surface structure will lead to a significant increase of the friction coefficient (LE HUU et al., 1996).

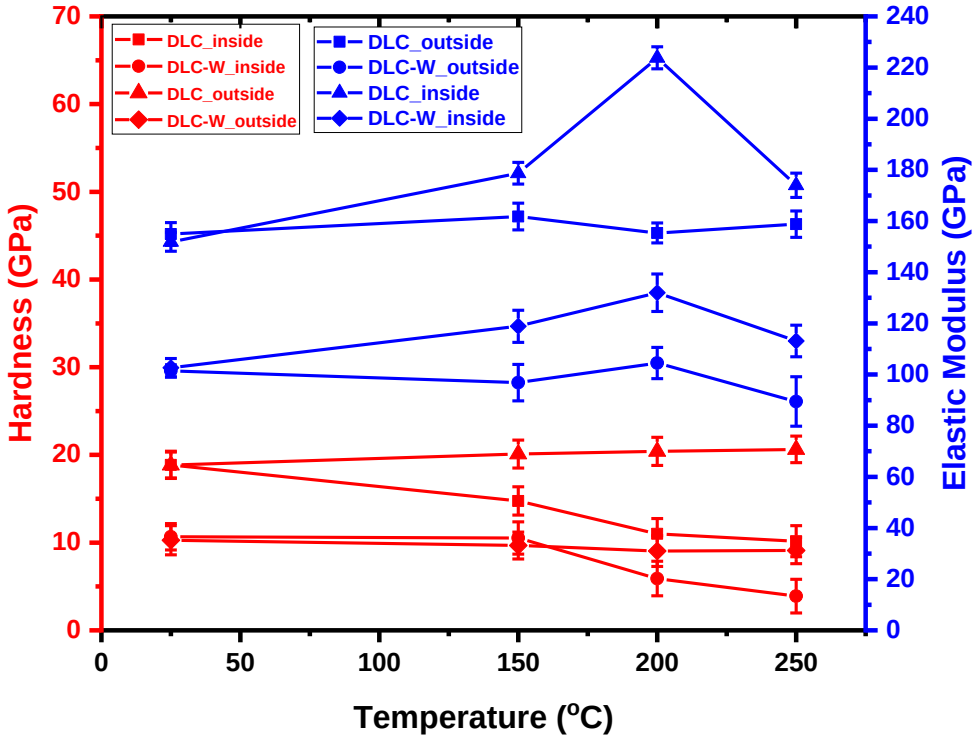

Figure 82: Hardness and Elastic modulus at different temperatures for CrN/DLC and DLC-W coatings.

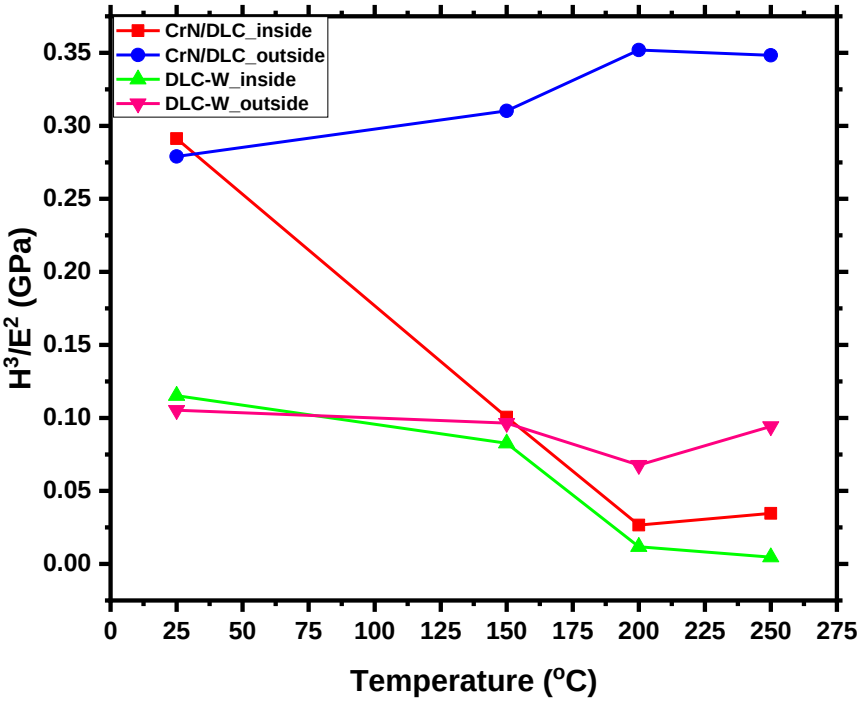

Figure 83: H^3/E^2 at different temperatures for CrN/DLC and DLC-W coatings.

6. CONCLUSIONS

The major contribution of the present thesis consists of investigating the mechanical and tribological properties of the CrN/DLC and DLC-W coatings at high temperatures (25^{o}C to 250^{o}C) on a valve tappet. The hardness and elastic modulus of the wear tracks were also studied. The conclusions to be made are drawn from the results presented in this work.

Both, CrN/DLC and DLC-W coatings exhibit excellent adhesion properties to the valve tappet substrate, both at the micro-scale and nano-scale having a hardness of 18.85 GPa and 9.88 GPa respectively, the uncoated valve tappet also had a hardness of 11.04 GPa. The Elastic recovery for the substrate, CrN/DLC and DLC-W were 31.65%, 71.04% and 67.12% respectively. AFM images revealed that the average roughness (Ra) and root mean square roughness for the uncoated valve tappet (Rq) were 2.73 nm and 4.37 nm, respectively. Both coatings possessed a nanocluster structure, however, the CrN/DLC coatings had a smoother topography compared to DLC-W. The CrN/DLC, the average roughness (Ra) – 5.77 nm and root mean square roughness (Rq) – 7.34 nm and the DLC-W had an average roughness (Ra) – 13.63 nm and root mean square roughness (Rq) – 17.49 nm. Nano-scratch were also analyzed using AFM to obtain a 3D image for CrN/DLC and DLC-W.

The results obtained from XPS and Raman suggest that CrN/DLC displayed higher sp^3 bond than DLC-W giving reason for its higher hardness. sp^2, sp^3, C-O and C=O bonds were revealed in CrN/DLC coatings and sp^2, sp^3, C-O and W-C in DLC-W from XPS analysis. ID/IG ratios for both coatings were obtained using Raman analysis. Raman was

also used to study the change in structure of the coatings in the wear track, displaying an increase in ID/IG ratio which was in agreement with the observed reduction in hardness and elastic modulus within the wear track.

TEM image of CrN/DLC with a dark top layer of DLC and a grey CrN, the CrN interlayer has a dense columnar structure with a Cauliflower shape on the top which is rough. The CrN has an amorphous interfacial region (approximately 5 nm thick) between the steel substrate and the columnar CrN. The EDS and EELS results of the CrN/DLC coating confirms the presence of C, N, Cr and O. TEM image of DLC-W with a single type multilayer, which has a columnar structure. The multilayers in the DLC-W coating have an interlaminar structure, these lamellae are rich in carbon and tungsten but, unfortunately, there are no evidences about WC carbide precipitation. The multilayer may consist of an amorphous matrix with WC nanoclusters of crystalline particles embedded which is approximately 2 nm in the WC lamellae and are equally distributed within the multilayer. EDS and EELS results of the DLC-W coating confirms the presence of C, W and O. The use of SAED to characterize the sublayers of DLC-W coatings, differentiating between the W-rich layer and the W-poor layer.

The lowest COF and wear rates for the uncoated valve tappet, CrN/DLC and DLC-W was at 25^{o}C, which increased as the temperature increased from 25^{o}C to 250^{o}C. However, the COF and wear rate of CrN/DLC was the lowest at all temperatures (25^{o}C – 250^{o}C), while the COF and wear rate of DLC-W also increased with an increase in temperature, and at 200^{o}C and 250^{o}C displayed very high wear rates, although was still lower than the wear rate and COF of the substrate at all temperatures (25^{o}C – 250^{o}C). The wear mechanism observed was mainly an abrasive wear mechanism. It was also

noticed that at high temperatures the oxidation occurs during the wear test. Tribo-layer from both coatings aided in reducing the wear during the wear. These results shows that CrN/DLC and DLC-W coatings can be successfully used at temperature up to 250^{o}C in automobile engines, but CrN/DLC having the better mechanical and tribological properties than DLC-W. However, the DLC-W coatings are beneficial under emergency situations, giving a low friction coefficient and a relative extensive lifetime.

7. SUGGESTIONS FOR FUTURE WORK

Evaluation of the wear rate and COF at small temperature intervals (25^{o}C) up to 600^{o}C, to have better understanding of the coatings performance during smaller temperature intervals. Study the effect of coating thickness of the CrN/DLC and DLC-W coatings at high temperatures. Variation of the load as a function of temperature, to determine the best load at which the coatings function optimally. Investigate the effect of Cr interlayer and WC interlayer on the mechanical and tribological properties of CrN/DLC and DLC-W coatings, respectively. To investigate the thermal cycle behavior of CrN/DLC and DLC-W coatings and their mechanical and tribological properties during the process to understand the heating and cooling behavior of the coatings. Corrosion and tribo-corrosion evaluation of the CrN/DLC and DLC-W coatings to determine their resistance against corrosion during their operations in automobile engines. Perform more characterization of the wear tracks and debris generated to understand the tribolayer mechanism.

8. BIBLIOGRAPHIC REFERENCES

ABDULLAH, T. H., et al. The effect of oil temperature and additive concentration on the wear of non-hydrogenated DLC coating. **Tribology International**, v. *77*, p. 65–71, 2014. https://doi.org/10.1016/j.triboint.2014.04.015.

AISENBERG, S.; CHABOT, R. Ion-Beam Deposition of Thin Films of Diamondlike Carbon. **Journal of Applied Physics**, v. *42, n.* 7, p. 2953–2958, 1971. https://doi.org/10.1063/1.1660654.

AL MAHMUD, K. A. H., et al. Tribological characteristics of amorphous hydrogenated (a-C: H) and tetrahedral (ta-C) diamond-like carbon coating at different test temperatures in the presence of commercial lubricating oil. **Surface and Coatings Technology**, v. 245, p. 133–147, 2014. https://doi.org/10.1016/j.surfcoat.2014.02.052.

ANSTIS, G. R., et al. Critical Evaluation of Indentation Techniques for Measuring Fracture Toughness: I, Direct Crack Measurements. **Journal of the American Ceramic Society**, v. 64, n. 9, p. 533–538, 1981. https://doi.org/10.1111/j.1151-2916.1981.tb10320.x.

ARSLAN, A., et al., Experimental investigation of tribological properties of laser textured tungsten doped diamond like carbon coating under dry sliding conditions at various loads. **Materials Research Express**, v. 6, n. 10, p. 106444, 2019. https://doi.org/10.1088/2053-1591/ab408c.

AMERICAN SOCIETY FOR TESTING AND MATERIALS. **ASTM C1624 – 05: Standard Test Method for Adhesion Strength and Mechanical Failure Modes of Ceramic Coatings by Quantitative Single Point Scratch Testing**. West Conshohocken, PA (USA): ASTM International, 2015. https://doi.org/10.1520/C1624-05R15.

AMERICAN SOCIETY FOR TESTING AND MATERIALS. **ASTM G171 Standard Test Method for Scratch Hard ness of Materials Using a Diamond Stylus**. West Conshohocken, PA (USA): ASTM International, 2009.

BAI, M., et al. Mechanical and tribological properties of Si and W doped diamond like carbon (DLC) under dry reciprocating sliding conditions. **Wear**, v. 484–485, p. 204046, 2021. https://doi.org/10.1016/j.wear.2021.204046.

BANERJI, A.; BHOWMICK, S.; ALPAS, A. T. High temperature tribological behavior of W containing diamond-like carbon (DLC) coating against titanium alloys. **Surface and Coatings Technology**, v. 241, p. 93–104, 2014. https://doi.org/10.1016/j.surfcoat.2013.10.075.

BAPTISTA, A., et al. Sputtering physical vapour deposition (PVD) coatings: A critical review on process improvement andmarket trend demands. **Coatings**, v. 8, n. 11, 2018. https://doi.org/10.3390/COATINGS8110402.

BEAKE, B. D., et al. Development of DLC coating architectures for demanding functional surface applications through nano- and micro-mechanical testing. **Surface and Coatings Technology,** v. 284, p. 334–343, 2015. https://doi.org/10.1016/j.surfcoat.2015.05.050.

BEWILOGUA, K., et al. Surface technology for automotive engineering. **CIRP Annals -**

Manufacturing Technology, v. 58, n. 2, p. 608–627, 2009. https://doi.org/10.1016/j.cirp.2009.09.001.

BEWILOGUA, K.; HOFMANN, D. History of diamond-like carbon films - From first experiments to worldwide applications. **Surface and Coatings Technology**, v. 242, p. 214–225, 2014. https://doi.org/10.1016/j.surfcoat.2014.01.031.

BHOWMICK, S.; BANERJI, A.; ALPAS, A. T. Tribological behaviour of W-DLC against an aluminium alloy subjected to lubricated sliding. **Tribology in Industry**, v. 37, n. 3, p. 277–283, 2015.

BONETTI, L. F., et al. Adhesion studies of diamond-like carbon films deposited on Ti6Al4V substrate with a silicon interlayer. **Thin Solid Films**, v. 515, n. 1, p. 375–379, 2006. https://doi.org/10.1016/j.tsf.2005.12.154.

BORGES, C. F. M.; PFENDER, E.; HEBERLEIN, J. Influence of nitrided and carbonitrided interlayers on enchanced nucleation of diamond on stainless steel 304. **Diamond and Related Materials**, v. 10, n. 11, p. 1983–1990, 2001.

BRIGGS, D.; WILEY, J. **Practical Surface Analysis by Auger and X-Ray Photoelectron Spectroscopy**, v. 1, p.1–8, 1983.

BUBENZER, A., et al. Rf-plasma deposited amorphous hydrogenated hard carbon thin films: Preparation, properties, and applications. **Journal of Applied Physics**, v. 54, n. 8, p. 4590–4595, 1983. https://doi.org/10.1063/1.332613.

BUJAK, J.; MICHALCZEWSKI, R. Characterization and properties of low-friction, multilayered Cr-doped diamond-like carbon coatings prepared by pulse biased filtered cathodic arc deposition. **Proceedings of the Institution of Mechanical Engineers, Part J: Journal of Engineering Tribology**, v. 225, n. 8, p. 875–882, 2011.

BULL, S. J. Failure modes in scratch adhesion testing. **Surface and Coatings Technology**, v. 50, n. 1, p. 25–32, 1991. https://doi.org/10.1016/0257-8972(91)90188-3.

BURNETT, P. J.; RICKERBY, D. S. The relationship between hardness and scratch adhesion. **Thin Solid Films**, v. 154, n. 1–2, p. 403–416, 1987.

CAO, H., et al. High temperature tribological performance and thermal conductivity of thick Ti/Ti-DLC multilayer coatings with the application potential for Al alloy pistons. **Diamond and Related Materials**, v. 117, p. 108466, 2021. https://doi.org/10.1016/j.diamond.2021.108466.

CAO, L., et al. Corrosion and tribocorrosion behavior of W doped DLC coating in artificial seawater. **Diamond and Related Materials**, v. 109, p. 108019, 2020. https://doi.org/10.1016/j.diamond.2020.108019.

CAPOTE, G., et al. Deposition of Adherent DLC Films Using a Low-Cost Enhanced Pulsed-DC PECVD Method. **Revista Brasileira de Aplicações de Vácuo**, v. 25, n. 4, p. 209–213, 2008.

CAPOTE, G.; MASTRAPA, G. C.; TRAVA-AIROLDI, V. J. Influence of acetylene precursor diluted with argon on the microstructure and the mechanical and tribological

properties of a-C:H films deposited via the modified pulsed-DC PECVD method. **Surface and Coatings Technology**, v. 284, p. 145–152, 2015. https://doi.org/10.1016/j.surfcoat.2015.08.065.

CASIRAGHI, C.; FERRARI, A. C.; ROBERTSON, J. Raman spectroscopy of hydrogenated amorphous carbons. **Physical Review B - Condensed Matter and Materials Physics**, v. 72, n. 8, p. 1–14, 2005. https://doi.org/10.1103/PhysRevB.72.085401.

CATHERINE, Y. **Preparation Techniques for Diamond-Like Carbon**. p. 193–227, 1991. https://doi.org/10.1007/978-1-4684-5967-8_10.

CAVALEIRO, A.; HOSSON, J. T. M. De. Nanostructured Coatings. In **Nanostructure Science and Technology,** v. 1, n. 69, 2006.

CEMIN, F.; BOEIRA, C. D.; FIGUEROA, C. A. On the understanding of the silicon-containing adhesion interlayer in DLC deposited on steel. **Tribology International**, v. 94, p. 464–469, 2016. https://doi.org/10.1016/j.triboint.2015.09.044.

CHA, S. C.; ERDEMIR, A. Coating technology for vehicle applications. **Coating Technology for Vehicle Applications**, p. 1–240, 2015.

CHOI, H. W., et al. Effects of thermal annealing and Si incorporation on bonding structure and fracture properties of diamond-like carbon films. **Diamond and Related Materials**, v. 18, n. 4, p. 615–619, 2009. https://doi.org/10.1016/j.diamond.2008.10.051.

CINIVIZ, M., et al. Ceramic Coating Applications and Research Fields for Internal Combustion Engines. **IntechOpen**, v. 7, p. 198 – 234, 2016.

COLLINS, C.; DAVANLOO, F. **The production and use of amorphic diamond**. v. 71, n. 10, 1992.

CONDE, F. F., et al. Dependence of wear and mechanical behavior of nitrocarburized/CrN/DLC layer on film thickness. **Materials Research**, v. *22,* n. 2, p. 1–10, 2019. https://doi.org/10.1590/1980-5373-MR-2018-0499.

CZYZNIEWSKI, A., et al. Microstructure and mechanical properties of W-C:H coatings deposited by pulsed reactive magnetron sputtering. **Surface and Coatings Technology**, v. 205, n. 19, p. 4471–4479, 2011. https://doi.org/10.1016/j.surfcoat.2011.03.062.

DAI, M. J., et al. Properties of W/DLC/W-S-C composite films fabricated by magnetron sputtering. **Transactions of Nonferrous Metals Society of China**, v. 25, n. 9, p. 3002–3011, 2015. https://doi.org/10.1016/S1003-6326(15)63927-9.

DEARNLEY, P. A., et al. Coatings tribology drivers for high density plasma technologies. **Surface Engineering**, v. *26, n.* 1–2, p. 80–96, 2010.

DJOUFACK, M. H., et al.Wear behaviour of hydrogenated DLC in a pin-on-disc model test under lubrication with different diesel fuel types. **Tribology International**, v. 92, p. 12–20, 2015. https://doi.org/10.1016/j.triboint.2015.05.020.

ER, K. H.; SO, M. G. Thermal annealing behavior of Si-doped diamond like-carbon films

deposited by reactive sputtering. **Journal of Ceramic Processing Research**, v. 11, n. 6, p. 760–764, 2010.

ERBULUT, D. U.; LAZOGLU, I. Biomaterials for improving the blood and tissue compatibility of total artificial hearts (TAH) and ventricular assist devices (VAD). **Biomaterials for Artificial Organs**, p. 207–235, 2010.

ERDEMIR, A.; FENSKE, G. R. Tribological performance of diamond and diamondlike carbon films at elevated temperatures. **Tribology Transactions**, v. 39, n. 4, p. 787–794, 1996. https://doi.org/10.1080/10402009608983596.

ERDEMIR, A.; DONNET, C. Tribology of diamond-like carbon films: Recent progress and future prospects. **Journal of Physics D: Applied Physics**, v. 39, n. 18, 2006. https://doi.org/10.1088/0022-3727/39/18/R01.

EVARISTO, M.; FERNANDES, F.; CAVALEIRO, A. Room and High Temperature Tribological Behaviour of W-DLC Coatings Produced by DCMS and Hybrid DCMS-HiPIMS Configuration. **Coatings**, v. 10, n. 4, p. 319, 2020. https://doi.org/10.3390/coatings10040319.

FARAJI, G.; KIM, H. S.; KASHI, H. T. **Introduction Severe Plastic Deformation**, p. 1–17, 2018. https://doi.org/10.1016/b978-0-12-813518-1.00020-5.

FEDOSENKO, G., et al. Pulsed PECVD deposition of diamond-like carbon films. **Diamond and Related Materials**, v. 11, n. 3–6, p. 1047–1052, 2002. https://doi.org/10.1016/S0925-9635(01)00612-4.

FERRARI, A. Diamond-like carbon for magnetic storage disks. **Surface and Coatings Technology**, v. 180–181, p. 190–206, 2004.

FERRARI, A. C., et al. Stress reduction and bond stability during thermal annealing of tetrahedral amorphous carbon. **Journal of Applied Physics**, v. 85, n. 10, p. 7191–7197, 1999. https://doi.org/10.1063/1.370531.

FERRARI, A. C.; ROBERTSON, J. Interpretation of Raman spectra of disordered and amorphous carbon. **Physical Review B**, v. 61, n. 20, p. 14095–14107, 2000.

FISCHER-CRIPPS, A. A review of analysis methods for submicron indentation testing. **Vacuum**, v. 58, p. 569–585, 2000. https://doi.org/10.1103/PhysRevB.61.14095.

FRANCESCHINI, D. F. Growth, structure, and properties of plasma-deposited amorphous hydrogenated carbon-nitrogen films. In **Thin Films and Nanostructures** v. 30, n. C. Elsevier Masson SAS, 2002. https://doi.org/10.1016/S1079-4050(02)80005-9.

FU, R. K. Y., et al. Thermal stability of metal-doped diamond-like carbon fabricated by dual plasma deposition. **Diamond and Related Materials**, v. 14, n. 9, p. 1489–1493, 2005. https://doi.org/10.1016/j.diamond.2005.03.006.

FU, Z. Q., et al. Influence of W content on tribological performance of W-doped diamond-like carbon coatings under dry friction and polyalpha olefin lubrication conditions. **Materials and Design**, v. 51, p. 775–779, 2013. https://doi.org/10.1016/j.matdes.2013.04.098.

GANGOPADHYAY, A. Coating technologies for automotive engine applications. **Coating Technology for Vehicle Applications**, p. 63–80, 2015. https://doi.org/10.1007/978-3-319-14771-0_4.

GHARAM, A. A., et al. High temperature tribological behavior of W-DLC against aluminum. **Surface and Coatings Technology**, v. 206, n. 7, p. 1905–1912, 2011. https://doi.org/10.1016/j.surfcoat.2011.08.002.

GRILL, A. Review of the tribology of diamond-like carbon. **Wear**, v. 168, n. 1–2, p. 143–153, 1993. https://doi.org/10.1016/0043-1648(93)90210-D.

GU, K., et al. Microstructure, mechanical and tribological properties of DLC/Cu-DLC/W-DLC composite films on SUS304 stainless steel substrates. **Materials Research Express**, v. 6, n. 8, 2019. https://doi.org/10.1088/2053-1591/ab197b.

HARDING, D. S.; OLIVER, W. C.; PHARR, G. M. Cracking during nanoindentation and its use in the measurement of fracture toughness. **Materials Research Society Symposium - Proceedings**, v. 356, p. 663–668, 1995.

HEDENQVIST, P.; HOGMARK, S. Experiences from scratch testing of tribological PVD coatings. **Tribology International**, v. 30, n. 7, p. 507–516, 1997. https://doi.org/10.1016/s0301-679x(97)00014-5.

HEF. **No Title,** 2021. https://hef-durferrit.com.br/category/material-tecnico/

HEINKE, W., et al. Evaluation of PVD nitride coatings, using impact, scratch and Rockwell-C adhesion tests. **Thin Solid Films**, v. 270, n. 1–2, p. 431–438, 1995. https://doi.org/10.1016/0040-6090(95)06934-8.

HOLMBERG, K.; ANDERSSON, P.; ERDEMIR, A. Global energy consumption due to friction in passenger cars. **Tribology International**, v. 47, p. 221–234, 2012. https://doi.org/10.1016/j.triboint.2011.11.022.

HOVSEPIAN, P. E., et al. Friction and wear behaviour of Mo-W doped carbon-based coating during boundary lubricated sliding. **Applied Surface Science**, v. 366, p. 260–274, 2016. https://doi.org/10.1016/j.apsusc.2016.01.007.

HUMPHREY, E., et al. Multiscale boundary frictional performance of diamond like carbon coatings. **Tribology International**, v. 149, p. 105539, 2020. https://doi.org/10.1016/j.triboint.2018.12.039.

IBRAHIM, T. M., et al. Enhancing vehicle's engine warm up using integrated mechanical approach. **IOP Conference Series: Materials Science and Engineering**, v. 210, n. 1, 2017. https://doi.org/10.1088/1757-899X/210/1/012064.

IRMER, G.; DORNER-REISEL, A. Micro-Raman studies on DLC coatings. **Advanced Engineering Materials**, v. 7, n. 8, p. 694–705, 2005. https://doi.org/10.1002/adem.200500006.

MOULDER, J. F., et al. **Handbook of X-ray Photoelectron Spectroscopy**, Perkin-Elmer Corporation Physical Electronics Division, US, 1992.

JANSEN, F., et al. The effects of hydrogenation on the properties of ion beam sputter deposited amorphous carbon. **Journal of Vacuum Science & Technology A: Vacuum, Surfaces, and Films**, v. 3, n. 3, p. 605–609, 1985. https://doi.org/10.1017/jmech.2016.106.

JENG, Y. R., et al. Investigation of Nano-Mechanical and- Tribological Properties of Hydrogenated Diamond Like Carbon (DLC) Coatings. **Journal of Mechanics**, v. 33, n. 6, p. 769–776, 2017. https://doi.org/10.1017/jmech.2016.106.

KANO, M. Overview of DLC-Coated Engine Components. **Coating Technology for Vehicle Applications**, p. 37–62, 2015. https://doi.org/10.1007/978-3-319-14771-0_3.

KHANMOHAMMADI, H., et al. Triboelectrochemical friction control of W- and Ag-doped DLC coatings in water–glycol with ionic liquids as lubricant additives. **RSC Advances**, v. 12, n. 6, p. 3573–3583, 2022. https://doi.org/10.1039/d1ra08814a.

KOIDL, P., et al. Plasma Deposition, Properties and Structure of Amorphous Hydrogenated Carbon Films. **Materials Science Forum**, v. 52–53, p. 41–70, 1991.

KONCA, E., et al. Elevated temperature tribological behavior of non-hydrogenated diamond-like carbon coatings against 319 aluminum alloy. **Surface and Coatings Technology**, v. 200, n. 12–13, p. 3996–4005, 2006. https://doi.org/10.1016/j.surfcoat.2005.02.202.

KONCA, E., et al. Transfer of 319 Al alloy to titanium diboride and titanium nitride based (TiAlN, TiCN, TiN) coatings: Effects of sliding speed, temperature and environment. **Surface and Coatings Technology**, v. 200, n. 7, p. 2260–2270, 2005. https://doi.org/10.1016/j.surfcoat.2004.10.008.

KRUMPIEGL, T., et al. Amorphous carbon coatings and their tribological behaviour at high temperatures and in high vacuum. **Surface and Coatings Technology**, v. 120–121, p. 555–560, 1999. https://doi.org/10.1016/S0257-8972(99)00435-1.

KRŽAN, B.; NOVOTNY-FARKAS, F.; VIŽINTIN, J. (2009). Tribological behavior of tungsten-doped DLC coating under oil lubrication. **Tribology International**, v. 42, n. 2, p. 229–235, 1999. https://doi.org/10.1016/j.triboint.2008.06.011.

KULA, P., et al. Effect of the Content of Retained Austenite and Grain Size on the Fatigue Bending Strength of Steels Carburized in a Low-Pressure Atmosphere. **Metal Science and Heat Treatment**, v. 56, n. 7–8, p. 440–443, 2014. https://doi.org/10.1007/s11041-014-9778-x.

LAWES, S. D. A.; FITZPATRICK, M. E.; HAINSWORTH, S. V. Evaluation of the tribological properties of DLC for engine applications. **Journal of Physics D: Applied Physics**, v. 40, n. 18, p. 5427–5437, 2007. https://doi.org/10.1088/0022-3727/40/18/S03.

LAWN, B. R.; FULLER, E. R. Equilibrium penny-like cracks in indentation fracture. **Journal of Materials Science**, v. 10, n. 12, p. 2016–2024, 1975. https://doi.org/10.1007/BF00557479.

LE HUU, T., et al. Transformation of sp^3 to sp^2 sites of diamond like carbon coatings during friction in vacuum and under water vapour environment. **Thin Solid Films**, v. 290–

291, p. 126–130, 1996. https://doi.org/10.1016/S0040-6090(96)09198-5.

LI, D. Scratch Hardness Measurement. **Technical Note**, p. 7, 2014.

LI, H., et al. Annealing effect on the structure, mechanical and tribological properties of hydrogenated diamond-like carbon films. **Thin Solid Films**, v. 515, n. 4, p. 2153–2160, 2006. https://doi.org/10.1016/j.tsf.2006.04.018.

LI, XIAOWEI; KE, P.; WANG, A. Probing the stress reduction mechanism of diamond-like carbon films by incorporating Ti, Cr, or W carbide-forming metals: Ab initio molecular dynamics simulation. **Journal of Physical Chemistry C**, v. 119, n. 11, p. 6086–6093, 2015. https://doi.org/10.1021/acs.jpcc.5b00058.

LI, XIN; MIAO, H.; ZHU, H. Deposition and characterization of diamond-like carbon films by electron cyclotron resonance microwave plasma enhanced unbalanced magnetron sputtering. **Chemical Engineering Transactions**, v. 66, p. 19–24, 2018. https://doi.org/10.3303/CET1866004.

LIEBERMAN, M. A.; LICHTENBERG, A. J. **Principles of Plasma Discharges and Materials Processing**: Second Edition, p. 1–757, 2005. https://doi.org/10.1002/0471724254.

LIFSHITZ, Y. Hydrogen-free amorphous carbon films: correlation between growth conditions and properties. **Diamond and Related Materials**, v. 5, n. 3–5, p. 388–400, 1996. https://doi.org/10.1016/0925-9635(95)00445-9.

LIU, Z., et al. Preparation and Characterization of Sulfurized Tungsten Doped Non-hydrogenated Diamond-Like Carbon Films. **Plasma Chemistry and Plasma Processing**, v. 35, n. 4, p. 769–783, 2015. https://doi.org/10.1007/s11090-015-9614-0.

LOUDA, P. Applications of thin coatings in automotive industry. **Journal of Achievements in Materials and Manufacturing Engineering**, v. 24, n. 1, p. 51–56, 2007.

LUKASZKOWICZ, K.; PARADECKA, A.; WIŚNIEWSKA, J. Structure and properties of CrN/DLC coating deposited by PVD ARC-cathodes and PACVD technology. **Archives of Materials Science and Engineering**, v. 64, n. 1, p. 40–44, 2013.

MA, W.; RUYS, A. J.; ZREIQAT, H. Diamond-like carbon (DLC) as a biocompatible coating in orthopaedic and cardiac medicine. **Cellular Response to Biomaterials**, p. 391–426, 2008. https://doi.org/10.1533/9781845695477.2.391.

MAEDA, T.; ENDO, F.; HOTTA, A. Highly Functionalized Polyethylene Terephthalate for Food Packaging. In **Poly(Ethylene Terephthalate) Based Blends, Composites and Nanocomposites**. Elsevier Inc, 2015. https://doi.org/10.1016/B978-0-323-31306-3.00011-7.

MALKOW, T.; BULL, S. J. Hardness measurements on thin IBAD CNx films - A comparative study. **Surface and Coatings Technology**, v. 137, n. 2–3, p. 197–204, 2001. https://doi.org/10.1016/S0257-8972(00)01101-4.

MAMUN, M. A.; AL, FURUTA, H.; HATTA, A. Pulsed DC plasma CVD system for the

deposition of DLC films. **Materials Today Communications**, v. 14, p. 40–46, 2018. https://doi.org/10.1016/j.mtcomm.2017.12.008.

MARRAY, T., et al. A Thermodynamic and Experimental Study of Low-Alloy Steels After Carbonitriding in a Low-Pressure Atmosphere. **Metal Science and Heat Treatment**, v. 56, n. 7–8, p. 434–439, 2014. https://doi.org/10.1007/s11041-014-9777-y.

MARSHALL, D. B.; LAWN, B. R. Indentation of Brittle Materials. **ASTM Special Technical Publication**, p. 26–46, 1985. https://doi.org/10.1520/stp32950s.

MATTHEWS, A., & ESKILDSEN, S. S. Engineering applications for diamond-like carbon. **Diamond and Related Materials**, v. 3, n. 4–6, p. 902–911, 1994. https://doi.org/10.1016/0925-9635(94)90297-6.

MCKENZIE, D. R. Tetrahedral bonding in amorphous carbon. **Reports on Progress in Physics**, v. 59, n. 12, p. 1611–1664, 1996. https://doi.org/10.1088/0034-4885/59/12/002.

MCKENZIE, D. R.; MULLER, D.; PAILTHORPE, B. A. Compressive-stress-induced formation of thin-film tetrahedral amorphous carbon. **Physical Review Letters**, v. 67, n. 6, p. 773–776, 1991. https://doi.org/10.1103/PhysRevLett.67.773.

MEMMING, R.; TOLLE, H. J.; WIERENGA, P. E. Properties of polymeric layers of hydrogenated amorphous carbon produced by a plasma-activated chemical vapour deposition process II: Tribological and mechanical properties. **Thin Solid Films**, v. 143, n. 1, p. 31–41, 1986. https://doi.org/10.1016/0040-6090(86)90144-6.

MIKI, H.; TAKENO, T.; TAKAGI, T. Tribological properties of multilayer DLC / W-DLC films on Si. **Thin Solid Films**, v. 516, p. 5414–5418, 2008. https://doi.org/10.1016/j.tsf.2007.07.113.

MOBARAK, H. M.; CHOWDHURY, M. Tribological performance of hydrogenated amorphous carbon (a-C: H) DLC coating when lubricated with biodegradable vegetal canola oil. **Tribology in Industry**, v. 36, n. 2, p. 163–171, 2014.

MORIGUCHI, H.; OHARA, H.; TSUJIOKA, M. History and Applications of diamond-like carbon manufacturing processes. **SEI Technical Review**, v. 82, p. 52–58, 2016.

MÜLLER, I. C., et al. Tribological response and characterization of Mo–W doped DLC coating. **Wear**, v. 376–377, p. 1622–1629, 2017. https://doi.org/10.1016/j.wear.2016.11.036.

MÜLLER, U., et al. Diamond-like carbon coatings on a CoCrMo implant alloy: A detailed XPS analysis of the chemical states at the interface. **Acta Materialia**, v. 59, n. 3, p. 1150–1161, 2011. https://doi.org/10.1016/j.actamat.2010.10.048.

MULLIGAN, C. P., et al. CrN, CrN/SiC, and CrN/DLC coatings deposited by a novel arc plasma acceleration process: Processing and properties. **Materials and Manufacturing Processes**, v. 29, n. 9, p. 1037–1043, 2014. https://doi.org/10.1080/10426914.2014.880470.

MUTAFOV, P., et al. DLC-W coatings tested in combustion engine - Frictional and wear analysis. **Surface and Coatings Technology**, v. 260, p. 284–289, 2014.

https://doi.org/10.1016/j.surfcoat.2014.06.072.

NAKAO, S., et al. Conductive diamond-like carbon films prepared by high power pulsed magnetron sputtering with bipolar type plasma based ion implantation system. **Diamond and Related Materials**, v. 77, p. 122–130, 2017. https://doi.org/10.1016/j.diamond.2017.06.011.

NIST X-RAY PHOTOELCTRON SPECTROSCOPY DATABASE, Naumkin, A.V.; Kraut-Vass, A.; Gaarenstroom, S.W.; Powell*,* C.J. **NIST Standard Reference Database** 20*, v. 4.1: htttp://srdata.nist.gov/XPS/*. (n.d.). 20.

OLIVER, W. C.; PHARR, G. M. 45{_}OliverPharr1992Nanoindentation. **Journal of Materials Research**, v. 7, n. 06, pp. 1564–1583, 1992.

PILCH, O., et al. Plasma nitriding of DIN 16MnCr5 steel. **METAL 2016 - 25th Anniversary International Conference on Metallurgy and Materials, Conference Proceedings**, p. 1145–1150, 2016.

PODGORNIK, B.; JACOBSON, S.; HOGMARK, S. DLC coating of boundary lubricated components - Advantages of coating one of the contact surfaces rather than both or none. **Tribology International**, v. 36, n. 11, p. 843–849, 2003. https://doi.org/10.1016/S0301-679X(03)00102-6.

PU, J.; HE, D.; WANG, L. Effects of WC phase contents on the microstructure, mechanical properties and tribological behaviors of WC/a-C superlattice coatings. **Applied Surface Science**, v. 357, p. 2039–2047, 2015. https://doi.org/10.1016/j.apsusc.2015.09.181.

RAO, X., et al. Tuning C–C sp^2/sp^3 ratio of DLC films in FCVA system for biomedical application. **Bioactive Materials**, v. 5, n .2, p. 192–200, 2020. https://doi.org/10.1016/j.bioactmat.2020.02.009.

RIGO, J.; FEINLE, P. **Encyclopedia of Lubricants and Lubrication**, 2014. https://doi.org/10.1007/978-3-642-22647-2.

ROBERTSON, J. Diamond-like amorphous carbon. **Materials Science and Engineering: R: Reports**, v. 37, n. 4–6, p. 129–281, 2002. https://doi.org/10.1016/s0927-796x(02)00005-0.

RONKAINEN, H., et al. Differentiating the tribological performance of hydrogenated and hydrogen-free DLC coatings. **Wear**, v. 249, n. 3–4, p. 260–266, 2001. https://doi.org/10.1016/S0043-1648(01)00558-0.

RÜBIG, B., et al. Tribological behavior of thick DLC coatings under lubricated conditions. **Surface and Coatings Technology**, v. 314, p. 13–17, 2017. https://doi.org/10.1016/j.surfcoat.2016.09.055.

SÁNCHEZ-LÓPEZ, J. C.; FERNÁNDEZ, A. Doping and alloying effects on DLC coatings. **Tribology of Diamond-Like Carbon Films: Fundamentals and Applications, DLC**, p. 311–328, 2008. https://doi.org/10.1007/978-0-387-49891-1_12.

SATTEL, S.; ROBERTSON, J.; EHRHARDT, H. Effects of deposition temperature on the

properties of hydrogenated tetrahedral amorphous carbon. **Journal of Applied Physics**, v. 82, n. 9, p. 4566–4576, 1997. https://doi.org/10.1063/1.366193.

SAVVIDES, N. Deposition parameters and film properties of hydrogenated amorphous silicon prepared by high rate dc planar magnetron reactive sputtering. **Journal of Applied Physics**, v. 55, n. 12, p. 4232–4238, 1984. https://doi.org/10.1063/1.333024.

SCHMID, G. Large metal clusters and colloids - Metals in the embryonic state. **Progress in Colloid and Polymer Science**, v. 111, p. 52–57, 1998. https://doi.org/10.1007/bfb0118109.

SCOFIELD, J. H. Hartree-Slater subshell photoionization cross-sections at 1254 and 1487 eV. **Journal of Electron Spectroscopy and Related Phenomena**, v. 8, n. 2, p. 129–137, 1976. https://doi.org/10.1016/0368-2048(76)80015-1.

SHAHSAVARI, F. et al. Nanoindentation and nanoscratch behaviors of DLC films growth on different thickness of Cr nanolayers. **Diamond and Related Materials**, v. 70, p. 76–82, 2016. https://doi.org/10.1016/j.diamond.2016.10.003.

SHIRAKURA, A., et al. Diamond-like carbon films for PET bottles and medical applications. **Thin Solid Films**, v. 494, n. 1–2, p. 84–91, 2006. https://doi.org/10.1016/j.tsf.2005.08.366.

SMITH, G. C. **Surface Analysis by Electron Spectroscopy***,* Plenum, New York, United States*,* 1994.

SNIDERMAN, D. **Coatings and Engineering Are Shaping Tomorrow ' S World**, 2016.

SOLIS, J., et al. Tribological performance of an H-DLC coating prepared by PECVD. **Applied Surface Science**, v. 383, p. 222–232, 2016. https://doi.org/10.1016/j.apsusc.2016.04.184.

TAKAHARA, Y., et al. Mesoporous tantalum oxide. 1. Characterization and photocatalytic activity for the overall water decomposition. **Chemistry of Materials**, v. 13, n. 4, p. 1194–1199, 2001. https://doi.org/10.1021/cm000572i.

TAKENO, T., et al. XPS and TEM study of W-DLC/DLC double-layered film. **Thin Solid Films**, v. 517, n. 17, p. 5010–5013, 2009. https://doi.org/10.1016/j.tsf.2009.03.033.

TAKENO, T., et al. A DLC / W-DLC multilayered structure for strain sensing applications. **Diamond and Related Materials**, v. 17, p. 713–716, 2008. https://doi.org/10.1016/j.diamond.2007.10.005.

TAKENO, T., et al. Deposition of DLC fi lm with adhesive W-DLC layer on stainless steel and its tribological properties. **Diamond & Related Materials,** v. 18, n. 5–8, p. 1023–1027, 2009. https://doi.org/10.1016/j.diamond.2009.01.029.

TANG, X. S., et al. Mo doped DLC nanocomposite coatings with improved mechanical and blood compatibility properties. **Applied Surface Science**, v. 311, p. 758–762, 2014. https://doi.org/10.1016/j.apsusc.2014.05.155.

TRAVA-AIROLDI, V. J., et al. A comparison of DLC film properties obtained by r.f. PACVD, IBAD, and enhanced pulsed-DC PACVD. **Surface and Coatings Technology**, v. 202, n. 3, p. 549–554, 2007. https://doi.org/10.1016/j.surfcoat.2007.06.030.

TREUTLER, C. P. O. Industrial use of plasma-deposited coatings for components of automotive fuel injection systems. **Surface and Coatings Technology**, v. 200, n. 5–6, p. 1969–1975, 2005. https://doi.org/10.1016/j.surfcoat.2005.08.012.

VEVERKOVA, J.; HAINSWORTH, S. V. Effect of temperature and counterface on the tribological performance of W-DLC on a steel substrate. **Wear**, v. 264, n. 7–8, p. 518–525, 2008. https://doi.org/10.1016/j.wear.2007.04.003.

VIDAKIS, N.; ANTONIADIS, A.; BILALIS, N. The VDI 3198 indentation test evaluation of a reliable qualitative control for layered compounds. **Journal of Materials Processing Technology**, v. 143–144, n. 1, p. 481–485, 2003. https://doi.org/10.1016/S0924-0136(03)00300-5.

VIJAI BHARATHY, P., et al. Reactive biased target ion beam deposited W-DLC nanocomposite thin films - Microstructure and its mechanical properties. **Diamond and Related Materials**, v. 23, p. 34–43, 2012. https://doi.org/10.1016/j.diamond.2011.12.016.

WANG, A. Y., et al. Structure and mechanical properties of W incorporated diamond-like carbon films prepared by a hybrid ion beam deposition technique. **Carbon**, v. 44, n. 9, p. 1826–1832, 2006. https://doi.org/10.1016/j.carbon.2005.12.045.

WANG, C.; SHAN, D.; GUO, B. DLC-Coated Tools for Micro-forming. In **Micromanufacturing Engineering and Technology: Second Edition,** 2015. https://doi.org/10.1016/B978-0-323-31149-6.00021-9.

WANG, D. Y.; CHANG, C. L.; HO, W. Y. Oxidation behavior of diamond-like carbon films. **Surface and Coatings Technology**, v. 120–121, p. 138–144, 1999. https://doi.org/10.1016/S0257-8972(99)00350-3.

WANG, L.; LI, L.; KUANG, X. Effect of substrate bias on microstructure and mechanical properties of WC-DLC coatings deposited by HiPIMS. **Surface and Coatings Technology**, v. 352, p. 33–41, 2018. https://doi.org/10.1016/j.surfcoat.2018.07.088.

WEI, Q., et al. Mechanical properties of diamond-like carbon composite thin films prepared by pulsed laser deposition. **Composites Part B: Engineering**, v. 30, n. 7, p. 675–684, 1999. https://doi.org/10.1016/S1359-8368(99)00035-9.

WEILER, M., et al. Deposition of tetrahedral hydrogenated amorphous carbon using a novel electron cyclotron wave resonance reactor. **Applied Physics Letters**, v. 72, n. 11, p. 1314–1316, 1998. https://doi.org/10.1063/1.121069.

WEILER, M. et al. Preparation and properties of highly tetrahedral hydrogenated amorphous carbon. **Physical Review B - Condensed Matter and Materials Physics**, v. 53, n. 3, p. 1594–1608, 1996. https://doi.org/10.1103/physrevb.53.1594.

WILD, C.; KOIDL, P. Structured ion energy distribution in radio frequency glow-discharge systems. **Applied Physics Letters**, v. 54, n. 6, p. 505–507, 1989.

https://doi.org/10.1063/1.100913.

WU, W. J.; HON, M. H. Thermal stability of diamond-like carbon films with added silicon. **Surface and Coatings Technology**, v. 111, n. 2–3, p. 134–140, 1999. https://doi.org/10.1016/S0257-8972(98)00719-1.

XUEMIN, W., Properties of W incorporated diamond-like carbon films prepared by pulsed-laser deposition. **Journal of Alloys and Compounds**, v. 479, n. 1–2, p. 741–745, 1999. https://doi.org/10.1016/j.jallcom.2009.01.044.

YANG, F. E. et al. Microstructure and properties of DLC/CNx films with different CNx sublayer thicknesses. **Surface and Coatings Technology**, v. 374, p. 418–423. https://doi.org/10.1016/j.surfcoat.2019.06.011.

YANG, L., et al. Friction reduction mechanisms in boundary lubricated W-doped DLC coatings. **Tribology International**, v. 70, p. 26–33, 2014. https://doi.org/10.1016/j.triboint.2013.09.020.

YASUDA, Y., et al. Research on diamond-like carbon coatings for low-friction valve lifters. **SAE Technical Papers**, 2003.

YONG, Q., et al. Influence of tungsten content on microstructure and properties of tungsten-doped graphite-like carbon films. **Journal of Materials Research**, v. 31, n. 23, p. 3766–3776, 2016. https://doi.org/10.1557/jmr.2016.433.

YUE, W., et al. Microstructure and friction-reducing performance of sulfurized W doped diamond-like carbon film. **Materials Letters**, v. 73, p. 202–205, 2012. https://doi.org/10.1016/j.matlet.2012.01.044.

YUE, W., et al. Effects of Tungsten Doping Contents on Tribological Behaviors of Tungsten-Doped Diamond-Like Carbon Coatings Lubricated by MoDTC. **Tribology Letters***,* 2015. https://doi.org/10.1007/s11249-015-0508-3.

ZAHID, R. et al. Effect of lubricant formulations on the tribological performance of self-mated doped DLC contacts: A review. **Tribology Letters**, v. 58, n. 2, p. 32, 2015. https://doi.org/10.1007/s11249-015-0506-5.

ZHANG, S.; BUI, X. L.; LI, X. Thermal stability and oxidation properties of magnetron sputtered diamond-like carbon and its nanocomposite coatings. **Diamond and Related Materials**, v. 15, n. 4–8, p. 972–976. 2006. https://doi.org/10.1016/j.diamond.2005.12.005.

ZHANG, T. H.; HUAN, Y. Nanoindentation and nanoscratch behaviors of DLC coatings on different steel substrates. **Composites Science and Technology**, v. 65, n. 9, p. 1409–1413, 2005. https://doi.org/10.1016/j.compscitech.2004.12.011.

ZOU, Y. S., et al. Mechanical properties and thermal stability of nitrogen incorporated diamond-like carbon films. **Vacuum**, v. 83, n. 11, p. 1406–1410, 2009. https://doi.org/10.1016/j.vacuum.2009.04.072.